UNIVERSITÄT
BAYREUTH

Clay-Based Barrier Films –

From Fundamentals to Sustainable Packaging

DISSERTATION

zur Erlangung des akademischen Grades eines

Doktors der Naturwissenschaften (Dr. rer. nat.)

in der Bayreuther Graduiertenschule für Mathematik und Naturwissenschaften

(BayNAT)

der Universität Bayreuth

vorgelegt von

Maximilian Röhrl

aus Regensburg

Bayreuth, 2023

II

Die vorliegende Arbeit wurde in der Zeit von Oktober 2019 bis Mai 2023 in Bayreuth am Lehrstuhl für Anorganische Chemie I unter Betreuung von Herrn Professor Dr. Josef Breu angefertigt.

Vollständiger Abdruck der von der Bayreuther Graduiertenschule für Mathematik und Naturwissenschaften (BayNAT) der Universität Bayreuth genehmigten Dissertation zur Erlangung des akademischen Grades eines Doktors der Naturwissenschaften (Dr. rer. nat.).

Form der Dissertation: Kumulative Dissertation

Dissertation eingereicht am: 20.06.2023

Zulassung durch das Leitungsgremium: 18.07.2023

Wissenschaftliches Kolloquium: 18.12.2023

Amtierender Direktor: Prof. Dr. Jürgen Köhler

Prüfungsausschuss:

Prof. Dr. Josef Breu (Gutachter)

Prof. Dr. Seema Agarwal (Gutachterin)

Prof. Dr. Rainer Schobert (Vorsitz)

Prof. Dr. Anna Schenk

IV

ACKNOWLEDGMENTS

Meinen Großeltern gewidmet

"How you do one thing is how you do everything."

Table of contents

Zusammenfassung

Im Jahr 2020 wurden 29,5 Millionen Tonnen „Post-Consumer"-Kunststoffabfälle in Europa gesammelt, von denen beachtliche 61% aus Verpackungsanwendungen stammen, was die Wichtigkeit von nachhaltigen Verpackungen unterstreicht. Die Sustainable Packaging Coalition® definiert nachhaltige Verpackung als eine Mischung aus breiter Nachhaltigkeit, die industrielle ökologische Ziele mit wirtschaftlichen Interessen und Strategien vereint. So sollten nachhaltige Verpackungen, um nur zwei Punkte zu nennen, die Marktkriterien für Qualität und Kosten erfüllen und zugleich den Einsatz von erneuerbaren oder recycelten Materialien vorantreiben. Wenn jedoch Kunststoffverpackungsabfälle in gemischten Abfallströmen (> 25% der gesamten Kunststoffabfälle) gesammelt werden, beträgt die Recyclingquote nur etwa 1% und beachtliche 37% der Kunststoffverpackungsabfälle landen auf Deponien. Daher ist es sinnvoll, biologisch abbaubare Verpackungsmaterialien, insbesondere Polymere, zu verwenden, wenn sie unsachgemäß in die Umwelt entsorgt werden oder auf Deponien landen. Biologisch abbaubare Polymere könnten fragmentiert und anschließend von Mikroorganismen zu CO_2, H_2O, CH_4 und Biomasse mineralisiert werden, sofern sie bestimmten Umweltbedingungen ausgesetzt werden. Allerdings ist die Verwendung biologisch abbaubarer Polymere aufgrund der unzureichenden Materialeigenschaften, insbesondere mangelnder Gasbarriereeigenschaften, begrenzt. In der Regel müssen diese durch Barrierebeschichtungen oder Laminierungen verbessert werden. Leider ist die Lösung auf die Frage, wie alle Anforderungen an Verpackungen erfüllt werden können, einschließlich der Materialeigenschaften wie Flexibilität, Transparenz, mechanische Stabilität und hervorragende Gasbarriereeigenschaften, ohne die Recyclingfähigkeit und die biologische Abbaubarkeit zu vernachlässigen, nach wie vor offen.

Es wurde eine Reihe von innovativen Konzepten erforscht, um fortschrittliche Barrierefilme mit verbesserten Eigenschaften für verschiedene Verpackungsanwendungen zu entwickeln. Barrierefilme auf Ton- oder Schichtsilikatbasis sind vielversprechend, um alle zuvor genannten Anforderungen in skalierbarer Weise miteinander zu vereinen, ohne dass die Recyclingfähigkeit oder biologische Abbaubarkeit beeinträchtigt wird. Im Rahmen dieser kumulativen Dissertation tragen die einzelnen wissenschaftlichen Publikationen zu ton-basierten Barrierefilmen dazu bei, die Schwierigkeiten und Herausforderungen zu überwinden denen sich die derzeitigen kommerziellen Ansätze für nachhaltige Verpackungen gegenübersehen.

Durch den Einsatz eines Schlitzdüsen-Beschichtungswerkzeugs konnten ton-basierte Barrierefilme mit perfekter Textur hergestellt werden. Die Verwendung der Schlitzdüse ermöglicht außerdem die Skalierung der Herstellung der Filme auf einen industriellen Maßstab mit hohem Durchsatz. Anhand umfangreicher Untersuchungen der rheologischen Eigenschaften nematischer Suspensionen eines synthetischen Hectorits (Hec) konnten die Beschichtungsparameter für die Schlitzdüse optimiert werden, was zur Herstellung von Hec-Barrierebeschichtungen führte, die sich hinsichtlich der Sauerstoffbarriere für Lebensmittelverpackungen als vielversprechend erwiesen.

Um die Umweltbedenken im Zusammenhang mit nicht abbaubarem Polyvinylalkohol (PVOH) im Abwasser auszuräumen, wurde erfolgreich eine biologisch abbaubare Alternative entwickelt. Mittels skalierbarer Schlitzdüsenbeschichtung wurde ein selbsttragendes Laminat hergestellt, das aus einer reinen Hec-Barriereschicht besteht, die zwischen zwei Schichten eines wasserlöslichen Polymers eingebettet ist. Diese wasserlöslichen Laminate weisen hervorragende optische, mechanische und Gasbarriere- Eigenschaften auf und eignen sich daher ideal für Einwegverpackungen von Konsumgütern wie Waschmitteln oder Spülmaschinentabs. Eine der Proben hat sich im Abwasser erfolgreich biologisch abgebaut, was die Eignung für wasserlösliche Verpackungsanwendungen unterstreicht, die im Abwasser ihr Lebensende finden.

Celluloseacetat-Derivate mit interessanten Eigenschaften wie dem Lotus-Effekt, hoher Transparenz und der Abbaubarkeit bei industrieller Kompostierung konnten durch quantitative Thio-Michael-Click-Reaktionen mit verschiedenen Thiolen synthetisiert werden. Die Compoundierung eines modifizierten Hec in ein Celluloseacetat-Derivat hat zu einem selbsttragenden Nanokomposit-Film geführt, der die unzureichenden Gasbarriereeigenschaften von reinen Celluloseacetat-Derivaten verbessert. Dieser Fortschritt ist vielversprechend für Lebensmittelverpackungen auf Celluloseacetatbasis.

Im Zuge des Bedürfnisses nach dehnbaren Gasbarrierefolien wurde ein perfekt geordneter und eindimensional kristalliner Nanokomposit-Film hergestellt, welcher aus abwechselnden Nano-Schichten von Polyethylenglykol und Hec-Nanoplättchen besteht. Diese einzigartige Bragg-Stack-Struktur kombiniert die hervorragenden Barriereeigenschaften von impermeablen Ton-Nanoplättchen mit der Dehnbarkeit der Polymermatrix. Ein selbsttragendes Laminat mit dem Bragg-Stack-Nanokomposit-Barrierefilm, der zwischen zwei äußeren PVOH-Schichten eingebettet ist, zeigte eine beeindruckende Dehnbarkeit von bis zu 15% ohne seine Wasserdampfbarriereeigenschaften zu verlieren. Diese Flexibilität macht das Laminat zu einer

idealen Wahl für flexible Verpackungen, bei denen herkömmliche aus der Gasphase abgeschiedene keramische oder glasartige Barriereschichten aufgrund ihrer Sprödigkeit versagen.

Darüber hinaus wurde eine Nanokomposit-Beschichtung durch Compoundierung von Hec in feuchtigkeitsempfindliches PVOH mittels Schlitzdüsen-Beschichtung hergestellt. Es konnte festgestellt werden, dass die Morphologie des Nanokomposits durch die Änderung der Trocknungstemperatur des nassen Films beeinflusst werden kann. Untersuchungen der Struktur-Eigenschafts-Beziehung zeigten auf, dass die ideal geordnete Bragg-Stack-Morphologie eine Feuchtigkeitsbeständigkeit bis zu 65% relativer Luftfeuchtigkeit aufweist, ohne eine Verschlechterung der Sauerstoffbarriere zu verzeichnen. Diese Morphologie macht das PVOH-Hec-Nanokomposit zu einer vielversprechenden Alternative zu Mikroplastik-assoziiertem Ethylen-Vinyl-Alkohol für Lebensmittelverpackungsanwendungen.

Summary

In 2020, 29.5 million tons of post-consumer plastic waste were collected in Europe, with an impressive 61% originating from packaging applications emphasizing the importance of sustainable packaging. The Sustainable Packaging Coalition® defines sustainable packaging as a blend of broad sustainability that combines industrial ecological objectives with business considerations and strategies. For instance, to name two points, sustainable packaging should meet market criteria for performance and cost while optimizing the use of renewable or recycled source materials. However, if the plastic packaging waste is collected in mixed waste streams (> 25% of total plastic waste), the recycling rate is only about 1%, and a notable 37% of plastic packaging waste ends in landfills. Consequently, it is meaningful to apply biodegradable packaging materials, particularly polymers, in case of inappropriate disposal or when finding their end-of-life at landfills. Biodegradable polymers can be fragmented and subsequently mineralized by microorganisms into CO_2, H_2O, CH_4 and biomass when exposed to certain environmental conditions. The use of biodegradable polymers is limited due to insufficient material properties, particularly inferior gas barrier properties, which usually must be enhanced with barrier coatings or laminations. Unfortunately, the overall solution to meet all mandatory packaging requirements, including material properties such as flexibility, transparency, mechanical resistance and superior gas barrier without neglecting recyclability and biodegradability, remains an open question.

A range of innovative approaches has been explored to develop advanced barrier films with improved properties for various packaging applications. Clay-based barrier films are auspicious in reconciling all mentioned requirements in a scalable manner without sacrificing recyclability or biodegradability. Within the scope of this cumulative thesis, the individual scientific publications on clay-based barrier films contribute to overcoming the problems and challenges faced by current commercial approaches to sustainable packaging.

Utilizing a slot die coating tool has enabled the production of highly textured clay-based barrier films, offering scalability to industrial production with high throughput. Extensive investigations of the rheological properties of nematic suspensions of a synthetic hectorite (Hec) have led to the optimization of operating parameters for the slot die, resulting in the production of Hec-only barrier coatings promising for food packaging in terms of the oxygen barrier properties.

To address the environmental concerns associated with non-degradable polyvinyl alcohol (PVOH) in wastewater, a biodegradable alternative has been successfully developed. A self-standing laminate has been fabricated by employing scalable slot die coating, comprising a Hec-only barrier layer sandwiched between two layers of a water-soluble polymer. These water-soluble laminates exhibit superior optical, mechanical, and gas barrier properties, making them ideal for single-use consumer goods packaging like laundry or dishwashing detergent pods and tabs. Notably, one sample has shown successful biodegradation in wastewater, highlighting its suitability for water-soluble packaging applications when finding their end-of-life in wastewater.

Cellulose acetate derivatives with interesting properties, including a Lotus effect, high transparency and disintegration under industrial composting conditions, have been synthesized through quantitative thio-Michael click reactions with various thiols. The incorporation of a modified Hec into a cellulose acetate derivative has resulted in a self-standing nanocomposite film that overcomes the insufficient gas barrier properties of neat cellulose acetate derivatives. This advancement holds excellent promise for cellulose acetate-based food packaging applications.

In the pursuit of stretchable gas barrier films, a perfectly ordered and one-dimensional crystalline nanocomposite film comprised of alternating molecular layers of polyethylene glycol and Hec nanosheets was yielded. This unique Bragg stack-type structure combines the superior barrier properties of impermeable clay nanosheets with the stretchability of the polymer matrix. A self-standing laminate with the Bragg stack nanocomposite barrier film sandwiched between two outer PVOH layers exhibited impressive stretchability of up to 15% elongation while maintaining excellent water vapor barrier properties. This flexibility makes it a favorable choice for flexible packaging where traditional vapor-deposited ceramic or glass-like barrier layers fail due to brittleness.

Furthermore, a nanocomposite coating was obtained by incorporating Hec into moisture-sensitive PVOH via slot die coating. Interestingly, it was found that the morphology of the nanocomposite can be altered by adjusting the drying temperature of the wet film. Through in-depth investigations of the structure-property relationship, the ideally ordered Bragg stack-type morphology displayed moisture resistance up to 65% relative humidity without showing oxygen barrier deterioration. This morphology renders the PVOH-Hec nanocomposite a promising alternative to ethylene vinyl alcohol, which is associated with microplastics, for food packaging.

List of abbreviations

1D	One-dimensional
CA	Cellulose acetate
CAAS18	Octadecanethiol-modified Cellulose Acetate
CAASFur	Furanyl-modified Cellulose Acetate
CW	Coating width
Δc	Concentration difference
D	Diffusion coefficient
D_0	Diffusion coefficient of neat polymer matrix
d_{001}	Basal spacing
Di	Dioctahedral sheet type
d_{inter}	Interlayer space between two adjacent nanosheets
Eq.	Equation
EVOH	Ethylene vinyl alcohol
FMCG	Fast-moving consumer goods
H	Thickness of nanoplatelet
Hec	Sodium fluorohectorite
HPMC	Hydroxypropyl methylcellulose
J	Diffusion/permeate flux
l	Film thickness
L	Lateral diameter of nanoplatelet
l'	Elongated diffusion pathway (tortuous path)
l_{wet}	Wet film thickness
$\langle N \rangle$	Mean number of nanoplatelets encountered by gas permeate
OP	Oxygen permeability
OTR	Oxygen transmission rate

P	Permeability
P&G	The Procter & Gamble Company
P_0	Permeability of neat polymer matrix
$P_{composite}$	Permeability of nanocomposite
PE	Polyethylene
PEG	Polyethylene glycol
PET	Polyethylene terephthalate
P_{rel}	Relative permeability
PVOH	Polyvinyl alcohol
Δp	Partial pressure difference
Q	Pump flow rate
RH	Relative humidity
S	Solubility coefficient
S_0	Solubility coefficient of neat polymer matrix
SAXS	Small-angle X-ray scattering
SEM	Scanning electron microscopy
SPC	Sustainable Packaging Coalition®
T	Drying temperature
TEM	Transmission electron microscopy
TGA	Thermogravimetric analysis
Tri	Trioctahedral sheet type
U	Substrate/web speed
WL	Water layer
WVP	Water vapor permeability
WVTR	Water vapor transmission rate
XRD	X-ray diffraction

Greek letters:

α	Aspect ratio of filler
μ	Geometrical factor in Cussler's equation
τ	Tortuosity
Φ	Volume content of filler

1. Introduction

1.1 Motivation

By 2021, the world has cumulatively produced an estimated 10 billion tons of plastics, which is more than one ton for every person alive today.[1-4] Between 1950 and 2015, an alarming amount of 4.9 billion tons – 60% of all plastics ever produced at that time – have been discarded or gone straight to landfills, and only 9% have been recycled (**Figure 1a**).[1] In 2021, 390.7 million tons of plastics were still produced globally, and the European plastics converters demand amounted to 50.3 million tons.[4, 5] Thereby, the European plastics industry generated a turnover of 405 billion €, ranking 8th in Europe in industrial value-added contribution.[5] Interestingly, the packaging sector, including commercial and industrial packaging, represents the largest share by far, accounting for over 39% of the total end-use market in Europe.[5] Moreover, an impressive 61% of 29.5 million tons of collected post-consumer plastics waste originated from packaging applications in 2020.[6] Unfortunately, if the plastics packaging waste is collected in mixed waste streams, accounting for 7.9 million tons (> 25% of total plastics waste), the recycling rate is only about 1%, and a notable 37% of plastics packaging waste ends in landfills.[5] It is remarkable, considering these latest data are based on a region of highly developed countries within Europe, yet vast amounts of plastic packaging waste cannot be sufficiently recycled in 2020.
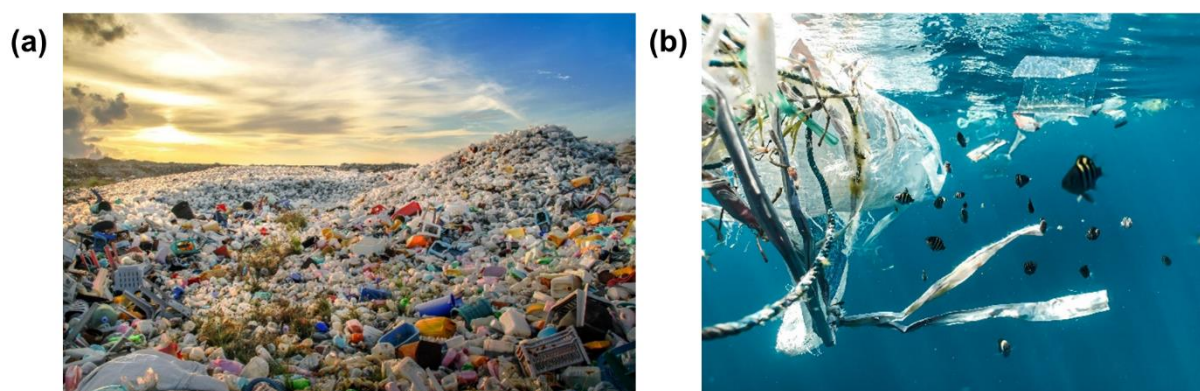
Figure 1: (a) Plastic waste at the Thilafushi Waste Disposal Site, Maldives. Reprint from Kaza et al. (Open Access).[7] Photo credit: Mohamed Abdulraheem (Shutterstock). (b) Marine plastic pollution is progressing at an alarming rate. Photo credit: Naja Bertolt Jensen (Unsplash).

Synthetic plastic waste accumulation is considered a serious environmental threat.[8] In particular, the term microplastics is causing quite a stir in the media and is mainly associated with marine pollution concerns. Facts like more than 5 trillion plastic particles are estimated to be floating across the world's surface oceans,[9] or forecasts that plastics outweigh fish by weight

in 2050 strengthen such concerns (**Figure 1b**).[10] In a conservative scenario where plastic emission stagnates at the rate of 2020, an alarming amount of 2.28 million tons of microplastic will accumulate in the surface ocean by 2050.[11] Besides inappropriate disposal into the environment, landfills may also act as non-negligible sources of microplastics.[12-14] Especially single-use plastics (plastic bags, cutlery, straws etc.) contribute to 60-95% of global marine plastic pollution.[15] Unfortunately, convenient single-use packaging such as sachets, pouches, containers or bags are very popular in Asia, and this region is responsible for more than 80% of global plastic waste emitted to the ocean.[3, 16] In the marine environment, single-use packaging items like plastic bags made from low-density polyethylene (PE) or milk bottles and laundry detergent containers made from high-density PE have estimated half-lives of a staggering 3.4 and 58 years, respectively.[17] Consequently, due to the long lifespan of most single-use plastics, marine life is at risk as marine plastic pollution can generally affect wildlife in three key encounter types: entanglement,[18, 19] ingestion,[18, 20, 21] and interaction.[3, 22] Entanglement, meaning the entrapping or encircling of marine animals by plastic debris, for instance, was found for all marine turtle species and 79% of encountering cases result in direct harm or death (**Figure 2**).[19] In comparison, ingesting plastic debris, particularly microplastic, only causes direct harm or death in 4% of cases.[19] However, in the long term, ingested microplastics have multiple impacts on organism health, such as oxidative stress,[23] metabolic disruptions,[24] reduced enzyme activity,[25] and cellular necrosis,[26] of which have been investigated in laboratory settings.[3]

Figure 2: The Hawksbill sea turtle "Little Tao" was entangled in a ghost net, missing the right front flipper and exhibiting fracture in the left front flipper. During her recovery, Little Tao excreted 144 ingested plastic pieces within two weeks that were previously mistaken as food and accidentally consumed.[27] Reprinted with permission. Photo credit: marinesavers.com

The growing accumulation of plastic waste can be described as one of the main environmental challenges currently faced by modern society.[8] At first glance, the previous facts suggest that modern plastic waste management strategies should not unexceptionally focus on recyclability or reusability but also on developing and applying materials, particularly for packaging, that can degrade in the case of improper disposal.[12]

1.2 Challenges for sustainable packaging: From the perspective of material properties

Recently, the European Commission proposed new rules on packaging within the European Green Deal, which aim to end wasteful packaging and boost reuse and recyclability.[28] In particular, the leading fast-moving consumer goods (FMCG) manufacturing companies have a responsibility to implement sustainable packaging solutions. The membership-based collaborative Sustainable Packaging Coalition® (SPC), involving renowned global players in the packaging industry, defines sustainable packaging as a blend of broad sustainability and industrial ecological objectives with business considerations and strategies:[29]

"Sustainable packaging i) is beneficial, safe & healthy for individuals and communities throughout its life cycle, ii) meets market criteria for performance and cost, iii) is sourced, manufactured, transported, and recycled using renewable energy, iv) optimizes the use of renewable or recycled source materials, v) is manufactured using clean production technologies and best practices, vi) is made from materials healthy throughout the life cycle vii) is physically designed to optimize materials and energy and viii) is effectively recovered and utilized in biological and/or industrial closed loop cycles."[29] (SPC, 2016, p. 1)

These criteria address the environmental concerns related to the value chain and life cycle of packaging by displaying the areas where transformation, innovation, and optimization are sought.[29] For instance, The Procter & Gamble Company (P&G) – a well-known FMCG manufacturer – is a member of the SPC and strives to make 100% of its consumer packaging recyclable or reusable.[30] They work on solutions so that no P&G packaging will find its way to the ocean, which they claim in their Ambition 2030.[30] Additionally, P&G aims to reduce their use of virgin petroleum-based plastics in packaging by 50% by 2030.[30]

In a nutshell, the challenge of solving plastic pollution, particularly arising from packaging, requires several targeted strategies and cannot be solved in a single approach.[12] From a materials standpoint, developing and applying sustainable packaging materials for all probable

end-of-life scenarios is relevant. The inherent stability of commodity polymers, e.g., PE or polyethylene terephthalate (PET), under thermal, chemical, and mechanical stress is a double-edged sword.[12] On the one hand, the stability of many commodity polymers, which were used to produce single-use disposable items, makes them a versatile material for a wide range of applications, on the other hand, it leads to criticism of being responsible for plastic pollution on a macro-scale as well as long-lasting microplastics.[12] In an ideal case, polymer materials should be designed to retain functionality as a commodity material for the required application period, e.g., in food packaging during storage, but degrade to non-toxic end products in a disposal environment.[31] For instance, biodegradable polymers could be released into the environment with fewer ecological concerns since they can be fragmented and subsequently mineralized by microorganisms into CO_2, H_2O, CH_4 and biomass when exposed to certain environmental conditions.[32] It is important to emphasize that biodegradation is a certified property occurring only under certain environmental conditions, i.e., a polymer being designated as biodegradable under one specific condition does not necessarily guarantee biodegradation in a different medium.[33] For instance, it was found for polycaprolactone, although it is designated as biodegradable, that no significant degradability in artificial seawater or freshwater for over one year was observed.[33] Designing sustainable packaging materials should therefore consider the presumed disposal medium.

Apparently, using biodegradable polymers for packaging applications seems to be auspicious but should not limit the recyclability and reusability of the packaging and should by no means provide a license to litter.[28] However, biodegradation of packaging materials is significant in case of improper disposal into the environment or when finding its end-of-life at landfills to counteract the growing accumulation of plastic waste. In addition, water-soluble and biodegradable polymers should be considered as materials for single-use packaging of dry consumer goods such as cosmetic powders, detergents, tablets or even food like flour, nuts or coffee powder. Since packaging made of water-soluble polymers obviously would not leave macro- or microplastic when accidentally finding its way into the ocean, the number of encounters harming marine wildlife in terms of ingestion or entanglement could additionally be decreased. Looking at those benefits, the question arises why biodegradable and/or water-soluble polymers are not yet standard for sustainable packaging applications. This leads to the general requirements for packaging materials and why undegradable and inert polymers are still widely used.

1.3 Scope and goal of the thesis: Reconciling the packaging requirements with a focus on barrier application

Besides being cheap or affordable, packaging materials are generally required to be mechanically resistant, flexible, transparent and protective against gas permeation.[34-36] The latter is especially essential in medicine or food packaging sectors, where excellent oxygen barrier properties are demanded.[35] For instance, exposing lipid or oil-rich food to oxygen can cause lipid oxidation, discoloration and off-flavor.[37, 38] Moreover, it can induce microbial spoilage, which, e.g., not only accelerates fruit aging but can also cause bacterial or fungal infections that bear some safety risks for ready-to-eat fresh products.[35] Water vapor barriers are also required, as moisture promotes crisp products to become stale. Hence, groceries may deteriorate by exposure to high levels of oxygen and moisture.[39] Considering that about 40% of all food produced spoils every year in the United States,[40] exceptional oxygen and water vapor barriers are meaningful, extending the best-before date and maintaining the freshness of food products during their determined shelf life.[35] This concludes that barrier properties of food packaging materials can significantly impact food taste, quality, longevity and marketability.[36]

Petro-based commodity polymers, e.g., PET or PE, often used as single-use plastics,[12] are ideal packaging materials as they exhibit good gas barrier properties or low gas permeabilities, respectively. For instance, PET has an oxygen permeability (OP) of ~ 1 cm^3 mm m^{-2} day^{-1} bar^{-1} at 23 °C and 50% relative humidity (RH),[41, 42] and, e.g., low-density PE has a water vapor permeability (WVP) of ~ 8 g mm m^{-2} day^{-1} bar^{-1} at 38 °C and 90% RH.[43] On the contrary, biodegradable polymers generally exhibit weak and underperforming gas barrier properties, a significant drawback limiting a wide range of applications.[41] In comparison to petro-based and non-degradable commodity polymers having either low OP (PET) or low WVP (PE), for instance, the OP of biodegradable poly(butylene adipate terephthalate) is as high as ~ 61 cm^3 mm m^{-2} day^{-1} bar^{-1} at 23 °C and 50% RH,[41] and the WVP of biodegradable polylactide is as high as ~ 166 g mm m^{-2} day^{-1} bar^{-1} at 38 °C and 90% RH.[43] Hence, improvements in gas barrier properties are necessary to be compatible with petro-based commodity plastics.[41]

This thesis focuses on developing clay-based gas barrier films to improve the barrier properties of otherwise impractical polymer films. Clay-based barrier films can be applied. e.g., as packaging for food or consumer goods, and additionally are auspicious as flexible barrier liners in hydrogen tanks.[44, 45] Within this scope, synthetic hectorite is applied either as pure clay

coating or as filler for nanocomposite films and coatings. In the case of nanocomposites, clay particles are used as fillers that are directly incorporated into a polymer matrix. Clay-based films improve the gas barrier since individual clay particles are impermeable to gas molecules and make them follow a more tortuous, i.e., extended diffusion pathway to pass through the film. The concept of the tortuous path is explained in detail in **Chapter 2.3**. In addition, the work aims to follow the 12 principles of green chemistry proposed by Anastas and Warner.[46] Herewith, the clay-based barrier films were primarily fabricated from green and aqueous processing using suspensions of superior synthetic hectorite without impurities (**Chapter 2.2**). Thereby, highly transparent clay-based barrier films were obtained, having the potential to overcome the drawbacks of current commercial state-of-the-art approaches (**Chapter 3**). There is promising research to solving the barrier issues (**Chapter 3**), however, many fail to implement them to commercial standards. Therefore, the concept of this work is based on a scalability perspective.

Figure 3: General requirements for sustainable packaging implemented within this thesis.

The cumulative thesis as a whole aims to reconcile all requirements on new materials for sustainable packaging, including scalability, flexibility, mechanical resistance, transparency, high barrier properties, and biodegradability by focusing on clay-based films (**Figure 3**). The following Theory chapter gives an overview of the fundamentals of clays, fabrication and application of clay-based barrier films required to understand subsequent scientific publications.

2. Theory

2.1 Clay Minerals: Structure, classification and economic importance

Clay minerals, also referred to as layered silicates, belong to the family of phyllosilicates (from greek phýllon 'leaf'), predominantly known for their layered crystal structure.[47] The characteristic building blocks of the layered silicates are SiO_4 tetrahedra, where three oxygen atoms form the basal plane and one the apex.[48] Within the basal plane, each tetrahedron is connected by the three oxygen corners, building an infinite layer of corner-sharing tetrahedra along the *a*, *b* crystallographic directions.[49] In an ideal configuration, the basal planes realize a hexagonal network, resulting in the least bond strain (**Figure 4a**).[48] The tetrahedral sheet has thus a composition of $SiO_{1/1}O_{3/2} = SiO_{5/2}$, Si_2O_5 respectively.[50]
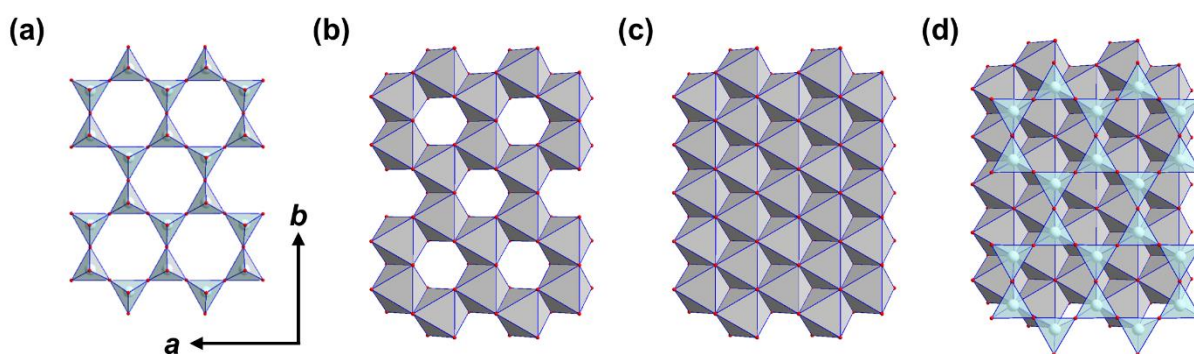
Figure 4. Structure of layered silicates along the a, b axis direction with silicon (blue) and oxygen (red). (a) Tetrahedral sheet. (b) Dioctahedral sheet – Gibbsite type. (c) Trioctahedral sheet – Brucite type. (d) Joined tetrahedral and trioctahedral sheets.

Another fundamental building block is the octahedral sheet, where connections between neighboring octahedra are made by sharing edges.[49] In principle, there are two types of octahedral sheets where either 2/3 octahedral vacancies (Gibbsite $Al(OH)_3$, BiI_3 type) or all octahedral vacancies (Brucite $Mg(OH)_2$, CdI_2 type) are occupied by cations M^{n+}.[50] These structures are referred to as di- or trioctahedral sheets (**Figure 4b, c**).[49] To complete a clay mineral layer, defined as clay lamella here, the tetrahedral and octahedral sheets are joined together.[51] Hereby, the apical oxygen atoms pointing perpendicular to the basal plane of the tetrahedral sheets are directly condensed to an octahedral sheet (**Figure 4d**).[52] The joined plane is complemented by unshared hydroxyl groups of the octahedral sheets lying at the center of each tetrahedral six-fold ring.[53] This type of structure is termed a 1:1 clay mineral where one surface of the clay lamella is entirely composed of oxygen atoms belonging to the tetrahedral sheet, while the other surface consists of hydroxyl groups of the octahedral sheet.[49] Moreover,

a 2:1 clay mineral is obtained by condensing an additional tetrahedral sheet to the opposite side of the octahedral sheet.[51] In this symmetric structure, the octahedral sheet is sandwiched by two tetrahedral sheets, and both basal surfaces contain oxygen atoms belonging to the tetrahedral sheet (**Chapter 2.2**, **Figure 5b**).[49] Hence, individual 2:1 clay lamellae are held together by only van-der-Waals interactions along the stacking direction, whereas stacks of unsymmetrical 1:1 clay lamellae are additionally retained by hydrogen bonds.[49, 53]

The clay lamella can either be neutral or negatively charged.[49] Electric neutrality is given if *i)* the tetrahedral sheet contains Si^{4+} in all tetrahedral sites, *ii)* trivalent cations M^{3+} occupy 2/3 of octahedral sites, leaving a vacancy in the third octahedral site, and *iii)* divalent cations M^{2+} occupy all octahedral sites in the octahedral sheet.[49] However, because of different geochemical formation conditions during the crystallization of natural clay minerals or special synthesis routes of synthetic clays, higher valent cations can be substituted with lower valent cations.[50] This type of isomorphous substitution results in a negative layer charge.[50] For instance, Si^{4+} can be substituted with Al^{3+} in the tetrahedral sites, or, e.g., the substitution of Al^{3+} with Zn^{2+} and Mg^{2+} with Li^+ in the octahedral sites can occur.[49] The charge balance is realized by interlayer cations or positively charged hydroxide sheets between the negatively charged clay lamellae.[50] Based on the layer charge per formula unit x (x = charge per Si_4O_{10}), the type of interlayer material and the layer structure type (1:1 or 2:1 clay mineral), clay minerals can be classified into seven major groups (**Table 1**).[54]

Because of the underlying layered structure, the cohesion between individual clay lamellae is weak compared to the in-plane ionic-covalent binding forces.[49, 53, 55] Hence, the interlayer space is available for various intracrystalline or catalytic reactions.[56] In particular, smectites feature high cationic exchange, intercalation, and swelling properties, allowing a wide variety of potential modifications and thus giving access to numerous industrial applications.[57] Other commercial applications use their inertness and stability.[56] Many industrial use cases are based on the plasticity of clays and the unique rheological properties of clay and clay mineral dispersions.[56, 58]

The economic importance of clays and clay minerals is reflected by the high revenue generated by the clay industry in the U.S., which the U.S. Geological Survey examines annually. In 2021, the mine production of clays in the United States alone was estimated to be 25 million tons of clay, valued at $1.5 billion.[59] Due to their natural abundance and low cost, they find relevance in many industrial branches such as agriculture, engineering, construction, food processing or carbon dioxide sequestration.[60] In industry, clays are distinguished into four types: *i)* bentonites,

Table 1. Classification of clay minerals (adapted from Martin et al. 1991).[63]

Layer structure type	Layer charge (x) and interlayer material	Group	Octahedral type	Examples
1:1	None or H$_2$O only x ~ 0	Serpentine-kaolin	Tri	Lizardite, Amesite
			Di	Kaolinite, Dickite
2:1	None x ~ 0	Talc-pyrophyllite	Tri	Talc, Willemseite
			Di	Pyrophyllite
	Hydrated exchangeable cations x ~ 0.2-0.6	Smectite	Tri	Hectorite, Saponite
			Di	Montmorillonite, Beidellite
	Hydrated exchangeable cations x ~ 0.6-0.9	Vermiculite	Tri	Tri. Vermiculite
			Di	Di. Vermiculite
	Non-hydrated monovalent cations x ~ 0.6-1.0	True (flexible) mica	Tri	Biotite, Lepidolite
			Di	Muscovite, Illite
	Non-hydrated divalent cations x ~ 1.8-2.0	Brittle mica	Tri	Clintonite, Anandite
			Di	Margarite
	Hydroxide sheet x ~ variable	Chlorite	Tri	Clinochlore
			Di	Donbassite

ii) kaolins, *iii)* fuller's earth, and *iv)* common clays.[61, 62] Bentonites, with their main constituent montmorillonite belonging to the smectite group,[63, 64] are mainly applied as drilling fluids, foundry sand, iron ore pelletizers, pet litters or absorbents in general.[64] Worldwide, about 18 million tons of bentonite are mined each year.[59] More than twice as much kaolin (45 million tons) is mined at the same time, with $160 per ton kaolin being currently the most expensive industrially used clay in the U.S.[59] The primary commercial application of kaolin is its use as paper coating or filler; besides that, it is utilized in paints and ceramics.[65] Fuller's earth accounts for only a small proportion of total clay production, and its main usage is as absorbents, including oil and grease or pet waste.[59] The constituent palygorskite is also employed as a thixotropic and viscosity builder in drilling fluids.[66] The industrial purpose of common clays lies mainly in the field of construction and structural products, e.g., structural and face brick, drain tile, quarry tile, vitrified clay pipes, or lightweight aggregates.[67] Over 50% (13 million tons in 2021) of total mined clays in the U.S. can be allocated to common clays alone, reflecting their commercial relevance.[59]

Clay minerals are believed to be recognized as the materials of the 21st century due to their abundance, inexpensiveness and eco-friendliness.[61] However, naturally mined and unrefined clays and clay minerals, e.g., bentonite and montmorillonite, have drawbacks such as impurities, inhomogeneities or varying and small particle sizes.[68-70] Hence, various processing steps are often required before allowing specific applications that, on the other hand, generate more costs or cause extra chemical waste.[71] Synthetic clays or clay minerals can be promising alternatives to overcome the drawbacks of natural ones. While natural clays are referred to as first-generation clays,[72] this work focuses on the barrier application of a second-generation synthetic clay (**Chapter 2.2**), where no further treatments are necessary.

2.2 The synthetic clay Sodium Fluorohectorite: Synthesis and main properties

The presented research is based on the synthetic clay sodium fluorohectorite (Hec), with the formula $[Na_{0.5}]^{inter}[Mg_{2.5}Li_{0.5}]^{oct}[Si_4]^{tet}O_{10}F_2$ that is produced by melt synthesis followed by long-term annealing.[73, 74] In the following, the already published synthesis is briefly summarized: The high-purity reagents of SiO_2, LiF, MgF_2, MgO and NaF were carefully weighed out in line with the composition corresponding to the formula. A molybdenum crucible is heated to 1600 °C inside an evacuated quartz tube using a copper high-frequency induction coil for cleaning purposes. After cleaning, the crucible is filled with the reagents inside an argon glovebox and residual water is removed by heating the crucible to 1200 °C inside the evacuated quartz tube. The crucible is then sealed with a molybdenum lid by heating it to the melting point of molybdenum using the copper induction coil. For synthesis, the crucible is placed horizontally in a graphite furnace and rotated at 1750 °C for 80 minutes under an argon atmosphere. After cooling and quenching, the synthesized Hec is ground using a planetary ball mill and subsequently dried under vacuum at 250 °C for 14 hours. The dried Hec is then filled into a cleaned molybdenum crucible inside an argon glovebox and subsequently sealed again using the copper induction coil. To improve the homogeneity of Hec, the crucible is placed inside an evacuated quartz ampule and annealed in a chamber furnace for 6 weeks at 1045 °C.

Compared to natural clay products, this melt synthesis, especially involving long-term annealing, provides advantageous properties, and the obtained Hec clay is unique in terms of particle size, charge homogeneity and purity.[74] The pristine Hec powder yields clay stacks of a mean lateral diameter of 20 µm (**Figure 5a**).[74] These so-called tactoids are built up by individual clay lamellae separated by the basal spacing d_{001} (also termed d-spacing),

representing the periodicity along the stacking direction (**Figure 5b**).[69] Thereby, the d_{001} is defined as the sum of the interlayer space and the thickness of an individual clay lamella comprising one trioctahedral and two tetrahedral sheets in the case of Hec.[63, 69] Similarly to non-charged talc,[75] wherein all octahedral sites are occupied by Mg^{2+}, upon partial isomorphic substitution of Mg^{2+} with lower-charged Li^+, a negative layer charge of 0.5 per formula unit is realized for the synthetic Hec. The negative layer charge is compensated by Na^+ cations in the interlayer space. Hence, the synthetic Hec can be classified as a 2:1 clay mineral within the group of smectites.[63]
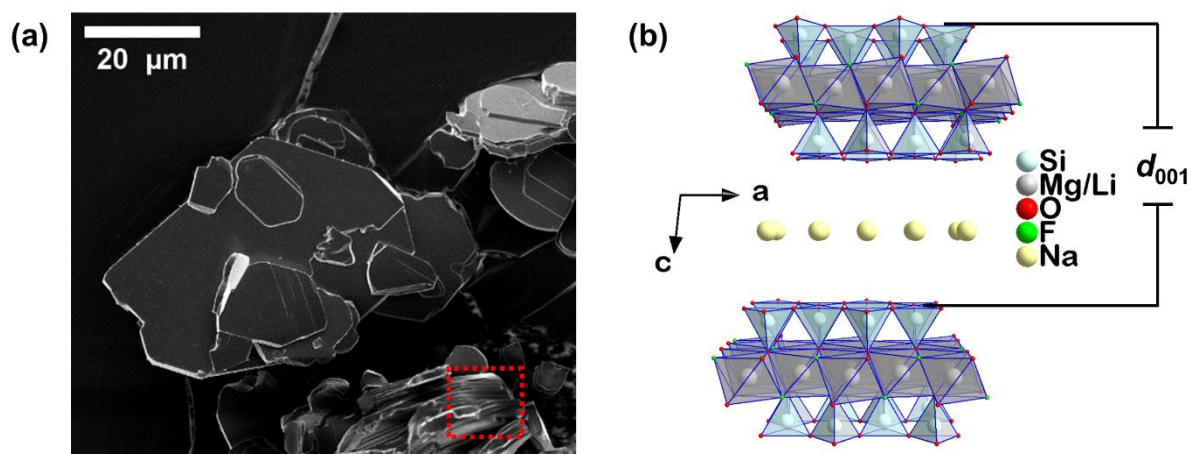
Figure 5: (a) Scanning electron microscopy (SEM) image of Sodium Fluorohectorite (Hec) tactoids after annealing. SEM sample preparation was conducted analog to a published procedure.[74] The dotted square points out a stack of Hec lamellae. (b) Crystal structure of Hec along the a, c-axis direction. Two Hec lamellae are shown, illustrating the basal spacing (d_{001}). One Hec lamella consists of two tetrahedral sheets (blue) and one trioctahedral sheet (grey).

Besides the exceptionally large diameter of Hec tactoids, the described synthesis provides a perfect distribution of isomorphous substitution, resulting in high charge homogeneity and uniform intracrytsalline reactivity.[73] This can be attributed to the synthesis temperature, which must be above 1000 K to achieve a statistical isomorphous substitution and, thus, prevent clustering of cations into domains of higher and lower charge density.[69, 76, 77]

The swelling of clay compounds yields first hints about the degree of charge homo- or heterogeneities, respectively.[69, 78] In general, swelling refers to the incorporation of neutral solvent molecules into the interlayer space, consequently leading to an expansion of the interlayer space.[69, 76] The process mainly depends on the type of interlayer cation,[79, 80] layer charge,[81] and charge homogeneity of the clay mineral.[69, 76] Belonging to the group of low-charged clay minerals, namely smectites, Hec even shows the rare phenomenon of osmotic swelling in water.[82, 83] By adding pristine Hec powder to bidistilled water, Hec tactoids

spontaneously separate into individual Hec lamellae - from now on, termed as Hec nanosheets - up to distances of hundreds of nanometers.[83, 84] The process of osmotic swelling is thermodynamically favored and requires no additional energy input.[84-87] It can simply be understood as the dissolution of ionic solids in water, and since the dissolution is obviously limited to the stacking direction of Hec nanosheets, it is termed one-dimensional (1D) dissolution.[83] The low layer charge, the uniform charge density, and the considerable enthalpy gain by hydration of the interlayer sodium cation render Hec a paradigm to explain the process of 1D dissolution in water (**Figure 6**).[83, 84]
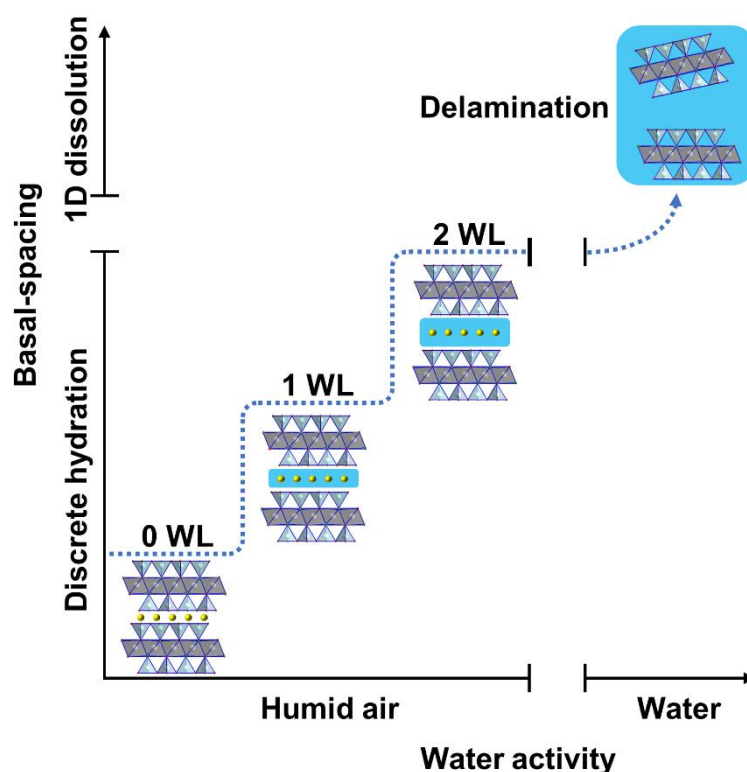
Figure 6: Transition of crystalline swelling to delamination via one-dimensional dissolution as a function of water activity. The process is exemplified for the synthetic Sodium Fluorohectorite with discrete water layers (WL) in the crystalline swelling regime. Adapted from Dudko et al. (Open Access).[83]

In the first regime at low water activity, Hec exhibits crystalline swelling where the separation of nanosheets is driven by hydration and occurs via discrete hydration steps of the interlayer sodium cation.[83, 84] In contact with humid air, the completely dried Hec transitions from a non-hydrated, i.e., no interlayer water (0 WL), to a hydrated state (1 WL) at 22% RH as indicated by adsorption isotherms.[84] Between 22% RH and 64% RH, the one water layer (1 WL) hydrate exists for Hec, involving a distinct increase in the basal spacing from 0.96 nm (0 WL) to 1.24 nm (1 WL).[74, 84] Above 64% RH, the one water layer (1 WL) transitions to two water layers (2 WL) involving an additional increase in the basal spacing of Hec from 1.24 nm (1 WL)

to 1.55 nm (2 WL).[74, 84, 88] In contrary, for natural smectites or clay minerals with lacking charge homogeneity, these discrete swelling steps are not observed, and rather interstratified domains with different hydration states simultaneously exist for any given RH reflected in a more continuous increase in the basal spacing.[69, 76, 89]

In the crystalline swelling regime, the interaction of adjacent negatively charged Hec nanosheets is attractive.[84] However, by adding Hec to bidistilled water and thus increasing the water activity, additional water molecules are intercalated, and at a certain threshold value of separation, the interlayer forces of negatively charged Hec nanosheets become repulsive.[83, 84] For Hec nanosheets, a threshold of ~ 0.87 nm (difference from d_{001}(3 WL) = 1.83 nm and d_{001}(0 WL) = 0.96 nm) must be reached. This corresponds to the three water layer (3 WL) structure (d_{001} ~ 1.83 nm) within the Gouy-Chapman regime.[84] Consequently, osmotic swelling is triggered, allowing to delaminate the entire material spontaneously into individual, single-layer Hec nanosheets of ~ 1 nm thickness separated up to hundreds of nanometers.[84] This gentle delamination procedure preserves the initial lateral diameter of ~ 20000 nm, and Hec nanosheets with an exceptional aspect ratio (ratio diameter to thickness) of 20000 are obtained.[74] Even at low concentrations (< 1 vol% of Hec in water), adjacent Hec nanosheets are hindered in rotation due to the high aspect ratio and are kept in a cofacial arrangement due to electrostatic repulsion resulting in a nematic liquid crystalline phase.[84] The homogeneity of aqueous Hec suspensions and the separation distances of adjacent Hec nanosheets are usually investigated by small-angle X-ray scattering (SAXS).

As discussed in the following chapters, the thermodynamically favored and soft top-down procedure of 1D dissolution is the ideal method to yield the maximum aspect ratio of clay nanosheets, which is essential for gas barrier application.[83] On the contrary, exfoliation describes the process of decomposition of large aggregates into smaller particles as defined by Lagaly.[90] In other words, exfoliation can be described as slicing clay tactoids into thinner stacks with multimodal thickness distributions using external forces such as mechanical shearing.[83] Please note the difference compared to the spontaneous delamination, that is, in the broad sense, the entire "exfoliation" of layered materials to the level of individual, single-layer nanosheets.[83] In this work, nematic suspensions of Hec nanosheets obtained by spontaneous delamination are the starting material for all experiments.

2.3 Polymer clay nanocomposites: Structure and permeability properties

To satisfy commercial and industrial demands on polymers, a well-known approach to modify the performances or overcome the limitations of polymers is the incorporation of fillers to obtain polymer-based nanocomposites (hybrids).[91-94] The addition of various fillers into polymers is known and can tune, e.g., the mechanical, thermal, optical or electrical properties.[91] In 1985, the first clay-based polymer nanocomposites were invented by Toyota, which introduced a new concept of polymer nanocomposites at that time.[95] Since then, polymer clay nanocomposites have been thoroughly studied and widely developed as the anisotropic and platy shape of clay particles lead to versatile and controlled properties of the resulting nanocomposites.[44, 91] For instance, incorporating clay particles can reduce flammability or enhance mechanical strength and gas barrier properties.[44]

In general, three different types of structures can be observed for polymer clay nanocomposites (**Figure 7**). The first type is the exfoliated structure, where single-layer clay nanosheets are homogeneously dispersed in a polymer matrix.[91] Hereby, relatively low filler contents are applied (< 10 wt%).[44] The second type is the phase-separated structure, where the polymer is not intercalated into the interlayer space. This type is observed mainly when the clay filler exhibits a relatively low interlayer reactivity.[91] The third type is the intercalated structure, where polymers are intercalated into the interlayer space as molecular layers between two clay nanosheets.[91]
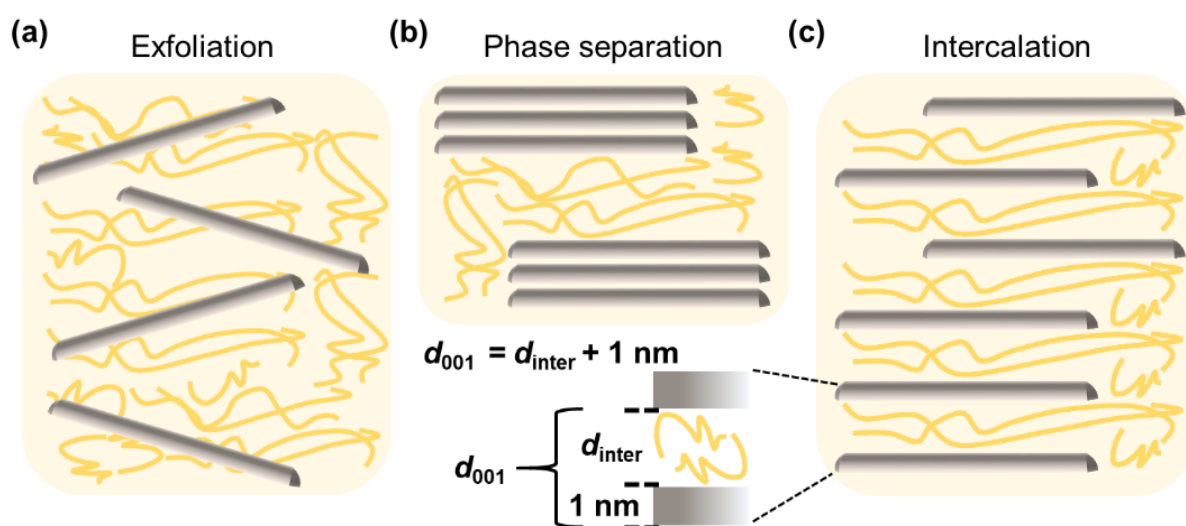
Figure 7: Sketch of the possible polymer (yellow) clay (grey) nanocomposite structures: (a) Exfoliation, (b) Phase separation, and (c) Intercalation. The inset displays the calculation of the basal spacing. The d_{001} is given by the sum of 1 nm thick clay nanosheets and d_{inter}, the interlayer space filled by intercalated polymer between two clay nanosheets. Adapted from Ogawa et al.[91]

A key parameter for the performance of polymer clay nanocomposites is the controlled dispersion of clay particles in the polymer matrices.[91] Usually, this is achieved by clay surface modifications for increased attractive interactions between polymers and clay fillers.[91] For the intercalated structure, the homogeneous distribution of individual clay nanosheets is essential since, in the ideal case, the structure comprises alternating molecular layers of polymer and clay nanosheets (**Figure 7c**). This type of structure is primarily characterized by the basal spacing d_{001} determined via X-ray diffraction (XRD).[91] Consequently, the extent of intercalated polymer in the interlayer space between two adjacent clay nanosheets (d_{inter}) can be calculated from the d_{001}, defined as the sum of 1 nm thick clay nanosheets and d_{inter} (**Figure 7**).

A convenient approach to yielding homogeneous polymer clay nanocomposites is based on a homogeneous starting material. As previously explained, nematic Hec suspensions can be obtained by immersing Hec in deionized water.[84] Mixing an aqueous suspension of utterly delaminated Hec nanosheets with water-soluble polymer results in a translationally homogeneous phase where the dissolved polymer diffuses between adjacent nanosheets that are separated up to several hundreds of nanometers.[77, 84] However, 1D dissolution for Hec is not limited to water. Recently, nematic Hec suspensions could be obtained in water-free organic solvents, also giving access to a wide range of hydrophobic polymer matrices.[96] This approach of solution blending allows high Hec (filler) loadings in polymer matrices solely defined by the ratio of Hec and polymer applied. Subsequently, films of polymer clay nanocomposites can be obtained by solution-casting the homogeneous ternary suspension with selected methods described in **Chapter 2.4**. Upon drying the wet film (solvent removal), the polymer and Hec nanosheets self-assemble in either the phase-separated (**Figure 7b**) or intercalated structure type (**Figure 7c**).[45, 97-100] In both cases, Hec stacks or individual Hec nanosheets are homogeneously distributed in the polymer matrix and, especially the intercalated structure is interesting for gas barrier applications.[44, 91]

Several factors can influence the gas barrier properties of packaging material, including external conditions like temperature and RH or material-specific characteristics like film structure, thickness, area and permeability to specific gases.[101] The quantitative evaluation of the gas barrier properties of a film generally uses the permeability (P) of the applied material.[101] In literature, P is defined as the quantification of permeate (gas molecule) transmission through a resisting material.[101, 102] In principle, the solution-diffusion model is used to understand and predict the gas permeation through polymer films/membranes and can be described as follows (**Figure 8**):[101, 103-105]

1.) Adsorption of the permeate on the surface of the polymer film (and dissolution of the permeate inside the polymer matrix).

2.) Diffusion of the permeate inside and through the polymer film/matrix (slowest and rate-determining step).

3.) Desorption of the permeate from the surface of the polymer film.
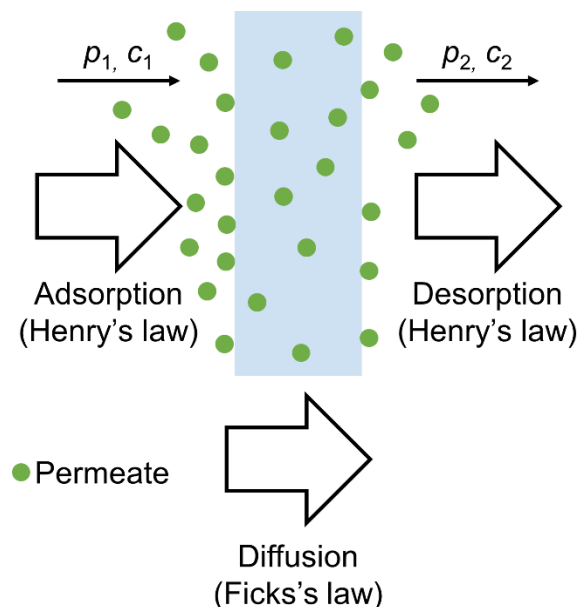
Figure 8: General gas permeation mechanism (green) through a polymer film (blue) with permeate partial pressure $p_1 > p_2$ and permeate concentration $c_1 > c_2$. Adapted from Siracusa.[101]

The gas permeation is driven by the difference in partial pressure (Δp) of the permeate ($p_1 > p_2$).[78, 101, 106] Hence, the permeate dissolves in the film matrix at the higher concentration side (c_1), diffuses through the film driven by the concentration gradient, and evaporates at the lower concentration side (c_2).[101] Gas permeation (P) for nonporous dense polymer films can therefore be expressed as the product of the diffusion coefficient (diffusivity, D) and solubility coefficient (S) using the solution-diffusion model (**Eq. 1**):[103]

$$P = D \cdot S \qquad \textbf{(Eq. 1)}$$

Combining Fick's first law of diffusion and Henry's law of solubility yields the overall equation for the permeation of small gas permeates.[103] For 1D diffusion through a polymer film and in steady-state, Ficks' first law can be written as (**Eq. 2**):[101]

$$J = -D \cdot \frac{\Delta c}{l} \qquad \textbf{(Eq. 2)}$$

Where J is the diffusion/permeate flux, Δc the concentration difference across the film, and l is the thickness of the film.[101] At steady-state, the equilibrium concentration (c) and partial pressure (p) of the gas obey Henry's law and, therefore, Δc can be replaced (**Eq. 3**):[101]

$$\Delta c = S \cdot \Delta p \qquad \textbf{(Eq. 3)}$$

Consequently, by inserting **Eq. 3** into **Eq. 2**, J becomes (**Eq. 4**):[101]

$$J = -D \cdot \frac{S \cdot \Delta p}{l} \qquad \textbf{(Eq. 4)}$$

Finally, by inserting **Eq.1** into **Eq. 4**, the permeability (P) of a polymer film can be written as (**Eq. 5**):[101]

$$P = -\frac{J \cdot l}{\Delta p} = D \cdot S \qquad \textbf{(Eq. 5)}$$

Since, in this thesis, clay-based barrier films are applied as coatings on substrates and in laminates, the contribution of individual layers to the total permeability of the laminate is crucial. In multi-layered films, the total permeability (P) can be estimated from the permeability P_i of an individual layer i with thickness l_i by (**Eq. 6**):[103]

$$\frac{1}{P} = \sum_{i=1}^{n} \frac{l_i}{P_i} \qquad \textbf{(Eq. 6)}$$

Based on the solution-diffusion model, the permeability of polymer films can be influenced in different ways. The gas permeation process can also be imagined as jumps of gas molecules through neighboring holes in the polymer matrix.[105] Herewith, the number and size of these holes (static free volume) are correlated to S, and the frequency of the jumps (dynamic free volume) is correlated to D.[105] Since S is a thermodynamic factor related to the interactions between the polymer matrix, and the gas permeates,[105] polar gas molecules, e.g., water vapor, are more soluble in hydrophilic polymer matrices and vice versa, leading to an increase or decrease in the permeability depending on the permeate-polymer matrix combination, respectively.[78] Moreover, external factors like temperature or RH influence the dynamic free volume originating from the segmental motion of polymer chains, and, e.g., softening consequently leads to increased permeability.[78, 97, 105, 107] In addition, the permeability depends on the crystallinity of the polymer, as gas molecules are insoluble in the crystalline regions and cannot permeate through these polymer crystallites.[101]

Alternatively, impermeable clay nanoplatelets (fillers) can be incorporated into the polymer matrix to decrease the permeability of a polymer film.[44, 105] In detail, the solubility coefficient (S) and the diffusion coefficient (D) are expected to decrease in the polymer clay nanocomposite due to a reduced permeable polymer matrix volume and an elongated, more tortuous path for diffusing gas permeates (**Figure 9**).[105]
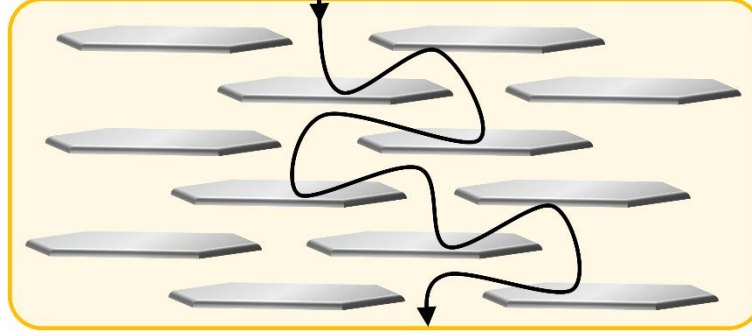
Figure 9. Reduction of gas permeability due to incorporating impermeable clay nanoplatelets (fillers) into the polymer matrix. Sketch of the tortuous path (black) for diffusing gas molecules within polymer clay nanocomposites. Adapted from Ebina.[44]

Consequently, this results in the following changes for S and D (**Eq. 7, 8**):[105]

$$S = S_0 \cdot (1 - \Phi) \qquad \textbf{(Eq. 7)}$$

$$D = \frac{D_0}{\tau} \qquad \textbf{(Eq. 8)}$$

Where S_0 and D_0 are the coefficients of the neat polymer matrix without filler. Φ is the volume content of the platy filler, and τ describes the tortuosity in the nanocomposite film, which is directly connected to the shape, size and degree of dispersion of the nanoplatelets and can be expressed as (**Eq. 9**):[105]

$$\tau = \frac{l'}{l} \qquad \textbf{(Eq. 9)}$$

Where l' is the elongated diffusion pathway (tortuous path) for a diffusing gas permeate in the nanocomposite film, and l is the thickness of the neat polymer film equivalent to the diffusion pathway of a gas permeate in the neat polymer film.[105] Inserting **Eq. 7** and **Eq. 8** into **Eq. 1** results in (**Eq. 10**):[105]

$$\frac{P_{\text{composite}}}{P_0} = \frac{1 - \Phi}{\tau} \qquad \textbf{(Eq. 10)}$$

Where $P_{composite}$ is the permeability of the nanocomposite film, and P_0 is the permeability of the neat polymer film.[105] The elongated diffusion pathway (l') can be estimated from the contribution of each nanoplatelet with lateral diameter L and the mean number of nanoplatelets $\langle N \rangle$ a gas permeate encounters diffusing through the nanocomposite film.[105] Since each nanoplatelet elongates the diffusion pathway by $L/2$ on average, l' can be expressed as (**Eq. 11**):[105]

$$l' = l + \langle N \rangle \cdot \frac{L}{2} \qquad \text{(Eq. 11)}$$

Where $\langle N \rangle$ is estimated from the thickness of the film (l), the volume content (Φ) and the thickness (H) of an individual nanoplatelet (**Eq. 12**):[105]

$$\langle N \rangle = l \cdot \frac{\Phi}{H} \qquad \text{(Eq. 12)}$$

By inserting **Eq. 12** into **Eq. 11** and combining it with **Eq. 9**, the tortuosity factor becomes (**Eq. 13**):[105]

$$\tau = 1 + \frac{\Phi}{2} \frac{L}{H} \qquad \text{(Eq. 13)}$$

It can be said that fully delaminated nanocomposites, which, for instance, is the case for Hec, display a higher tortuosity (τ) and maximum aspect ratio (α) compared to only partially exfoliated nanocomposites.[105] Considering $\alpha = L/H$ and inserting **Eq. 13** in **Eq. 10**, the derivation after Nielsen yields (**Eq. 14**):[105, 108]

$$\frac{P_{composite}}{P_0} = \frac{1 - \Phi}{1 + \frac{\alpha}{2} \cdot \Phi} \qquad \text{(Eq. 14)}$$

The equation shows that $P_{composite}$ can be decreased with increasing Φ and α. However, for $\Phi \geq$ 10 vol%, the Model of Nielsen becomes inaccurate.[105] Cussler et al. extended this approach by considering the geometrical shape of the nanoplatelets and the pores/slits into which a gas permeate must enter to diffuse through the nanocomposite film.[105, 109] Therefore, Cussler's model most accurately describes half-diluted polymer clay nanocomposite systems with clay fillers exhibiting high aspect ratios.[109] In contrast to Nielsen, the Cussler model already predicts a rapid reduction of the permeability at small volume contents Φ.[105] The Cussler equation can be expressed as follows (**Eq. 15**):[105, 109]

$$P_{\text{rel}} = \frac{P_{\text{composite}}}{P_0} = \left(1 + \mu \left(\frac{\alpha^2 \Phi^2}{1 - \Phi}\right)\right)^{-1} \qquad \text{(Eq. 15)}$$

Where P_{rel} is the relative permeability, and μ is the geometrical factor. In summary, the main factors influencing the permeability and gas barrier properties of polymer clay nanocomposites are the volume content of the clay filler, the aspect ratio of the clay filler and their orientation relative to the diffusion direction of the gas permeates.[44, 105]

2.4 Fabrication of clay-based barrier films by solution-casting

As introduced, the thesis deals with barrier films made of pure clays and polymer clay nanocomposites. In principle, there are two ways of applying clay-based films as barriers.[44] The first type comprises thin clay-based coatings that can be applied onto a polymer substrate to improve the barrier properties of the laminate. The second type is a self-supporting clay-based film. Both variants are feasible with pure clay and nanocomposites, whereby the second type is mainly related to polymer clay nanocomposites.

Polymer clay nanocomposites can generally be fabricated by melt processing, in-situ polymerization or solution-based methods.[106, 110, 111] The latter involves methods such as solution-casting, layer-by-layer assembly, Langmuir-Blodgett technique or spin-coating.[112, 113] Since only nematic suspensions of Hec are used as starting material in this work, the method of solution-casting is employed. Solution-casting processes bear the advantage of very high Hec contents in nanocomposites up to the possibility of applying pure Hec barrier films. In addition, the high aspect ratio from gentle 1D dissolution is preserved. Both criteria are essential for the application as gas barrier films (**Chapter 2.3**).[44, 83, 105] The third critical criterion for low permeabilities relies on the homogeneous dispersion of the nanoplatelet filler in the polymer matrix, where nanoplatelets are ideally aligned orthogonal to the diffusion direction ensured by suitable fabrication methods.[105, 114] In contrast, the main drawbacks of melt compounding include a limitation in filler content and a reduced aspect ratio since processing involves high mechanical shearing to achieve a homogeneous distribution of the filler, which consequently leads to the breakage of nanoplatelets.[69, 78]

The solution-casting processes used in this thesis include classic solution-casting, spray coating, doctor blade coating, and slot die coating, briefly described in the following (**Figure 10**). All embodiments have in common that the nematic Hec suspension is cast onto a flat surface followed by solvent evaporation (**Figure 10**).[112] Water as a solvent enables environmentally

friendly processing. However, organic solvents could also be used, as solvent vapor recovery and recycling are feasible on an industrial scale.[115, 116] Upon drying, Hec nanosheets settle on the flat surface or, in the case of polymer Hec nanocomposites, self-assemble into one of the discussed structures (**Figure 7**). Subsequently, if a self-supporting film is desired, it can be peeled off the flat surface/substrate. Alternatively, a thin Hec-based film is applied as a barrier coating, enhancing the barrier properties of the substrate/laminate. The thickness of the resulting film can be varied by the concentration of Hec in the nematic suspension.
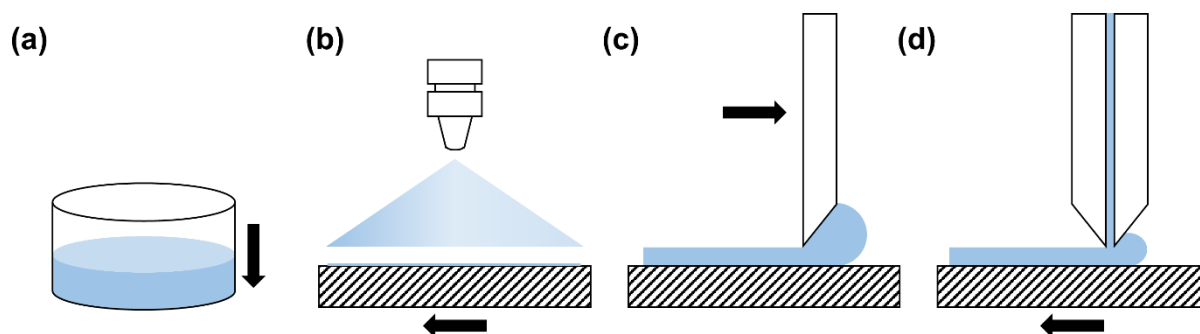
Figure 10: Fabrication methods of clay-based barrier films employing solution-casting: (a) Classic solution-casting. (b) Spray coating. (c) Doctor blade coating. (d) Slot die coating.

Classic solution-casting:

The classic approach is casting the nematic Hec suspension into a container that, e.g., can be a Petri or Teflon dish (**Figure 10a**). Due to its simplicity, it is suitable for first experiments at lab scale. However, Hec nanosheets tend to fold,[117] and the desired orientation of the nanosheets orthogonal to the diffusion direction may be insufficient. Furthermore, smooth drying conditions and extended drying times are necessary as Hec nanosheets develop a sealing barrier layer since the film dries from the surface to the core, hindering further solvent evaporation. This bears the risk of trapping solvent in the film and creating defects upon drying that impair the barrier performance of the film.[118]

Spray coating:

Another solution-casting method is to spray a dilute nematic Hec suspension onto a substrate surface (**Figure 10b**). [45, 119] In the spraying process, coating and subsequent drying occur in several cycles. The drying problem with classic solution-casting mentioned above is negligible in spray coating since only small amounts of suspension are applied in each cycle, resulting in homogeneous drying.[120] Additionally, the sequential application of many thin layers reduces the likelihood of defects in the final Hec-based barrier film. Moreover, spraying is not limited to flat surfaces, and 3D objects can also be coated.[78] However, one significant disadvantage of

this process is the time required to produce a Hec-based barrier film. Since cyclic deposition means that only very thin coatings are progressively applied with already diluted nematic Hec suspensions, the time factor is considerable for thicker coatings.[78]

Doctor blade coating:

In the case of doctor blade coating, the nematic Hec dispersion is applied pre-metered on the substrate and subsequently drawn/coated over the substrate using a doctor blade (**Figure 10c**). This process can be fully automated or be employed manually (box-shaped, wire bar).[118, 121] Since the doctor blade exerts shear forces during the coating process, the Hec nanosheets preferably align parallel to the substrate. The time factor is negligible compared to spray coating, and the film can be produced in a single step. However, upon drying, the wet film suffers from a sealing effect similar to classic solution-casting.[78, 118] Moreover, it was found for a polymer Hec nanocomposite that a less 1D crystalline nanocomposite film was obtained by doctor blading compared to spray coating.[42]

Slot die coating:

Slot die coating is a versatile process widely used for producing uniform films and is mainly applied for manufacturing thin films and electrodes, e.g., in polymer electrolyte fuel cells, solar cells, and lithium-ion batteries.[122] However, the method is relatively new in the production of polymer clay nanocomposites and barrier coatings. During the slot die coating process, the nematic Hec suspension is delivered through a fixed slot width onto a moving substrate, filling the coating gap between the lips of the die and the substrate (**Figure 10d**). Since slot die coating is a pre-metered process, the wet film thickness (l_{wet}) can be precisely controlled by the flow rate of the liquid fed to the die (pump flow rate, Q), the substrate/web moving speed (U), and the coating width (CW) (**Eq. 16**):[122]

$$l_{\text{wet}} = \frac{Q}{U \cdot CW} \qquad \textbf{(Eq. 16)}$$

Slot die coating is a complex process, and the main challenge is to find the optimum operating parameters, such as coating speed, flow rate, and coating gap and combine them with the characteristics of the coating fluid, such as surface tension, liquid viscosity, and rheological properties.[122] Moreover, the substrate must be considered regarding wetting problems or surface roughness. For instance, the coating window is a popular concept for determining operating limits.[122] Outside of the coating window, defects can occur, including air entrainment or break lines.[122, 123]

However, the complexity makes it a broadly applicable coating tool, and once the operating parameters have been established at the laboratory scale, they can be easily transferred to an industrial scale, where slot die coating is employed in roll-to-roll processing. Another advantage of slot die coating for Hec-based barrier films is the high shear forces applied to the nematic Hec suspension during the coating process, perfectly aligning Hec nanosheets parallel to the substrate.[124] The Hec nanosheets remain in this position upon drying, and remarkable oxygen barrier properties have been obtained.[124]

2.5 Principle of a water vapor barrier measurement
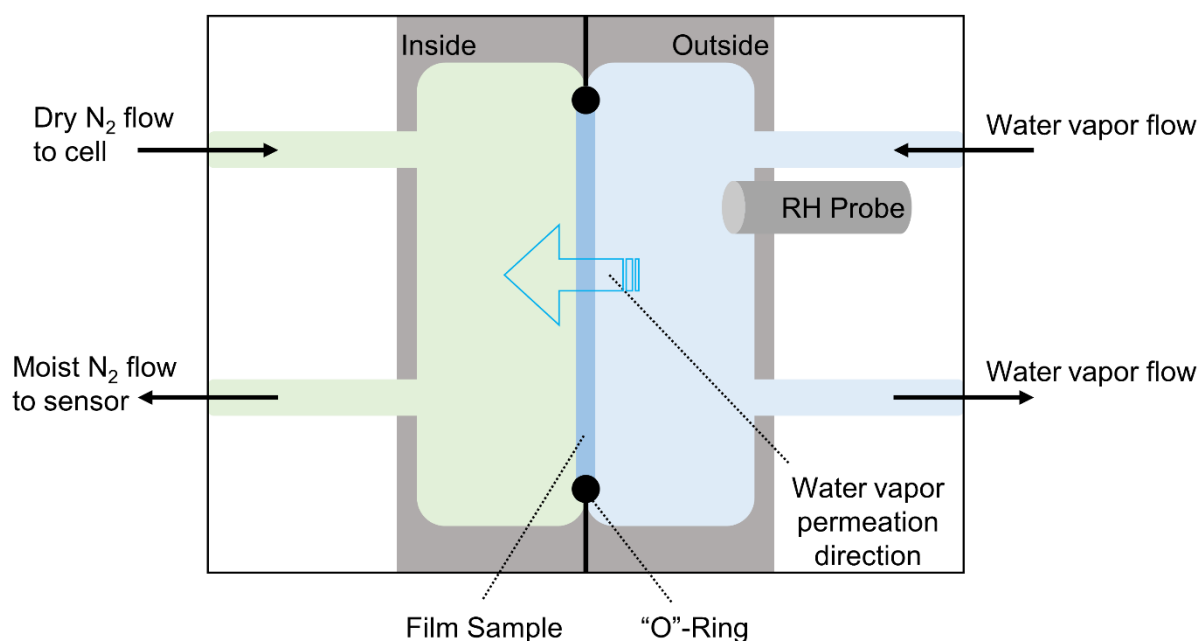
Figure 11: Principle of a water vapor barrier measurement employing a Mocon Permatran-W® 3/33 with automatic relative humidity generation. The film sample separates the inside and outside chambers. High vacuum grease and a rubber O-Ring seal the test cell. Adapted from Mocon instrumental.[125]

Gas barrier properties are demanded in low-tech areas, e.g., as introduced for food packaging,[35] and high-tech areas, e.g., encapsulation of oxygen- and moisture-sensitive solar cells and organic light-emitting diodes.[78] To investigate gas barrier properties, instruments are applied that measure gas transmission rates. The principle is exemplified for a water vapor barrier measurement using a Mocon Permatran-W® 3/33 (**Figure 11**) complying with ASTM F1249.[125] The Mocon Permatran-W® 3/33 system utilizes a patented modulated infrared sensor to detect water vapor transmission in flat materials and packages with outstanding sensitivity in parts per million.[125] The flat film sample is positioned in a test cell divided into two chambers, separated by the film sample, to perform the test. The outer chamber is filled with water vapor (test gas), while the inner chamber is filled with nitrogen (carrier gas). The RH/concentration

of the test gas is automatically generated and cross-checked by an RH probe. The water molecules, transported to the outer chamber by the test gas, diffuse through the film to the inner chamber and are then carried to the sensor by the carrier gas (for details on permeation see **Chapter 2.3**).[125] It is important to ensure adequate conditioning until an equilibrated water vapor concentration gradient is achieved. The computer tracks the increase in water vapor concentration in the carrier gas and displays the value on the screen as the water vapor transmission rate (WVTR) in g m^{-2} day^{-1}.[125]

WVTR values are more relevant for commercial applications but depend on the thickness of the film. By multiplying the WVTR with the thickness of the film (*l*) and considering the water vapor partial pressure difference (*Δp*) on both film sides, the WVP can be calculated by (**Eq. 17**):[103]

$$WVP = \frac{WVTR \cdot l}{\Delta p} \qquad\qquad \textbf{(Eq. 17)}$$

This equation is similar to **Eq. 5**, and the WVP can be used to compare different materials with varying thicknesses. However, this is subject to some errors since a linear dependence of WVP on thickness is assumed, which is questioned in the literature and not necessarily true for WVP.[119, 126]

3. Synopsis

In commercial practice, the barrier properties of plastics are generally enhanced by coatings or lamination processes.[36, 41] Impermeable aluminum foils or metalized coatings provide excellent gas barrier properties owing to the metallic crystal structure and low porosity.[36] However, metalized laminates are hard to recycle, do not break down in the environment in the case of improper disposal and come with transparency issues.[36] Alternatively, if transparency is desired, thin ceramic Al_2O_3 or glass-like SiO_x coatings can be applied by vapor deposition, forming high water vapor and oxygen barriers.[34, 127, 128] But such thin inorganic coatings suffer from brittleness and poor flex and crack resistance, consequently generating pinholes and destroying the barrier integrity.[34, 36] The high cost of these materials and the vulnerability to mechanical stress renders the plastic laminate only suitable for special applications.[34, 36] Alternatively, coatings of water-soluble polymers in laminates are attractive because they offer mechanical flexibility and can be easily washed off, facilitating recycling processes. Furthermore, e.g., water-soluble polyvinyl alcohol (PVOH) exhibits an exceptionally low OP of 0.02 cm^3 mm m^{-2} day^{-1} bar^{-1} at 23 °C and dry conditions (0% RH).[34] However, a PVOH barrier is prone to swelling and humid conditions because when the RH is increased from 0% to 90% RH, the OP concomitantly increases by a staggering three orders of magnitude.[129] To counteract the moisture-induced OP deterioration rendering PVOH barrier coatings unusable in real-world applications that require at least 65% RH, ethylene vinyl alcohol (EVOH) is commercially used. The hydrophobicity and onset of swelling of an EVOH barrier can be fine-tuned by adjusting the ethylene content.[130] EVOH is transparent and flexible, accessible in large amounts, and provides good OP at the relevant 65% RH.[130, 131] However, it is known to be not degradable, and EVOH-correlated microplastics were found in seafood, drinking water and beach sediments.[132-134]

The current industrial approaches to improving the barrier properties of plastic materials are still unsatisfactory, and innovative solutions are needed to reconcile all requirements for sustainable packaging materials. The development of new barrier technologies is broadly diversified, encompassing many branches, e.g., material and polymer science, engineering, physics, and chemistry. Research to improve gas barriers is carried out on *i)* the material properties such as tailoring polymer structure, cross-linking, crystallization or orientation, *ii)* using blends of polymers or advanced multi-layers, e.g., layer-by-layer assembly, *iii)* employing innovative processing techniques or putting established coating methods in a new context and *iv)* applying new materials, additives or fillers to produce polymer

nanocomposites.[34-36, 41] Especially the latter is a promising approach involving materials such as graphene oxide, cellulose nanomaterials, and clays.[35, 36, 41] As discussed within the scope of the thesis (**Chapter 1.3**), this work focuses on clay-based barrier films overcoming the drawbacks of current industrial approaches and trying to reconcile all requirements for sustainable packaging.

The present cumulative thesis contains five scientific publications (**Figure 12**). In the first part of the thesis, pure Hec barrier films are investigated with a focus on scalability and biodegradability (**Chapters 6.1** and **6.2**). In the second part of the thesis, polymer Hec nanocomposite barrier films are discussed with a focus on biodegradability, flexibility, and moisture resistance (**Chapters 6.3**, **6.4**, and **6.5**). All Hec-based barrier films are highly transparent, allowing for visual inspection of packaged goods, which is a significant advantage compared to metalized and, thus, non-transparent polymer films.

- In **Chapter 3.1**, the publication "Shear orientation of nematic phases of clay nanosheets: processing of barrier coatings" (**Chapter 6.1**) is presented.[124] The coating tool of a slot die was established to produce Hec-based barrier films easily transferable to an industrial scale at high throughput. The rheological properties of nematic Hec suspensions were investigated, and the results were subsequently used to identify ideal operating parameters for the slot die to produce highly textured Hec-only barrier coatings interesting for food packaging.

- In **Chapter 3.2**, the publication "Green and scalable processing of water-soluble, biodegradable polymer/clay barrier films" (**Chapter 6.2**) is presented.[135] A biodegradable barrier film was obtained as a substitute for non-biodegradable PVOH in the medium wastewater. A self-standing laminate comprised of a Hec-only barrier layer sandwiched between two layers of a water-soluble polymer was fabricated by scalable slot die coating. The water-soluble self-standing laminates possess superior optical, mechanical and barrier properties, making them auspicious for single-use consumer goods packaging such as laundry and detergent pods or dishwasher tabs. One sample has successfully biodegraded in wastewater, the end-of-life medium for this application.

- In **Chapter 3.3**, the publication "New Functional Polymer Materials via Click Chemistry-Based Modification of Cellulose Acetate" (**Chapter 6.3**) is presented.[117] Cellulose acetate acrylate underwent quantitative thio-Michael click reactions with various thiols providing functional cellulose acetate (CA) polymers with interesting

properties such as a Lotus effect, high transparency and disintegration under industrial composting conditions. Incorporating a modified Hec into a CA derivative yields a self-standing nanocomposite film overcoming the insufficient barrier properties of neat CA derivatives, making it promising for food packaging.

- In **Chapter 3.4**, the publication "Stretchable Clay Nanocomposite Barrier Film for Flexible Packaging" (**Chapter 6.4**) is presented.[120] A perfectly ordered and 1D crystalline nanocomposite barrier film was obtained with alternating layers of polyethylene glycol (PEG) and Hec nanosheets. This Bragg stack-type structure combines the best of two worlds: The superior barrier properties of the clay and the stretchability of the polymer. The self-standing laminate with the Bragg stack nanocomposite barrier film sandwiched between two outer PVOH layers is stretchable up to 15% elongation, almost not displaying any WVTR deterioration. This renders it auspicious for flexible packaging where vapor-deposited ceramic or glass-like barrier layers fail due to brittleness.

- In **Chapter 3.5**, the publication "Disorder–Order Transition—Improving the Moisture Sensitivity of Waterborne Nanocomposite Barriers" (**Chapter 6.5**) is presented.[97] By incorporating Hec into moisture-sensitive PVOH, a nanocomposite barrier coating was obtained via slot die coating, for which the drying temperature can alter the nanocomposite morphology. Studying the structure-property relationship of the nanocomposites revealed an ideally ordered Bragg stack morphology to be moisture resistant, reflected by no OP deterioration up to 65% RH. This morphology positions the PVOH Hec nanocomposite as an ideal candidate to replace EVOH for food packaging, which is associated with microplastic concerns.
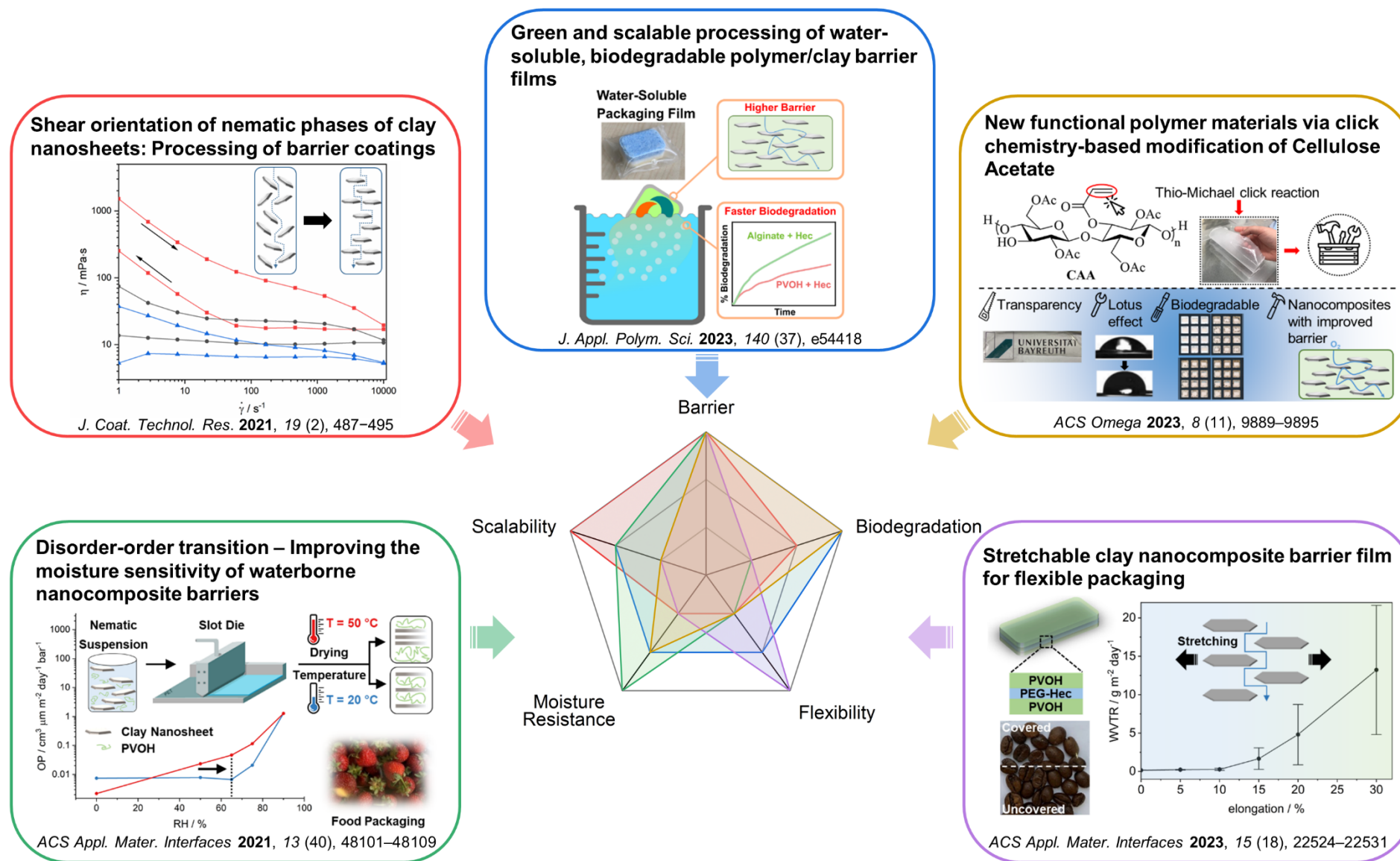
Figure 12. Graphical synopsis of the cumulative thesis presenting the five scientific publications reconciling the packaging requirements. Reprinted with permission.

3.1 Shear orientation of nematic phases of clay nanosheets: Processing of barrier coatings

The current applications and prospects of flow-induced alignment in composite materials have recently been reviewed.[136] Texturing via shear forces has been effectively applied for fabricating composite films with nanosheet fillers.[137-139] However, the methods used for this purpose are restricted to low shear rates and can be challenging to scale up, such as in the case of dip coating.[138] As highlighted by Cussler's theory of the tortuous path,[109] to optimize the barrier properties of polymer clay nanocomposite films, it is essential to achieve perfect parallel alignment of the impermeable nanosheets towards the substrate. Textured nanosheets that are aligned in parallel play a crucial role in achieving low gas permeabilities since they maximize the diffusion pathway for a gas permeate, and the tortuosity significantly reduces when the nanosheets are tilted in relation to the diffusion direction (**Figure 13a**).[114] Consequently, it is important to employ an appropriate coating tool for the fabrication of Hec-based barrier films providing scalability and efficient shear texturing while maintaining sufficient inertness to prevent loss of texture due to reorientation upon solvent evaporation.[124] Slot dies exerting high shear fields already during the coating procedure seem promising for this task.
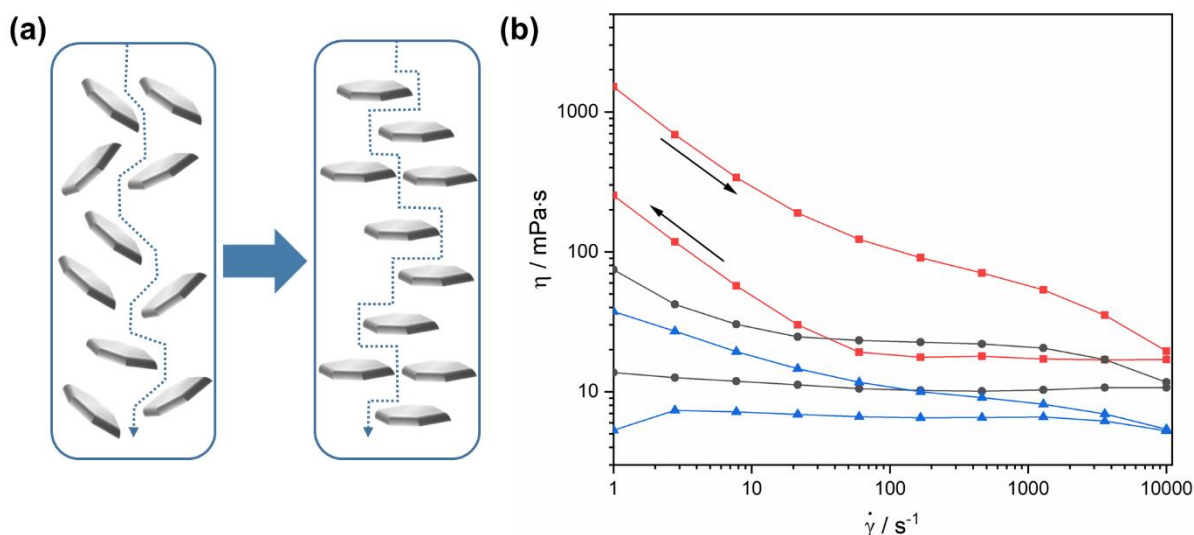
Figure 13: (a) Sketch of the tortuous path for a gas permeate depending on the orientation of nanosheets in a polymer matrix. (b) Effective viscosity measurements of nematic Hec suspensions of varying concentrations: 3 wt% (red), 1.5 wt% (gray) and 0.75 wt% (blue). Reprinted with permission (Open access).[124]

In nematic Hec suspensions, Hec nanosheets are already held in a cofacial arrangement within domains, while individual domains are statistically oriented. These domains are gradually oriented by applying shear stress, and with increasing shear rates, Hec nanosheets can be

perfectly aligned in parallel, as indicated by viscosity-shear rate profiles (**Figure 13b**). The nematic Hec suspensions of varying concentration show a shear thinning behavior with a significant hysteresis. Remarkably, the textures of cofacially aligned Hec nanosheets in parallel to the rheometer plate persist for a long time, even after the texture-producing shear field is reduced. As a result, the measured viscosities remain constant despite a decrease in shear stress, confirming the high stability of textures of shear-oriented Hec nanosheets. The shear alignment of Hec nanosheets in the suspension was further corroborated by directly recording Cryo-SEM images of vitrified suspension films.

Moreover, the formation time for aligning Hec nanosheets in nematic suspension in parallel to the rheometer plate and cofacially to each other was identified, which is inversely proportional to the applied shear rate. The resulting time was applied to deduce geometrical requirements for slot dies and identify ideal operating parameters to produce pure Hec barrier films with Hec nanosheets perfectly oriented parallel to the substrate. It was found that slot dies with "long lips" and coating procedures at slow substrate/web moving speeds are required.

Applying these findings on a slot die to coat a nematic Hec suspension onto a PET substrate, a 1.5 µm thick Hec-only barrier film consisting of overlapping Hec nanosheets was obtained as visualized in SEM images. Thereby, the formation of perfectly aligned Hec nanosheets parallel to the substrate was already achieved within the shear field of the slot die. The texture of shear-oriented nanosheets exhibits sufficient inertness upon drying, corroborated by two-dimensional SAXS and XRD investigations. Furthermore, the quality of the texture of the film is displayed by the superior gas barrier properties. The Hec-only coating shows oxygen transmission rates (OTR) comparable to vacuum-deposited aluminum coatings.[34] An OP as low as 2.2 cm^3 µm m^{-2} day^{-1} bar^{-1} at 23 °C and 50% RH was obtained, orders of magnitude lower than the OP of commodity polymers, making it promising for the application as food packaging. For instance, PET exhibits an OP of approximately 1000 cm^3 µm m^{-2} day^{-1} bar^{-1} at the same conditions.[34]

Rheological investigations of nematic Hec suspensions give valuable insights into the texturing of Hec nanosheets and enable the design of ideal slot dies that assure shear orientation. Consequently, slot die coating can combine the best of two worlds: The high shear fields during coating yield perfectly textured Hec-only barrier films and represent technically benign processing that can easily be adapted to large scale and high throughput at an industrial level.

3.2 Green and scalable processing of water-soluble, biodegradable polymer/clay barrier films

Water-soluble packaging with intentional disposal into wastewater provides premeasured convenience for households and industry, such as delivering dishwater and laundry detergents, pesticides, fertilizers, dyes and cement additives.[140] The packaging is designed to quickly dissolve and be released into the environment during use, particularly into wastewater streams. PVOH is the most commonly used polymer for this application as it is abundant and widely accepted as biodegradable. However, the kinetics of degradation in wastewater are very slow, showing only 2% biodegradation within 33 days, as we found in this work, and PVOH can actually be considered a recalcitrant pollutant.[141] Natural renewable and water-soluble biopolymers, including whey protein, cellulose, or alginate,[142, 143] seem promising for this application, but they lack sufficient gas barrier properties and mechanical toughness. Therefore, Hec seems auspicious to improve the barrier and mechanical properties of water-soluble biopolymers, which has previously been demonstrated to impart barrier improvements to biodegradable polymers.[144, 145]
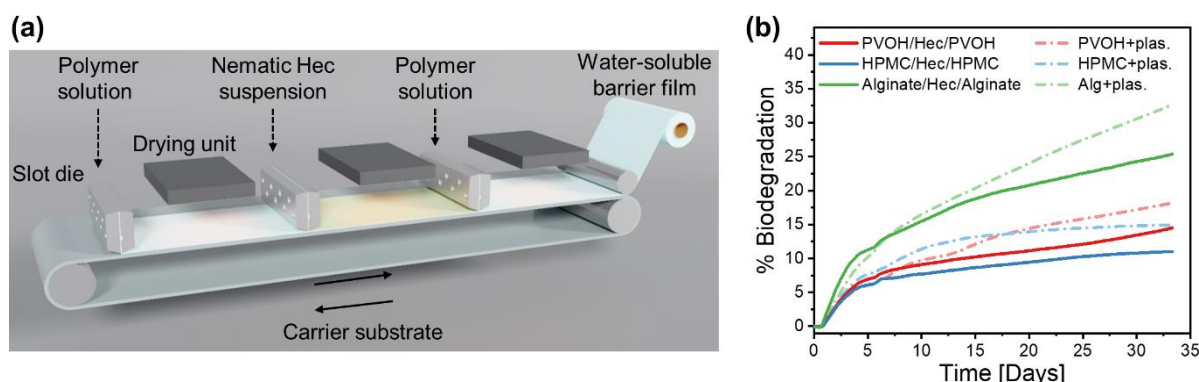
Figure 14. (a) Proposal of a potential roll-to-roll coating process applicable at an industrial level with high throughput based on three consecutive slot dies and drying units. The same concept was used at the lab scale to produce the multi-layered water-soluble films (polymer/Hec/polymer). (b) Biodegradation results of the three multi-layered films. Dashed lines display neat plasticized polymers without Hec. Reprinted with permission (Open access).[135]

Water-soluble films as packaging material for single-serving pouches were fabricated by sequential coating and drying of aqueous solutions of polymers and nematic Hec suspensions employing an industrially scalable slot die coater. The water-borne multi-layered structure comprises two plasticized polymer layers sandwiching a Hec-only barrier layer (polymer/Hec/polymer). PVOH, hydroxypropyl methylcellulose (HPMC) and alginate were used as polymer layers yielding the film samples of PVOH/Hec/PVOH, HPMC/Hec/HPMC

and Alginate/Hec/Alginate. The sandwich-like structure and applied process enable the incorporation of multiple functional layers and prevent complications from compounding a nematic Hec suspension with biopolymers like high viscosities, filler aggregation, or embrittlement that limits higher clay loadings.[146]

The slot die coating method employed at the lab scale to produce the multi-layered films can simply be translated into large-scale roll-to-roll processing (**Figure 14a**). Moreover, slot die coating provides efficient shear texturing of Hec nanosheets (**Chapter 6.1**) and uniform layers of outer polymer (30 µm) and inner Hec barrier (6 µm), as corroborated by SEM images. However, it appears that coating a nematic Hec suspension onto the dried PVOH layer in the interim step leads to partial "re"-dissolution of the polymer and allows it to diffuse between adjacent Hec nanosheets that are separated to 30.5 nm in the nematic state. Consequently, an in-situ nanocomposite interphase was formed upon drying, as visible in transmission electron microscope (TEM) images of film cross-sections, providing excellent interlayer adhesion between Hec and polymer layers.

Furthermore, the three multi-layered films were evaluated regarding their water-solubility, gas barrier, mechanical, optical and biodegradation properties. Compared to the neat plasticized polymer films dissolving within seconds, the incorporated Hec barrier layer extends dissolution and disintegration times making it more practical for real-world applications where accidental exposure to water does not immediately destroy the packaging integrity. The Hec barrier layer can also impart competitive properties to films of biodegradable alginate, and the corresponding Alginate/Hec/Alginate film exhibits an OP and WVP of 0.063 cm^3 mm m^{-2} day^{-1} bar^{-1} (23 °C and 65% RH) and 53.8 g mm m^{-2} day^{-1} bar^{-1} (23 °C and 85% RH), respectively. In addition, the inner Hec barrier layers act as structural reinforcement and improve the elastic modulus of all three multi-layered films. Despite all multi-layered films showing good optical properties, the Alginate/Hec/Alginate film has slightly increased haziness and decreased clarity. As expected, PVOH displayed almost no biodegradation in wastewater within 33 days, but surprisingly, biobased HPMC showed even less biodegradation in the applied medium (**Figure 14b**). However, biodegradation for the neat plasticized alginate and alginate/Hec/alginate films of 33% and 25%, respectively, was recorded within 33 days.

In summary, a slot die coating method was established that can be translated into large-scale roll-to-roll manufacturing of high-barrier, mechanically reinforced and transparent self-standing biodegradable films for water-soluble packaging applications.

3.3 New functional polymer materials via click chemistry-based modification of Cellulose Acetate

Cellulose is a biobased and abundant polysaccharide accessible from plants, and via acetylation/partial deacetylation, CA can be obtained, which is interesting for various applications.[117] CA can be seen as a promising substitute for petro-based polymers since the degradation by several mild methods is known.[147] However, the kinetics of degradation strongly depends on the degree of substitution and environmental conditions,[147, 148] and approaches for accelerated degradation of CA are a matter of research.[147] Moreover, as already mentioned in the Introduction for biodegradable polymers in general (**Chapter 1.3**), CA also exhibits insufficient water vapor barrier properties and requires plasticizers necessary for processability, both preventing a broader application of this material so far, e.g., in food packaging.[149, 150] Incorporating Hec nanosheets seems to be a promising concept to improve barrier properties of CA,[117] which has previously been reported in a similar approach on PLA and also did not harm the degradability of PLA.[146]

By partial acrylation of CA (degree of acryl substitution of 0.2), the resulting CA acrylate underwent quantitative thio-Michael click reactions with various thiols yielding a toolbox of functional CA polymers. Thereby, thiols with fatty alkyl chains such as dodecanethiol, hexadecanethiol, octadecanethiol, and eicosanethiol, with esters such as ethyl 2-mercaptoacetate and butyl 3-mercaptopropionate, and with arenes such as furan-2-ylmethylthiol were applied as modifying agents yielding CA derivatives in high yield (90%). The derivatives showed improved optical properties compared to neat CA, and highly transparent films were obtained. Moreover, as proof of principle, the furanyl-modified CA (CAASFur) was selected for studying the disintegration under composting conditions according to ISO 20200. After 69 days, CAASFur showed complete degradation indicating the potential of the material to be biodegradable. In addition, the modifications of CA with fatty alkyl thiols yielded hydrophobic polymer materials exhibiting large water drop contact angles. As expected, increasing contact angles were observed with an increasing length of the fatty alkyl chain. This observation is further corroborated by WVP measurements as a sensitive method to probe the hydrophobicity. The lowest WVP was obtained from the CA modification having the highest aliphatic chain length.

However, the WVP values of the CA derivatives are still distinctively below the food packaging requirements. Therefore, as proof of principle, the CA derivative altered with octadecanethiol

(CAAS18) was selected to incorporate a modified Hec into the polymer matrix to improve the barrier properties, yielding a transparent nanocomposite film (**Figure 15a**). The CAAS18/Hec nanocomposite film exhibits a WVP (at 23 ° and 85% RH) and OP (at 23 °C and 50% RH) as low as 0.09 g mm m^{-2} day^{-1} and 0.16 cm^3 mm m^{-2} day^{-1} atm^{-1}, respectively. The WVP of neat CAAS18 of 24.8 g mm m^{-2} day^{-1} could be reduced by 99.6%.
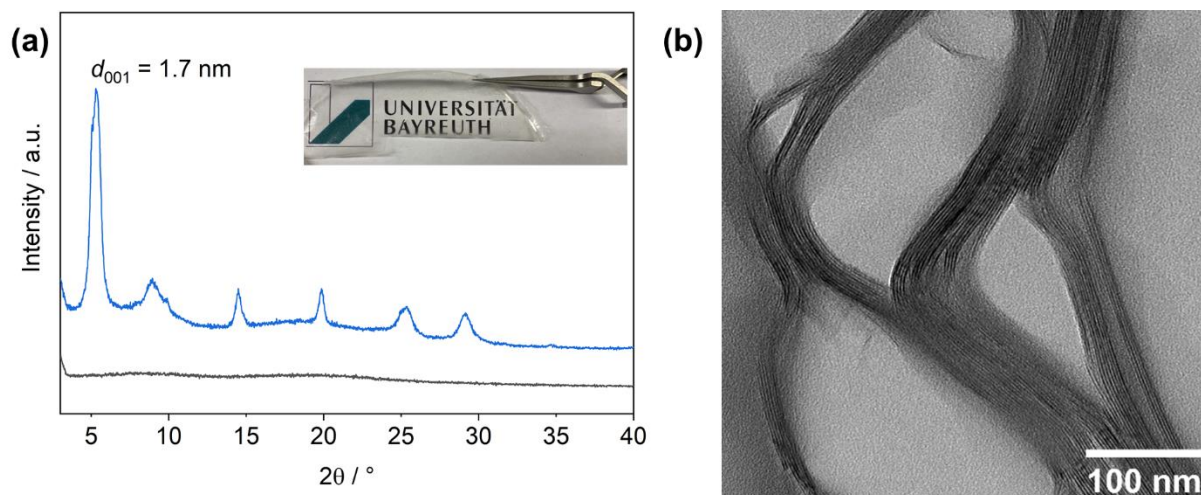

Figure 15. (a) XRD pattern of neat CAAS18 (black) and CAAS18/Hec nanocomposite film (blue). The inset shows the transparent CAAS18/Hec nanocomposite film. (b) The TEM image of the CAAS18/Hec nanocomposite film cross-section indicates segregated domains of CAAS18 (bright) and restacked Hec (dark). Reprinted with permission (Open access).[117]

Although the applied nematic ternary suspension used for classic solution casting and producing the nanocomposite film is homogeneous, CAAS18 and Hec segregate into separate domains upon drying, as indicated in the XRD pattern (**Figure 15a**). The d_{001} of 1.7 nm can be assigned to the intercalated 18C6 crown ether complexing the sodium interlayer cation of Hec required for 1D dissolution of Hec in the applied organic solvent.[96, 146] Hence, intercalation of CAAS18 into the interlayer space can be excluded. CAAS18 shows an XRD pattern of an amorphous polymer. The phase separation is confirmed by TEM images revealing segregated domains of CAAS18 and restacked Hec nanosheets (**Figure 15b**). However, we have previously shown that such phase segregation accelerates the kinetics of biodegradation of PLA nanocomposite films and might also be advantageous in this case regarding the degradation of CA nanocomposites.[146]

In summary, the transparent CAAS18/Hec film outperforms commonly applied packaging polymers in terms of barrier properties, and the likelihood of biodegradation renders the CA nanocomposite a promising alternative for currently used packaging materials.

3.4 Stretchable clay nanocomposite barrier film for flexible packaging

Packaging materials for pharmaceuticals or food must be sufficiently flexible and exhibit high gas barrier properties at the same time.[35, 151, 152] High-end barriers can often only be met by lamination of the polymer foil with inorganic layers such as thin vapor-deposited aluminum, ceramic Al_2O_3 or glass-like SiO_x coatings.[127, 128] However, these thin inorganic layers tend to be brittle and mechanical stress will inevitably cause pinholes detrimental to the barrier.[41] Since a wide range of applications requires stretching up to 10% or more,[153] these brittle laminates become impractical as, e.g., a vapor-deposited SiO_x coating on a PET foil tolerates deformations up to only 4%.[34] A promising approach to reconciling the high gas barrier properties of inorganic layers with the flexibility of polymers applies polymer Hec nanocomposites.[120]
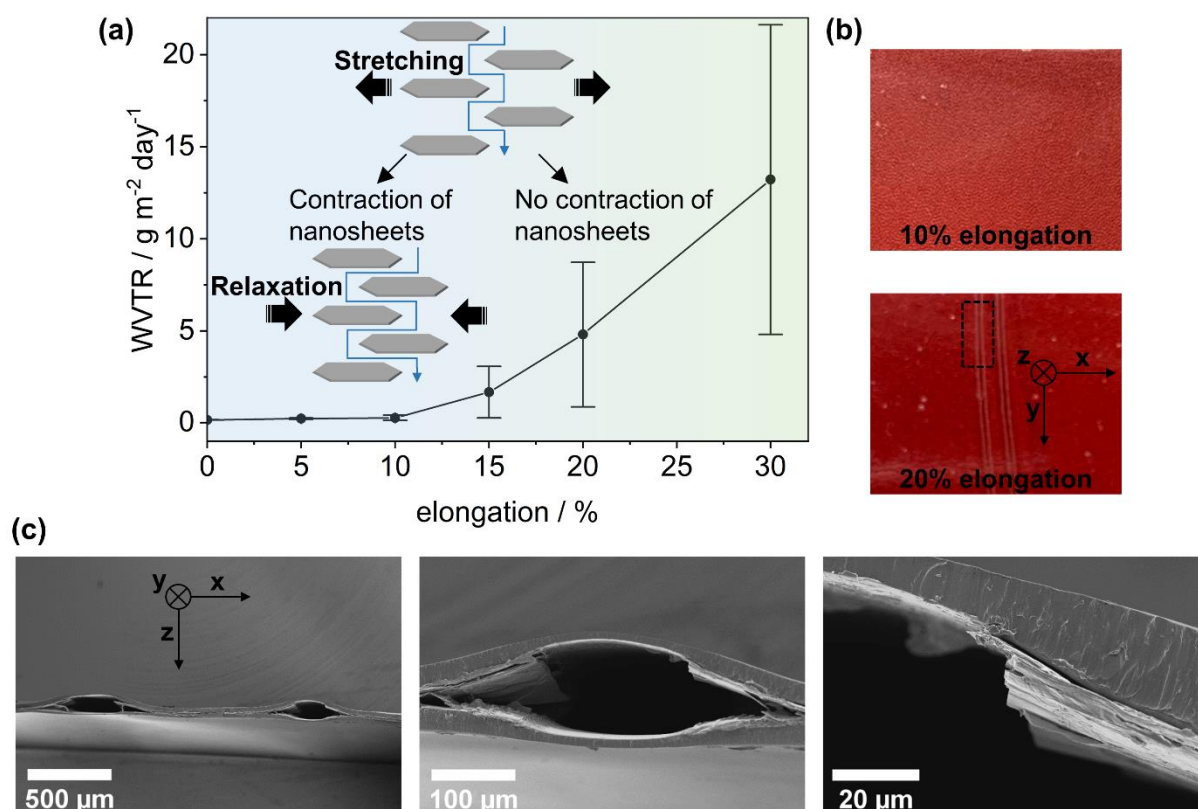
Figure 16: Stretching experiments of the self-standing barrier laminate. (a) WVTR measured at 40 °C and 50% RH as a function of uniaxial elongation (x-direction). The inset sketches the behavior of Hec nanosheets and the dependence of the tortuous path of a gas permeate upon stretching and relaxation. (b) Photographs of the sample upon 10% and 20% elongation, respectively. (c) SEM images of cross-sections of the sample upon 20% elongation displayed in different scales focusing on the rupture (dashed rectangle from (b)). Reprinted with permission.[120]

In this study, a perfectly ordered and 1D crystalline nanocomposite barrier film comprised of alternating layers of PEG and Hec nanosheets was produced via spray coating (similar to **Figure 7c**). The monodomain Bragg stack-type structure was evidenced by XRD and TEM analysis, and no phase segregation was observed, corroborated by thermogravimetric analysis. Subsequently, a transparent self-standing barrier laminate was obtained by sandwiching the PEG-Hec Bragg stack barrier film between two outer layers of plasticized PVOH.

To test for the mechanical resistance of the barrier, the WVTRs were measured as a function of the uniaxial elongation of the self-standing barrier laminate. An in-house built stretching device was applied, mimicking real-world thermoforming processes involving stretching and relaxation. Interestingly, up to 15% elongation, the WVTR increases only moderately (**Figure 16a**). This can be traced back to two significant reasons. First, in Bragg stacks, adjacent Hec nanosheets are mechanically decoupled by molecular layers of PEG. Upon stretching, it allows individual Hec nanosheets to slide along the PEG layers to some extent, decreasing the tortuosity (**Figure 16a**). Upon relaxation and below 10% elongation (**Figure 16b**), Hec nanosheets rearrange and rebuild the tortuous path reflected by the constant WVTR values. Second, even if microcracks are formed in the PEG-Hec nanocomposite barrier during stretching, the edges are held opposite to each other and upon strain release, they are pressed together due to the shrinkage of the outer PVOH "buffering" layers restoring the tortuosity.

Nonetheless, above 15% elongation, the WVTR collapses and sliding of Hec nanosheets becomes irreversible, as indicated by the substantially increased WVTR values (**Figure 16a**). Additionally, after 20% elongation, fatal macroscopic ruptures are observed perpendicular (y-direction) to the uniaxial stretching direction (x-direction), which no longer "heal" upon shrinkage of outer PVOH "buffering" layers (**Figure 16b**). This observation is supported by SEM images of the fatal rupture from the 20% elongation sample where the PEG-Hec nanocomposite barrier is entirely destructed (**Figure 16c**), explaining the surge in WVTR.

At 23 °C and 85% RH, the self-standing barrier laminate exhibits a WVP of 2.8 g mm m^{-2} day^{-1}bar$^{-1,}$ outperforming commercially used thermoformable polymers for packaging, which is remarkable for an entirely water-soluble film obtained from green and aqueous processing. Furthermore, the barrier resistance to mechanical stress reported in this work makes the self-standing barrier laminate interesting as flexible liners for ultra-light hydrogen tanks as needed in the automotive sector since excellent hydrogen barrier properties of a Hec nanocomposite barrier liner have already been demonstrated.[45]

3.5 Disorder-order transition – Improving the moisture sensitivity of waterborne nanocomposite barriers

PVOH is a commercially affordable and water-soluble polymer allowing eco-friendly waterborne processing.[154-156] Moreover, PVOH is approved for food contact by the Food and Drug Administration in the US,[155] can be biodegraded under specific conditions (**Chapter 6.2**) and possesses excellent oxygen barrier properties with an OP as low as 0.02 cm^3 mm m^{-2} day^{-1} bar^{-1} at 23 °C and dry conditions.[34] However, as stated before, above 55% RH swelling sets in, and the OP increases by three orders of magnitude between 0% and 90% RH making it unsuitable for food packaging.[129] To address the issue of moisture-induced OP deterioration, copolymerized EVOH is commonly used instead.[157] Especially for EVOH films, the hydrophobicity and onset of swelling can be easily fine-tuned by adjusting the ethylene content. This provides sufficient oxygen barrier properties at 65% RH relevant for food packaging.[130, 158] As mentioned before, EVOH is not biodegradable, and EVOH-correlated microplastics have been found in seafood, drinking water, and beach sediments.[132-134] Alternatively, Hec nanosheets can be incorporated into PVOH to reduce the moisture sensitivity of PVOH and push the onset of swelling to higher RH. By triggering a disorder-order transition, superior oxygen barrier properties at an elevated 65% RH are obtained.[97]
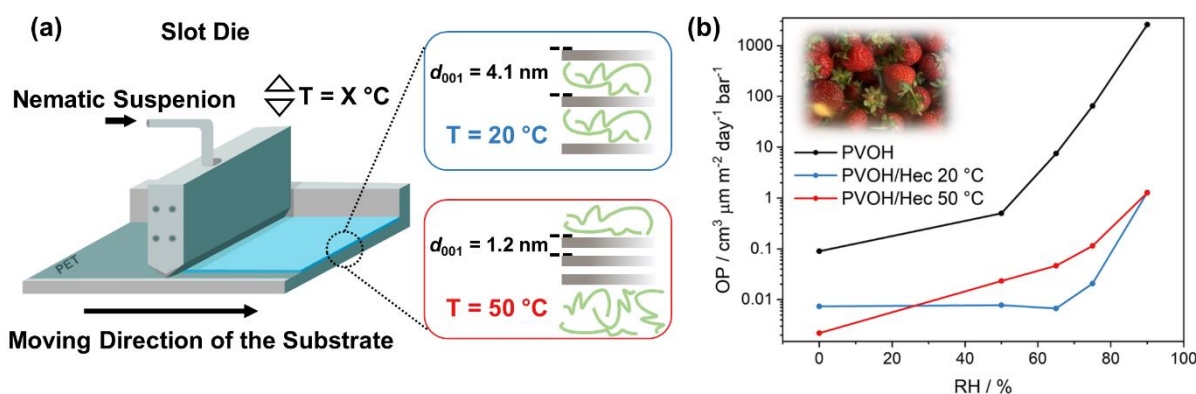
Figure 17. (a) Slot die coating of an aqueous nematic PVOH/Hec suspension. Depending on the drying temperature (*T*) of the wet coating, different morphologies of PVOH/Hec nanocomposites were observed upon water removal. Monodomain hybrid Brag stacks (PVOH/Hec 20 °C) at *T* = 20 °C and completely phase-segregated nanocomposites (PVOH/Hec 50 °C) at *T* = 50 °C were obtained. (b) OP at 23 °C of neat PVOH, PVOH/Hec 20 °C, and PVOH/Hec 50 °C nanocomposites. The inset shows the high transparency of a PVOH/Hec 20 °C coating on PET represented as a strawberry packaging. Reprinted with permission.[97]

The PVOH/Hec nanocomposite barriers were fabricated via scalable slot die coating of a ternary aqueous suspension on a PET substrate providing perfectly shear-aligned Hec nanosheets (**Chapter 6.1**). Interestingly, depending on the drying temperature (*T*) of the wet

coating, different PVOH/Hec nanocomposite morphologies can be obtained upon water removal (**Figure 17a**). Increasing T from 20 °C to 50 °C for the same ternary nematic suspension triggers phase segregation, and disordered PVOH/Hec nanocomposites are obtained, while at 20 °C, 1D crystalline and ordered intercalated nanocomposites are formed. For the ratio of PVOH and Hec applied, monodomain hybrid Bragg stacks (PVOH/Hec 20 °C) are yielded at 20 °C, exhibiting a d-spacing of 4.1 nm (**Figure 17a**). The equidistant spacing between alternating Hec nanosheets and PVOH layers for the PVOH/Hec 20 °C sample is further corroborated by TEM imaging. Upon increasing the drying temperature, phase segregation sets in, and the PVOH/Hec nanocomposite gradually becomes biphasic, as evidenced via XRD. At 50 °C, the phase segregation is almost complete, as displayed by the d-spacing of 1.2 nm of the PVOH/Hec 50 °C sample corresponding to randomly interstratified domains of clay-only ($d_{001} = 0.96$ nm) and some intercalated stacks (**Figure 17a**). Moreover, as visible in TEM images of cross-sections of the PVOH/Hec 50 °C sample, segregated neat PVOH lenses up to 92 nm thickness are present. The disorder-order transition is attributed to the increasing entropic cost of confining PVOH in the interlayer space of Hec nanosheets at elevated temperatures until phase segregation is finally preferred.

For the first time, this disorder-order transition allows studying the impact of crystallinity vs. disordered morphology on the gas barrier properties and moisture sensitivity while the composition, type of filler, and processing are kept constant. WVTR is a sensitive probe to measure the moisture sensitivity of films. A clear trend was observable for all PVOH/Hec nanocomposites in the 0 - 90% RH range, where the WVTR values decrease at any given RH with decreasing drying temperature. In other words, the 1D crystalline and ordered intercalated PVOH/Hec 20 °C sample is less moisture sensitive than the disordered segregated PVOH/Hec films dried at higher temperatures. Further investigations showed that incorporating Hec into PVOH decreases the OP of neat PVOH by order of magnitudes independently of the drying temperature (**Figure 17b**). However, the onset of swelling of the 1D crystalline morphology PVOH/Hec 20 °C is pushed to significantly higher RH and it was found that the OP is not affected up to an RH of 65%.

In summary, realizing the 1D crystalline monodomain Bragg stack structure makes the PVOH/Hec nanocomposite film less prone to swelling, and the OP at elevated 65% RH relevant for food packaging is by far superior compared to the OP of EVOH. This renders the transparent PVOH/Hec 20 °C sample highly appropriate for food packaging (**Figure 17b**).

4. Literature

1.   Geyer, R.; Jambeck, J. R.; Law, K. L., Production, use, and fate of all plastics ever made. *Science Advances* **2017**, *3* (7), e1700782.

2.   OECD, Plastics use in 2019. https://www.oecd-ilibrary.org/content/data/efff24eb-en (accessed **25.05.2023**).

3.   Ritchie, H.; Roser, M., Plastic Pollution. https://ourworldindata.org/plastic-pollution (accessed **25.05.2023**).

4.   Statista-Research-Department, Annual production of plastics worldwide from 1950 to 2021.   https://www.statista.com/statistics/282732/global-production-of-plastics-since-1950/ (accessed **13.05.2023**).

5.   Plastics - the Facts 2022. *PlasticsEurope*: Brussels, Belgium, **2022**. https://plasticseurope.org/knowledge-hub/plastics-the-facts-2022/ (accessed **23.05.2023**).

6.   The Circular Economy for Plastics – A European Overview. *PlasticsEurope*: Brussels, Belgium, **2022**. https://plasticseurope.org/knowledge-hub/the-circular-economy-for-plastics-a-european-overview-2/ (accessed **23.05.2023**).

7.   Kaza, S.; Yao, L. C.; Bhada-Tata, P.; Van Woerden, F., What a Waste 2.0: A Global Snapshot of Solid Waste Management to 2050. *World Bank*: Washington, DC, **2018**.

8.   Ali, S. S.; Elsamahy, T.; Al-Tohamy, R.; Zhu, D.; Mahmoud, Y. A. G.; Koutra, E.; Metwally, M. A.; Kornaros, M.; Sun, J., Plastic wastes biodegradation: Mechanisms, challenges and future prospects. *Science of The Total Environment* **2021**, *780*, 146590.

9.   Eriksen, M.; Lebreton, L. C. M.; Carson, H. S.; Thiel, M.; Moore, C. J.; Borerro, J. C.; Galgani, F.; Ryan, P. G.; Reisser, J., Plastic Pollution in the World's Oceans: More than 5 Trillion Plastic Pieces Weighing over 250,000 Tons Afloat at Sea. *PLOS ONE* **2014**, *9* (12), e111913.

10.   The New Plastics Economy — Rethinking the future of plastics. *World Economic Forum, Ellen MacArthur Foundation, McKinsey & Company*: **2016**. http://www.ellenmacarthurfoundation.org/publications (accessed **26.11.2022**).

11.   Lebreton, L.; Egger, M.; Slat, B., A global mass budget for positively buoyant macroplastic debris in the ocean. *Scientific Reports* **2019**, *9* (1), 12922.

12.   Millican, J. M.; Agarwal, S., Plastic Pollution: A Material Problem? *Macromolecules* **2021**, *54* (10), 4455-4469.

13.   Silva, A. L. P.; Prata, J. C.; Duarte, A. C.; Soares, A. M. V. M.; Barceló, D.; Rocha-Santos, T., Microplastics in landfill leachates: The need for reconnaissance studies and remediation technologies. *Case Studies in Chemical and Environmental Engineering* **2021**, *3*, 100072.

14.   Shen, M.; Xiong, W.; Song, B.; Zhou, C.; Almatrafi, E.; Zeng, G.; Zhang, Y., Microplastics in landfill and leachate: Occurrence, environmental behavior and removal strategies. *Chemosphere* **2022**, *305*, 135325.

15.   Schnurr, R. E. J.; Alboiu, V.; Chaudhary, M.; Corbett, R. A.; Quanz, M. E.; Sankar, K.; Srain, H. S.; Thavarajah, V.; Xanthos, D.; Walker, T. R., Reducing marine pollution from single-use plastics (SUPs): A review. *Marine Pollution Bulletin* **2018**, *137*, 157-171.

16.   Meijer, L. J. J.; van Emmerik, T.; van der Ent, R.; Schmidt, C.; Lebreton, L., More than 1000 rivers account for 80% of global riverine plastic emissions into the ocean. *Science Advances* **2021**, *7* (18), eaaz5803.

17.   Chamas, A.; Moon, H.; Zheng, J.; Qiu, Y.; Tabassum, T.; Jang, J. H.; Abu-Omar, M.; Scott, S. L.; Suh, S., Degradation Rates of Plastics in the Environment. *ACS Sustainable Chemistry & Engineering* **2020**, *8* (9), 3494-3511.

18.   Kühn, S.; Bravo Rebolledo, E. L.; van Franeker, J. A., Deleterious Effects of Litter on Marine Life. In *Marine Anthropogenic Litter*, Bergmann, M.; Gutow, L.; Klages, M., Eds. Springer International Publishing: Cham, **2015**; pp 75-116.

19.   Gall, S. C.; Thompson, R. C., The impact of debris on marine life. *Marine Pollution Bulletin* **2015**, *92* (1), 170-179.

20.   de Stephanis, R.; Giménez, J.; Carpinelli, E.; Gutierrez-Exposito, C.; Cañadas, A., As main meal for sperm whales: Plastics debris. *Marine Pollution Bulletin* **2013**, *69* (1), 206-214.

21.   Day, R. H.; Wehle, D. H. S.; Coleman, F., Ingestion of plastic pollutants by marine birds. *Proceedings of the Workshop on the Fate and Impact of Marine Debris* **1985**, 344-386.

22.   Law, K. L., Plastics in the Marine Environment. *Ann Rev Mar Sci* **2017**, *9*, 205-229.

23.   Browne, M. A.; Niven, S. J.; Galloway, T. S.; Rowland, S. J.; Thompson, R. C., Microplastic Moves Pollutants and Additives to Worms, Reducing Functions Linked to Health and Biodiversity. *Current Biology* **2013**, *23* (23), 2388-2392.

24.   Cedervall, T.; Hansson, L.-A.; Lard, M.; Frohm, B.; Linse, S., Food Chain Transport of Nanoparticles Affects Behaviour and Fat Metabolism in Fish. *PLOS ONE* **2012**, *7* (2), e32254.

25.   Oliveira, M.; Ribeiro, A.; Hylland, K.; Guilhermino, L., Single and combined effects of microplastics and pyrene on juveniles (0+ group) of the common goby Pomatoschistus microps (Teleostei, Gobiidae). *Ecological Indicators* **2013**, *34*, 641-647.

26.   Rochman, C. M.; Hoh, E.; Kurobe, T.; Teh, S. J., Ingested plastic transfers hazardous chemicals to fish and induces hepatic stress. *Scientific Reports* **2013**, *3* (1), 3263.

27.   Marine-Savers, Sea Turtles And Plastic. https://marinesavers.com/2019/03/sea-turtles-eating-plastics/ (accessed **23.05.2023**).

28.   European Green Deal: Putting an end to wasteful packaging, boosting reuse and recycling. *European Commission*: Brussels, **2022**. https://ec.europa.eu/commission/presscorner/detail/en/ip_22_7155 (accessed **23.05.2023**).

29.   Definition of Sustainable Packaging. *Sustainable Packaging Coalition®, GreenBlue®*: **2011**. https://sustainablepackaging.org/wp-content/uploads/2017/09/Definition-of-Sustainable-Packaging.pdf (accessed **23.05.2023**).

30.   P&G Ambition 2030 Report. *Procter&Gamble*: **2021**. https://us.pg.com/Ambition2030.pdf (accessed **23.05.2023**).

31.   Ammala, A.; Bateman, S.; Dean, K.; Petinakis, E.; Sangwan, P.; Wong, S.; Yuan, Q.; Yu, L.; Patrick, C.; Leong, K. H., An overview of degradable and biodegradable polyolefins. *Progress in Polymer Science* **2011**, *36* (8), 1015-1049.

32.   Agarwal, S., Biodegradable Polymers: Present Opportunities and Challenges in Providing a Microplastic-Free Environment. *Macromolecular Chemistry and Physics* **2020**, *221* (6), 2000017.

33.   Bagheri, A. R.; Laforsch, C.; Greiner, A.; Agarwal, S., Fate of So-Called Biodegradable Polymers in Seawater and Freshwater. *Global Challenges* **2017**, *1* (4), 1700048.

34.   Lange, J.; Wyser, Y., Recent innovations in barrier technologies for plastic packaging—a review. *Packaging Technology and Science* **2003**, *16* (4), 149-158.

35.   Zabihzadeh Khajavi, M.; Ebrahimi, A.; Yousefi, M.; Ahmadi, S.; Farhoodi, M.; Mirza Alizadeh, A.; Taslikh, M., Strategies for Producing Improved Oxygen Barrier Materials Appropriate for the Food Packaging Sector. *Food Engineering Reviews* **2020**, *12* (3), 346-363.

36.   Wang, J.; Gardner, D. J.; Stark, N. M.; Bousfield, D. W.; Tajvidi, M.; Cai, Z., Moisture and Oxygen Barrier Properties of Cellulose Nanomaterial-Based Films. *ACS Sustainable Chemistry & Engineering* **2018**, *6* (1), 49-70.

37.   Johnson, D. R.; Decker, E. A., The Role of Oxygen in Lipid Oxidation Reactions: A Review. *Annual Review of Food Science and Technology* **2015**, *6* (1), 171-190.

38.   Min, D. B.; Boff, J. M., Chemistry and Reaction of Singlet Oxygen in Foods. *Comprehensive Reviews in Food Science and Food Safety* **2002**, *1* (2), 58-72.

39.   Akelah, A., Polymers in Food Packaging and Protection. In *Functionalized Polymeric Materials in Agriculture and the Food Industry*, Springer US: Boston, MA, **2013**; pp 293-347.

40.   Gunders, D.; Bloom, J., Wasted: How America is losing up to 40 percent of its food from farm to fork to landfill. *Natural Resources Defense Council*: **2012**. https://www.nrdc.org/sites/default/files/wasted-food-IP.pdf (accessed **23.05.2023**).

41.   Wu, F.; Misra, M.; Mohanty, A. K., Challenges and new opportunities on barrier performance of biodegradable polymers for sustainable packaging. *Progress in Polymer Science* **2021**, *117*, 101395.

42.   Tsurko, E. S.; Feicht, P.; Nehm, F.; Ament, K.; Rosenfeldt, S.; Pietsch, I.; Roschmann, K.; Kalo, H.; Breu, J., Large Scale Self-Assembly of Smectic Nanocomposite Films by Doctor Blading versus Spray Coating: Impact of Crystal Quality on Barrier Properties. *Macromolecules* **2017**, *50* (11), 4344-4350.

43.   Grewal, R.; Sweesy, W.; Jur, J. S.; Willoughby, J., Moisture Vapor Barrier Properties of Biopolymers for Packaging Materials. In *Functional Materials from Renewable Sources*, American Chemical Society: **2012**; Vol. 1107, pp 271-296.

44.   Ebina, T., Development of Clay-Based Films. *The Chemical Record* **2018**, *18* (7-8), 1020-1032.

45.   Habel, C.; Tsurko, E. S.; Timmins, R. L.; Hutschreuther, J.; Kunz, R.; Schuchardt, D. D.; Rosenfeldt, S.; Altstädt, V.; Breu, J., Lightweight Ultra-High-Barrier Liners for Helium and Hydrogen. *ACS Nano* **2020**, *14* (6), 7018-7024.

46.   Anastas, P. T.; Warner, J. C., Principles of green chemistry. *Green chemistry: Theory and practice* **1998**, *29*.

47.   Bibi, I.; Icenhower, J.; Niazi, N. K.; Naz, T.; Shahid, M.; Bashir, S., Chapter 21 - Clay Minerals: Structure, Chemistry, and Significance in Contaminated Environments and Geological CO2 Sequestration. In *Environmental Materials and Waste*, Prasad, M. N. V.; Shih, K., Eds. Academic Press: **2016**; pp 543-567.

48.   Bleam, W. F., Chapter 3 - Clay Mineralogy and Clay Chemistry. In *Soil and Environmental Chemistry*, Bleam, W. F., Ed. Academic Press: Boston, **2012**; pp 85-116.

49.   Brigatti, M. F.; Galan, E.; Theng, B. K. G., Chapter 2 Structures and Mineralogy of Clay Minerals. In *Developments in Clay Science*, Bergaya, F.; Theng, B. K. G.; Lagaly, G., Eds. Elsevier: **2006**; Vol. 1, pp 19-86.

50.   Moore, D. M.; Reynolds, R. C., X-ray Diffraction and the Identification and Analysis of Clay Minerals. *Oxford university press*: Oxford, **1989**; Vol. 322.

51.   Brown, G.; Nadeau, P.; Fowden, L.; Barrer, R. M.; Tinker, P. B., Crystal structures of clay minerals and related phyllosilicates. *Philosophical Transactions of the Royal Society of London. Series A, Mathematical and Physical Sciences* **1984**, *311* (1517), 221-240.

52.   Murray, H. H., Chapter 2 Structure and Composition of the Clay Minerals and their Physical and Chemical Properties. In *Developments in Clay Science*, Murray, H. H., Ed. Elsevier: **2006**; Vol. 2, pp 7-31.

53.   Brindley, G. W.; Brown, G., Crystal Structures of Clay Minerals and their X-Ray Identification. *Mineralogical Society of Great Britain and Ireland*: **1980**; Vol. 5.

54.   Bergaya, F.; Lagaly, G., Chapter 1 General Introduction: Clays, Clay Minerals, and Clay Science. In *Developments in Clay Science*, Bergaya, F.; Theng, B. K. G.; Lagaly, G., Eds. Elsevier: **2006**; Vol. 1, pp 1-18.

55.   Nicolosi, V.; Chhowalla, M.; Kanatzidis, M. G.; Strano, M. S.; Coleman, J. N., Liquid Exfoliation of Layered Materials. *Science* **2013**, *340* (6139), 1226419.

56.   Harvey, C. C.; Lagaly, G., Chapter 4.2 - Industrial Applications. In *Developments in Clay Science*, Bergaya, F.; Lagaly, G., Eds. Elsevier: **2013**; Vol. 5, pp 451-490.

57.   Zhou, C.; Tong, D.; Yu, W., 7 - Smectite Nanomaterials: Preparation, Properties, and Functional Applications. In *Nanomaterials from Clay Minerals*, Wang, A.; Wang, W., Eds. Elsevier: **2019**; pp 335-364.

58.   Christidis, G. E., Chapter 4.1 - Assessment of Industrial Clays. In *Developments in Clay Science*, Bergaya, F.; Lagaly, G., Eds. Elsevier: **2013**; Vol. 5, pp 425-449.

59.   Simmons, K. J., Mineral Commodity Summaries 2022 - Clays. *U.S. Geological Survey*: **2022**. https://pubs.usgs.gov/periodicals/mcs2022/mcs2022-clays.pdf (accessed **23.05.2023**).

60.   Murray, H. H., Chapter 1 Introduction. In *Developments in Clay Science*, Murray, H. H., Ed. Elsevier: **2006**; Vol. 2, pp 1-6.

61.   Bergaya, F.; Lagaly, G., Chapter 1 - Introduction to Clay Science: Techniques and Applications. In *Developments in Clay Science*, Bergaya, F.; Lagaly, G., Eds. Elsevier: **2013**; Vol. 5, pp 1-7.

62.   Hosterman, J. W.; Patterson, S. H., Bentonite and Fuller's Earth Resources of the United States. *U.S. Geological Survey*: Washington, **1992**. https://pubs.usgs.gov/pp/1522/report.pdf (accessed **23.05.2023**).

63.   Martin, R. T.; Bailey, S. W.; Eberl, D. D.; Fanning, D. S.; Guggenheim, S.; Kodama, H.; Pevear, D. R.; Środoń, J.; Wicks, F. J., Report of the Clay Minerals Society Nomenclature Committee: Revised Classification of Clay Materials. *Clays and Clay Minerals* **1991**, *39* (3), 333-335.

64.   Murray, H. H., Chapter 6 Bentonite Applications. In *Developments in Clay Science*, Murray, H. H., Ed. Elsevier: **2006**; Vol. 2, pp 111-130.

65.   Murray, H. H., Chapter 5 Kaolin Applications. In *Developments in Clay Science*, Murray, H. H., Ed. Elsevier: **2006**; Vol. 2, pp 85-109.

66.   Murray, H. H., Chapter 7 Palygorskite and Sepiolite Applications. In *Developments in Clay Science*, Murray, H. H., Ed. Elsevier: **2006**; Vol. 2, pp 131-140.

67.   Murray, H. H., Chapter 8 Common Clays. In *Developments in Clay Science*, Murray, H. H., Ed. Elsevier: **2006**; Vol. 2, pp 141-145.

68.   Sattler, K., Polyethen-Schichtsilicat-Nanokomposite mit synthetischen Hectoriten (In situ Polymerisation mittels geträgerter Metallocenkatalysatoren). Bayreuth, **2008**.

69.   Stöter, M.; Rosenfeldt, S.; Breu, J., Tunable Exfoliation of Synthetic Clays. *Annual Review of Materials Research* **2015**, *45* (1), 129-151.

70.   Kunz, D. A.; Schmid, J.; Feicht, P.; Erath, J.; Fery, A.; Breu, J., Clay-Based Nanocomposite Coating for Flexible Optoelectronics Applying Commercial Polymers. *ACS Nano* **2013**, *7* (5), 4275-4280.

71.   Hakan, C., An Introduction to Montmorillonite Purification. In *Montmorillonite Clay*, Faheem, U., Ed. IntechOpen: Rijeka, **2021**.

72.   Fischer, B., Mikromechanische Wirkungsweise von Schichtsilikaten der zweiten Generation : ein neuartiger Nanofüllstoff zur Steigerung der Steifigkeit und Zähigkeit von PMMA. Bayreuth, **2018**.

73.   Breu, J.; Seidl, W.; Stoll, A. J.; Lange, K. G.; Probst, T. U., Charge Homogeneity in Synthetic Fluorohectorite. *Chemistry of Materials* **2001**, *13* (11), 4213-4220.

74.   Stöter, M.; Kunz, D. A.; Schmidt, M.; Hirsemann, D.; Kalo, H.; Putz, B.; Senker, J.; Breu, J., Nanoplatelets of Sodium Hectorite Showing Aspect Ratios of ≈20 000 and Superior Purity. *Langmuir* **2013**, *29* (4), 1280-1285.

75.   Perdikatsis, B.; Burzlaff, H., Strukturverfeinerung am Talk $Mg_3[(OH)_2Si_4O_{10}]$. *Zeitschrift für Kristallographie - Crystalline Materials* **1981**, *156* (3-4), 177-186.

76.   Loch, P., Developing Functional Layered Materials : From Synthesis and Characterization towards Applications. Bayreuth, **2022**.

77.   Dörres, T., Hybrid Bragg stacks - polymer-clay nanocomposites defined by ultraconfinement. *Universität Bayreuth, Bayreuther Graduiertenschule für Mathematik und Naturwissenschaften - BayNAT*, Bayreuth, **2022**.

78.   Habel, C., Polymer-Schichtsilikat-Nanokomposite - die Allrounder: Vom Lebensmittelregal bis in den Weltraum? Bayreuth, **2021**.

79.   Möller, M. W.; Handge, U. A.; Kunz, D. A.; Lunkenbein, T.; Altstädt, V.; Breu, J., Tailoring Shear-Stiff, Mica-like Nanoplatelets. *ACS Nano* **2010**, *4* (2), 717-724.

80.   Young, D. A.; Smith, D. E., Simulations of Clay Mineral Swelling and Hydration: Dependence upon Interlayer Ion Size and Charge. *The Journal of Physical Chemistry B* **2000**, *104* (39), 9163-9170.

81.   Kalo, H.; Möller, M. W.; Kunz, D. A.; Breu, J., How to maximize the aspect ratio of clay nanoplatelets. *Nanoscale* **2012**, *4* (18), 5633-5639.

82.   Lerf, A., Storylines in intercalation chemistry. *Dalton Transactions* **2014**, *43* (27), 10276-10291.

83.   Dudko, V.; Khoruzhenko, O.; Weiß, S.; Daab, M.; Loch, P.; Schwieger, W.; Breu, J., Repulsive Osmotic Delamination: 1D Dissolution of 2D Materials. *Advanced Materials Technologies* **2022**, *8* (3), 2200553.

84.   Rosenfeldt, S.; Stöter, M.; Schlenk, M.; Martin, T.; Albuquerque, R. Q.; Förster, S.; Breu, J., In-Depth Insights into the Key Steps of Delamination of Charged 2D Nanomaterials. *Langmuir* **2016**, *32* (41), 10582-10588.

85.   Daab, M.; Eichstaedt, N. J.; Habel, C.; Rosenfeldt, S.; Kalo, H.; Schießling, H.; Förster, S.; Breu, J., Onset of Osmotic Swelling in Highly Charged Clay Minerals. *Langmuir* **2018**, *34* (28), 8215-8222.

86.   Daab, M.; Eichstaedt, N. J.; Edenharter, A.; Rosenfeldt, S.; Breu, J., Layer charge robust delamination of organo-clays. *RSC Advances* **2018**, *8* (50), 28797-28803.

87.   Daab, M.; Rosenfeldt, S.; Kalo, H.; Stöter, M.; Bojer, B.; Siegel, R.; Förster, S.; Senker, J.; Breu, J., Two-Step Delamination of Highly Charged, Vermiculite-like Layered Silicates via Ordered Heterostructures. *Langmuir* **2017**, *33* (19), 4816-4822.

88.   Kalo, H.; Milius, W.; Breu, J., Single crystal structure refinement of one- and two-layer hydrates of sodium fluorohectorite. *RSC Advances* **2012**, *2* (22), 8452-8459.

89.   Ferrage, E.; Lanson, B.; Sakharov, B. A.; Geoffroy, N.; Jacquot, E.; Drits, V. A., Investigation of dioctahedral smectite hydration properties by modeling of X-ray diffraction profiles: Influence of layer charge and charge location. *American Mineralogist* **2007**, *92* (10), 1731-1743.

90.   Gardolinski, J. E. F. C.; Lagaly, G., Grafted organic derivatives of kaolinite: II. Intercalation of primary n-alkylamines and delamination. *Clay Minerals* **2005**, *40* (4), 547-556.

91.   Teepakakorn, A.; Ogawa, M., Interactions of layered clay minerals with water-soluble polymers; structural design and functions. *Applied Clay Science* **2022**, *222*, 106487.

92.   Bailey, E. J.; Winey, K. I., Dynamics of polymer segments, polymer chains, and nanoparticles in polymer nanocomposite melts: A review. *Progress in Polymer Science* **2020**, *105*, 101242.

93.   Fu, S.; Sun, Z.; Huang, P.; Li, Y.; Hu, N., Some basic aspects of polymer nanocomposites: A critical review. *Nano Materials Science* **2019**, *1* (1), 2-30.

94.   Hussain, F.; Hojjati, M.; Okamoto, M.; Gorga, R. E., Review article: Polymer-matrix Nanocomposites, Processing, Manufacturing, and Application: An Overview. *Journal of Composite Materials* **2006**, *40* (17), 1511-1575.

95.   Okada, A.; Usuki, A., Twenty Years of Polymer-Clay Nanocomposites. *Macromolecular Materials and Engineering* **2006**, *291* (12), 1449-1476.

96.   Dudko, V.; Ottermann, K.; Rosenfeldt, S.; Papastavrou, G.; Breu, J., Osmotic Delamination: A Forceless Alternative for the Production of Nanosheets Now in Highly Polar and Aprotic Solvents. *Langmuir* **2021**, *37* (1), 461-468.

97.   Röhrl, M.; Federer, L. K. S.; Timmins, R. L.; Rosenfeldt, S.; Dörres, T.; Habel, C.; Breu, J., Disorder–Order Transition—Improving the Moisture Sensitivity of Waterborne Nanocomposite Barriers. *ACS Applied Materials & Interfaces* **2021**, *13* (40), 48101-48109.

98.   Schilling, T.; Habel, C.; Rosenfeldt, S.; Röhrl, M.; Breu, J., Impact of Ultraconfinement on Composite Barriers. *ACS Applied Polymer Materials* **2020**, *2* (7), 3010-3015.

99.   Dörres, T.; Bartkiewicz, M.; Herrmann, K.; Schöttle, M.; Wagner, D.; Wang, Z.; Ikkala, O.; Retsch, M.; Fytas, G.; Breu, J., Nanoscale-Structured Hybrid Bragg Stacks with Orientation- and Composition-Dependent Mechanical and Thermal Transport Properties:

Implications for Nacre Mimetics and Heat Management Applications. *ACS Applied Nano Materials* **2022**, *5* (3), 4119-4129.

100. Habel, C.; Maiz, J.; Olmedo-Martínez, J. L.; López, J. V.; Breu, J.; Müller, A. J., Competition between nucleation and confinement in the crystallization of poly(ethylene glycol)/ large aspect ratio hectorite nanocomposites. *Polymer* **2020**, *202*, 122734.

101. Siracusa, V., Food Packaging Permeability Behaviour: A Report. *International Journal of Polymer Science* **2012**, *2012*, 302029.

102. Gajdoš, J.; Galić, K.; Kurtanjek, Ž.; Ciković, N., Gas permeability and DSC characteristics of polymers used in food packaging. *Polymer Testing* **2000**, *20* (1), 49-57.

103. McKeen, L. W., 1 - Introduction to Permeation of Plastics and Elastomers. In *Permeability Properties of Plastics and Elastomers (Third Edition)*, McKeen, L. W., Ed. William Andrew Publishing: Oxford, **2012**; pp 1-20.

104. Stannett, V., The transport of gases in synthetic polymeric membranes — an historic perspective. *Journal of Membrane Science* **1978**, *3* (2), 97-115.

105. Choudalakis, G.; Gotsis, A. D., Permeability of polymer/clay nanocomposites: A review. *European Polymer Journal* **2009**, *45* (4), 967-984.

106. Cui, Y.; Kumar, S.; Rao Kona, B.; van Houcke, D., Gas barrier properties of polymer/clay nanocomposites. *RSC Advances* **2015**, *5* (78), 63669-63690.

107. Choudalakis, G.; Gotsis, A. D., Free volume and mass transport in polymer nanocomposites. *Current Opinion in Colloid & Interface Science* **2012**, *17* (3), 132-140.

108. Nielsen, L. E., Models for the Permeability of Filled Polymer Systems. *Journal of Macromolecular Science: Part A - Chemistry* **1967**, *1* (5), 929-942.

109. Cussler, E. L.; Hughes, S. E.; Ward, W. J.; Aris, R., Barrier membranes. *Journal of Membrane Science* **1988**, *38* (2), 161-174.

110. Uysal Unalan, I.; Cerri, G.; Marcuzzo, E.; Cozzolino, C. A.; Farris, S., Nanocomposite films and coatings using inorganic nanobuilding blocks (NBB): current applications and future opportunities in the food packaging sector. *RSC Advances* **2014**, *4* (56), 29393-29428.

111. Guo, F.; Aryana, S.; Han, Y.; Jiao, Y., A Review of the Synthesis and Applications of Polymer–Nanoclay Composites. *Applied Sciences* **2018**, *8* (9), 1696.

112. Umemura, Y., 12 - Preparation and application of clay mineral films. In *Developments in Clay Science*, Schoonheydt, R.; Johnston, C. T.; Bergaya, F., Eds. Elsevier: **2018**; Vol. 9, pp 377-396.

113. Zhou, C.-H.; Shen, Z.-F.; Liu, L.-H.; Liu, S.-M., Preparation and functionality of clay-containing films. *Journal of Materials Chemistry* **2011**, *21* (39), 15132-15153.

114. Bharadwaj, R. K., Modeling the Barrier Properties of Polymer-Layered Silicate Nanocomposites. *Macromolecules* **2001**, *34* (26), 9189-9192.

115. Henning, K.-D., Solvent recycling, removal, and degradation. *Handbook of Solvents* **2001**, 1507-1570.

116. Oldal, D. G.; Szekely, G., 8 Solvent recovery and recycling. In *Sustainable Process Engineering*, De Gruyter: Berlin, Boston, **2021**; pp 141-157.

117. Röhrl, M.; Ködel, J. F.; Timmins, R. L.; Callsen, C.; Aksit, M.; Fink, M. F.; Seibt, S.; Weidinger, A.; Battagliarin, G.; Ruckdäschel, H.; Schobert, R.; Breu, J.; Biersack, B.,

New Functional Polymer Materials via Click Chemistry-Based Modification of Cellulose Acetate. *ACS Omega* **2023**, *8* (11), 9889-9895.

118.   Möller, M. W.; Kunz, D. A.; Lunkenbein, T.; Sommer, S.; Nennemann, A.; Breu, J., UV-Cured, Flexible, and Transparent Nanocomposite Coating with Remarkable Oxygen Barrier. *Advanced Materials* **2012**, *24* (16), 2142-2147.

119.   Tsurko, E. S.; Feicht, P.; Habel, C.; Schilling, T.; Daab, M.; Rosenfeldt, S.; Breu, J., Can high oxygen and water vapor barrier nanocomposite coatings be obtained with a waterborne formulation? *Journal of Membrane Science* **2017**, *540*, 212-218.

120.   Röhrl, M.; Timmins, R. L.; Rosenfeldt, S.; Schuchardt, D. D.; Uhlig, F.; Nürmberger, S.; Breu, J., Stretchable Clay Nanocomposite Barrier Film for Flexible Packaging. *ACS Applied Materials & Interfaces* **2023**, *15* (18), 22524-22531.

121.   Chiang, H.-C.; Kolibaba, T. J.; Eberle, B.; Grunlan, J. C., Super Gas Barrier of a Polyelectrolyte/Clay Coacervate Thin Film. *Macromolecular Rapid Communications* **2021**, *42* (4), 2000540.

122.   Patidar, R.; Burkitt, D.; Hooper, K.; Richards, D.; Watson, T., Slot-die coating of perovskite solar cells: An overview. *Materials Today Communications* **2020**, *22*, 100808.

123.   Bhamidipati, K. L.; Didari, S.; Harris, T. A. L., Slot die coating of polybenzimiazole based membranes at the air engulfment limit. *Journal of Power Sources* **2013**, *239*, 382-392.

124.   Röhrl, M.; Mettke, J. H.; Rosenfeldt, S.; Schmalz, H.; Mansfeld, U.; Timmins, R. L.; Habel, C.; Breu, J.; Durst, F., Shear orientation of nematic phases of clay nanosheets: processing of barrier coatings. *Journal of Coatings Technology and Research* **2021**, *19* (2), 487-495.

125.   Mocon®, Mocon Permatran-W® 3/33. https://inspectionsystems.com.au/wp-content/uploads/2012/07/Permatran-W-333-Plus.pdf (accessed **29.04.2023**).

126.   Xianda, Y.; Anlai, W.; Suqin, C., Water-vapor permeability of polyvinyl alcohol films. *Desalination* **1987**, *62*, 293-297.

127.   Hirvikorpi, T.; Vähä-Nissi, M.; Harlin, A.; Karppinen, M., Comparison of some coating techniques to fabricate barrier layers on packaging materials. *Thin Solid Films* **2010**, *518* (19), 5463-5466.

128.   Dukalska, L.; Ungure, E.; Augspole, I.; Muizniece-Brasava, S.; Levkane, V.; Tatjana, R.; Krasnova, I., Evaluation of the Influence of Various Biodegradable Packaging Materials on the Quality and Shelf Life of Different Food Products. *Rural Sustainability Research* **2014**, *30* (1), 20-34.

129.   Grunlan, J. C.; Grigorian, A.; Hamilton, C. B.; Mehrabi, A. R., Effect of clay concentration on the oxygen permeability and optical properties of a modified poly(vinyl alcohol). *Journal of Applied Polymer Science* **2004**, *93* (3), 1102-1109.

130.   Zhang, Z.; Britt, I. J.; Tung, M. A., Permeation of oxygen and water vapor through EVOH films as influenced by relative humidity. *Journal of Applied Polymer Science* **2001**, *82* (8), 1866-1872.

131.   Exceval™ – Attractive protection for your food. https://www.kuraray-poval.com/fileadmin/technical_information/brochures/poval/Kuraray_Exceval_attractive_protection_for_your_food_engl.pdf (accessed **23.05.2023**).

132. Shruti, V. C.; Kutralam-Muniasamy, G.; Pérez-Guevara, F.; Roy, P. D.; Elizalde-Martínez, I., Free, but not microplastic-free, drinking water from outdoor refill kiosks: A challenge and a wake-up call for urban management. *Environmental Pollution* **2022**, *309*, 119800.

133. Atwood, E. C.; Falcieri, F. M.; Piehl, S.; Bochow, M.; Matthies, M.; Franke, J.; Carniel, S.; Sclavo, M.; Laforsch, C.; Siegert, F., Coastal accumulation of microplastic particles emitted from the Po River, Northern Italy: Comparing remote sensing and hydrodynamic modelling with in situ sample collections. *Marine Pollution Bulletin* **2019**, *138*, 561-574.

134. Saha, M.; Naik, A.; Desai, A.; Nanajkar, M.; Rathore, C.; Kumar, M.; Gupta, P., Microplastics in seafood as an emerging threat to marine environment: A case study in Goa, west coast of India. *Chemosphere* **2021**, *270*, 129359.

135. Röhrl, M.; Timmins, R. L.; Ghosh, D.; Schuchardt, D. D.; Rosenfeldt, S.; Nürmberger, S.; Bölz, U.; Agarwal, S.; Breu, J., Green and scalable processing of water-soluble, biodegradable polymer/clay barrier films. *Journal of Applied Polymer Science* **2023**, *140* (37), e54418.

136. Bénard, A.; Guell, D., 1 - Flow-induced alignment in composite materials: an update on current applications and future prospects. In *Flow-Induced Alignment in Composite Materials (Second Edition)*, Papathanasiou, T. D.; Bénard, A., Eds. Woodhead Publishing: **2022**; pp 1-29.

137. Zhao, C.; Zhang, P.; Zhou, J.; Qi, S.; Yamauchi, Y.; Shi, R.; Fang, R.; Ishida, Y.; Wang, S.; Tomsia, A. P.; Liu, M.; Jiang, L., Layered nanocomposites by shear-flow-induced alignment of nanosheets. *Nature* **2020**, *580* (7802), 210-215.

138. Ding, F.; Liu, J.; Zeng, S.; Xia, Y.; Wells, K. M.; Nieh, M.-P.; Sun, L., Biomimetic nanocoatings with exceptional mechanical, barrier, and flame-retardant properties from large-scale one-step coassembly. *Science Advances* **2017**, *3* (7), e1701212.

139. Hong, S. I.; Lee, J. H.; Bae, H. J.; Koo, S. Y.; Lee, H. S.; Choi, J. H.; Kim, D. H.; Park, S. H.; Park, H. J., Effect of Shear Rate on Structural, Mechanical, and Barrier Properties of Chitosan/Montmorillonite Nanocomposite Film. *Journal of Applied Polymer Science* **2011**, *119* (5), 2742-2749.

140. Cooper, T. A., 4 - Developments in plastic materials and recycling systems for packaging food, beverages and other fast-moving consumer goods. In *Trends in Packaging of Food, Beverages and Other Fast-Moving Consumer Goods (FMCG)*, Farmer, N., Ed. Woodhead Publishing: **2013**; pp 58-107.

141. Ben Halima, N., Poly(vinyl alcohol): review of its promising applications and insights into biodegradation. *RSC Advances* **2016**, *6* (46), 39823-39832.

142. Nilsen-Nygaard, J.; Fernández, E. N.; Radusin, T.; Rotabakk, B. T.; Sarfraz, J.; Sharmin, N.; Sivertsvik, M.; Sone, I.; Pettersen, M. K., Current status of biobased and biodegradable food packaging materials: Impact on food quality and effect of innovative processing technologies. *Comprehensive Reviews in Food Science and Food Safety* **2021**, *20* (2), 1333-1380.

143. Martău, G. A.; Mihai, M.; Vodnar, D. C., The Use of Chitosan, Alginate, and Pectin in the Biomedical and Food Sector—Biocompatibility, Bioadhesiveness, and Biodegradability. *Polymers* **2019**, *11* (11), 1837.

144. Habel, C.; Schöttle, M.; Daab, M.; Eichstaedt, N. J.; Wagner, D.; Bakhshi, H.; Agarwal, S.; Horn, M. A.; Breu, J., High-Barrier, Biodegradable Food Packaging. *Macromolecular Materials and Engineering* **2018**, *303* (10), 1800333.

145. Zhu, J.; Kumar, A.; Hu, P.; Habel, C.; Breu, J.; Agarwal, S., Layering-Triggered Delayering with Exfoliated High-Aspect Ratio Layered Silicate for Enhanced Gas Barrier, Mechanical Properties, and Degradability of Biodegradable Polymers. *Global Challenges* **2020**, *4* (9), 2000030.

146. Timmins, R. L.; Kumar, A.; Röhrl, M.; Havlíček, K.; Agarwal, S.; Breu, J., High Barrier Nanocomposite Film with Accelerated Biodegradation by Clay Swelling Induced Fragmentation. *Macromolecular Materials and Engineering* **2021**, *307* (6), 2100727.

147. Puls, J.; Wilson, S. A.; Hölter, D., Degradation of Cellulose Acetate-Based Materials: A Review. *Journal of Polymers and the Environment* **2011**, *19* (1), 152-165.

148. Robertson, R. M.; Thomas, W. C.; Suthar, J. N.; Brown, D. M., Accelerated degradation of cellulose acetate cigarette filters using controlled-release acid catalysis. *Green Chemistry* **2012**, *14* (8), 2266-2272.

149. Chen, K.; Yu, J.; Huang, J.; Tang, Q.; Li, H.; Zou, Z., Improved mechanical, water vapor barrier and UV-shielding properties of cellulose acetate films with flower-like metal-organic framework nanoparticles. *International Journal of Biological Macromolecules* **2021**, *167*, 1-9.

150. Phuong, V. T.; Verstiche, S.; Cinelli, P.; Anguillesi, I.; Coltelli, M.-B.; Lazzeri, A., Cellulose Acetate Blends - Effect of Plasticizers on Properties and Biodegradability. *Journal of Renewable Materials* **2014**, *2* (1), 35-41.

151. Zadbuke, N.; Shahi, S.; Gulecha, B.; Padalkar, A.; Thube, M., Recent trends and future of pharmaceutical packaging technology. *J Pharm Bioallied Sci* **2013**, *5* (2), 98-110.

152. Lacroix, M., Mechanical and Permeability Properties of Edible Films and Coatings for Food and Pharmaceutical Applications. In *Edible Films and Coatings for Food Applications*, Huber, K. C.; Embuscado, M. E., Eds. Springer New York: New York, NY, **2009**; pp 347-366.

153. White, M. S.; Kaltenbrunner, M.; Głowacki, E. D.; Gutnichenko, K.; Kettlgruber, G.; Graz, I.; Aazou, S.; Ulbricht, C.; Egbe, D. A. M.; Miron, M. C.; Major, Z.; Scharber, M. C.; Sekitani, T.; Someya, T.; Bauer, S.; Sariciftci, N. S., Ultrathin, highly flexible and stretchable PLEDs. *Nature Photonics* **2013**, *7* (10), 811-816.

154. Aslam, M.; Kalyar, M. A.; Raza, Z. A., Polyvinyl alcohol: A review of research status and use of polyvinyl alcohol based nanocomposites. *Polymer Engineering & Science* **2018**, *58* (12), 2119-2132.

155. Baker, M. I.; Walsh, S. P.; Schwartz, Z.; Boyan, B. D., A review of polyvinyl alcohol and its uses in cartilage and orthopedic applications. *Journal of Biomedical Materials Research Part B: Applied Biomaterials* **2012**, *100B* (5), 1451-1457.

156. Goodship, V.; Jacobs, D., Polyvinyl Alcohol: Materials, Processing and Applications. *Smithers Rapra Technology*: **2009**.

157. Kim, J. M.; Lee, M. H.; Ko, J. A.; Kang, D. H.; Bae, H.; Park, H. J., Influence of Food with High Moisture Content on Oxygen Barrier Property of Polyvinyl Alcohol (PVA)/Vermiculite Nanocomposite Coated Multilayer Packaging Film. *Journal of Food Science* **2018**, *83* (2), 349-357.

158.   López-Rubio, A.; Hernández-Muñoz, P.; Gimenez, E.; Yamamoto, T.; Gavara, R.; Lagarón, J. M., Gas barrier changes and morphological alterations induced by retorting in ethylene vinyl alcohol–based food packaging structures. *Journal of Applied Polymer Science* **2005**, *96* (6), 2192-2202.

5. Explanation of contributions to the publications

5.1 Shear orientation of nematic phases of clay nanosheets: Processing of barrier coatings

J. Coat. Technol. Res. **2021**, *19* (2), 487−495

Authors: Maximilian Röhrl, Judith H. Mettke, Sabine Rosenfeldt, Holger Schmalz, Ulrich Mansfeld, Renee L. Timmins, Christoph Habel, Josef Breu, and Franz Durst

Contributions: Prof. Dr. Josef Breu, Prof. Dr. Dr. h.c. Franz Durst, and I conceptualized the paper. I prepared the films via slot die coating and performed oxygen barrier measurements. I performed further film characterization, including XRD and SEM analysis. Judith H. Mettke performed and interpreted the rheological experiments. Dr. Sabine Rosenfeldt performed and interpreted the SAXS measurements. Dr. Holger Schmalz and Dr. Ulrich Mansfeld performed and interpreted cryo-SEM experiments. Renee L. Timmins and Dr. Christoph Habel provided scientific discussion and contributed to data processing and interpretation. Prof. Dr. Dr. h.c. Franz Durst assisted with experimental design and scientific input regarding rheological measurements and slot die coating calculations. The paper was written by Prof. Dr. Josef Breu, Prof. Dr. Dr. h.c. Franz Durst, and myself, with editing and proofreading from all authors.

Own contribution: 60%

5.2 Green and scalable processing of water-soluble, biodegradable polymer/clay barrier films

J. Appl. Polym. Sci. **2023**, *140* (37), e54418

Authors: Maximilian Röhrl, Renee L. Timmins, Dipannita Ghosh, Dominik D. Schuchardt, Sabine Rosenfeldt, Simon Nürmberger, Uwe Bölz, Seema Agarwal, and Josef Breu

Contributions: Prof. Dr. Josef Breu, Renee L. Timmins, and I conceptualized the paper. I prepared the films via slot die coating and performed gas barrier and optical property measurements. I performed further film characterization, including TGA, XRD, SEM and TEM analysis. Renee L. Timmins performed mechanical testing and contributed to data processing and interpretation. Dipannita Ghosh performed biodegradation testing, Dominik D. Schuchardt provided scientific discussion regarding barrier measurements, and Dr. Sabine Rosenfeldt performed and interpreted the SAXS measurement. Simon Nürmberger performed the water

solubility testing and measured the film thickness. Dr. Dr. Uwe Bölz provided scientific discussion. Prof. Dr. Seema Agarwal assisted with experimental design and scientific input regarding biodegradation testing. The paper was written by Prof. Dr. Josef Breu, Renee L. Timmins, and myself, with editing and proofreading from all authors. Renee L. Timmins and I contributed equally to this work.

Own contribution: 40%

5.3 New functional polymer materials via click chemistry-based modification of Cellulose Acetate

ACS Omega **2023**, *8* (11), 9889–9895

Authors: Maximilian Röhrl, Justus F. Ködel, Renee L. Timmins, Christoph Callsen, Merve Aksit, Michael F. Fink, Sebastian Seibt, Andy Weidinger, Glauco Battagliarin, Holger Ruckdäschel, Rainer Schobert, Josef Breu, and Bernhard Biersack

Contributions: Dr. Bernhard Biersack, Prof. Dr. Josef Breu, Justus F. Ködel, and I conceptualized the paper. I prepared the nanocomposite films and performed gas barrier measurements. I performed further film characterization, including XRD and TEM analysis. Justus F. Ködel synthesized the polymers and cast the polymer films. Renee L. Timmins provided scientific discussion regarding barrier measurements and nanocomposite preparation. Dr. Christoph Callsen and Dr. Merve Aksit performed and interpreted optical property measurements. Michael F. Fink performed and interpreted contact angle measurements, and Sebastian Seibt performed and interpreted TGA and differential scanning calorimetric measurements. Andy Weidinger supported the polymer synthesis and provided scientific discussion. Dr. Glauco Battagliarin assisted with experimental design and scientific input regarding decomposition testing. Prof. Dr. Holger Ruckdäschel and Prof. Dr. Rainer Schobert provided funding and scientific discussion. The paper was written by Dr. Bernhard Biersack, Prof. Dr. Josef Breu, Prof. Dr. Holger Ruckdäschel, Prof. Dr. Rainer Schobert and myself, with editing and proofreading from all authors. Justus F. Ködel and I contributed equally to this work.

Own contribution: 35%

5.4 Stretchable clay nanocomposite barrier film for flexible packaging

ACS Appl. Mater. Interfaces **2023**, *15* (18), 22524–22531

Authors: Maximilian Röhrl, Renee L. Timmins, Sabine Rosenfeldt, Dominik D. Schuchardt, Felix Uhlig, Simon Nürmberger, and Josef Breu

Contributions: Prof. Dr. Josef Breu and I conceptualized the paper. I prepared the films and performed water vapor barrier and optical property measurements. I performed further film characterization, including TGA, XRD, SEM and TEM analysis. Renee L. Timmins assisted with experimental design and scientific input regarding stretching experiments. Dominik D. Schuchardt contributed to data processing and interpretation of filler characterization. Dr. Sabine Rosenfeldt performed and interpreted the SAXS measurement. Felix Uhlig provided scientific discussion regarding barrier measurements. Simon Nürmberger performed the stretching experiments and measured film thickness. The paper was written by Prof. Dr. Josef Breu and myself, with editing and proofreading from all authors.

Own contribution: 80%

5.5 Disorder-order transition – Improving the moisture sensitivity of waterborne nanocomposite barriers

ACS Appl. Mater. Interfaces **2021**, *13* (40), 48101–48109

Authors: Maximilian Röhrl, Lukas K. S. Federer, Renee L. Timmins, Sabine Rosenfeldt, Theresa Dörres, Christoph Habel, and Josef Breu

Contributions: Prof. Dr. Josef Breu and I conceptualized the paper. I prepared the films via slot die coating and performed gas barrier and optical property measurements. I performed further film characterization, including TGA, XRD, SEM and TEM analysis. Lukas K. S. Federer provided scientific discussion, assisted with film preparation and measured film thickness. Renee L. Timmins contributed to data processing and experimental design for moisture sensitivity experiments. Dr. Sabine Rosenfeldt performed and interpreted the SAXS measurement. Dr. Theresa Dörres and Dr. Christoph Habel provided scientific discussion and contributed to data processing and interpretation. The paper was written by Prof. Dr. Josef Breu and myself, with editing and proofreading from all authors.

Own contribution: 80%

6. Results

6.1 Shear orientation of nematic phases of clay nanosheets: Processing of barrier coatings

Authors: Maximilian Röhrl, Judith H. Mettke, Sabine Rosenfeldt, Holger Schmalz, Ulrich Mansfeld, Renee L. Timmins, Christoph Habel, Josef Breu, and Franz Durst

Shear orientation of nematic phases of clay nanosheets: processing of barrier coatings

Maximilian Röhrl, Judith H. Mettke, Sabine Rosenfeldt, Holger Schmalz, Ulrich Mansfeld, Renee L. Timmins, Christoph Habel, Josef Breu ⓘ, Franz Durst

Abstract When suspensions are exposed to shear forces, the particles may form ordered structures depending on their shapes, concentrations, and the material. For some processes, e.g., for wet-film coating, it is important to know how fast these structures form in shear fields and for how long the structures persist when the shear is relaxed. To obtain information on the particle structure formation and the decay time, the effective viscosity of nematic suspensions of Na-hectorite nanosheets was investigated by rheology employing a cone-plate measurement geometry. The necessary time for the formation textured nematic films could be deduced by carrying out effective viscosity measurements at constant time steps. Information could also be obtained on the lifetime of the platelet textures when shear is relaxed. All this information was employed to identify geometrical requirements for slot dies to produce barrier liners with nanosheet layers oriented parallel to PET substrates. Thereby, we obtained green and simple coatings that are in line with state-of-the-art high-performance materials such as metalized plastic foils in terms of oxygen barrier properties.

M. Röhrl, S. Rosenfeldt, H. Schmalz, U. Mansfeld,
R. L. Timmins, C. Habel, J. Breu (✉)
Bavarian Polymer Institute and Department of Chemistry,
University of Bayreuth, Universitätsstr. 30, 95447 Bayreuth,
Germany
e-mail: josef.breu@uni-bayreuth.de

J. H. Mettke, F. Durst (✉)
FMP Technology GmbH, Am Weichselgarten 34,
91058 Erlangen, Germany
e-mail: f.durst@fmp-technology.com

Introduction

When small particles are added to a fluid and shear is applied, as in a Couette flow, the moving suspensions show effective viscosities of different complexities. The latter depend on the suspension medium, the particle concentration, its size and shape, and also on the hydrophobic or hydrophilic surface properties of the particle material.[1] For instance, Laun et al. showed that the measured effective viscosities as a function of the applied shear stress of polystyrene–ethyl acrylate latex particles in water depend on the particle concentration and the surface charge characteristics of the latex particles.[2,3] In his seminal work, Giesekus[4,5] showed that spherical particles, when exposed to shear flows, arrange themselves in such a way that they form "strings of particles". These particle structures were formed when an aqueous dispersion of particles was "moved by hand" between two glass plates. Since the work of Giesekus, it has been found that the effective viscosity of fluid–particle systems changes in such a way that an increase in structured particle arrangements results in a decrease in the measured effective viscosity. In turn, this means that effective viscosity measurements can be employed to reveal structural changes of suspensions induced by increasing shear rates. In particular, shear thinning indicates major structural changes. Such suspensions still comprise of a fluid with its original viscosity, but the interactions of the fluid with dispersed particles and particle–particle interactions yield forces that are recorded by viscometers as a decrease in the measured momentum of a rheometer.[5,6] The increase in the regularity of the

487

particle arrangements in the suspension decreases the viscosity.

Very persistent particle structures can be expected for suspensions of nanosheets with high aspect ratios.[7] In particular, when the aspect ratio is high enough at a given concentration of the suspension to hinder rotation of adjacent nanosheets, nematic liquid crystalline phases are formed,[8] as evidenced by small-angle X-ray scattering (SAXS). This is even the case for dilute aqueous suspensions of negatively charged nanosheets of the synthetic clay sodium fluorohectorite (NaHec),[9] where the nanosheets are known to adopt a cofacial arrangement due to strong electrostatic repulsion. For instance at 2.3 vol% of NaHec, adjacent clay nanosheets with a diameter of 20 μm are separated to only 32 nm and consequently, in this nematic state are confined in a cofacial geometry. Individual domains with cofacial arrangement are, however, randomly oriented (Fig. 1a).[8]

Such high aspect ratio nanosheets are perfectly suited for high-performance polymer nanocomposites as needed for a wide variety of applications, ranging from food packaging all the way to encapsulation of optoelectronic devices like organic photovoltaic and organic light emitting devices.[10] As pointed out by Cussler's theory of the tortuous path[11,12] for optimization of the barrier properties, perfect parallel alignment of the impermeable nanosheets on the substrate is crucial. Parallel aligned (textured) nanosheets are the key to achieve low gas permeabilities as the diffusion pathway for a gas permeant is hereby maximized and the tortuosity strongly decreases once nanosheets become tilted with respect to the diffusion direction (Fig. 1b).[13]

Flow-alignment of composite materials has been explored for some time.[14] In particular for the fabrication of composite films of nanosheet fillers, texturing *via* shear forces has been successfully applied,[15–18] although the applied methods are limited to rather low shear rates and difficult to scale up, for instance dip coating. A scalable and universally applicable coating process like slot die coating ensures efficient shear

texturing and sufficient inertness with respect to loss of this texture by reorientation to allow freezing of the textured film structure during evaporation of solvent.

Here, we study the shear orientation of nematic NaHec phases as a function of concentration and shear rate to establish the "formation time" of textured NaHec suspensions. Moreover, the rheological information was used to lay out slot dies for coating suspensions of NaHec nanosheets on PET substrates in a single-step procedure and the permeability of these clay–only barriers was determined.

Experimental

Materials and sample preparation

Carboxymethyl cellulose (CMC) with a mean molecular weight of 250000 g mol^{-1} was purchased from Daicel Corporation (Japan) and was dissolved in deionized water to obtain a 0.3 wt% solution. The solution was stable, and no sedimentation appeared. The synthetic clay $[Na_{0.5}]^{inter}[Mg_{2.5}Li_{0.5}]^{oct}[Si_4]^{tet}O_{10}F_2$ (NaHec) was synthesized via melt synthesis followed by annealing according to a published procedure and the material featured a cation exchange capacity (CEC) of 1.27 mmol g^{-1}.[19,20] Upon immersion in deionized water, the pristine material swells osmotically producing a nematic suspension with delaminated individual nanosheets of an average diameter of ≈ 20 μm, separated by 32 nm at 6 wt%, which corresponds to 2.3 vol%. The viscous suspension was placed in an overhead shaker for 7 days to assure equilibration to a uniform swelling state. Less concentrated suspensions were made by diluting this stock suspension with deionized water. A corona-treated PET (36 μm) substrate was obtained from Bleher KG (Germany).

Characterization methods

Small-angle X-ray scattering (SAXS) was performed using the system "Ganesha Air" (SAXSLAB, Denmark), equipped with a rotating anode X-ray source (copper, MicroMax 007HF, Rigaku Corporation, Japan). A position-sensitive detector (PILATUS 300K, Dectris, Switzerland) was used and different sample-to-detector positions were chosen to cover a wide range of scattering vectors. Measurements of the suspension were performed in 1 mm glass capillaries (Hilgenberg, Germany) at room temperature. The one-dimensional (1D) data [$I(q)$ vs. q with intensity I and scattering vector q] are in absolute scale and background corrected. The birefringence of the dispersion was evaluated with a self-made crossed polarizer.

Powder X-ray diffraction (PXRD) experiments were performed using Cu Kα radiation on a Bragg–Brentano-type diffractometer (Empyrean, Malvern
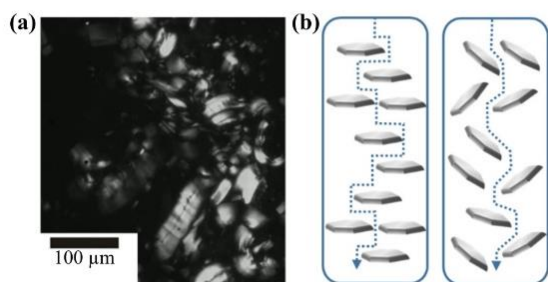
Fig. 1: (a) Optical microscopic image of statistically oriented, swollen NaHec tactoids between crossed polarizers. (b) Scheme of tortuous path for diffusion of permeant depending on the arrangement of nanosheets in a matrix

488

Panalytical BV, The Netherlands) equipped with a pixel detector. The XRD pattern of the coated clay film was recorded and subsequently analyzed using Malvern Panalytical's HighScore Plus software. Prior to the measurement, the sample was equilibrated at 43% relative humidity (r.h.).

All rheological experiments were performed with a shear rheometer (Type Physica MCR 101, Anton Paar, Austria) by using a CP50-1 cone and plate geometry with a plate diameter of $D = 50$ mm, cone angle of $\beta = 1°$ and truncation gap of $\kappa = 0.102$ mm. For determination of the formation time, the viscosity was measured as a function of the time and measuring time steps were set to 0.1 s.

Cryo scanning electron microscopy (CryoSEM) micrographs were recorded at 2 kV with a secondary electron (Everhart-Thornley) detector on a Zeiss Ultra plus SEM equipped with a Leica VCT cryo stage cooled to $-155°C$. For sample preparation, the specimen was sheared in the rheometer directly on the SEM sample holder (Figs. S1, S2) that was subsequently plunged in liquid nitrogen and after cooling was transferred with a Leica EM VCT100 shuttle into a Leica EM MED020 freeze-fracture unit, where fractured surfaces were generated by impacting the specimen with a blade. After sputter coating with a thin layer of tungsten, the sample was transferred with the shuttle to the precooled cryo stage within the SEM for imaging.

Oxygen transmission rates (OTRs) were determined on a Mocon OX-TRAN 2/21 system with a lower detection limit of 0.05 cm^3 m^{-2} day^{-1} atm^{-1}. The measurements were performed at 23°C and 50% and 90% r.h. A mixture of 98% nitrogen and 2% hydrogen (v/v) was used as the carrier gas and pure oxygen as permeant (>99.95%, Linde Sauerstoff 3.5).

The thickness of the NaHec barrier coating was measured with a High-Accuracy Digimatic Micrometer (Mitutoyo, Japan) with a measuring range of 0–25 mm and a resolution of 0.1 μm. A mean value was determined by ten measurements on different spots in the permeability area.

Coating experiments

An aqueous 6 wt% NaHec suspension was used for coating on corona-treated PET foils. The corona treatment guarantees to maintain a uniform wetting of the coated film after the fluid left the slot die. Prior to coating, the suspension was homogenized in a SpeedMixer DAC 400.2 VAC-P (Hauschild, Germany) to remove air bubbles under vacuum (5 min, 50 mbar and up to 2500 rpm). The coating experiments were conducted using a TSE Table Coater with a 1-Layer Slot Die 300 mm, AAA (TSE Troller AG, Switzerland). For the coating procedure, the coating width was set to 0.21 m. The pump flow rate (3.4 ml min^{-1}) and the table speed (0.2 m min^{-1}) were adjusted accordingly. The table temperature was set to 25°C and

the coating gap set to 86 μm (36 μm PET + 50 μm coating height).

The obtained wet films were dried in-line applying a slight under pressure by an airflow of approximately 1.5 m^3 min^{-1} generated by a Side Channel Blower Type 1SD 510 (Elektror Airsystems GmbH, Germany). A microporous surface below the airflow guarantees a soft and uniformly solvent removal over the entire film surface.

Results and discussion

Shear orientation of NaHec nanosheets

Viscosity measurements are usually carried out using a plate–cone rotating viscometer to obtain the dynamic viscosity η of liquids. Plain liquids, comprised of low molecular weight molecules, show Newtonian behavior meaning that shear viscosity remains constant and is independent of shear rate. When, however, high molecular weight polymers are dissolved in water at sufficiently high concentration, e.g., carboxymethyl cellulose (CMC), a shear thinning behavior is observed. According to Mezger,[6] this is related to the disentanglement of the high molecular weight polymers (Fig. 2 inset). For CMC, shear thinning is perfectly reversible with no hysteresis. When the distribution of η is measured with increasing and decreasing shear rate $\dot{\gamma}$, the lines overlap (Fig. 2). This indicates that the timeframe available for each η measurement is sufficient to yield the η value characteristic for each adjusted $\dot{\gamma}$ selected by the rheometer. Owing to limitations of the measurement technology,
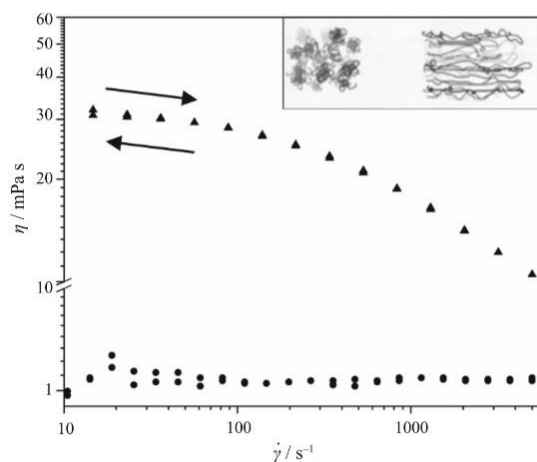

Fig. 2: Viscosity measurements for increasing and decreasing shear rates for water (black circle) and 0.3 wt% carboxymethyl cellulose solution (black triangle). The black arrows indicate the measurement direction. The inset shows the disentanglement of polymer chains under shear

the data show a scattering for small shear rates with low-viscosity fluids. Therefore, η distributions are shown only for $\dot{\gamma} > 10$ s^{-1}.

The synthetic clay NaHec belongs to a few layered compounds that show the rare phenomenon of osmotic swelling,[21] which leads to spontaneous delamination into single NaHec nanosheets by immersing the clay in deionized water.[8] A lateral dimension of 20 µm with a thickness of 1 nm for such a nanosheet yields an aspect ratio of ~ 20000.[9] Due to this high aspect ratio, nanosheets are hindered in rotation, giving a nematic liquid crystalline phase as evidenced by SAXS (Fig. 3). Even a concentrated (6 wt%, corresponding to 2.3 vol%) NaHec suspension represents a translationally symmetric, stable, and homogeneous phase owing to the strong electrostatic repulsion of negatively charged clay nanosheets.[8] Therefore, nanosheets are forced to adopt a cofacial arrangement with single NaHec nanosheets separated to 32 nm. The SAXS curve shows a q^{-2} dependence at low and intermediate q range that is characteristic for platelet-like objects. Moreover, the osmotic swelling and platelet-like geometry are proven further by employing a simple model of disks with radius $R = 10$ µm and thickness $h = 1$ nm separated to $d_{001} = 32 \pm 3.2$ nm using a Gauss distribution (Fig. 3 inset).

The inset in Fig. 4a shows schematically the behavior of nanosheets in a fluid under shear, according to Mezger.[6] Please note that contrary to what was proposed by Mezger, NaHec suspensions used here are not isotropic but due to the large diameter, the nanosheets are held in a coplanar arrangement within domains, as evidenced in the SAXS measurements (Fig. 3). The individual domains, however, are statistically oriented. When shear stress is applied, these
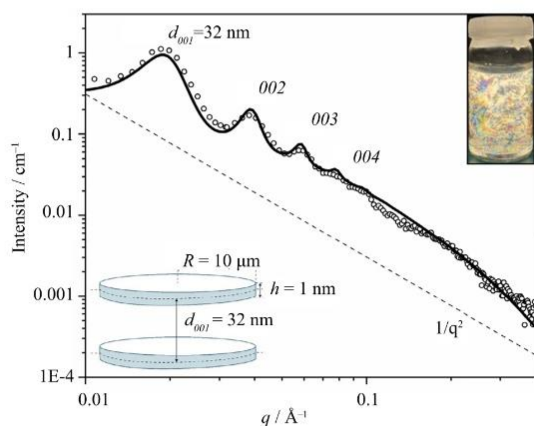
Fig. 3: SAXS pattern of a 6 wt% NaHec suspension indicating a nematic phase with a uniform separation of 32 nm between adjacent nanosheets (circle, measured, black line, calculated). The insets show birefringence of the diluted (~1 wt%) nematic suspension between crossed polarizers and the model (separated disks) used for fitting

domains are gradually oriented resulting in a quasi-single crystalline state, where all nanosheets are rearranged into a cofacial orientation while still being separated to a uniform distance. With increasing shear rate, the suspension will then eventually represent a Bragg stack (1D single crystal) that is perfectly textured parallel to the rheometer plate (Fig. 4a).

Viscosity–shear rate distributions obtained for Na-Hec suspensions of varying concentration with increasing and decreasing $\dot{\gamma}$ measurements showed shear thinning and a pronounced hysteresis (Fig. 4a). As expected, the initial viscosity decreased significantly with decreasing concentration. When shear is relaxed, the textures of cofacially aligned NaHec nanosheets, generated by the velocity shear field of the suspension, persist for a long time although the texture–producing shear field is reduced. Hereby, the measured viscosities stay constant though the shear stress is decreased confirming the high stability of textures of shear oriented NaHec nanosheets. This phenomenon is more pronounced for suspensions of lower NaHec concentrations. As the dominating interparticle force is electrostatic repulsion,[22] which increases with r^{-1}, this observation is somewhat counterintuitive. If shear thinning is related to the alignment of domains and individual nanosheets in the direction of the shear force, the increase in η with decreasing shear rate should be related with tilting and potentially undulating nanosheets in respect to the shear flow. This should actually be more difficult at higher repulsion.

Shear alignment of nanosheets in the suspension was additionally visualized by directly taking CryoSEM images of vitrified suspension films. To suppress crystallization of water that would destroy the pristine suspension structures, for this experiment, the concentrations had to be increased to 20 wt% and additionally 30% of glycerol had to be added (see the supporting information for experimental details, Figs. S1, S2). After applying shear stress (up to 1000 s^{-1}) while the plate was replaced with a SEM sample holder for the NaHec suspension, it was vitrified and subsequently CryoSEM micrographs were recorded at freeze-fractured surfaces (Fig. 4b, c). As expected based on the rheology experiments, band-like structures with parallel plates translocated relative to each other were the dominating feature.

To investigate the formation time Δt_f of oriented nematic phases with nanosheets aligned in parallel to the plate and cofacially to each other, three different but constant shear rates for the rheometer were set and the effective viscosity of a 1.5 wt% NaHec suspension was measured over a period of time (Fig. 5). During the formation time, the instantaneously applied shear is responsible for the imposed forces acting on the nanosheets that cause the nanosheets to orientate towards the direction of the flow lines. Hereby, the effective viscosity varies and finds a minimum once the nanosheets aligned themselves in parallel to the walls of the rotating plate of the rheometer. After approximately twice the formation time, the nanosheets

490
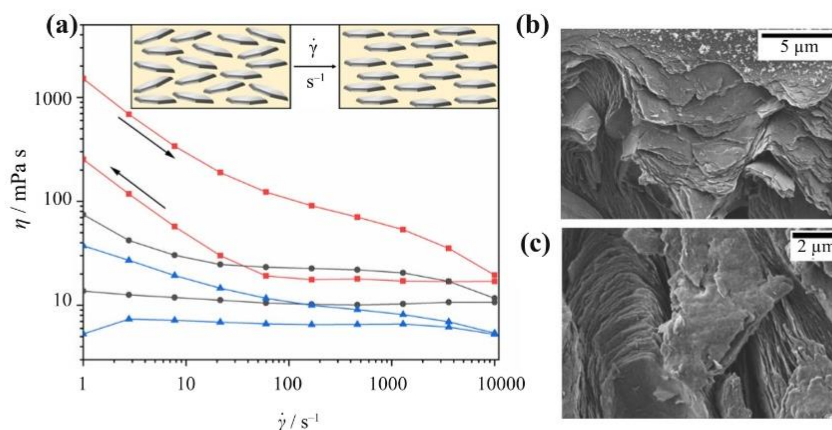
Fig. 4: (a) Effective viscosity measurements of NaHec suspensions of different concentrations: 3 wt% (red), 1.5 wt% (gray) and 0.75 wt% (blue). The black arrows indicate the measurement direction, which is identical for each concentration. The inset shows schematically the behavior of nanosheets under shear. (b), (c) CryoSEM images of shear oriented NaHec suspensions (20 wt%) in a water/glycerol 70/30 w/w mixture
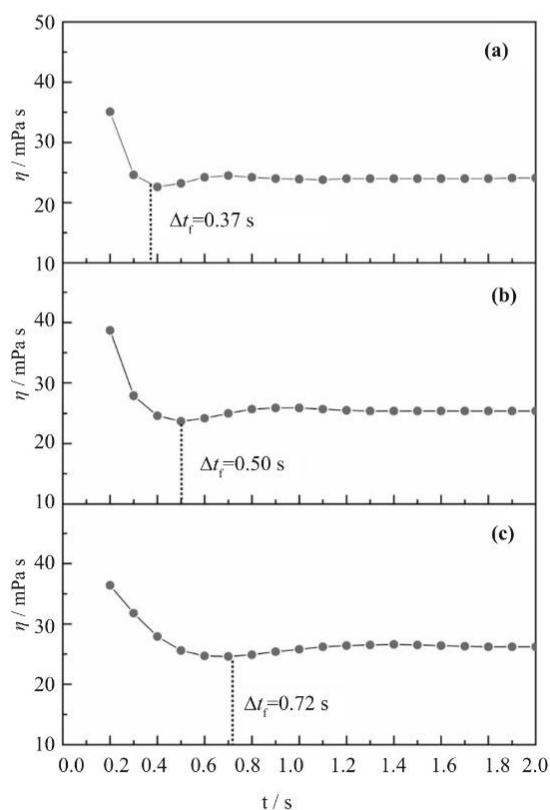
Fig. 5: Measured formation time Δt_f of oriented nematic phases in a 1.5 wt% NaHec suspension for different shear rates: (a) 100 s^{-1}; (b) 70 s^{-1}; (c) 50 s^{-1}

moved back into their final position, and the viscosity reaches a constant value characteristic of the textured nematic phase. While η converges to the same value within experimental errors, the formation times increase with decreasing constant shear field $\dot{\gamma}$ applied. The limiting value of η is characteristic for a given concentration (Fig. S3) indicating that the quality of texture approached is the same, although it takes longer to achieve it.

From these measurements, a formation time of the shear oriented texture can be deduced that corresponds to the minimum of the viscosity. Multiplying Δt_f with each shear rate applied yields the following relation:

$$\Delta t_f = \frac{36}{\dot{\gamma}} \qquad (1)$$

Hence, the stronger the applied shear field is, the faster the aligned nematic phase forms. The constant 36 was determined as a mean value of the three measurements. So far, our results indicate that effective shear viscosity measurements permit information to be obtained about texturing of nanosheet suspensions. Next, this information will be transformed into scalable processing of barrier films that require such a texture.

Slot die coating

One of the major applications of nanosheets is barrier coatings applied in a technically benign processing on substrates. Since the viscosity of nanosheet suspensions is considerable, the concentrations that can be processed are low (Fig. 4). Shear thinning helps but since evaporation of large amounts of suspension medium

takes time, sufficient inertness of the shear alignment is required. The observed rheological behavior of NaHec suspensions suggests that high shear fields should be employed to yield aligned nanosheets parallel to the substrate already within the applied coating tool. Slot dies of the kind illustrated in Fig. 6 promise to be advantageous for this task. The suspension enters the slot die *via* the fluid supply slot. The actual coating region is located between the lips l of the die and the substrate to be coated, that moves with a certain web velocity U_w. The flow regions underneath the lips possess the shear field of a Couette flow and, if this flow dominates, a nanosheet suspension is exposed to this shear field for the following experimental time Δt_{ex}:

$$\Delta t_{ex} = \frac{3l}{U_w} \qquad (2)$$

After the suspension leaves the fluid supply slot (Fig. 6), it moves first to the direction of the back meniscus and then passes two more times the lip length l before it leaves the shear field between the lips and the substrate at the front meniscus. This yields three times the length of the lips l as given in equation (1), assuming the slot width is negligible. By including the coating gap d, the actual shear rate $\dot{\gamma}_{ex}$ to which the suspension is exposed can be calculated as follows:

$$\dot{\gamma}_{ex} = \frac{U_w}{d} \qquad (3)$$

Taking the formation time Δt_f of the nanosheet textures into account, i.e., equation (1), allows the following time consideration to be written:

$$\Delta t_{ex} \geq \Delta t_f = \frac{36}{\dot{\gamma}} = 36\frac{d}{U_w} \qquad (4)$$

If this time condition is maintained, the nanosheet suspension is exposed for a sufficiently long time to form the shear oriented structures that were seen using the Anton Paar rheometer. Combining equations (2) and (4) yields

$$\frac{3l}{U_w} \geq 36\frac{d}{U_w} \qquad (5)$$

$$\frac{l}{12} \geq d \qquad (6)$$

Hence, the rheological measurements combined with the above considerations give access to the geometry of slot dies needed to achieve sufficient nanosheet alignment in the coating process. If one decides to employ a slot die in its "bead coating" mode, the following condition[23,24] must hold:

$$d \geq 2h \qquad (7)$$

where h is the coated layer thickness (Fig. 6) and hence equations (6) and (7) can be combined to give

$$l \geq 24h \qquad (8)$$

Coating textured films of nanosheets require slot dies with "long lips" to be employed, as equation (8) shows. Alternatively, a slow web velocity U_w can be applied for the coating procedure that increases the experimental time Δt_{ex}, as equation (4) suggests. In summary, increasing the lip length l and decreasing U_w both will increase Δt_{ex}, and the combination will ideally produce highly textured films. We emphasize that this implies that rheological measurements that yield effective viscosities of nanoparticle suspensions provide useful information for the design of coating tools.
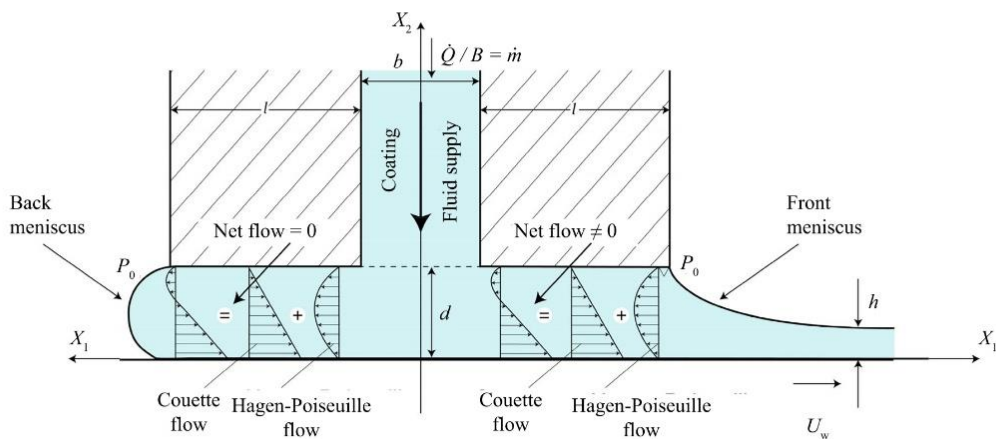

Fig. 6: Schematic representation of the coating flow of a slot die intended for coating flow considerations. The scheme was redrawn according to Dongari et al.[23]

To coat nanosheet suspensions appropriately to produce foils with good barrier layers, it is essential to choose a suitable slot die design for the requested layer thickness h, according to equation (8). We employed a slot die with lip length $l = 600$ μm allowing to coat layers of $h \leq 25$ μm. Therefore, the requirements discussed above were fulfilled. The coating and drying process was performed using the equipment shown in Fig. 7 that can easily be adapted to large scale and high throughput at an industrial level. A NaHec suspension (6 wt%) was coated onto a corona pre-treated PET foil with a coating gap of 50 μm yielding a wet film thickness of approximately 25 μm. In addition, a slow web velocity U_w of 0.2 m min^{-1} was applied to guarantee sufficiently experimental time Δt_{ex} for the formation of aligned nanosheet textures in parallel to the substrate already within the shear field of the slot die. In this way, a 1.5 μm thick clay–only barrier coating consisting only of overlapping NaHec nanosheets was obtained as visualized in the SEM image (Fig. S4). Apparently, this hints at the sufficient inertness of the shear oriented textures upon drying and solvent removal. The NaHec nanosheets are perfectly aligned with respect to the PET substrate.

The quality of texture of the NaHec coating was investigated by 2D SAXS measurements (Fig. 8a). The sample was oriented parallel to the beam direction. The weak halos along the q_y-axis are characteristic of the PET substrate and appear vertically to the beam direction (compare Fig. S5). In parallel with the PET domains, *001* Bragg reflections of the 1D crystalline NaHec films are visible along the q_y-axis, indicating parallel arrangement of the NaHec nanosheets relative to the PET substrate. The absence of other peaks in the 2D SAXS pattern proves that the clay nanosheets are aligned perfectly parallel and no other orientation is present. For comparison, the inset at the bottom half shows the theoretical scattering of perfectly aligned disks ($R = 10$ μm, $h = 1$ nm, $d_{001} = 1.3$ nm). The SAXS data thus confirm that a perfect texture was achieved

by shear orientation below the slot die during the coating process, and moreover, that this texture is preserved upon drying of the wet film.

Furthermore, the NaHec film was equilibrated at 43% r.h. and subsequently analyzed by powder X-ray diffraction (PXRD). A series of basal reflections was visible up to fourth order with a low coefficient of variation (CV) of 0.1% (Fig. 8b), which according to Meuring's rules[25] indicates a perfect 1D crystallinity with constant separation of adjacent nanosheets. The broad peak at $26°$ 2θ marked with an asterisk arises from the PET substrate (Fig. S6). The basal spacing of 12.6 Å, moreover, agrees within experimental error with the value observed for pristine, as synthesized NaHec.[19] This together with the low CV indicates that upon drying a perfect 1D "single crystalline" film was formed by restacking cofacially aligned nanosheets into a perfectly textured Bragg stack oriented parallel to the PET foil as already indicated by the SAXS data. Faults in the 1D periodicity caused by misalignment or inclusion of crumbled or folded nanosheets or larger voids could not be detected. This is further corroborated by the high transparency of the NaHec coating (Fig. 8b inset), as larger voids would cause scattering.

According to the tortuous path model[11,12] and in addition to the aspect ratio of the filler, the quality of texture plays an important role in achieving superior gas barrier properties, and the perfect parallel alignment of nanosheets is expected to produce films with low permeability. And indeed, the clay–only films produced by slot die coating showed oxygen transmission rates (OTRs) comparable to vacuum-deposited aluminum coatings (Table 1).[26] All OTRs were measured at 23°C and equilibration to the applied r.h. was guaranteed.

The OTR of neat PET could be decreased by a factor of more than 20 at 50% r.h. and 23°C by applying this thin coating (1.5 μm) of NaHec. Absolute transmission values are relevant for industrial applications, but they depend strongly on the thickness of the investigated barrier liner. For better comparison with other materials, transmission rates were converted into permeabilities by multiplying with the overall thickness of the coated PET foil. Moreover, the contribution of the PET substrate to the total OTR is subtracted by applying a series expansion according to Roberts et al.[27] Thereby, an oxygen permeability (OP) of 2.2 cm^3 μm m^{-2} day^{-1} bar^{-1} was obtained for the neat NaHec coating, which surpasses that of commonly used polymer materials in the packaging segment by orders of magnitude. For instance, the OP for PET applied as substrate is 1321 cm^3 μm m^{-2} day^{-1} bar^{-1} and that for poly(vinyl chloride) is $\sim$ 2000–8000 cm^3 μm m^{-2} day^{-1} bar^{-1} (2–8 cm^3 mm m^{-2} day^{-1} bar^{-1}, respectively)[26] at 23°C and 50% r.h. Quite surprisingly and despite the known increased swelling of NaHec at elevated r.h.,[8] the OP of the NaHec coating at 23°C and 90% r.h. deteriorates by only 80%. The observed OP of 3.9 cm^3 μm m^{-2} day^{-1} bar^{-1} at this r.h. indicates a lower moisture sensitivity as hydrophobized
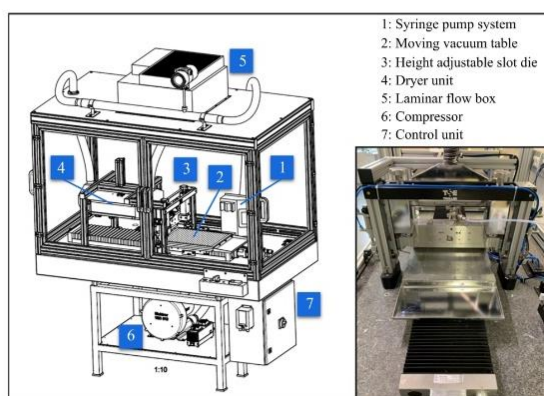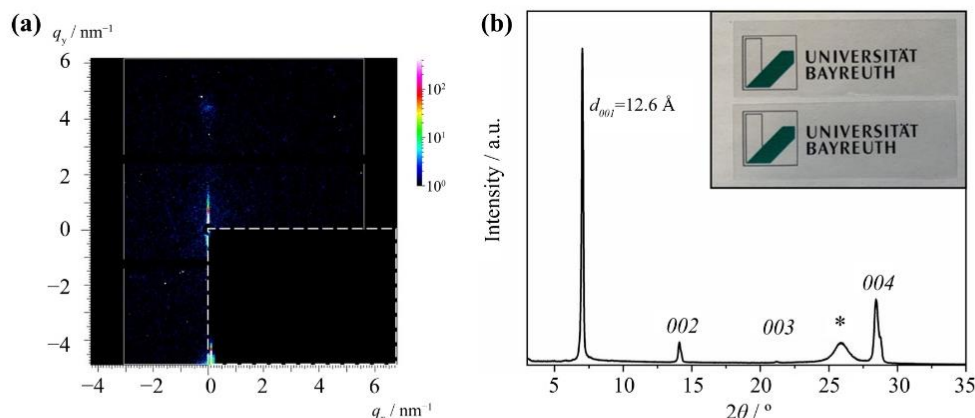

Fig. 7: Sketch of the coating and drying facility. The inset shows the operating slot die (TSE Troller AG)

1: Syringe pump system
2: Moving vacuum table
3: Height adjustable slot die
4: Dryer unit
5: Laminar flow box
6: Compressor
7: Control unit

Fig. 8: (a) 2D SAXS pattern of NaHec films on PET measured in parallel geometry. The inset at the bottom half shows the theoretical pattern with a *001* Bragg reflection at 1.3 nm (b) PXRD pattern of NaHec coating. The inset shows transparent PET (top) and NaHec (bottom) films

Table 1: OTRs of slot die coated NaHec films (1.5 µm) measured at 23°C and different r.h.

Film	OTR / cm^3 m^{-2} day^{-1} bar^{-1}	
	23°C, 50% r.h.	23°C, 90% r.h.
PET (36 µm)	36.7	33.0
PET (36 µm) + NaHec	1.4	2.4

poly(ethylene-co-vinyl alcohol) (EVOH). An EVOH type with an ethylene content of 27 mol%, typically used for food packaging, shows an OP deterioration by a factor of ~85 in the range between 50 and 90% r.h.[28]

Comparing our results with previously published, clearly inferior OP of synthetic LiHec coatings obtained by doctor blading on polypropylene substrate (60 cm^3 µm m^{-2} day^{-1} bar^{-1} at 23°C and 50% r.h.),[29] would indicate that optimized processing by appropriate slot die coating makes a major contribution to the excellent barrier performance.

Inorganic NaHec clay–only coatings in combination with the studied slot die coating process are a green and smart solution to producing high oxygen barrier layers that provide stable protection towards gas permeation at elevated r.h.

Conclusions

Viscosity–shear rate distributions give valuable insight into the kinetics and the required shear stress for shear orientation of nanosheet suspensions. The formation time of these textures is inversely proportional to the applied shear rate in a plate–cone rheometer. With this information, a relation could be deduced that in turn allows for designing slot dies that assure shear orien-

tation of nematic nanosheet suspensions within the geometry of the slot die. Applying such a slot die to high aspect ratio NaHec nanosheets suspensions, perfectly aligned 1D "single crystalline" wet films can be obtained with sufficient inertness to maintain their orientation for a long enough time allowing to obtain textured dry films. Slot die coating, therefore, represents a technically benign coating process appropriate to obtain perfectly textured nanosheet films as required for barrier coatings.

References

1. Sharma, AK, Tiwari, AK, Dixit, AR, "Rheological Behaviour of Nanofluids: A Review." *Renew. Sustain. Energy Rev.*, **53** 779–791 (2016)
2. Laun, HM, "Rheological Properties of Aqueous Polymer Dispersions." *Die Angew. Makromol. Chem.*, **123** (1) 335–359 (1984)
3. Laun, HM, "Rheological Properties of Polymer Dispersions with Respect to Shear-Induced Particle Structures." In: Giesekus, H, Hibberd, MF (ed.) *Progress and Trends in Rheology II*, pp. 287–290. Steinkopff, Heidelberg (1988)
4. Giesekus, H, "Strömungen Mit Konstantem Geschwindigkeitsgradienten und Die Bewegung von Darin Suspendierten Teilchen." *Rheol. Acta*, **2** (2) 112–122 (1962)
5. Giesekus, H, *Phänomenologische Rheologie: Eine Einführung*. Springer, Berlin, Heidelberg (1994)
6. Mezger, TG, *Das Rheologie Handbuch: Für Anwender von Rotations- und Oszillations-Rheometern*. Vincentz Network GmbH & Co. KG, Hannover (2016)
7. Litchfield, D, Baird, D, "The Rheology of High Aspect Ratio Nanoparticle Filled Liquids." *Rheol. Rev.*, 1–60 (2006)
8. Rosenfeldt, S, Stöter, M, Schlenk, M, et al. "In-Depth Insights into the Key Steps of Delamination of Charged 2D Nanomaterials." *Langmuir*, **32** (41) 10582–10588 (2016)
9. Stöter, M, Kunz, DA, Schmidt, M, et al. "Nanoplatelets of Sodium Hectorite Showing Aspect Ratios of ≈20 000 and Superior Purity." *Langmuir*, **29** (4) 1280–1285 (2013)
10. Ebina, T, "Development of Clay-Based Films." *Chem. Rec.*, **18** (7–8) 1020–1032 (2018)
11. Cussler, EL, Hughes, SE, Ward, WJ, et al. "Barrier Membranes." *J. Membr. Sci.*, **38** (2) 161–174 (1988)
12. DeRocher, JP, Gettelfinger, BT, Wang, J, et al. "Barrier Membranes with Different Sizes of Aligned Flakes." *J. Membr. Sci.*, **254** (1) 21–30 (2005)
13. Bharadwaj, RK, "Modeling the Barrier Properties of Polymer-Layered Silicate Nanocomposites." *Macromolecules*, **34** (26) 9189–9192 (2001)
14. Papathanasiou, TD, Guell, DC, *Flow-Induced Alignment in Composite Materials*. Elsevier, Amsterdam (1997)
15. Zhao, C, Zhang, P, Zhou, J, et al. "Layered Nanocomposites by Shear-Flow-Induced Alignment of Nanosheets." *Nature*, **580** (7802) 210–215 (2020)
16. Ding, F, Liu, J, Zeng, S, et al. "Biomimetic Nanocoatings with Exceptional Mechanical, Barrier, And Flame-Retardant Properties From Large-Scale One-Step Coassembly." *Sci. Adv.*, **3** (7) e1701212 (2017)
17. Hong, SI, Lee, JH, Bae, HJ, et al. "Effect of Shear Rate on Structural, Mechanical, and Barrier Properties of Chitosan/Montmorillonite Nanocomposite Film." *J. Appl. Polym. Sci.*, **119** (5) 2742–2749 (2011)
18. Tsurko, ES, Feicht, P, Nehm, F, et al. "Large Scale Self-Assembly of Smectic Nanocomposite Films by Doctor Blading versus Spray Coating: Impact of Crystal Quality on Barrier Properties." *Macromolecules*, **50** (11) 4344–4350 (2017)
19. Breu, J, Seidl, W, Stoll, AJ, et al. "Charge Homogeneity in Synthetic Fluorohectorite." *Chem. Mater.*, **13** (11) 4213–4220 (2001)
20. Kalo, H, Möller, MW, Ziadeh, M, et al. "Large Scale Melt Synthesis in an Open Crucible of Na-Fluorohectorite with Superb Charge Homogeneity and Particle Size." *Appl. Clay Sci.*, **48** (1) 39–45 (2010)
21. Lerf, A, "Storylines in Intercalation Chemistry." *Dalton Trans.*, **43** (27) 10276–10291 (2014)
22. Daab, M, Eichstaedt, NJ, Habel, C, et al. "Onset of Osmotic Swelling in Highly Charged Clay Minerals." *Langmuir*, **34** (28) 8215–8222 (2018)
23. Dongari, N, Sambasivam, R, Durst, F, "Slot Coaters Operating in Their Bead Mode." *Coating*, **40** (12) 10–15 (2007)
24. Durst, F, Haas, R, Raszillier, H, "Stabilität vom Filmen in der Fliesser-Filmbeschichtung." *Sonderdr. Coat.*, **22** (1990)
25. Moore, DM, Reynolds, RC, *X-ray Diffraction and the Identification and Analysis of Clay Minerals*. Oxford University Press, Oxford (1989)
26. Lange, J, Wyser, Y, "Recent Innovations in Barrier Technologies for Plastic Packaging—A Review." *Packag. Technol. Sci.*, **16** (4) 149–158 (2003)
27. Roberts, AP, Henry, BM, Sutton, AP, et al. "Gas Permeation in Silicon-Oxide/Polymer (SiOx/PET) Barrier Films: Role of the Oxide Lattice, Nano-Defects and Macro-Defects." *J. Membr. Sci.*, **208** (1) 75–88 (2002)
28. GmbH, KE. "EVAL™ Properties." December 2020]; Available from: http://www.evalevoh.com/en/eval-properties/barrier-to-oxygen/relative-humidity.aspx.
29. Möller, MW, Lunkenbein, T, Kalo, H, et al. "Barrier Properties of Synthetic Clay with a Kilo-Aspect Ratio." *Adv. Mater.*, **22** (46) 5245–5249 (2010)

Supporting Information

Shear Orientation of Nematic Phases of Clay Nanosheets – Processing of Barrier Coatings

Maximilian Röhrl[1], Judith H. Mettke[2], Sabine Rosenfeldt[1], Holger Schmalz[1], Ulrich Mansfeld[1], Renee L. Timmins[1], Christoph Habel[1], Josef Breu[1]*, Franz Durst[2]*

[1]Bavarian Polymer Institute and Department of Chemistry, University of Bayreuth, Universitätsstr. 30, 95440 Bayreuth, Germany

[2]FMP Technology GmbH, Am Weichselgarten 34, 91058 Erlangen, Germany

*Correspondence to: josef.breu@uni-bayreuth.de

                                          f.durst@fmp-technology.com

Experimental

Shear orientation prior to CryoSEM. Shear orientation of a 20 wt% NaHec suspension at 20 °C was conducted on an Anton Paar MCR302 rheometer equipped with a Peltier plate (P-PTD 200) for temperature control. For these experiments a parallel plate geometry with a plate diameter of D = 12 mm was used and the sample was directly applied on a SEM sample holder for easy transfer to the freeze fracture unit for CryoSEM investigations (Fig. S1). The sample was first pre-sheared at a shear rate of γ = 0.01 s^{-1} for 60 s, followed by a continuous increase to γ = 1000 s^{-1} (logarithmic shear rate profile, Fig. S2), which was held for additional 60 s to complete sample orientation.

SEM images were recorded using the instrument ZEISS LEO 1530 (Carl, Zeiss AG, Germany) operating at 3.0 kV equipped with an in-lens secondary detector. A cross-section of the coating was obtained employing a scalpel, and cutting was performed towards the substrate side to protect the coating.

Fig. S1: Experimental setup for the shear orientation of a 20 wt% NaHec suspension applied to prepare samples for CryoSEM images.
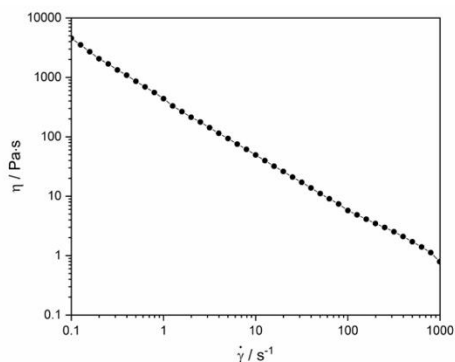

Fig. S2: Flow curve measurements of a 20 wt% NaHec suspension in a water/glycerol 70/30 w/w mixture applied to prepare samples for CryoSEM images. Glycerol was used as antifreeze agent to guarantee a homogeneous vitrification. The sample was vitrified after shear-induced alignment of NaHec nanosheets at a shear rate of 1000 s^{-1} and subsequently CryoSEM micrographs were recorded.

2
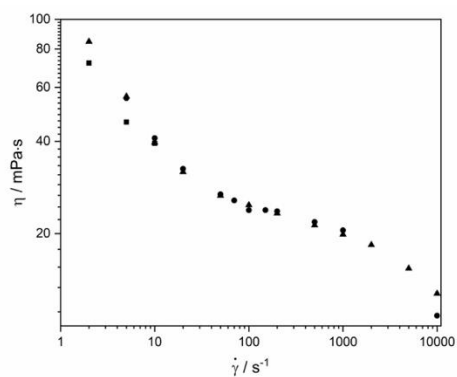
Fig. S3: η_∞-effective measured for different shear rates $\dot{\gamma}$. With increasing $\dot{\gamma}$, η_∞-effective decreases indicating an improved texturing. Triangles, squares and dots indicate different series of measurements that were performed with a 1.5 wt% NaHec suspension.
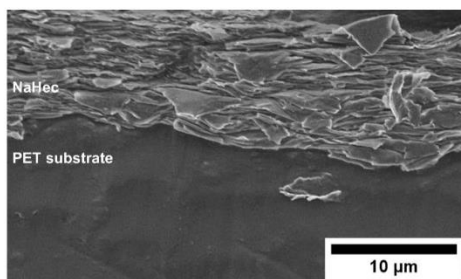
Fig. S4: Cross-sectional SEM image of the NaHec coating.

3
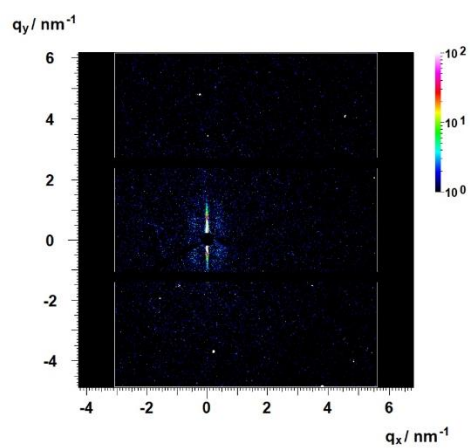
Fig. S5: Two-dimensional SAXS pattern of PET substrate.
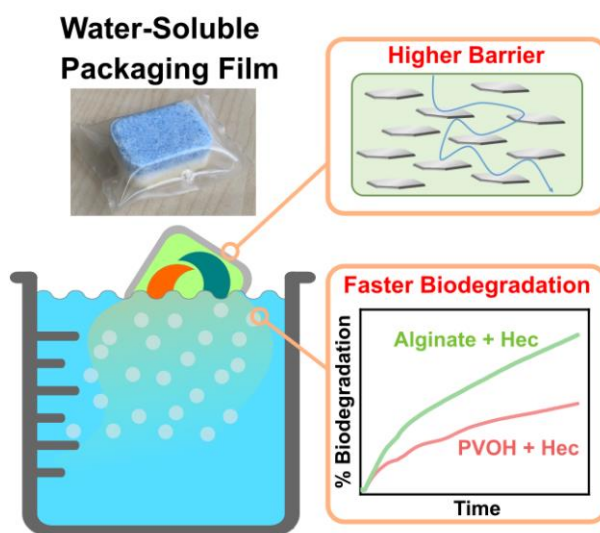

Fig. S6: PXRD pattern of the neat corona pre-treated PET substrate.

4

6.2 Green and scalable processing of water-soluble, biodegradable polymer/clay barrier films

Authors: Maximilian Röhrl, Renee L. Timmins, Dipannita Ghosh, Dominik D. Schuchardt, Sabine Rosenfeldt, Simon Nürmberger, Uwe Bölz, Seema Agarwal, and Josef Breu

RESEARCH ARTICLE

Green and scalable processing of water-soluble, biodegradable polymer/clay barrier films

Maximilian Röhrl[1] | Renee L. Timmins[1] | Dipannita Ghosh[2] |
Dominik D. Schuchardt[1] | Sabine Rosenfeldt[3] | Simon Nürmberger[1] |
Uwe Bölz[4] | Seema Agarwal[2] | Josef Breu[1]

[1]Bavarian Polymer Institute, Department of Chemistry, University of Bayreuth, Bayreuth, Germany

[2]Macromolecular Chemistry II, Bavarian Polymer Institute, Department of Chemistry, University of Bayreuth, Bayreuth, Germany

[3]Physical Chemistry I, Bavarian Polymer Institute, Department of Chemistry, University of Bayreuth, Bayreuth, Germany

[4]HPX Polymers GmbH, Tutzing, Germany

Correspondence
Josef Breu, Bavarian Polymer Institute and Department of Chemistry, University of Bayreuth, Bayreuth 95447, Germany.
Email: josef.breu@uni-bayreuth.de

Funding information
H2020 Marie Skłodowska-Curie Actions, Grant/Award Number: 860720; Deutsche Forschungsgemeinschaft, Grant/Award Number: SFB 1357-391977956

Abstract

Poly(vinyl alcohol) (PVOH) based water-soluble packaging with intentional disposal into wastewater provides great convenience for both households and industry. In this paper, we demonstrate with CO_2 evolution testing that only insignificant fractions ($\sim$2%) of PVOH biodegrade in wastewater within 33 days. To avoid unintentional environmental build-up and the accompanying consequences to marine life, alternative materials with a suitable balance of performance and biodegradability are needed. Until now, the barrier properties of biodegradable biopolymers could not compete with state-of-the-art water-soluble packaging materials like PVOH films. In this paper, we report on waterborne, sandwich-structured films using hydroxypropyl methylcellulose or alginate produced with an industrially scalable slot-die coater system. The inner layer of the film consists of a collapsed nematic suspension of high aspect ratio synthetic clay nanosheets that act as an impermeable wall. Such a film structure not only allows for barrier filler loadings capable of sufficiently reducing oxygen and water vapor permeability of alginate to 0.063 cm^3 mm m^{-2} day^{-1} bar^{-1} and 53.8 g mm m^{-2} day^{-1} bar^{-1}, respectively, but also provides mechanical reinforcement to the biopolymer films facilitating scalable processing. Moreover, the films disintegrated in water in less than 6 min while rapid biodegradation of the dissolved polymer was observed.

KEYWORDS

biodegradable and water-soluble packaging, microplastic, oxygen and water vapor barrier, slot die coating, sustainability

1 | INTRODUCTION

Water-soluble packaging films provide premeasured convenience to the delivery of dishwasher and laundry detergents, pesticides, fertilizer, dyes, and cement additives.[1]

Maximilian Röhrl and Renee L. Timmins contributed equally to this study.

They are designed to dissolve and be released into the environment during use——particularly into wastewater streams. Poly(vinyl alcohol) (PVOH) is the most commonly employed polymer for such packaging as it is widely accepted as biodegradable. However, the kinetics of degradation in conventional wastewater are so slow that PVOH is actually considered a recalcitrant pollutant.[2]

Removal of PVOH from industrial wastewater is not accomplished through standard procedures, which consist of biological treatment with microbial stems that are commonly encountered in communal sewage plants to break down organic matter contaminates. The persistence of PVOH has led some to suggest the addition of advanced oxidation processes (ozonation, persulfate oxidation, electrochemical oxidation, etc.) to wastewater treatment facilities to reduce the level of contamination.[3–5] Unfortunately, this suggestion does not address the root of the problem and overlooks the poor worldwide accessibility to state-of-the-art wastewater treatment facilities.

Certain microorganisms, such as Pseudomonas (Sphingomonads) strains, are capable of biodegrading PVOH after acclimating in heavily contaminated waters, but the conditions for sufficient acclimation are highly specific. Such wastewater streams are primarily those of paper and textile treatment plants that continuously expel PVOH in large quantities.[2,6,7] Even with acclimated microorganisms, the kinetics of PVOH removal depends on various additional factors, including molecular weight, degree of hydrolysis, and the presence of salts.[8,9] PVOH contamination in natural water bodies has already brought consequences including increases in the chemical oxygen demand and inhibition of aerobic microorganisms, suffocating surface foam, and mobilization of heavy metals within water streams.[5,10,11]

Products that employ water-soluble films having an intentional disposal into the environment should be designed in a more responsible manner that does not contribute to wastewater pollution. The challenge is matching the excellent properties that PVOH provides with a more readily biodegradable alternative that meets the requirements during usage while allowing for being washed away. An ideal sustainable, water-soluble packaging film would exhibit biodegradability in wastewater, high gas barrier, flexible mechanical properties, transparent optical properties, as well as being suitable for high-volume manufacturing.

While natural biopolymers, including cellulose, alginate, whey protein, and so forth,[12] are quite attractive for use as alternative packaging material because they are readily water-soluble as well as biocompatible, nontoxic, and renewable,[13] they lack sufficient gas barrier and mechanical toughness. Both water vapor and oxygen barrier performance are critical considerations for commercial packaging

materials to prevent the breakdown of the film under ambient conditions and degradation of oxygen or water vapor sensitive products.[14] Some successful attempts to fabricate biopolymer films with properties relevant to water-soluble packaging offering a considerable water vapor barrier have been made at the lab scale, however, the fabrication techniques, including solvent casting or electrospinning, would not be practical for large-scale production.[15,16]

Improving the barrier of natural biopolymers can be accomplished effectively by the use of barrier fillers. The synthetic clay sodium hectorite (Hec) has imparted massive barrier improvements to biodegradable polymers in the past thanks to its exceptional aspect ratio and complete intercalation by water-soluble polymers.[17,18] Our group reported recently that band-like aggregates of Hec, even without an intercalated polymer matrix, provide an excellent barrier to oxygen due to the perfect clay nanosheet alignment induced during application by slot die coating.[19]

Slot die coating is a relatively unexplored lab-scale film preparation method that can easily be translated into a large-scale and low-cost roll-to-roll process. The instrument uses a die head having a thin slot from which metered solution exits onto a moving substrate. The encountered shear thinning on the applied solution is particularly useful to improve barrier properties due to the alignment of polymer chains and suspended barrier filler in the resulting film.[20,21]

In this work, we report a slot die coating method that can be translated into large-scale roll-to-roll manufacturing of high-barrier, self-standing biodegradable films for water-soluble packaging applications. Waterborne layered films made of Hec with either PVOH, hydroxypropyl methylcellulose (HPMC), or sodium alginate (alginate) were evaluated as a packaging material in terms of water solubility, gas barrier properties, mechanical performance, and optical properties. CO_2 evolution of the layered films in wastewater is compared to the same polymer film without Hec to ensure improvements in physical properties do not come at a sacrifice to biodegradability.

A roll-to-roll process easily enables the incorporation of multiple functional layers, unlike traditional solvent casting which is practically limited to a single monolayer. The layered structure of these films prevents complications that come with compounding a nematic Hec suspension with biopolymers like high viscosities, aggregation of filler, or embrittlement that limits high clay loadings.[19] At the same time, the exceptional barrier enhancement expected from the use of high aspect ratio nanosheets is ensured, producing biodegradable, high-performance, and scalable packaging films. With water being the only solvent employed, the production of the films aims to fulfill the 12 Principals of Green Chemistry.[22]
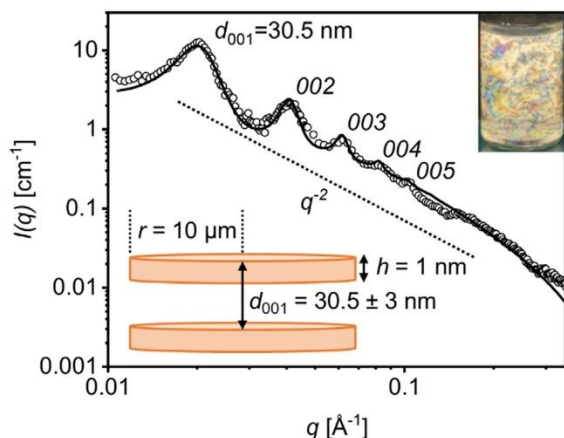
FIGURE 1 Small angle x-ray scattering (SAXS) pattern of a 6 wt% (≈2.3 vol%) aqueous Hec suspension with nanosheets uniformly separated to 30.5 nm (∘measured, —calculated). The top inset shows birefringence of the diluted nematic Hec suspension between crossed polarizers. The bottom inset displays the model of disks used for the calculated SAXS intensity. [Color figure can be viewed at wileyonlinelibrary.com]

2 | RESULTS AND DISCUSSION

2.1 | Film fabrication

A quantitatively delaminated suspension of Hec can be prepared by simply mixing the bulk clay in water. The rare phenomenon of thermodynamically allowed one-dimensional dissolution (i.e., osmotic swelling) that is accessible to this material provides single layers of negatively charged nanosheets without the use of mechanical force.[23] Fully delaminated Hec nanosheets have a preserved platelet diameter of ≈20,000 nm with a single layer thickness of 1 nm, yielding an exceptionally large aspect ratio (ratio of platelet diameter to thickness).[24] Such a high aspect ratio of ≈20,000 hinders rotation of adjacent Hec nanosheets in solution even at concentrations as low as 1 vol%,[25] giving a nematic liquid crystalline phase as indicated by the birefringence observed under cross-polarized light (Figure 1, top inset). Under closer inspection employing small angle x-ray scattering (SAXS), we can confirm a highly ordered liquid crystal structure with single Hec nanosheets separated to 30.5 nm corresponding to a 6 wt% (≈2.3 vol%) aqueous Hec suspension (Figure 1). The q^{-2}-dependence of the SAXS curve at the low and intermediate q-range is characteristic for platy two-dimensional objects.[26] This geometry is further corroborated by applying a calculated model of disks with a radius of 10,000 nm (±15%) and a thickness of 1 nm (±7%) separated to a d-spacing of

30.5 ± 3 nm using a Gaussian distribution (Figure 1, bottom inset). Observable reflexes up to *005* and an absence of peaks in the high q region that would indicate an undelaminated fraction verifies the presence of a translationally homogeneous nematic phase. The nematic nature of the Hec suspension is a critical aspect to obtain superior barrier properties since coated Hec nanosheets should lie parallel to the substrate and perpendicular to the direction of gas diffusion.[27] Retention of this structural order during processing will be ensured by employing a slot die coating instrument.

Separate polymer solutions of PVOH, HPMC, and Alginate were prepared by mixing the respective polymers with the plasticizers sorbitol and glycerol in a weight ratio of 80/10/10 (polymer/sorbitol/glycerol) in water. Plasticizers were added to obtain soft and flexible films as required for single-serving pouch applications. Solution concentrations and wet-coat heights were adjusted to warrant viscosities appropriate for slot die coating.

Due to the repulsive nature of the nanosheets that constitute liquid crystalline, delaminated Hec, suspensions of this material are highly viscous even at solid contents as low as 3 wt%.[28] The Hec suspension was prepared as 6 wt% in double distilled water, reflecting the maximum viscosity processible with the in-house slot die coater.

The polymer blends and the Hec suspension were then applied sequentially onto a PLA carrier substrate using a slot-die coater. The choice of material for the carrier substrate is inconsequential, as it will be removed from the layered films prior to analysis. In a similar fashion to the production of commercial layered films, the lab-scale slot-die coater provides precise and programmable solution deposition to make customizable layer structures. For this work, we chose a sandwich structure consisting of three layers arranged as polymer/Hec/polymer. With this structure, a suitable Hec content can be added without the concern of increasing viscosity of the polymer solution into ranges unsuitable for processing, as would be the case when working with a single, combined polymer/Hec suspension. Unlocking filler restrictions also gives access to properties of biopolymer nanocomposites that are unattainable with a homogenous blend. A sandwich structure produced on a large-scale roll-to-roll process would consist of three sequential slot die heads, separated by drying units, and a collecting roll to remove the film from the carrier substrate when the addition of layers is complete (Figure 2a).

In our current laboratory setup, we are limited to a single slot die head, so the roll-to-roll process is stimulated by drying coated layers with a lamellar airflow dryer, then exchanging the solution in the slot die and
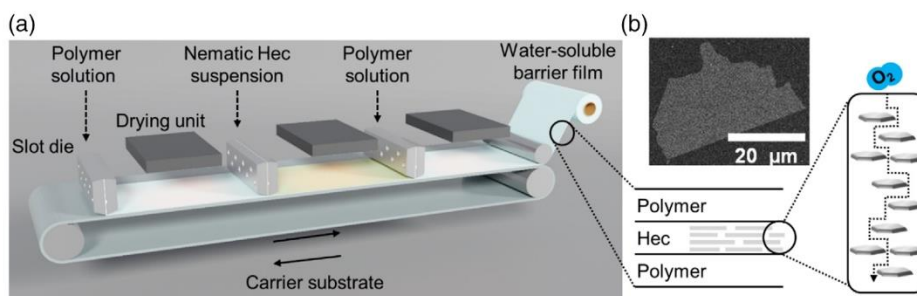
FIGURE 2 (a) Sketch of the potential roll-to-roll processing method employing three consecutive slot die heads and drying units. In this way, a multi-layered film can be fabricated in-line and at high throughput by applying different coating solutions. Here we propose a layered sandwich structure with a first inner layer of water-soluble polymer, a second barrier layer of Hec and a third sealing layer of water-soluble polymer on top. The layered film is peeled-off and rolled-up while the carrier substrate can be reused. The inset highlights the tortuous path that a sandwiched Hec barrier layer provides against gas permeation. (b) Scanning electron microscopy (SEM) image of a single Hec nanosheet with a diameter >20 μm. [Color figure can be viewed at wileyonlinelibrary.com]

coating the next layer on top of the dry one. Given a desired dry film thickness and solution solid content, the wet coating thickness is adjusted by means of the pump flow rate, table speed, and coating gap. The final dry film can be easily peeled from the carrier substrate for analysis. A sandwich polymer film was produced from each of the three polymer solutions prepared. Due to the staggered stacking of platelets within a nematic Hec suspension and the large lateral extension of these sheets, we expect that the collapse of the structure upon drying will create a solid and nearly impermeable wall with a band-like structure and a diffusion path for permeates that is dramatically tortuous (Figure 2b).[29]

The final clay content of the PVOH, HPMC, and alginate layered films was determined from the residue that remains after a temperature ramp during thermal gravimetric analysis (Figure S1) as 21, 22, and 40 wt%, respectively. For comparison, monolayer films of each polymer (without Hec) were also prepared from the same polymer/plasticizer solution to ensure identical plasticizer content.

2.2 | Imaging

Cross-sections of each of the prepared films were observed with scanning electron microscopy (SEM) (Figure S2). The consecutive coating of individual layers provides highly uniform outer polymer layers of ≈30 μm sandwiching the inner Hec layer. The slight detachment of the top layer of polymer from the Hec layer is an artifact from preparation for imaging. The center Hec layer, which exhibits the proposed barrier wall structure, is ≈6 μm thick, neglecting the area of detachment. The ideal parallel alignment of the nanosheets can be attributed to the shear forces that
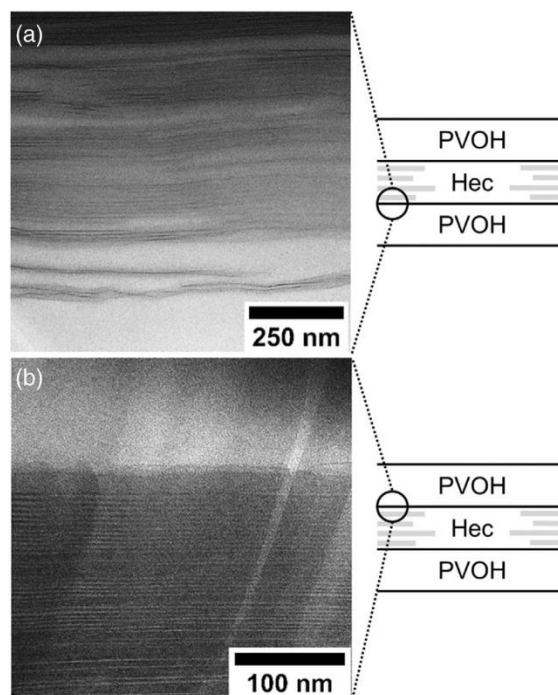
FIGURE 3 Transmission electron microscope (TEM) cross-sections of the PVOH/Hec/PVOH film. (a) Interface between first PVOH sublayer and second Hec barrier layer. (b) Interface between second Hec barrier layer and top PVOH layer.

suspensions are subjected to within the slot die coating head, which retains the highly ordered, liquid crystalline Hec structure during processing.[28] Electron dispersive x-ray (EDX) element mapping of the film cross-sections with silicon from Hec represented in cyan and carbon from the PVOH represented in red aid in distinguishing the defined layer structure.

The layer interfaces within the PVOH/Hec/PVOH film were further investigated by transmission electron microscope (TEM) of the cross-sections prepared by cryo-ion-slicing (Figure 3). Observation of HPMC/Hec/HPMC and alginate/Hec/alginate films with TEM imaging was not possible as the ion beam used to prepare ultra-thin slices damages the biopolymers.

It appears that coating an aqueous Hec suspension onto the water-soluble PVOH sublayer leads to a partial re-dissolution of the dried polymer layer. This mobilizes the polymer, allowing it to diffuse between adjacent nanosheets that are separated to 30.5 nm in the liquid nematic state. The in-situ formed nanocomposite interface reaches only 1 μm into the Hec layer due to the tortuosity imparted by the impermeable nanosheets that restrict further diffusion as drying progresses (Figure 3a). Such a structure at the interface provides excellent layer adhesion between the Hec and polymer domains. The amount of diffusion from the top layer of PVOH into the Hec region is less than the bottom layer of PVOH (Figure 3b), which explains its higher susceptibility to delayering as observed in the SEM image. Such behavior is not a surprise as a Hec layer is less prone to swelling upon removal of water and restacking of platelets. This suggests that the size of the nanocomposite interface could be modified by the drying treatment of the layers. Earlier studies have also demonstrated that the degree of PVOH intercalation into Hec can be modified by decreasing the drying temperature.[20]

The formation of an interfacial nanocomposite is assumed to form in the HPMC and alginate layered films as well due to their XRD patterns (Figure S3), which reflect a *d*-spacing of 1.6 and 1.4 nm, respectively. These values are substantially higher than the basal spacing of neat Hec ($d_{001} = 0.96$ nm).[24] The PVOH layered film also exhibits a *d*-spacing of 1.6 nm.

2.3 | Characterization and application

2.3.1 | Water solubility tests

The desired time for a water-soluble packaging film to disintegrate depends upon the mode of application. For household use, like in detergent pods, dissolution within minutes is desired, but it must be balanced with some degree of resistance to moisture or water vapor that may be encountered during transport and storage.

To evaluate film behavior when exposed to water, each film underwent water solubility testing according to the MSTM-205 testing standard (Figure S4). Films were held still in vigorously mixing water at room temperature. Disintegration time is defined as the time it takes until film breakage is observed, and dissolution time as

TABLE 1 Disintegration and dissolution time of water-soluble films according to the method "MSTM-205 Solubility Test with Plastic Holder" in distilled water at a temperature of 23°C.

Film	Disintegration time (min)	Dissolution time (min)
PVOH/Hec/PVOH	5.7 ± 1.3	9.7 ± 2.1
HPMC/Hec/HPMC	5.9 ± 2.1	7.4 ± 2.1
Alginate/Hec/ Alginate	2.9 ± 0.9	4.3 ± 0.6
PVOH	0.3 ± 0.1	0.4 ± 0
HPMC	0.3 ± 0.1	0.5 ± 0.1
Alginate	0.1 ± 0	0.1 ± 0

the time it takes until fragments of the film are no longer detectable by eye. Comparative tests were performed with neat polymer films (Table 1).

All of the plasticized polymer films exhibited disintegration in 0.3 min or less and underwent complete dissolution in no longer than 0.5 min, with HPMC taking the longest to do so. This is an expected result for these highly hydrophilic and water-soluble polymers. As a sandwich layered film, the time to disintegration was delayed to 2.9 min for alginate and 5.7 and 5.9 min for PVOH and HMPC, respectively. The time to disintegration, comparable to the time it would take for a pouch to release its contents, could be characterized for the desired application, for example, rapid release pouch (alginate film) or a standard release time (PVOH and HPMC film). Dissolution time of the three films ranged from 4.3 min for the alginate/Hec/alginate film to 9.7 min for the PVOH/Hec/PVOH film. The sandwich film structure proved able to provide some hydrophobicity when added to water-soluble polymers without totally hindering their ability to disintegrate rapidly. Hydrophobization has also been observed in intercalated Hec nanocomposites with other water-soluble polymers by means of an increased resistance to swelling and the improved water vapor barrier.[17,30] This slight modification of film properties makes them much more practical for real-world use where accidental exposure to water should not cause premature disintegration and exposure to humid conditions should not initiate excessive swelling that ruins film integrity and barrier. Films of the plasticized polymers themselves disintegrate within 20 s of exposure to water, which would lead to much wasted product if storage conditions are not strictly monitored. Although the layering of Hec within these same plasticized polymers increases their disintegration time, their ability to dissolve fully under 10 min at room temperature was not impeded. A range of disintegration and dissolution times could be customized by altering the film layer structure and by using different polymers to match expected packaging conditions.

Films/polymers	OP at 23°C and 50% RH $(cm^3\ mm\ m^{-2}\ day^{-1}\ bar^{-1})$	WVP at 23°C and 85% RH $(g\ mm\ m^{-2}\ day^{-1}\ bar^{-1})$
PVOH/Hec/PVOH	0.008 (65% RH)	8.4
HPMC/Hec/HPMC	0.001 (65% RH)	12.5
Alginate/Hec/Alginate	0.063 (65% RH)	53.8
PVOH[a]	0.02 (0% RH)	1260
Poly(ethylene terephthalate) (PET)[a]	1–5	21–84
Polypropylene (PP)[a]	50–100	8–17
Polyethylene (PE)[a]	50–200	21–84
Poly(vinyl chloride) (PVC)[a]	2–8	42–84
Poly(lactic acid) (PLA)[b]	3–15 (0%/50% RH)	158–855
Poly(butylene adipate terephthalate) (PBAT)[b]	61	3450 (100% RH)
EVOH 32 mol%[c]	0.01 (65% RH)	-
Exceval[d]	0.002 (65% RH)	-

TABLE 2 Oxygen permeability (OP) and water vapor permeability (WVP) of the water-soluble films compared with common polymers used for packaging and biodegradable polymers.

Note: Unless otherwise stated, the OP and WVP are given at test conditions of 23°C and 50% RH, 85% RH, respectively. Values are partially converted from their originally reported units allowing a consistent comparison.
[a]Lange and Wyser.[31]
[b]Wu et al.[40]
[c]Mitsubishi Gas Chemical.[41]
[d]Kuraray.[32]

2.3.2 | Gas barrier properties

Despite being water-soluble, the layered films provide exceptional protection against permeates, like oxygen and water vapor, that cause deteriorative reactions in many products. Oxygen transmission rate (OTR) and water vapor transmission rate (WVTR) values recorded for our layered films were converted into oxygen permeability (OP) and water vapor permeability (WVP) to normalize for film thickness and allow comparison across commercial and literature reports (Table 2). At a 65% relative humidity (RH), the PVOH, and HPMC layered films have an OP of 0.008 and 0.001 $cm^3\ mm\ m^{-2}\ day^{-1}\ bar^{-1}$, respectively. These values are comparable to the high-performance Exceval and outperform other common non-degradable packaging materials like polyethylene terephthalate (PET), polyethylene (PE), and poly(vinyl chloride) (PVC) measured at a lower 50% RH.[31,32] WVP values at a challenging 85% RH for PVOH and HPMC layered films are 8.4 and 12.5 $g\ mm\ m^{-2}\ day^{-1}\ bar^{-1}$, respectively, once again outperforming the same commercial films.

While hydrophilic polymers like Exceval and ethylene vinyl alcohol (EVOH) swell at elevated RH, which degrades barrier performance,[30,33] the Hec barrier layer blocks diffusion of absorbed water and slows the swelling process. This becomes evident when comparing the WVP of 1260 $g\ mm\ m^{-2}\ day^{-1}\ bar^{-1}$ for neat water-soluble PVOH with the low WVP of 8.4 $g\ mm\ m^{-2}\ day^{-1}\ bar^{-1}$ found for the Hec loaded PVOH layered film at a demanding high 85% RH.[31] The incorporated Hec barrier layer hampers swelling and concomitant breakdown of barrier as indicated by a barrier improvement factor of 150.

Our processing strategy easily achieves top OP and WVP performance for HPMC among other HPMC systems reported in literature across various fillers and blends.[34] Although the layered alginate film falls slightly behind our other layered films and Exceval, it nevertheless outperforms several commercial packaging films and is competitive with the same materials in terms of WVP. The OP and WVP values for the alginate layered film of 0.063 $cm^3\ mm\ m^{-2}\ day^{-1}\ bar^{-1}$ and 53.8 $g\ mm\ m^{-2}\ day^{-1}\ bar^{-1}$, respectively, surpass previously reported barrier values for this material, even compared to other nanocomposites or crosslinked structures.[35–39] All of our layered films are orders of magnitude better in both OP and WVP when compared to commercial biodegradable films like PLA and poly(butylene adipate terephthalate) (PBAT). In general, the high barrier requirements for packaging are usually out of range for unfilled biodegradable materials.[40]
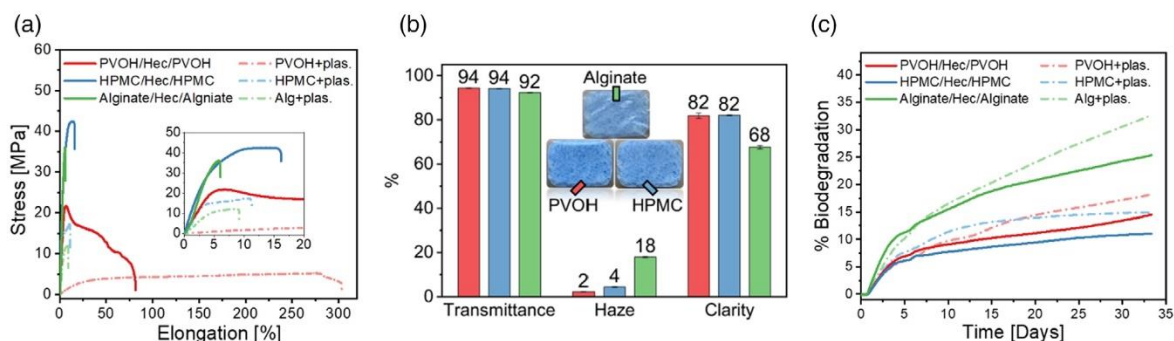
FIGURE 4 Characterization of the films. (a) Mechanical properties of the plasticized polymers (10 wt% of each plasticizer, sorbitol, and glycerol) and their layered films with Hec. (b) Optical properties of layered films. (c) Biodegradation measured in terms of conversion to CO_2 of the plasticized polymers (10 wt% of each plasticizer, sorbitol, and glycerol) and their layered films with Hec. [Color figure can be viewed at wileyonlinelibrary.com]

2.3.3 | Mechanical properties

With an excellent barrier to permeating gases, the evaluation of these layered films as a packaging material continues with the examination of mechanical performance. These water-soluble polymer layered films also exhibited excellent tensile properties suitable for flexible packaging films (Figure 4a, Table S1). The addition of the Hec layer improved the elastic modulus of all three of the plasticized polymers, establishing further functionality as a structural reinforcement. For alginate, the Hec layer boosts its elastic modulus from 35 to 1100 MPa. HPMC layered films exhibited nearly a 300% increase in its tensile strength. Naturally, percent elongation at break was reduced in all samples from the clay layer, however, severe embrittlement that is often observed in dispersed nanocomposite systems, even at much lower clay loadings than reported here, was avoided.[38,42,43] Moreover, the stretchability of PVOH is retained despite 22 wt% Hec, although delamination of the film layers was observed starting around 40% elongation.

A balance of suitable mechanical performance and suitable barrier properties has plagued degradable clay nanocomposites in the past due to how the same rigid, impermeable fillers that elongate the diffusion pathway for permeates also cause embrittlement of the polymer matrix.[44] These competing effects limited clay loading to below 5 wt% in dispersed nanocomposites and thus limited barrier performance. In this way, achieving high performance regarding both barrier and mechanical properties in a single material presented a huge hurdle to the implementation of biodegradable packaging materials with competitive performance. By the addition of common plasticizers and a sandwich-layered structure, we have evidently succeeded in mitigating

this embrittlement effect. The simple and scalable method of producing barrier films that we report here provides a promising solution to such critical hurdles of the past.

2.3.4 | Optical properties

Characterization of the optical properties of the layered films was performed to demonstrate how these films also meet the consumer preference for transparent packaging (Figure 4b). The PVOH layered film provides the most transparent film, while the alginate layered film suffers from slight haziness. Nevertheless, all three of the layered materials exhibit excellent optical properties that are suitable for transparent packaging needs, as displayed in an example of packaged dishwasher tablets (Figure 4b, inset).

2.3.5 | CO_2 evolution testing for biodegradation

Dissolution of polymers can favor biodegradation kinetics since, in the dissolved state, polymers have a maximized exposed surface area available to chain scission via hydrolysis. The oligomeric pieces may then be mineralized by microbial assimilation. However, this assimilation by microbes is not guaranteed simply by dissolution but additionally requires an appropriate match of enzymes and chain functionalities.

Therefore, the sandwich layered films and the plasticized polymer films were evaluated for their biodegradation in wastewater sludge by monitoring conversion into CO_2 for 33 days. Wastewater sludge was sourced from

the local wastewater treatment plant in Bayreuth, Germany. Cumulative CO_2 production was converted into percent biodegradation (Figure 4c), and aniline was used as the positive control. As additional references, the neat plasticizers were also evaluated under the same conditions (Figure S5). Sorbitol biodegraded 92% by the end of the 33 days, while glycerol degraded just 27% in the same time. With 10 wt% of each sorbitol and glycerol added to all films, we can therefore assume that ~12% of their total biodegradation in 33 days can be attributed to that of the plasticizers.

Taking a closer look at the biodegradation behavior of the plasticized polymer films reveals that PVOH and HPMC degradation reaches 14% and 11%, respectively. This biodegradation should be primarily, if not entirely, attributed to the plasticizers, exemplifying that although dissolved in water, these materials are incapable of degradation by microorganisms encountered in a typical communal sewage plant (or degrade too slowly to be non-persistent). As reported in the introduction, PVOH biodegradation requires a specialized environment with adapted microbes that are not common for communal sewage plants.[2] HPMC has shown to be biodegradable in soil,[45] however, this behavior is evidently not directly translatable to wastewater on a relevant timescale.

On the other hand, biodegradation on day 33 for the plasticized alginate and alginate/Hec/alginate of 33% and 25%, respectively, was recorded. Given that only 12% of the plasticizers would be assimilated at that point, the degradation of both the alginate samples substantially exceeds what could be attributed to the plasticizers. Clearly, alginate films are not only dissolved in freshwater but are also biodegraded in this wastewater environment.

Similarly to the dissolution kinetics, the biodegradation kinetics are slightly slowed down by the incorporation of a Hec layer into the center of the polymer films, likely attributed to its barrier effect. These biodegradation curves confirm that a sandwich-layered film with the barrier reinforcement material in the center provides optimal improvement in physical properties while also leaving the polymer accessible to biodegradation.

3 | CONCLUSION

Water-soluble packaging films provide unmatched convenience for dispensing both household and commercial products. In this work, we demonstrated the insignificant biodegradation of a commonly employed material, PVOH, in the disposal medium that it is designed for: wastewater. Similarly, and somewhat surprisingly, even a bio-based HPMC film showed no significant biodegradation, while the alginate films demonstrated up to 33% biodegradation in 33 days. With rapid biodegradation and low production costs,[46] sodium alginate could make a viable commercial alternative to PVOH.

However, biopolymers, like alginate, cannot compete alone in demanding packaging applications due to their weak barrier and mechanical properties. By employing an industrially scalable slot die coating system (roll-to-roll processing), sandwich-structured films containing an inner hectorite clay barrier layer were obtained. This barrier layer could impart competitive properties to films of sodium alginate, including an OP and WVP of 0.063 cm^3 mm m^{-2} day^{-1} bar^{-1} and 53.8 g mm m^{-2} day^{-1} bar^{-1}, respectively. The layered film architecture, moreover, lifts previously encountered limitations on hectorite content related to rapidly increasing viscosity even at low filler contents. The shear-induced alignment of hectorite platelets during processing creates a highly ordered 6 µm thick impermeable barrier wall. An interfacial nanocomposite with the outer polymer layers that formed in situ during processing provided excellent layer adhesion and polymer confinement-induced barrier improvement. Possibilities of increasing the size of this nanocomposite area by varying the drying treatment have implications on further tuning interfacial adhesion, dissolution behavior, barrier properties, and possibly even mechanical properties to meet application-specific needs, which motivates a follow-up study.

4 | EXPERIMENTAL

4.1 | Materials and sample preparation

4.1.1 | Materials

The synthetic clay sodium fluorohectorite (Hec) with the formula $[Na_{0.5}]^{inter}[Mg_{2.5}Li_{0.5}]^{oct}[Si_4]^{tet}O_{10}F_2$ was synthesized according to a published literature procedure and features a cation exchange capacity of 1.27 mmol g^{-1}.[24,47] Poly(vinyl alcohol) (PVOH, Selvol 205, degree of hydrolysis 88%, ex Sekisui Chemicals Co., Japan), hydroxypropyl methylcellulose (HPMC, E15LV, ex Parchem Chemicals, United States), NaAlginate (alginate, Vivastar CS002, ex JRS, Germany), glycerol (CremerGLYC 3109921, ex Cremer Ole, Germany) and sorbitol (Neosorb® P 100 T, Roquette, France) were used without further purification. Biodegradable poly(lactic acid) (PLA, BoPLA-Folie NTSS 25 NT/25 µm, Pütz GmbH, Germany) films were used as substrates without further surface treatment.

4.1.2 | Sample preparation

Hec was added to double-distilled water to obtain a 6 wt % Hec suspension. The suspension was placed for 7 days

in an overhead shaker to guarantee complete delamination into single Hec nanosheets.

One hundred grams of each of the three plasticized polymer suspensions (PVOH, HPMC, and alginate) were prepared by adding the polymer to double-distilled water in a round flask at 30 wt% for the PVOH, 20 wt% for the HPMC, and 15 wt% for the alginate suspension. The solid content was adjusted to achieve similar viscosities for slot die coating. The solutions were kept at 85°C under reflux for 2 h while stirring at 200 rpm using a magnetic stirring bar. Then the plasticizers were added to the polymer solutions so that the solid content of each was comprised of 80 wt% polymer, 10 wt% glycerol, and 10 wt% sorbitol.

4.1.3 | Slot die coating

The single water-soluble layers were produced consecutively by slot die coating (Table Coater equipped with a 1-Layer Slot Die 300 mm, AAA, TSE Troller AG, Switzerland). Prior to slot die coating, the polymer solutions and the Hec suspensions were homogenized, defoamed, and degassed under vacuum (50 mbar) for 5 min at 2500 rpm using a Speed-Mixer DAC 400.2 VAC-P (Hauschild, Germany). The applied shim ensures a coating width of 210 mm and a slot height of 165 μm. The coating gap was adjusted according to the desired wet film thickness. The pump flow rate and the table speed were set accordingly depending on the coating gap. The vacuum table supported and fixed the PLA substrate needed for the first wet layer.

The table temperature, referred to as the drying temperature, was adjusted to the respective coated layer. The obtained wet films were dried in-line, generating a slight under pressure with an airflow of 1.5 m^3 min^{-1}. The adjustable airflow was created by a Side Channel Blower Type 1SD 510 (Elektor Airsystems GmbH, Germany). A microporous surface below the airflow guarantees a soft and uniform solvent removal over the entire wet film surface.

For details on the slot die coating settings applied for each layer, please refer to the Data S1. After drying was complete, the films were peeled off the PLA carrier substrate for analysis.

4.2 | Characterization methods

4.2.1 | Small-angle x-ray scattering

SAXS experiments were performed by employing the system Ganesha Air (SAXSLAB, Denmark). The system is equipped with a rotating anode copper x-ray source MicroMax 007HF (Rigaku Corp., Japan) and a position-

sensitive detector PILATUS 300K (Dectris, Switzerland) with adjustable sample-to-detector positions covering a wide range of scattering vectors q. The measurement of the suspension was conducted in 1 mm glass capillaries (Hilgenberg, Germany) at room temperature. The resulting one-dimensional (1D) data ($I(q)$ [cm^{-1}] vs. q [Å^{-1}], with intensity $I(q)$) are background corrected and displayed in absolute scale.

The birefringence of a diluted Hec suspension was checked with a self-made crossed polarizer.

4.2.2 | Thermogravimetric analysis

Thermogravimetric analysis measurements were conducted on a Linseis STA PT 1600 (Linseis Messgeräte GmbH, Germany). The films were dried under vacuum (10^{-3} bar) at 70°C for 7 days. The dry samples were heated up from room temperature to 1000°C under an argon atmosphere with a heating rate of 10°C min^{-1}.

4.2.3 | Scanning electron microscopy

SEM images of a singular Hec nanosheet (Figure 2b) were recorded using the microscope ZEISS LEO 1530 (Carl Zeiss AG, Germany) operating at 3 kV and equipped with an InLens secondary electron detector. For sample preparation, the Hec suspension was diluted to 0.001 wt% and then drop-casted on a plasma-treated silicon wafer. Subsequently, the sample was sputtered with 1.2 nm of platinum.

SEM images of the cross-sections of the films were recorded using the microscope ZEISS Ultra plus (Carl Zeiss AG, Germany) operating at 5 kV and equipped with an InLens and secondary electron detector. The cross-sections were obtained by cutting the substrate-supported films with a scalpel toward the substrate side in order to protect the films. Subsequently, the films were carefully peeled off from the substrate. The film samples were sputtered with 1.2 nm of platinum. In addition, the cross-sections of the films were analyzed via EDX by employing an UltraDry-EDX detector (Thermo Fisher Scientific, United States).

4.2.4 | Transmission electron microscopy

TEM images of the cross sections were recorded employing a JEOL-JEM-2200FS (JEOL GmbH, Germany) microscope. Cross sections were prepared from the peeled-off films using a JEOL EM-09100IS Cryo Ion Slicer (JEOL GmbH, Germany).

4.2.5 | X-ray diffraction

Diffraction patterns were obtained on a Bragg–Brentano-type instrument (Empyrean Malvern Panalytical BV, The Netherlands). The diffractometer is equipped with a PIXcel-1D detector, and Cu K_α radiation ($\lambda = 1.54187$ Å) was used. The patterns were analyzed by applying Malvern Panalytical's Highscore Plus software.

4.2.6 | Water-solubility tests

The water-solubility of the films was tested according to the method "MSTM 205 Solubility Test with Plastic Holder." The setup is displayed in Figure S4. An average of three measurements for each film was taken.

4.2.7 | Barrier properties

OTR were determined on the system OX-TRAN 2/21 (Mocon, United States) at 65% RH and 23°C. A mixture of 98 vol% nitrogen and 2 vol% hydrogen as carrier gas and pure oxygen (>99.95 vol%, Linde Sauerstoff 3.5) as permeant were used. WVTR were determined on the system PERMA-TRAN-W 3/33 (Mocon, United States) at 85% RH and 23°C. All samples were sufficiently equilibrated to guarantee moisture conditioning.

4.2.8 | Coating thickness

The total film thickness was determined by employing High-Accuracy Digimatic Micrometer (Mitutoyo, Japan) with a measuring range of 0–25 mm and a resolution of 0.1 µm. A mean value of 10 measuring points within the permeability measurement area of the film was taken.

4.2.9 | Mechanical properties

Stress–strain tests were performed with a tensile instrument (Zwick/Roell, BT1-FR0.5TN.D14). The samples for the tensile measurement were cut to a size of 3 mm × 30 mm for a pristine effective tensile length of 10 mm. Prior to testing, the samples were equilibrated at 53% RH in a desiccator for 5 days. The test was performed with a crosshead speed of 5 mm min^{-1} at room temperature for at least 10 measurements. The slope of the linear region of the stress–strain curves was used to determine the elasticity modulus. All samples were measured at least 5 times, with the statistical average given as the result.

4.2.10 | Optical properties

Optical properties were analyzed on a BYK-Gardner Haze-Gard Plus (BYK-Gardner GmbH, Germany). An average of five measurements per film sample were taken for transmittance, haze, and clarity values.

4.2.11 | Biodegradation properties

The prepared films were tested for biodegradation in wastewater sludge under aerobic environment in triplicate for 33 days. The test method was based on DIN ISO 14851:2019. Activated sludge (after nitrification) collected from the wastewater treatment plant at Bayreuth, Germany, was used in the experiment as an inoculum. Aniline was used as the positive sample. Activated sludge in the same concentration was used as a control. Around 70 mg of the films were added in 100 mL test medium, with 95 mL of standard medium and 5 mL of supernatant of activated sludge. The Micro-Oxymax Respirometer furnished with a paramagnetic O_2 and CO_2 sensor (Columbus Instruments International, United States) was used for this biodegradation test.

The percentage of biodegradation was analyzed by observing the production of CO_2 using the following equation:

$$\%\text{Biodegradation} = \frac{(\text{mgCO}_2\,\text{produced})_T - (\text{mgCO}_2\,\text{produced})_B}{\text{ThCO}_2} \times 100 \tag{1}$$

where $(\text{mgCO}_2\,\text{produced})_T$ and $(\text{mgCO}_2\,\text{produced})_B$ were the amounts of CO_2 evolved in the test material and blank flask, respectively, given in milligrams. ThCO_2 is the theoretical amount of CO_2 expected to be evolved by the test material when completely mineralized and is calculated by:

$$\text{ThCO}_2 = \text{Specimen (mg)} \times \frac{\text{TOC}\,(\%)}{100} \times \frac{44}{12} \tag{2}$$

where 44 is the molecular weight of CO_2 and 12 is the molecular weight of C, TOC (%) is the total carbon content of the test specimen determined by elemental analysis.

AUTHOR CONTRIBUTIONS

Maximilian Röhrl: Conceptualization (lead); data curation (equal); methodology (lead); visualization (equal); writing – original draft (equal); writing – review and

editing (supporting). **Renee Timmins:** Conceptualization (equal); data curation (equal); methodology (supporting); visualization (equal); writing – original draft (equal); writing – review and editing (equal). **Dipannita Ghosh:** Formal analysis (supporting); methodology (equal); writing – review and editing (supporting). **Dominik Schuchardt:** Investigation (supporting); methodology (supporting); validation (supporting); writing – review and editing (supporting). **Sabine Rosenfeldt:** Data curation (supporting); methodology (supporting); software (equal); validation (supporting); writing – review and editing (supporting). **Simon Nürmberger:** Investigation (supporting); methodology (supporting). **Uwe Bölz:** Conceptualization (supporting); methodology (supporting); validation (supporting); writing – review and editing (supporting). **Seema Agarwal:** Funding acquisition (equal); project administration (equal); writing – review and editing (supporting). **Josef Breu:** Funding acquisition (lead); project administration (lead); supervision (lead); writing – review and editing (lead).

CONFLICT OF INTEREST STATEMENT
The authors declare no conflict of interest.

DATA AVAILABILITY STATEMENT
The data that support the findings of this study are available in the supplementary material of this article.

ORCID
Josef Breu https://orcid.org/0000-0002-2547-3950

REFERENCES
[1] T. A. Cooper, _Trends in Packaging of Food, Beverages and Other Fast-Moving Consumer Goods (FMCG)_, Woodhead Publishing, Cambridge, UK **2013**, p. 58.

[2] N. Ben Halima, _RSC Adv._ **2016**, _6_, 39823.

[3] J. A. Giroto, R. Guardani, A. C. S. C. Teixeira, C. A. O. Nascimento, _Chem. Eng. Process.: Process Intesif._ **2006**, _45_, 523.

[4] C.-C. Lin, L.-T. Lee, _J. Ind. Eng. Chem._ **2015**, _21_, 569.

[5] W. Sun, L. Chen, J. Wang, _J. Adv. Oxid. Technol._ **2017**, _20_, 20170018.

[6] E. Chiellini, A. Corti, R. Solaro, _Polym. Degrad. Stab._ **1999**, _64_, 305.

[7] R. Solaro, A. Corti, E. Chiellini, _Polym. Adv. Technol._ **2000**, _11_, 873.

[8] E. Chiellini, A. Corti, S. D'Antone, R. Solaro, _Prog. Polym. Sci._ **2003**, _28_, 963.

[9] T. Vaclavkova, J. Ruzicka, M. Julinova, R. Vicha, M. Koutny, _Appl. Microbiol. Biotechnol._ **2007**, _76_, 911.

[10] S. Mondellini, M. Schott, M. G. Löder, S. Agarwal, A. Greiner, C. Laforsch, _Sci. Total Environ._ **2022**, _847_, 157608.

[11] H. Schonberger, A. Baumann, W. Keller, P. Pogopetris, _Am. Dyestuff Rep._ **1997**, _86_, 9.

[12] J. Nilsen-Nygaard, E. N. Fernández, T. Radusin, B. T. Rotabakk, J. Sarfraz, N. Sharmin, M. Sivertsvik, I. Sone, M. K. Pettersen, _Compr. Rev. Food Sci. Food Saf._ **2021**, _20_, 1333.

[13] G. A. Martău, M. Mihai, D. C. Vodnar, _Polymer_ **2019**, _11_, 1837.

[14] K. K. Mokwena, J. Tang, _Criti. Rev. Food Sci. Nutr._ **2012**, _52_, 640.

[15] M. S. Abdel Aziz, H. E. Salama, M. W. Sabaa, _LWT_ **2018**, _96_, 455.

[16] B. Akinalan Balik, S. Argin, J. M. Lagaron, S. Torres-Giner, _Appl. Sci._ **2019**, _9_, 5136.

[17] C. Habel, M. Schöttle, M. Daab, N. J. Eichstaedt, D. Wagner, H. Bakhshi, S. Agarwal, M. A. Horn, J. Breu, _Macromol. Mater. Eng._ **2018**, _303_, 1800333.

[18] J. Zhu, A. Kumar, P. Hu, C. Habel, J. Breu, S. Agarwal, _Global Chall._ **2020**, _4_, 2000030.

[19] R. L. Timmins, A. Kumar, M. Röhrl, K. Havlíček, S. Agarwal, J. Breu, _Macromol. Mater. Eng._ **2022**, _307_, 2100727.

[20] M. Röhrl, L. K. S. Federer, R. L. Timmins, S. Rosenfeldt, T. Dörres, C. Habel, J. Breu, _ACS Appl. Mater. Interfaces_ **2021**, _13_, 48101.

[21] M. Röhrl, J. H. Mettke, S. Rosenfeldt, H. Schmalz, U. Mansfeld, R. L. Timmins, C. Habel, J. Breu, F. Durst, _J. Coat. Technol. Res._ **2021**, _19_, 487.

[22] P. T. Anastas, J. C. Warner, _Green Chemistry: Theory and Practice_, Oxford University Press, Oxford, UK **1998**.

[23] V. Dudko, O. Khoruzhenko, S. Weiß, M. Daab, P. Loch, W. Schwieger, J. Breu, _Adv. Mater. Technol._ **2022**, _8_, 2200553.

[24] M. Stöter, D. A. Kunz, M. Schmidt, D. Hirsemann, H. Kalo, B. Putz, J. Senker, J. Breu, _Langmuir_ **2013**, _29_, 1280.

[25] S. Rosenfeldt, M. Stöter, M. Schlenk, T. Martin, R. Q. Albuquerque, S. Förster, J. Breu, _Langmuir_ **2016**, _32_, 10582.

[26] L. Boldon, F. Laliberte, L. Liu, _Nano Rev._ **2015**, _6_, 25661.

[27] R. K. Bharadwaj, _Macromolecules_ **2001**, _34_, 9189.

[28] M. Röhrl, J. H. Mettke, S. Rosenfeldt, H. Schmalz, U. Mansfeld, R. L. Timmins, C. Habel, J. Breu, F. Durst, _J. Coat. Technol. Res._ **2022**, _19_, 487.

[29] E. L. Cussler, S. E. Hughes, W. J. Ward, R. Aris, _J. Membr. Sci._ **1988**, _38_, 161.

[30] T. Schilling, C. Habel, S. Rosenfeldt, M. Röhrl, J. Breu, _ACS Appl. Polym. Mater._ **2020**, _2_, 3010.

[31] J. Lange, Y. Wyser, *Packag. Technol. Sci.* **2003**, *16*, 149.

[32] Exceval™ – Attractive protection for your food. https://www.kuraray-poval.com/fileadmin/technical_information/brochures/poval/Kuraray_Exceval_attractive_protection_for_your_food_engl.pdf (accessed: May 2023)

[33] J. C. Grunlan, A. Grigorian, C. B. Hamilton, A. R. Mehrabi, *J. Appl. Polym. Sci.* **2004**, *93*, 1102.

[34] R. Ghadermazi, S. Hamdipour, K. Sadeghi, R. Ghadermazi, A. Khosrowshahi Asl, *Food Sci. Nutr.* **2019**, *7*, 3363.

[35] S. X. Weng, N. Yousefi, N. Tufenkji, *ACS Appl. Nano Mater.* **2019**, *2*, 1431.

[36] M. Yang, Y. Xia, Y. Wang, X. Zhao, Z. Xue, F. Quan, C. Geng, Z. Zhao, *J. Appl. Polym. Sci.* **2016**, *133*, 43489.

[37] H. Lee, B. Rukmanikrishnan, J. Lee, *Int. J. Biol. Macromol.* **2019**, *141*, 538.

[38] M. Alboofetileh, M. Rezaei, H. Hosseini, M. Abdollahi, *J. Food Eng.* **2013**, *117*, 26.

[39] S. Roy, J. W. Rhim, *Int. J. Biol. Macromol.* **2020**, *164*, 37.

[40] F. Wu, M. Misra, A. K. Mohanty, *Prog. Polym. Sci.* **2021**, *117*, 101395.

[41] Gas Barrier Properties. https://www.mgc.co.jp/eng/products/ac/nmxd6/barrier.html (accessed: September 2003)

[42] A. A. Sapalidis, F. K. Katsaros, T. A. Steriotis, N. K. Kanellopoulos, *J. Appl. Polym. Sci.* **2012**, *123*, 1812.

[43] K. E. Strawhecker, E. Manias, *Chem. Mater.* **2000**, *12*, 2943.

[44] J.-W. Rhim, H.-M. Park, C.-S. Ha, *Prog. Polym. Sci.* **2013**, *38*, 1629.

[45] C. G. Otoni, B. D. Lodi, M. V. Lorevice, R. C. Leitão, M. D. Ferreira, M. R. de Moura, L. H. Mattoso, *Ind. Crops Prod.* **2018**, *121*, 66.

[46] O. Adeyeye, E. R. Sadiku, A. Babu Reddy, A. S. Ndamase, G. Makgatho, P. S. Sellamuthu, A. B. Perumal, R. B. Nambiar, V. O. Fasiku, I. D. Ibrahim, *Green Biopolymers and Their Nanocomposites*, Springer, Singapore **2019**, p. 137.

[47] H. Kalo, M. W. Möller, M. Ziadeh, D. Dolejš, J. Breu, *Appl. Clay Sci.* **2010**, *48*, 39.

SUPPORTING INFORMATION

Additional supporting information can be found online in the Supporting Information section at the end of this article.

Supporting Information

Green and scalable processing of water-soluble, biodegradable polymer/clay barrier films

Maximilian Röhrl[‡1], Renee L. Timmins[‡1], Dipannita Ghosh[2], Dominik D. Schuchardt[1], Sabine Rosenfeldt[3], Simon Nürmberger[1], Uwe Bölz[4], Seema Agarwal[2] and Josef Breu[1]*

[1]M. Röhrl, R. L. Timmins, D. D. Schuchardt, S. Nürmberger, J. Breu
Bavarian Polymer Institute and Department of Chemistry, University of Bayreuth, Bayreuth 95447, Germany
*E-mail (corresponding author): josef.breu@uni-bayreuth.de
ORCID ID: https://orcid.org/0000-0002-2547-3950

[2]D. Ghosh, S. Agarwal
Macromolecular Chemistry II, Bavarian Polymer Institute and Department of Chemistry, University of Bayreuth, Bayreuth 95447, Germany

[3]S. Rosenfeldt
Physical Chemistry I, Bavarian Polymer Institute and Department of Chemistry, University of Bayreuth, Bayreuth 95447, Germany

[4]U. Bölz
HPX Polymers GmbH, Tutzing 82327, Germany

‡: M.R. and R.L.T. contributed equally to this work.

1. Film Fabrication

1.1 Poly(vinyl alcohol) (PVOH)-based water-soluble film

For PVOH-based films, the drying temperature was set to 60 °C. The first water-soluble polymer layer was coated from a 30 wt% PVOH solution on a poly(lactic acid) (PLA) film. The coating gap was adjusted to 205 μm, and the pump flow rate was set to 2.52 ml min^{-1} and the table speed to 0.1 m min^{-1} accordingly. The film was dried for 15 min. The composition of the dry film was 80% PVOH, 10% glycerol, and 10% sorbitol.

The water-dispersible nanosheet layer was then added on top by coating a 6 wt% Hec suspension. The coating gap was adjusted to 385 μm, and the pump flow rate was set to 4.6 ml min^{-1} and the table speed to 0.1 m min^{-1} accordingly. The film was removed from the table and dried for 7 days under ambient conditions. The composition of the dry nanosheet layer was 100% Hec.

A second single water-soluble polymer layer was coated from a 30 wt% PVOH solution on top of the Hec barrier layer. The coating gap was adjusted to 250 μm, and the pump flow rate was set to 2.52 ml min^{-1} and the table speed to 0.1 m min^{-1} accordingly. The film was dried for 30 min, and the composition of the dry film was 80% PVOH, 10% glycerol, and 10% sorbitol.

1.2 Hydroxypropyl methylcellulose (HPMC)-based water-soluble film

For HPMC-based films, the drying temperature was set to 20 °C. The first water-soluble polymer layer was coated from a 20 wt% HPMC solution on a PLA film. The coating gap was adjusted to 450 μm, and the pump flow rate was set to 5.9 ml min^{-1} and the table speed to 0.1 m min^{-1} accordingly. The film was dried for 1 h, and the composition of the dry film was 80% HPMC, 10% glycerol, and 10% sorbitol.

The water-dispersible nanosheet layer was then added on top by coating a 6 wt% Hec suspension. The coating gap was adjusted to 385 μm, and the pump flow rate was set to 4.6 ml min^{-1} and the table speed to 0.1 m min^{-1} accordingly. The film was removed from the table and dried for 7 days under ambient conditions. The composition of the dry nanosheet layer was 100% Hec.

A second single water-soluble polymer layer was coated from a 20 wt% HPMC solution on top of the Hec barrier layer. The coating gap was adjusted to 480 μm, and the pump flow rate was set to 5.9 ml min^{-1} and the table speed to 0.1 m min^{-1} accordingly. The film was dried for 2 h, and the composition of the dry film was 80% HPMC, 10% glycerol, and 10% sorbitol.

**1.3 NaAlginate-based water-soluble film**

For alginate-based films, the drying temperature was set to 20 °C. Prior to slot die coating, the alginate suspension and the slot die were heated using a heat gun. The first water-soluble polymer layer was coated from a heated 15 wt% Alginate solution on a PLA film. The coating gap was adjusted to 475 μm, and the pump flow rate was set to 1.92 ml min^{-1} and the table speed to 0.03 m min^{-1} accordingly. The film was dried for 1 h, and the composition of the dry film was 80% Alginate, 10% glycerol, and 10% sorbitol.

The water-dispersible nanosheet layer was then added on top by coating a 6 wt% Hec suspension. The coating gap was adjusted to 385 μm, and the pump flow rate was set to 4.6 ml min^{-1} and the table speed to 0.1 m min^{-1} accordingly. The film was removed from the table and dried for 7 days under room conditions. The composition of the dry nanosheet layer was 100% Hec.

A second single water-soluble polymer layer was coated from a heated 15 wt% Alginate solution on top of the Hec barrier layer. The coating gap was adjusted to 500 μm, and the pump flow rate was set to 1.92 ml min^{-1} and the table speed to 0.03 m min^{-1} accordingly. The film was dried for 2 h, and the composition of the dry film was 80% Alginate, 10% glycerol, and 10% sorbitol.
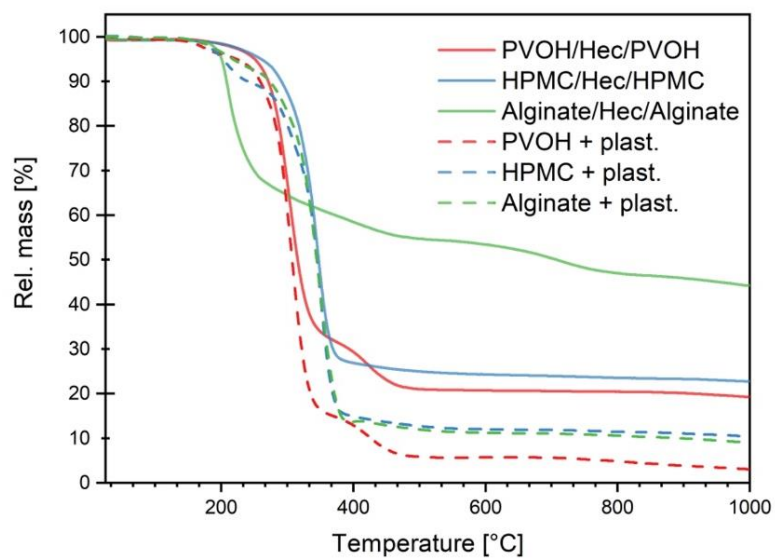
Figure S1. TGA curves of water-soluble films. The mass loss corresponds to the degradation of the polymer layers. The solid residue can be assigned to neat Hec minus the residue from corresponding neat plasticized polymer films (dotted lines). The water-soluble films are made of approximately 21 wt% Hec for the PVOH, 22 wt% Hec for HPMC, and 40 wt% for the Alginate case.
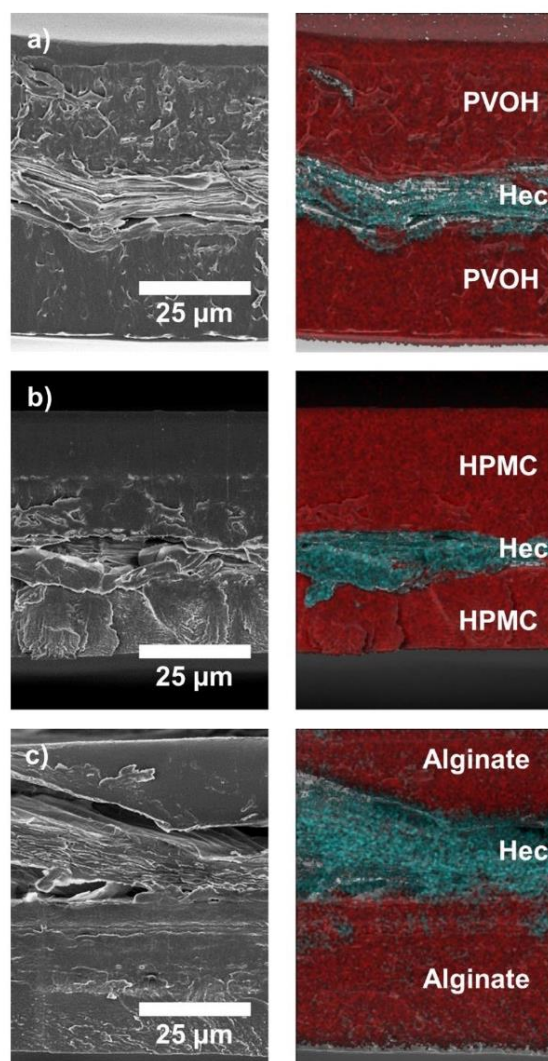
Figure S2. SEM cross-sections of the foils. a) PVOH/Hec/PVOH, b) HPMC/Hec/HPMC and c) Alginate/Hec/Alginate. The respective right images show the elemental distribution of Si (cyan) and C (red) *via* EDX spectroscopy.
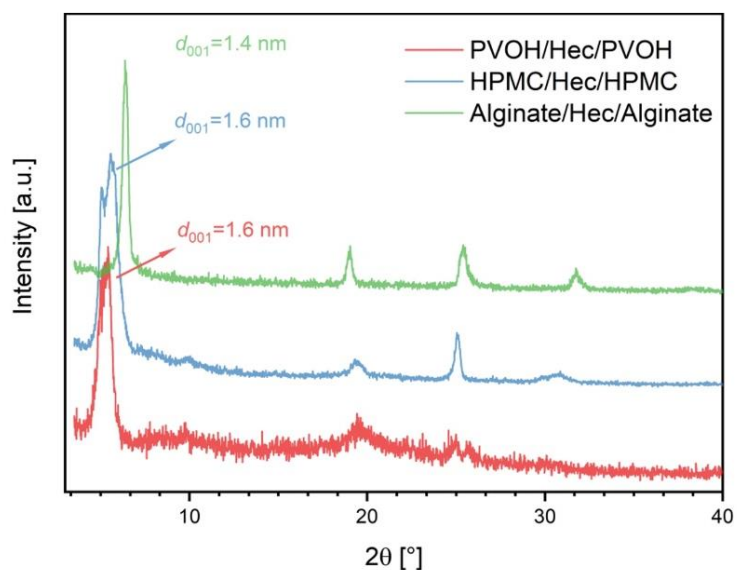
Figure S3. XRD pattern of water-soluble films. The d_{001} corresponds to a two-water layer hydrate of the interlayer sodium cation of neat Hec nanosheets, *i.e.* no intercalation of polymer occurred during the coating process. The polymers show typical amorphous pattern.
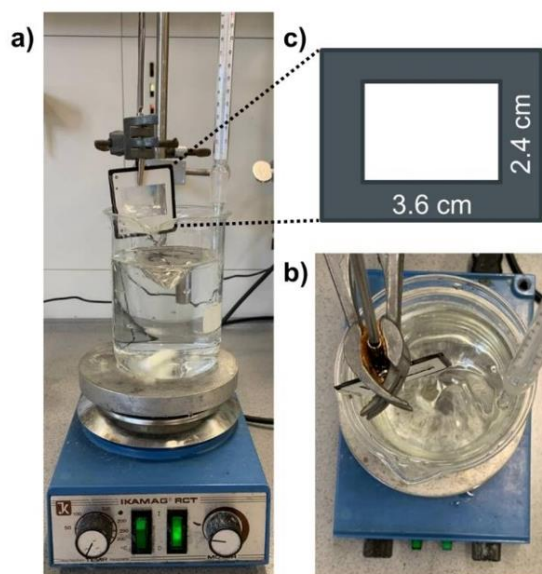
Figure S4. Test setup for the water-solubility tests according to MSTM-205: Solubility Test with Plastic Holder. a) Front view, b) Top view, and c) Dimensions of the sample holder.

Table S1. Mechanical properties of plasticized polymers (10 wt% sorbitol, 10 wt% glycerol) and their layered films with Hec. Values are a statistical average from measuring at least 6 runs.

Sample:	PVOH	PVOH/ Hec/ PVOH	HPMC	HPMC/ Hec/ HPMC	Alginate	Alginate/ Hec/ Alginate
Tensile Strength (MPa)	5.6	27	15	43	23	35
Elongation at break (%)	260	71	8.1	14	12	5.0
Elastic Modulus (MPa)	21	570	790	970	390	1100
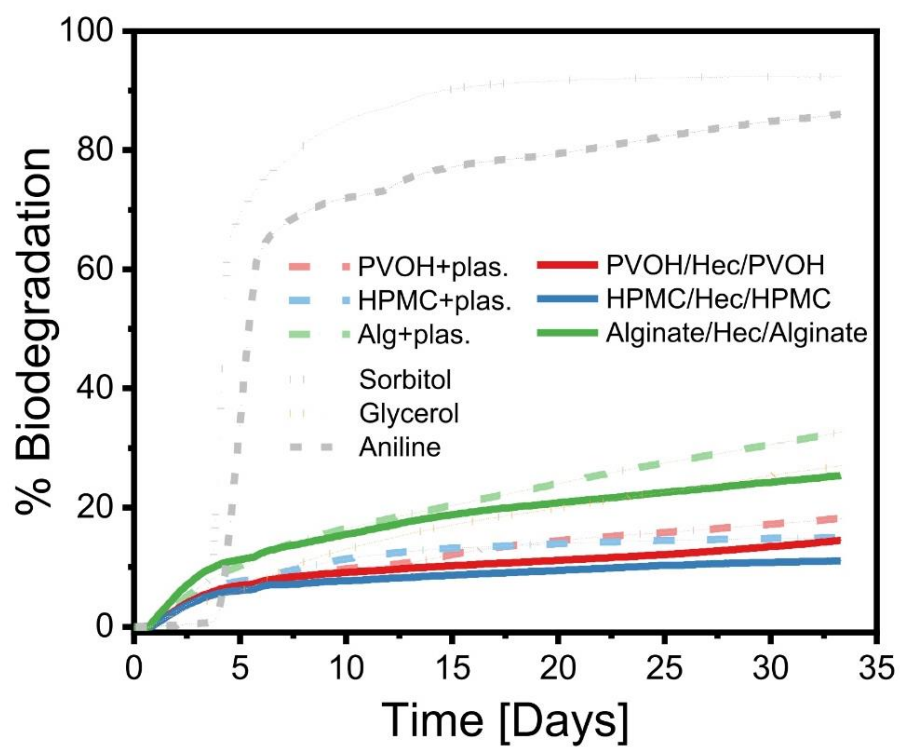
Figure S5. Biodegradation measured in terms of conversion to CO_2 for plasticized polymer films (10 wt% glycerol, 10 wt% sorbitol), the plasticized polymers as a layered film with Hec, the neat plasticizers, and aniline as the internal positive standard.

6.3 New functional polymer materials via click chemistry-based modification of Cellulose Acetate

Authors: Maximilian Röhrl, Justus F. Ködel, Renee L. Timmins, Christoph Callsen, Merve Aksit, Michael F. Fink, Sebastian Seibt, Andy Weidinger, Glauco Battagliarin, Holger Ruckdäschel, Rainer Schobert, Josef Breu, and Bernhard Biersack

New Functional Polymer Materials via Click Chemistry-Based Modification of Cellulose Acetate

Maximilian Röhrl, Justus F. Ködel, Renee L. Timmins, Christoph Callsen, Merve Aksit, Michael F. Fink, Sebastian Seibt, Andy Weidinger, Glauco Battagliarin, Holger Ruckdäschel, Rainer Schobert, Josef Breu,* and Bernhard Biersack*

Read Online

ACCESS | 📊 Metrics & More | 📄 Article Recommendations | 🆘 Supporting Information

ABSTRACT: Cellulose acetate (CA) was partially acrylated, and the resulting cellulose acetate acrylate (acryl-substitution degree of 0.2) underwent quantitative thio-Michael click reactions with various thiols. A toolbox of functional CA polymers was obtained in this way, and their properties were studied. The modification with fatty alkyl thiols led to hydrophobic materials with large water drop contact angles. Octadecylthio-, butoxycarbonylpropylthio-, and furanylthio-modifications formed highly transparent materials. The new derivative CAASFur disintegrated completely under industrial composting conditions. Films of modified CA polymers were cast and investigated in terms of barrier properties. The nanocomposite of CAAS18 compounded with a synthetic layered silicate (hectorite) of a large aspect ratio showed permeabilities as low as 0.09 g mm m^{-2} day^{-1} for water vapor and 0.16 cm^3 mm m^{-2} day^{-1} atm^{-1} for oxygen. This portfolio of functional CA polymers opens the door to new applications.

1. INTRODUCTION

Natural and re-growing sources for the preparation of functional polymer materials are getting more and more important.[1] Cellulose, for example, is an abundant polysaccharide accessible from plants. In particular, cellulose acetate (CA), obtained from acetylation of cellulose followed by partial deacetylation, can be applied for various purposes.[2] In addition, the degradation of CA by various mild methods was thoroughly studied.[3] Hence, CA can be an attractive surrogate for petrol-based polymers and plastics. However, CA also has disadvantages, such as insufficient water vapor barrier properties, which have prevented a wider application of this material so far.[4] Plasticizers are also needed to process cellulose acetate at low temperatures.[5] Modifications of CA such as cellulose acetate butyrate (CAB), cellulose acetate propionate (CAP), or cellulose acetate phthalate (CAPh) can overcome some of these drawbacks and improve the thermal and solubility properties as compared to unmodified CA.[6,7] Processing and mechanical properties of these materials are, however, still inadequate in comparison with other commodity polymers such as PP (polypropylene) and PE (polyethylene). Therefore, further efforts are needed in order to overcome these problems of CA-based polymers.[8]

The concept of "click chemistry" was initially described by Kolb, Finn, and Sharpless in 2001 and is a reasonable option for modifying polysaccharides in mild and quantitative ways.[9,10] The thiol-ene click reaction, for instance, has found numerous applications in material science.[11−13] Cellulose and cellulose derivatives such as CA were successfully modified via thiol-ene reactions.[14−16] These reports described complex reactions and modifications with expensive reagents and catalysts for synthesizing the precursors required for the thiol-ene reaction. A simple protocol for the acrylation of CA to generate the known acryl ester CAA (substitution degree of 0.2) was previously published.[17] In the present work, we describe the modification of CAA by the thiol-Michael reaction with various commercially available thiols, leading to new functionalized cellulose esters. Furthermore, by incorporating impermeable silicate nanosheets of delaminated hectorite (Hec) into a modified CAA, we were able to cast nanocomposite films that show excellent barrier properties.

2. MATERIALS AND METHODS

2.1. General. Cellulose acetate (medium $M_n \sim 30.000$, 39.3−40.3 wt % acetyl) was obtained from Sigma Aldrich, and the other starting materials were purchased from Alfa Aesar (acryloyl chloride, 1-eicosanethiol, 1-hexadecanethiol), Fluka (1-octadecanethiol), Sigma Aldrich (butyl 3-mercaptopropionate, 1-dodecanethiol), and TCI (ethyl thioglycolate). CAA

was prepared according to a literature procedure.[17] Infrared (IR) spectra: Perkin-Elmer Spectrum One FT-IR spectrophotometer with an ATR-sampling unit. Nuclear magnetic resonance (NMR) spectra: Bruker Avance 300 spectrometer, chemical shifts are given in parts per million (δ) downfield from tetramethylsilane as the internal standard.

2.2. Thiol-Michael Click Reaction: Typical Procedure. CAA (1.14 g, 0.03 mmol, substitution degree of 0.2) was placed in a flask and dissolved in DMSO (10 mL) under stirring, whereupon triethylamine (3 equiv) was added. Then, the respective thiol (6 equiv) was added and the reaction mixture was stirred at room temperature for 24 h. The product was precipitated by the addition of water (200 mL). The formed solid was collected by suction and washed twice with water (25 mL), followed by washing with EtOH (2 × 25 mL). The crude product obtained was dissolved in THF (50 mL), precipitated by the addition of n-pentane (200 mL), and collected. The filter cake was washed twice with n-pentane (25 mL). Yield: 90%. The ^{1}H NMR data given below list only selected signals of the thiol residues for better clarity, while the IR data and ^{13}C NMR data enumerate all bands and peaks of the product polymers.

2.2.1. CAAS12. Colorless solid; IR (ATR) ν = 3502, 2924, 2856, 1740, 1639, 1433, 1367, 1216, 1161, 1126, 1034, 952, 901, 836, 692 cm^{-1}; ^{1}H NMR (300 MHz, CDCl$_3$, δ): 0.85 (t, J = 6.3 Hz; dodecyl-Me), 1.2−1.4 (dodecyl-CH$_2$), 1.5−1.7 (dodecyl-CH$_2$); ^{13}C NMR (75.5 MHz, CDCl$_3$, δ): 14.1, 20.4, 20.6, 20.8, 22.7, 26.7, 28.9, 29.3, 29.6, 31.9, 32.2, 34.6, 62.0, 71.8, 72.8, 100.5, 169.3, 169.7, 170.2.

2.2.2. CAAS16. Colorless solid; IR (ATR) ν = 3452, 2924, 2854, 1739, 1644, 1435, 1367, 1317, 1221, 1162, 1127, 1031, 953, 901, 839, 811, 698 cm^{-1}; ^{1}H NMR (300 MHz, CDCl$_3$, δ): 0.85 (t, J = 6.3 Hz; hexadecyl-Me), 1.2−1.4 (hexadecyl-CH$_2$), 1.5−1.7 (hexadecyl-CH$_2$); ^{13}C NMR (75.5 MHz, CDCl$_3$, δ): 14.1, 20.5, 20.8, 22.7, 26.8, 28.9, 29.3, 29.6, 29.7, 31.9, 32.2, 34.6, 62.0, 71.8, 72.8, 100.5, 169.2, 169.7, 170.2.

2.2.3. CAAS18. Colorless solid; IR (ATR) ν = 3471, 2924, 2855, 1740, 1435, 1367, 1216, 1125, 1033, 952, 901, 840, 808 cm^{-1}; ^{1}H NMR (300 MHz, CDCl$_3$, δ): 0.85 (t, J = 6.3 Hz; octadecyl-Me), 1.2−1.4 (octadecyl-CH$_2$), 1.5−1.7 (octadecyl-CH$_2$); ^{13}C NMR (75.5 MHz, CDCl$_3$, δ): 14.1, 20.5, 20.8, 22.7, 26.7, 28.9, 29.3, 29.6, 29.7, 31.9, 32.2, 34.6, 62.0, 71.8, 72.8, 100.5, 169.3, 169.7, 170.2.

2.2.4. CAAS20. Colorless solid; IR (ATR) ν = 3473, 2924, 2851, 1739, 1632, 1436, 1410, 1367, 1319, 1218, 1164, 1124, 1031, 953, 900, 836, 809, 698 cm^{-1}; ^{1}H NMR (300 MHz, CDCl$_3$, δ): 0.84 (t, J = 6.3 Hz; eicosyl-Me), 1.2−1.3 (eicosyl-CH$_2$), 1.5−1.6 (eicosyl-CH$_2$); ^{13}C NMR (75.5 MHz, CDCl$_3$, δ): 14.1, 20.4, 20.5, 20.7, 22.6, 26.6, 28.9, 29.3, 29.6, 31.9, 32.0, 62.0, 71.8, 72.8, 100.5, 169.2, 169.7, 170.2.

2.2.5. CAASFur. Colorless solid; IR (ATR) ν = 3488, 2932, 1738, 1643, 1542, 1523, 1505, 1435, 1367, 1217, 1155, 1122, 1033, 956, 935, 902, 840, 744 cm^{-1}; ^{1}H NMR (300 MHz, CDCl$_3$, δ): 6.1−6.3 (furan-H), 7.3−7.4 (furan-H); ^{13}C NMR (75.5 MHz, CDCl$_3$, δ): 20.6, 20.8, 26.6, 28.5, 34.4, 62.0, 71.8, 72.8, 100.6, 107.9, 110.6, 142.4, 169.3, 169.7, 170.2.

2.2.6. CAASE2MA. Colorless solid; IR (ATR) ν = 3473, 2953, 2876, 1739, 1432, 1367, 1224, 1157, 1125, 1034, 900, 843, 685 cm^{-1}; ^{1}H NMR (300 MHz, CDCl$_3$, δ): 0.91 (t, J = 7.1 Hz; ethyl-Me), 4.07 (t, J = 7.1 Hz; ethyl-CH$_2$O); ^{13}C NMR (75.5 MHz, CDCl$_3$, δ): 14.2, 20.5, 20.6, 20.8, 27.6, 33.8, 34.9, 41.5, 45.4, 61.5, 62.1, 71.8, 72.8, 100.5, 169.3, 169.7, 170.2, 171.1.

2.2.7. CAASB3MP. Colorless solid; IR (ATR) ν = 3476, 2964, 2878, 1738, 1432, 1367, 1217, 1163, 1131, 1034, 952, 901, 839, 675 cm^{-1}; ^{1}H NMR (300 MHz, CDCl$_3$, δ): 0.91 (t, J = 7.4 Hz; butyl-Me), 1.3−1.4 (CH$_2$), 1.5−1.7 (CH$_2$), 4.07 (t, J = 6.7 Hz; butyl-CH$_2$O); ^{13}C NMR (75.5 MHz, CDCl$_3$, δ): 13.7, 19.1, 20.5, 20.6, 20.8, 26.9, 27.2, 30.6, 34.5, 34.8, 62.1, 64.6, 71.8, 72.8, 100.5, 169.2, 169.7, 170.2, 171.9.

2.3. Thermal Stability and Decomposition Behavior. Thermal decomposition was monitored by combined TG-DSC using a Linseis STA PT 1600 thermobalance with DSC sensor head type S. All specimens were investigated in air atmosphere using linear heating rates between r.t. and 1000 °C.

2.4. Contact Angle. Samples of polymer plates were prepared by the dissolution of the indicated polymers (0.5 g) in acetone (7 mL) and subsequent casting of the solution into a glass Petri dish with a diameter of 40 mm. The solvent evaporated completely in the open air overnight, leaving polymer foils in the Petri dishes, which were cut into pieces of 4 cm^2 for contact angle investigations. A drop of 10 μL of water was added to each sample, and the contact angles were investigated after 1 min by drop contour analysis using a Krüss G10 machine. Results are described as means of the left and right angles of each sample drop.

2.5. Transparency. For the preparation of the polymer films, the polymers were ground in a ball mill at 250 rpm for 1 h. The powder obtained was pressed to plates of 0.5 mm thickness in a melting press. Transmission, haze, and clarity of the polymer films were investigated with a BYK-Gardner Haze-Gard Plus hazemeter using visible light according to ISO 13468 (total transmittance) and ISO/DIS 14782 (transmission haze).

2.6. Disintegration Test under Industrial Composting Conditions. The test set-up was executed according to ISO 20200 Plastics—Determination of the degree of disintegration of plastic materials under simulated composting conditions in a laboratory-scale test (2015).

Films (thickness of 100 μm) of the polymer sample CAASFur were mounted on slide frames (12 replicates) and were positioned horizontally in a mixture of 1.2 kg of 14-weeks-old compost (provided by OWS, Belgium) sieved to a particle size of <10 mm and 0.3 kg of fresh vegetables in plastic boxes with holes for aeration. The samples were incubated at 58 ± 2 °C in the dark. The compost was mixed at regular intervals, the moisture content was checked and adjusted when needed, and the test items were visually monitored and scanned for documentation.

2.7. Barrier Properties. Samples of polymer films were prepared by dissolution of the indicated polymers (0.5 g) in acetone (7 mL) and casting the solution into a glass Petri dish with a diameter of 40 mm. For the preparation of the nanocomposite film, refer to chapter 2.8.

2.7.1. Water Vapor Transmission Rates. Water vapor transmission rate (WVTR) values of the casted nanocomposite and polymer films were measured on a Mocon PERMATRAN-W Model 3/33 (Mocon Inc., USA). The measurements were conducted at 23 °C and 85% RH. Sufficient time for moisture conditioning was guaranteed.

2.7.2. Oxygen Transmission Rates. Oxygen transmission rate (OTR) values of the casted nanocomposite and polymer films were determined by employing a Mocon OX-TRAN 2/21 (Mocon Inc., USA) at 23 °C and 50% RH. The CAAS18/Hec film was carefully equilibrated at 50% RH. A mixture of 98 vol % nitrogen and 2 vol % hydrogen gas was used as the

carrier gas and pure oxygen gas as the permeant (>99.95%, Linde Sauerstoff 3.5). Sufficient time for moisture conditioning was guaranteed.

2.7.3. Thickness Determination. The thickness of the casted films was determined by employing a High Accuracy Digimatic Micrometer (Mitutoyo, Japan) with a measuring range of 0−25 mm and a resolution of 0.1 μm.

2.8. Hectorite Nanocomposites. *2.8.1. Materials and Sample Preparation.* Synthetic clay sodium fluorohectorite (Hec, $[Na_{0.5}]^{inter}[Mg_{2.5}Li_{0.5}]^{oct}[Si_4]^{tet}O_{10}F_2$) was synthesized and annealed according to a published literature procedure.[18,19] For modification, 18-crown-6 (18C6) with 99% purity was provided by abcr GmbH, and *N*-methyl formamide (NMF) was used as a dispersant with 99% purity provided by Alfa Aesar.

A 4 wt % solution of CAAS18 in NMF was prepared by mixing overnight in an overhead shaker positioned in an oven set to 60 °C. The 18C6/Hec suspension (3 wt % Hec) was prepared by adding 0.15 g of Hec and an amount of 18C6 corresponding to 300% of the cation exchange capacity of Hec (0.151 g) to NMF, followed by mixing in an overhead shaker for three days. The suspension used to prepare the self-standing barrier film (total solid content 3.9 wt %) was prepared by adding 8.7 g of the CAAS18 solution to 1.3 g of the Hec suspension, followed by mixing overnight in an overhead shaker. This suspension was then cast in a Teflon dish (diameter of ∼80 mm) and transferred to an oven at 50 °C to dry for two weeks. To ensure complete solvent removal at the end of two weeks, the dish was transferred to a vacuum oven at 50 °C and 10^{-3} bar for 24 h before peeling the CAAS18/Hec film out of the dish.

*2.8.2. Characterization of Nanocomposite Films.* *2.8.2.1. X-ray Diffraction.* The XRD pattern of the nanocomposite film was recorded on a Bragg−Brentano-type diffractometer (Empyrean, Malvern Panalytical BV, The Netherlands) using Cu K-α radiation (λ = 1.5406 Å). The diffractometer was equipped with a PIXcel-1D detector. All patterns were analyzed using Malvern Panalyticals's HighScore Plus software.

2.8.2.2. Transmission Electron Microscopy. Cross-sections were prepared from the films by employing a Leica Ultramicrotome UC-7 equipped with a diamond cutter type Diatome Ultra 35° MF-3763 at room temperature. TEM images of these cross-sections were recorded by applying a JEOL-JEM-2200FS (JEOL GmbH, Germany) microscope.

3. RESULTS AND DISCUSSION

Initially, acryl-modified CA (CAA) with an acryl-substitution degree of 0.2 was prepared by esterification of CA with acryloyl chloride.[17] CAA was used as the starting material for the thiol-Michael reactions with various thiols. Thiols with long alkyl chains such as dodecanethiol, hexadecanethiol, octadecanethiol, eicosanethiol, and esters such as ethyl 2-mercaptoacetate and butyl 3-mercaptopropionate, and with arenes such as furan-2-ylmethylthiol were applied as modifying agents of CAA (Scheme 1). Fatty alkyl modified CA derivatives CAAS12, CAAS16, CAAS18, and CAAS20, the ethyl ester CAASE2MA and butyl ester CAASB3MP, and the furanyl-modified CAASFur were synthesized in this way in high yields (90%). DMSO was used as a solvent for the click reactions, but THF was also applied successfully as an alternative organic solvent, leading to comparable yields. The modified polymer products showed excellent solubility in organic solvents such as acetone.

**Scheme 1. Reagents and Conditions: Thiol (6 equiv), Et$_3$N (3 equiv), DMSO or THF, r.t., 24 h**
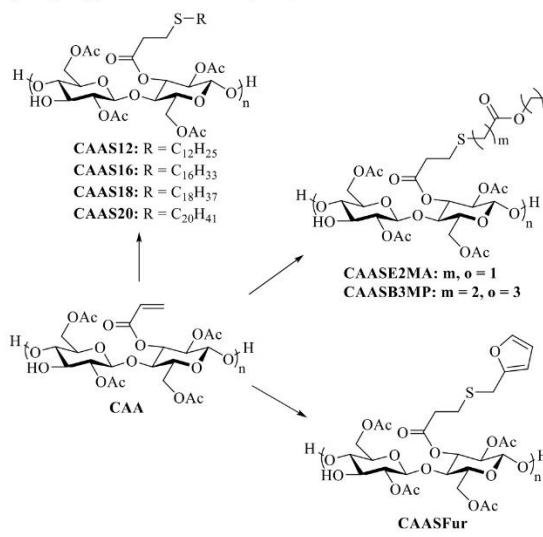
The obtained modified CA materials were colorless to off-white solids. They were analyzed by NMR and IR spectroscopy (see the Supporting Information for original ^{1}H and ^{13}C NMR spectra). The fatty alkyl rests of polymers CAAS12−20 are clearly visible in the NMR and IR spectra. Strong alkyl bands between 2800 and 3000 cm^{-1} were observed in the IR spectra. A weak broad signal between 3400 and 3500 cm^{-1} indicates the presence of hydroxyl groups, which were kept in the new polymer molecules at the carbohydrate backbone in line with the acryl-substitution degree of 0.2. ^{1}H NMR spectra displayed distinct peaks for the terminal methyl groups at δ = 0.84−0.85 ppm, as well as strong methylene signals at δ = 1.2−1.7 ppm. The terminal methyl groups were also visible in the ^{13}C NMR spectra at δ = 14.1 ppm. Similar signals were observed in the NMR spectra of the ester-modified polymers CAASE2MA and CAASB3MP (^{1}H NMR, δ = 0.91 ppm, ^{13}C NMR, δ = 13.7 and 14.2 ppm). In contrast, the furanyl derivative CAASFur exhibited characteristic downfield signals in its NMR spectra, which can be attributed to the furanyl ring (δ = 6.1−6.3, 7.3−7.4 ppm in the ^{1}H NMR spectrum; 100.6, 107.9, and 110.6 ppm in the ^{13}C NMR spectrum). In the ^{1}H NMR spectra, the integrals of the signals attributed to the modification were in line with the acryl-substitution degree of 0.2 of the CAA starting compound.

Thermogravimetric analyses (TGA) and differential scanning calorimetry (DSC) of the modified CA polymers did not reveal significant differences when compared with pure CA (see the Supporting Information). The new polymer derivatives were amorphous solids without visible crystalline components nor with distinct melting points of crystalline components as to the obtained DSC spectra. Plates and foils of selected polymer derivatives were cast from solutions in acetone upon evaporation of the solvent and compared with casted plates made of CA.

3.1. Contact Angles. The contact angles of water drops on the surface of plates prepared from the alkyl-modified CA derivatives CAAS12, CAAS16, CAAS18, and CAAS20 were determined in order to evaluate the hydrophobic surface

properties of these polymers, and the results were compared with the contact angles observed for plates of the starting material CA and the hydrophobic synthetic polymer PS (Figure 1A). The contact angle depended on the fatty alkyl
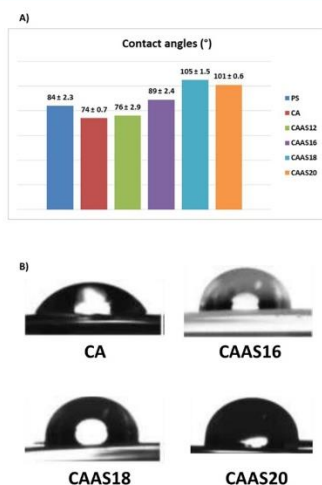
Figure 1. (A) Contact angles of water drops on plates made from derivatives CAAS12-20 or from the control polymers PS and CA after 1 min (means of the left and right angles). (B) Representative images of water drops on the indicated polymer plates after 1 min.

chain and as expected, increased with longer alkyl chains. Hence, polymers such as CAAS18 and CAAS20 had considerably more hydrophobic surfaces (contact angles above 100°) than CA (74°), PS (84°), and the close dodecyl and hexadecyl analogs CAAS12 (76°) and CAAS16 (89°) (Figure 1B).

3.2. Transparency. A hazemeter was used to determine the transparency parameters of the plates of the new polymer materials CAAS18, CAASB3MP, and CAASFur in comparison with plates of CA and PS. The plates of all three tested modified CA polymers exhibited improved optical properties in terms of transmission, haze, and clarity when compared with CA (Table 1). The modified polymers also showed trans-

**Table 1. Transparency of CA Polymers CAAS18, CAASB3MP, and CAASFur in Comparison with PS and CA[a]**

polymer	transmission (%)	haze (%)	clarity (%)
PS	94.2	4.72	95.8
CA	93.2	33.9	72.9
CAAS18	94.3	1.0	99.0
CAASB3MP	94.4	1.0	99.1
CAASFur	94.8	0.94	99.4

[a]Plates of 0.5 mm thickness were prepared from each sample for testing.

mission values similar to PS, as well as reduced haze and increased clarity compared to PS. These results indicate that the new polymers CAAS18, CAASB3MP, and CAASFur can be applied as transparent films/foils and plastic glass materials, which can replace oil-based plastics for these applications. The transparencies of these new CA-based polymers can be explained by a low or absent crystallinity and their strongly

amorphous solid character, along with excellent solubility in low-boiling organic solvents. In nanocomposites of starch nanocrystals acetate (SNA) with hydrophobic cellulose laurate ester, the cellulose ester was the well-transmitting component whose transmission was reduced by increasing amounts of SNA.[20] The combination of high transparency with considerable hydrophobicity in cellulose acetate-based polymers can lead to valuable applications such as sensoring and electronics, UV protection, and packaging including active packaging.[21−25]

3.3. Disintegration under Industrial Composting Conditions. As a proof of principle, the polymer sample CAASFur was selected and its disintegration under industrial composting conditions was investigated according to ISO 20200. Films with a thickness of 100 μm were used for this experiment. Although disintegration does not give ultimate proof of complete biodegradation of the material, it can indicate the potential of the material to be biodegraded by natural microbes. The polymer sample passed the test successfully and disintegrated completely after 69 days (Figure 2). Substantial disintegration was already observed after 42 days.
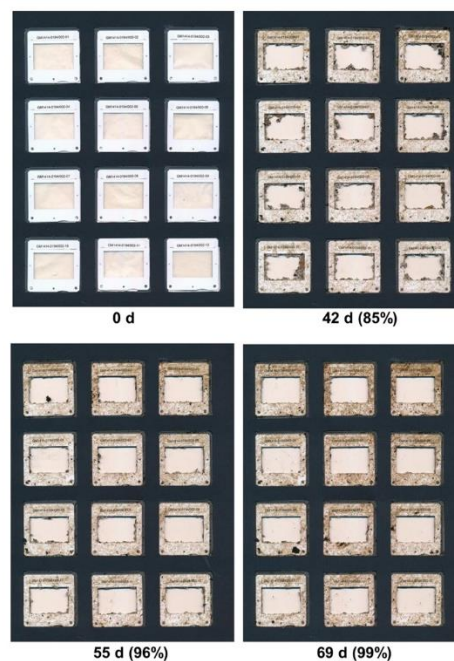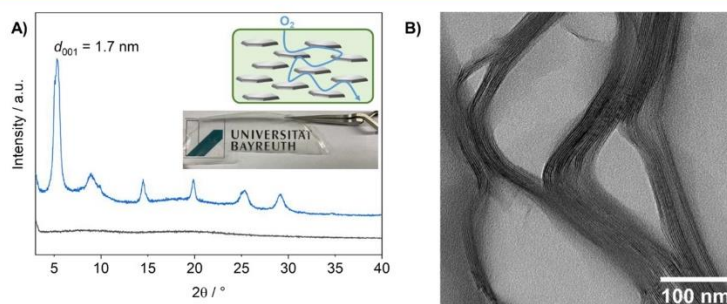

Figure 2. Time-dependent disintegration (in %) of the new polymer CAASFur under industrial composting conditions according to ISO 20200.

3.4. Barrier Properties and Nanocomposite Preparation. The water vapor barrier properties of some modified CA polymers were evaluated by measuring the water vapor transmission rates through casted films. With this sensitive measurement method, the hydrophobicity of the differently modified CA derivatives can be probed. However, gas transmission rates strongly depend on the thickness of the films, and therefore, the values were normalized to 1 mm, yielding water vapor permeability (WVP). Permeability values

Table 2. WVP and OP at 23 °C and Respective RH

polymer	WVP/g mm m^{-2} day^{-1} at 85% RH	OP/cm^3 mm m^{-2} day^{-1} atm^{-1} at 50% RH
CAAS16	36.4	
CAAS18	24.8	
CAAS20	9.9	
CAASB3MP	21.5	
CAAS18/Hec	0.09	0.16
PET	0.5−2	1−5
PP	0.2−0.4	50−100
PE	0.5−2	50−200
PS	1−4	100−150
PVC	1−2	2−8

Figure 3. Characterization of the CAAS18/Hec nanocomposite film. (A) XRD pattern of the neat CAAS18 film (black) and CAAS18/Hec nanocomposite film (blue). Top inset sketches the tortuous path theory for an oxygen molecule. Bottom inset shows the transparent CAAS18/Hec nanocomposite film. (B) TEM image of the CAAS18/Hec cross-section indicating segregated domains of CAAS18 slabs (bright) and restacked Hec-only domains (dark).

facilitate comparison with other polymers (Table 2) at 85% relative humidity (RH).[26]

In general, the permeability (P) of a barrier material can be expressed as $P = S \times D$ with the solubility parameter (S) and diffusivity parameter (D) of the permeate.[27] Polar molecules like water are less soluble in hydrophobic matrices and vice versa. As expected, an increase in the chain length of the alkyl side groups of CAAS derivatives led to a decrease in the WVP due to a more hydrophobic character of the polymers (Table 2). Increasing the aliphatic chain length of the fatty alkyls from 16 carbons in CAAS16 to 20 carbons in CAAS20 reduced the WVP by more than a factor of three. This can be attributed to the reduced solubility parameter S. The butyl-ester-modified CAASB3MP ranks between the CAAS derivatives in terms of WVP. Nevertheless, the barrier values of neat polymer films were still distinctly below the requirements for food packaging and the specifications of commonly used polymer foils. Thus, further improvement is needed.

Compositing polymers with impermeable clay nanosheets improves the barrier properties of polymer matrices based on the tortuous path theory (Figure 3A top inset).[28] The incorporation of large aspect ratio synthetic sodium fluorohectorite (Hec) was shown to improve the WVP and oxygen permeability (OP) by orders of magnitudes.[29−32] To illustrate this concept for the new CA-based polymers presented in this study, CAAS18 was selected and mixed with a modified Hec, yielding a high barrier and transparent nanocomposite film upon drying (Figure 3A bottom inset).[33] The obtained CAAS18/Hec film showed WVP at 85% RH and OP at 50% RH as low as 0.09 g mm m^{-2} day^{-1} and 0.16 cm^3 mm m^{-2} day^{-1} atm^{-1}, respectively. Hereby, the WVP of the pristine CAAS18 could be reduced by 99.6% compared to the

initial WVP of 24.8 g mm m^{-2} day^{-1}. Besides the hydrophobization arising from the fatty alkyl side groups in CAAS18, the modification of Hec additionally reduces its ability to swell in the presence of water vapor, explaining the solid WVP at a high 85% RH for the CAAS18/Hec nanocomposite.[33] While the suspensions applied for wet coating were homogeneous, segregation was observed upon drying. TEM images revealed separated domains of neat CAAS18 and restacked Hec-only domains with a thickness of up to 100 nm (Figure 3B). This thermodynamically induced phase segregation was further evidenced via XRD. The XRD pattern of CAAS18/Hec exhibits a basal spacing of 1.7 nm that can be assigned to the intercalated 18C6 crown ether complexing the sodium interlayer cation (Figure 3A).[27] Pure CAAS18 shows a typical XRD pattern of an amorphous polymer, which corroborates the observed transparencies and DSC spectra of CAAS18 and its closely related hydrophobic derivatives. The segregation might actually be advantageous when it comes to degradation. We could recently show that such phase segregation accelerates the biodegradation of nanocomposite films due to fragmentation and concomitantly increased the surface area by swelling of the Hec domains.[34] The transparent CAAS18/Hec nanocomposite film outperforms commonly applied packaging polymers like PET, PE, or PVC in terms of water vapor and oxygen barrier properties (Table 2), rendering these biobased materials promising alternatives for currently applied packaging materials.

4. CONCLUSIONS

In summary, we described a simple and efficient method for the preparation of a series of new CA-derived polymers with interesting and adjustable functionalities. For instance,

modified CA polymers with considerable barrier properties and hydrophobic surfaces were obtained this way. The barrier properties of CAAS18 were significantly improved by adding large aspect ratio nanosheets of a synthetic clay (hectorite), leading to nanocomposite materials with excellent water vapor and oxygen barriers. In addition, rapid disintegration of the cellulose polymers under laboratory industrial composting conditions was observed, proving the potential of these materials to be biodegraded by natural microbes. Hence, these modified CA derivatives could be an interesting alternative to conventional plastics, although further investigations based on respirometric methods are needed to prove their biodegradability. The described method also enables fine-tuning of materials by using appropriate thiol compounds for the thio-Michael click reaction.

■ ASSOCIATED CONTENT

ⓢ Supporting Information

The Supporting Information is available free of charge at https://pubs.acs.org/doi/10.1021/acsomega.2c06811.

TGA/DSC spectra and NMR spectra of the new polymers (PDF)

■ AUTHOR INFORMATION

Corresponding Authors

Josef Breu − *Inorganic Chemistry 1, University of Bayreuth, 95440 Bayreuth, Germany;* ⓞ orcid.org/0000-0002-2547-3950; Email: josef.breu@uni-bayreuth.de

Bernhard Biersack − *Organic Chemistry 1, University of Bayreuth, 95440 Bayreuth, Germany;* ⓞ orcid.org/0000-0001-7305-346X; Email: bernhard.biersack@uni-bayreuth.de

Authors

Maximilian Röhrl − *Inorganic Chemistry 1, University of Bayreuth, 95440 Bayreuth, Germany*

Justus F. Ködel − *Fachgruppe Chemie, Wirtschaftswissenschaftliches und Naturwissenschaftlich-Technologisches Gymnasium Bayreuth, 95448 Bayreuth, Germany*

Renee L. Timmins − *Inorganic Chemistry 1, University of Bayreuth, 95440 Bayreuth, Germany*

Christoph Callsen − *Department of Polymer Engineering, Faculty of Engineering Science, University of Bayreuth, 95440 Bayreuth, Germany*

Merve Aksit − *Department of Polymer Engineering, Faculty of Engineering Science, University of Bayreuth, 95440 Bayreuth, Germany*

Michael F. Fink − *Chair of Electrochemical Process Engineering, Faculty of Engineering Science, University of Bayreuth, 95447 Bayreuth, Germany;* ⓞ orcid.org/0000-0002-2039-4735

Sebastian Seibt − *Linseis Messgeräte GmbH, 95100 Selb, Germany*

Andy Weidinger − *Fachgruppe Chemie, Wirtschaftswissenschaftliches und Naturwissenschaftlich-Technologisches Gymnasium Bayreuth, 95448 Bayreuth, Germany*

Glauco Battagliarin − *Biopolymers and Biodegradability Research, BASF, 67056 Ludwigshafen am Rhein, Germany*

Holger Ruckdäschel − *Department of Polymer Engineering, Faculty of Engineering Science, University of Bayreuth, 95440 Bayreuth, Germany;* ⓞ orcid.org/0000-0001-5985-2628

Rainer Schobert − *Organic Chemistry 1, University of Bayreuth, 95440 Bayreuth, Germany;* ⓞ orcid.org/0000-0002-8413-4342

Complete contact information is available at:
https://pubs.acs.org/10.1021/acsomega.2c06811

Author Contributions

The manuscript was written through the contributions of all authors. All authors have given approval to the final version of the manuscript. M.R. and J.F.K. contributed equally.

Notes

The authors declare no competing financial interest.

■ ACKNOWLEDGMENTS

■ ABBREVIATIONS

CA, cellulose acetate; CAA, cellulose acetate acrylate; DMSO, dimethyl sulfoxide; DSC, differential scanning calorimetry; Hec, hectorite; NMF, *N*-methyl formamide; OP, oxygen permeability; PE, polyethylene; PET, polyethylene terephthalate; PP, polypropylene; PS, polystyrene; PVC, polyvinylchloride; RH, relative humidity; SNA, starch nanocrystals acetate; TEM, transmission electron microscopy; TGA, thermogravimetric analysis; THF, tetrahydrofuran; WVP, water vapor permeability; XRD, X-ray diffraction

■ REFERENCES

(1) Chen, G.-Q.; Patel, M. K. Plastics derived from biological sources: present and future: a technical and environmental review. *Chem. Rev.* **2012**, *112*, 2082−2099.

(2) Edgar, K. *Encyclopaedia of Polymer Science and Technology, Vol. 9. Organic cellulose esters*; Mark, H. F., Ed.; Wiley: New York, USA, 2004; pp. 129−158.

(3) Puls, J.; Wilson, S.; Hölter, D. Degradation of cellulose acetate-based materials: a review. *J. Polym. Environ.* **2011**, *19*, 152−165.

(4) Mostafa, N. A.; Farag, A. A.; Abo-dief, H. M.; Tayeb, A. M. Production of biodegradable plastic from agricultural wastes. *Arab. J. Chem.* **2018**, *11*, 546−553.

(5) Phuong, V. T.; Verstiche, S.; Cinelli, P.; Anguillesi, I.; Coltelli, M.-B.; Lazzeri, A. Cellulose acetate blends − effect of plasticizers on properties and biodegradability. *J. Renewable Mater.* **2014**, *2*, 35−41.

(6) Mohanty, A. K.; Wibowo, A.; Misra, M.; Drzal, L. T. Effect of process engineering on the performance of natural fiber reinforced cellulose acetate biocomposites. *Compos. A Appl. Sci. Manuf.* **2004**, *35*, 363−370.

(7) Misra, M.; Mohanty, A. K.; Drzal, L. T. Sustainable bio-composites from renewable resources: opportunities and challenges in the green materials world. *J. Polym. Environ.* **2002**, *10*, 19−26.

(8) Wojciechowska, P. *Recent Advances in Plasticizers*; Luqman, M., Ed.; InTech: Rijeka, Croatia, 2012; pp. 141−164.

(9) Kolb, H. C.; Finn, M. G.; Sharpless, K. B. Click chemistry: diverse chemical function from a few good reactions. *Angew. Chem., Int. Ed.* **2001**, *40*, 2004−2021.

(10) Meng, X.; Edgar, K. J. "Click" reactions in polysaccharide modification. *Prog. Polym. Sci.* **2016**, *53*, 52−85.

(11) Hoyle, C. E.; Bowman, C. N. Thiol-ene click chemistry. *Angew. Chem., Int. Ed.* **2010**, *49*, 1540−1573.

(12) Lowe, A. B. Thiol-ene "click" reactions and recent applications in polymer and materials synthesis: a first update. *Polym. Chem.* **2014**, *5*, 4820−4870.

(13) Nair, D. P.; Podgórski, M.; Chatani, S.; Gong, T.; Xi, W.; Fenoli, C. R.; Bowman, C. N. The thiol-Michael addition click reaction: a powerful and widely used tool in materials chemistry. *Chem. Mater.* **2014**, *26*, 724−744.

(14) Tingaut, P.; Hauert, R.; Zimmermann, T. Highly efficient and straightforward functionalization of cellulose films with thiol-ene click chemistry. *J. Mater. Chem.* **2011**, *21*, 16066−16076.

(15) Zhao, G.-L.; Hafrén, J.; Deiana, L.; Córdova, A. Heterogeneous "organoclick" derivatization of polysaccharides: photochemical thiol-ene click modification of solid cellulose. *Macromol. Rapid Commun.* **2010**, *31*, 740−744.

(16) Meng, X.; Choudhury, S. R.; Edgar, K. J. Multifunctional cellulose esters by olefin cross-metathesis and thiol-Michael addition. *Polym. Chem.* **2016**, *7*, 3848−3856.

(17) Moreira, G.; Fedeli, E.; Ziarelli, F.; Capitani, D.; Mannina, L.; Charles, L.; Viel, S.; Gigmes, D.; Lefay, C. Synthesis of polystyrene-grafted cellulose acetate copolymers via nitroxide-mediated polymerization. *Polym. Chem.* **2015**, *6*, 5244−5253.

(18) Breu, J.; Seidl, W.; Stoll, A. J.; Lange, K. G.; Probst, T. U. Charge homogeneity in synthetic fluorohectorite. *Chem. Mater.* **2001**, *13*, 4213−4220.

(19) Stöter, M.; Kunz, D. A.; Schmidt, M.; Hirsemann, D.; Kalo, H.; Putz, B.; Senker, J.; Breu, J. Nanoplatelets of sodium hectorite showing aspect ratios of ~20000 and superior purity. *Langmuir* **2013**, *29*, 1280−1285.

(20) Huang, F.-Y.; Wu, X.-J.; Yu, Y.; Lu, Y.-H. Preparation and properties of cellulose laurate (CL)/starch nanocrystals acetate (SNA) bio-nanocomposites. *Polymers* **2015**, *7*, 1331−1345.

(21) Zhang, Q.; Wang, X.; Decker, V.; Meyerhoff, M. E. Plasticizer-free thin-film sodium-selective optodes inkjet-printed on transparent plastic for sweat analysis. *ACS Appl. Mater. Interface* **2020**, *12*, 25616−25624.

(22) Luoma, E.; Välimäki, M.; Ollila, J.; Heikkinen, K.; Immonen, K. Bio-based polymeric substrates for printed hybrid electronics. *Polymers* **2022**, *14*, 1863.

(23) Raouf, R. M.; Wahab, Z. A.; Ibrahim, N. A.; Talib, Z. A.; Chieng, B. W. Transparent blend of poly(methylmethacrylate)/cellulose acetate butyrate for the protection from ultraviolet. *Polymers* **2016**, *8*, 128.

(24) Tran, T. N.; Mai, B. T.; Setti, C.; Athanassiou, A. Transparent bioplastic derived from CO_2-based polymer functionalized with oregano waste extract toward active food packaging. *ACS Appl. Mater. Interfaces* **2020**, *12*, 46667−46677.

(25) Arrieta, M. P.; Garrido, L.; Faba, S.; Galotto, M. J.; de Dicastillo, C. L. *Cucumis metuliferus* fruit extract loaded acetate cellulose coatings for antioxidant active packaging. *Polymers* **2020**, *12*, 1248.

(26) Lange, J.; Wyser, Y. Recent innovations in barrier technologies for plastic packaging − a review. *Packaging Technol. Sci.* **2003**, *16*, 149−158.

(27) Thomas, S.; Joseph, K.; Malhotra, S. K.; Goda, K.; Sreekala, M. S. *Polymer Composites, Macro- and Microcomposites*; Wiley-VCH Verlag: Weinheim, Germany, 2012.

(28) Cussler, E. L.; Hughes, S. E.; Ward, W. J.; Aris, R. Barrier membranes. *J. Membr. Sci.* **1988**, *38*, 161−174.

(29) Habel, C.; Schöttle, M.; Daab, M.; Eichstaedt, N. J.; Wagner, D.; Bakhshi, H.; Agarwal, S.; Horn, M. A.; Breu, J. High-barrier, biodegradable food packaging. *Macromol. Mater. Eng.* **2018**, *303*, No. 1800333.

(30) Habel, C.; Tsurko, E. S.; Timmins, R. L.; Hutschreuther, J.; Kunz, R.; Schuchardt, D. D.; Rosenfeldt, S.; Altstädt, V.; Breu, J. J. Lightweight ultra-high-barrier liners for helium and hydrogen. *ACS Nano* **2020**, *14*, 7018−7024.

(31) Schilling, T.; Habel, C.; Rosenfeldt, S.; Röhrl, M.; Breu, J. Impact of ultraconfinement on composite barriers. *ACS Appl. Polym. Mater.* **2020**, *2*, 3010−3015.

(32) Röhrl, M.; Federer, L.; Timmins, R. L.; Rosenfeldt, S.; Dörres, T.; Habel, C.; Breu, J. Disorder−order transition—improving the moisture sensitivity of waterborne nanocomposite barriers. *ACS Appl. Mater. Interfaces* **2021**, *13*, 48101−48109.

(33) Dudko, V.; Ottermann, K.; Rosenfeldt, S.; Papastavrou, G.; Breu, J. Osmotic delamination: a forceless alternative for the production of nanosheets now in highly polar and aprotic solvents. *Langmuir* **2021**, *37*, 461−468.

(34) Timmins, R. L.; Kumar, A.; Röhrl, M.; Havlícek, K.; Agarwal, S.; Breu, J. High barrier nanocomposite film with accelerated biodegradation by clay swelling induced fragmentation. *Macromol. Mater. Eng.* **2022**, *307*, No. 2100727.

Supporting Information

New functional polymer materials via click chemistry-based modification of cellulose acetate

Maximilian Röhrl[§,1], Justus F. Ködel[#,1], Renee L. Timmins[§], Christoph Callsen[‡], Merve Aksit[‡], Michael F. Fink[&], Sebastian Seibt[$], Andy Weidinger[#], Glauco Battagliarin[|], Holger Ruckdäschel[‡], Rainer Schobert[†], Josef Breu[§,]*, and Bernhard Biersack[†,]*

[§]Inorganic Chemistry 1, University of Bayreuth, Universitätsstrasse 30, 95440 Bayreuth, Germany
E-mail: josef.breu@uni-bayreuth.de

[#]Fachgruppe Chemie, Wirtschaftswissenschaftliches und Naturwissenschaftlich-Technologisches Gymnasium Bayreuth, Am Sportpark 1, 95448 Bayreuth, Germany

[†]Organic Chemistry 1, University of Bayreuth, Universitätsstrasse 30, 95440 Bayreuth, Germany
E-mail: bernhard.biersack@uni-bayreuth.de

[‡]Department of Polymer Engineering, Faculty of Engineering Science, University of Bayreuth, Universitätsstrasse 30, 95440 Bayreuth, Germany

[&]Chair of Electrochemical Process Engineering, Faculty of Engineering Science, University of Bayreuth, Universitätsstrasse 30, 95447 Bayreuth, Germany

[$]Linseis Messgeräte GmbH, Vielitzerstrasse 43, 95100 Selb, Germany

[|]Biopolymers and Biodegradability Research, BASF, Carl-Bosch-Str. 38, 67056 Ludwigshafen am Rhein, Germany

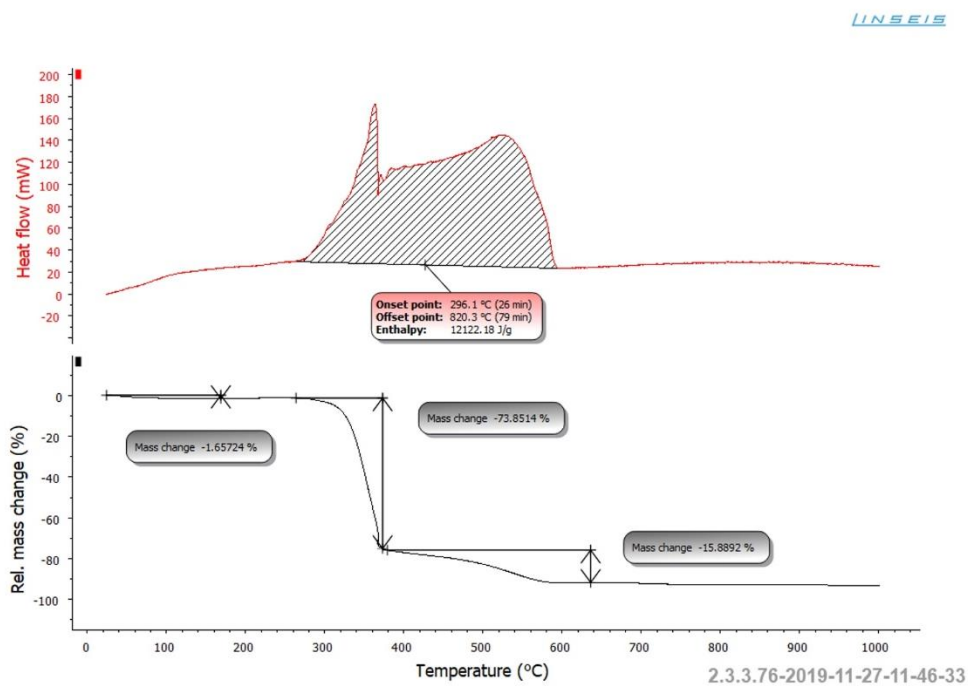[1]Authors contributed equally to this work.
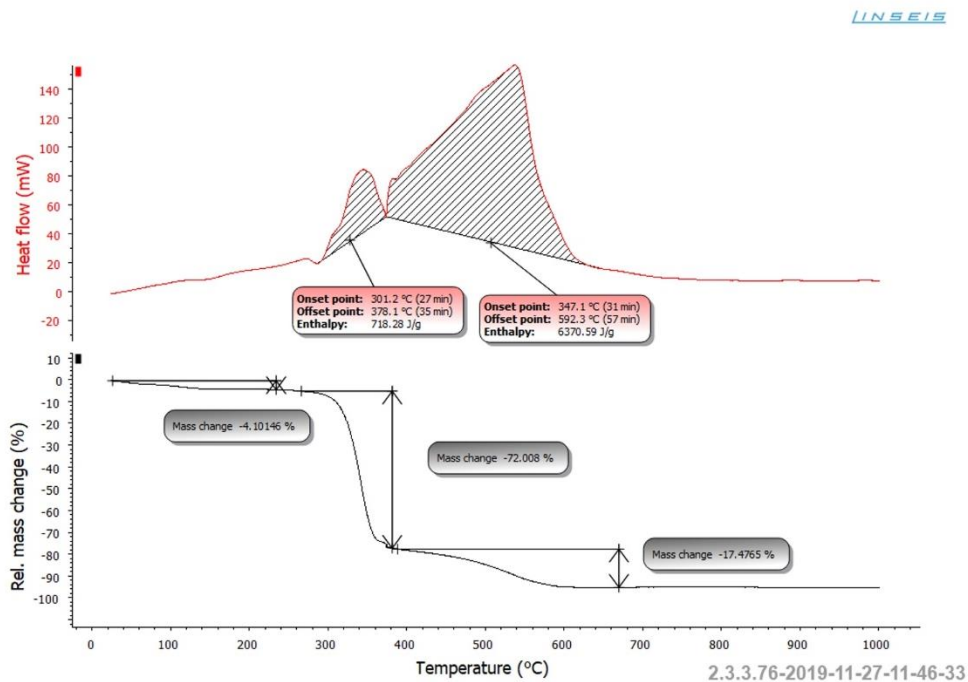
Figure S1. TGA and DSC of CA
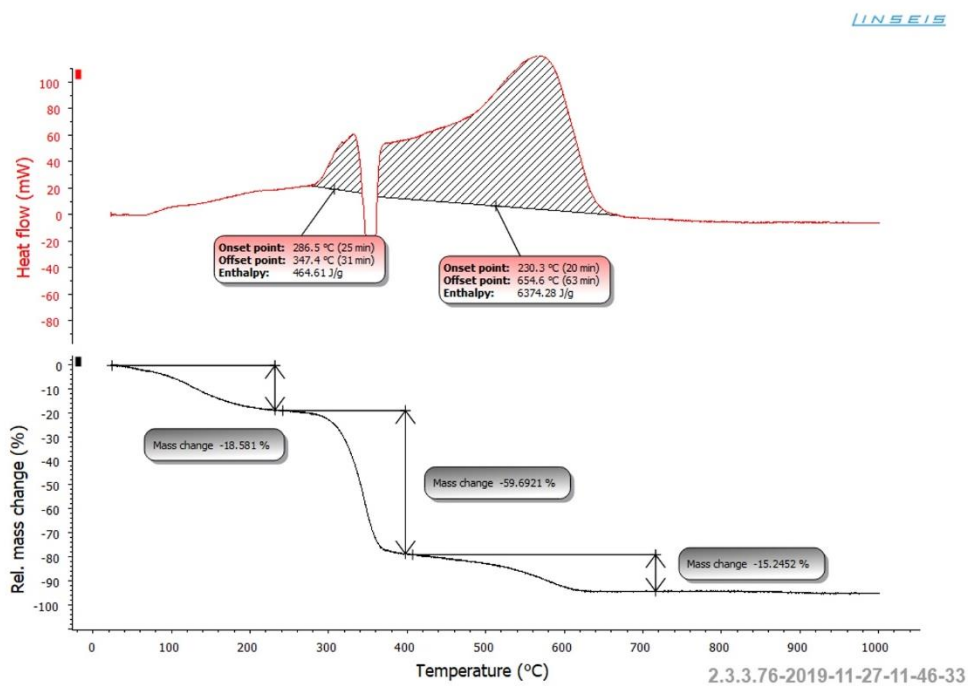

Figure S2. TGA and DSC of CAAS12
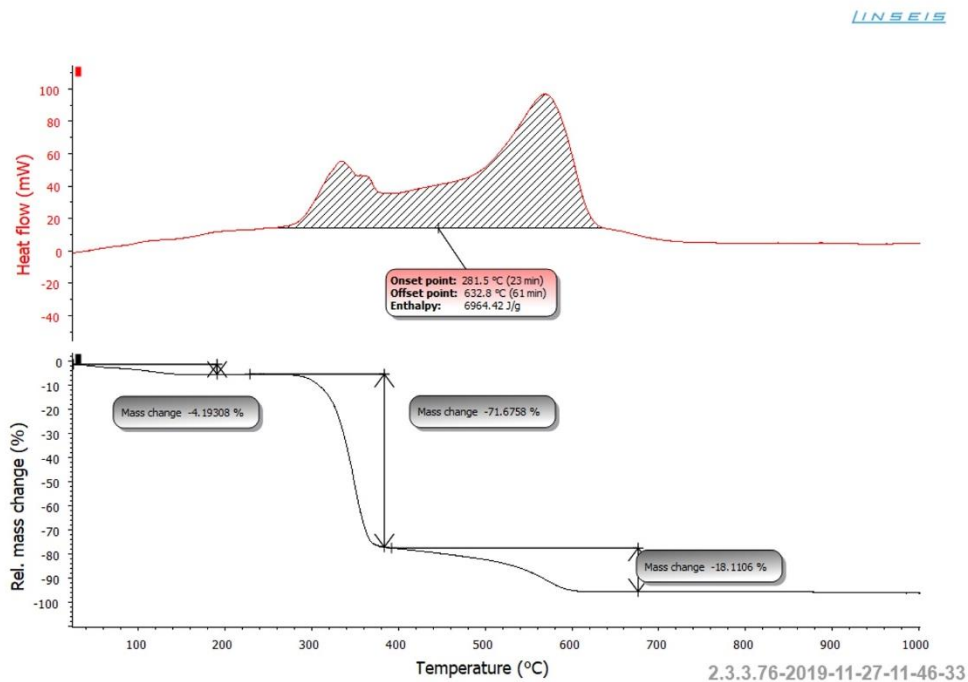
S2

Figure S3. TGA and DSC of CAAS16
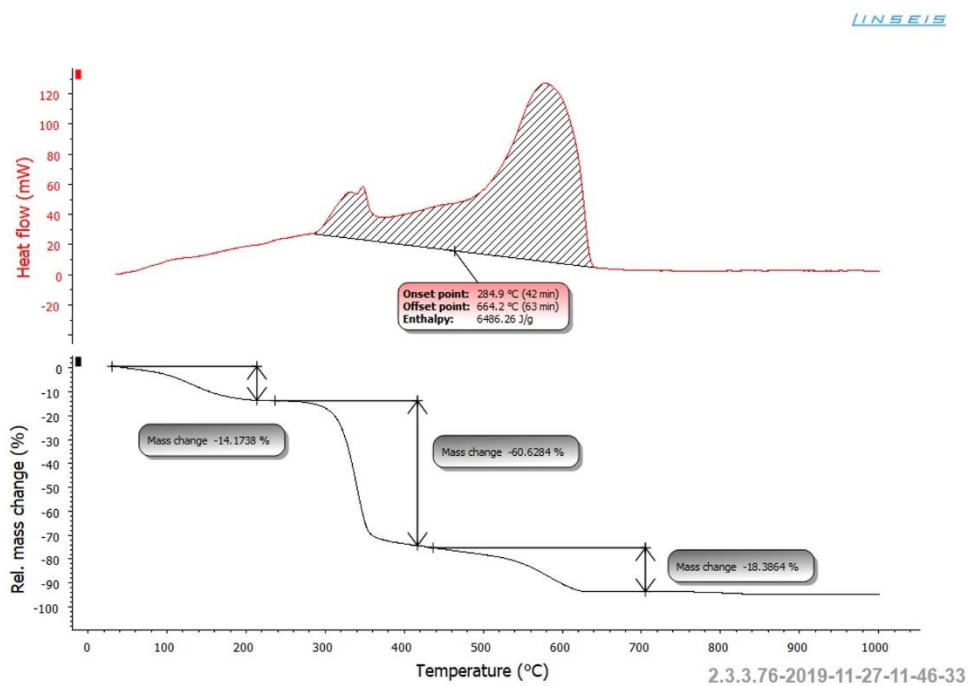

Figure S4. TGA and DSC of CAAS18
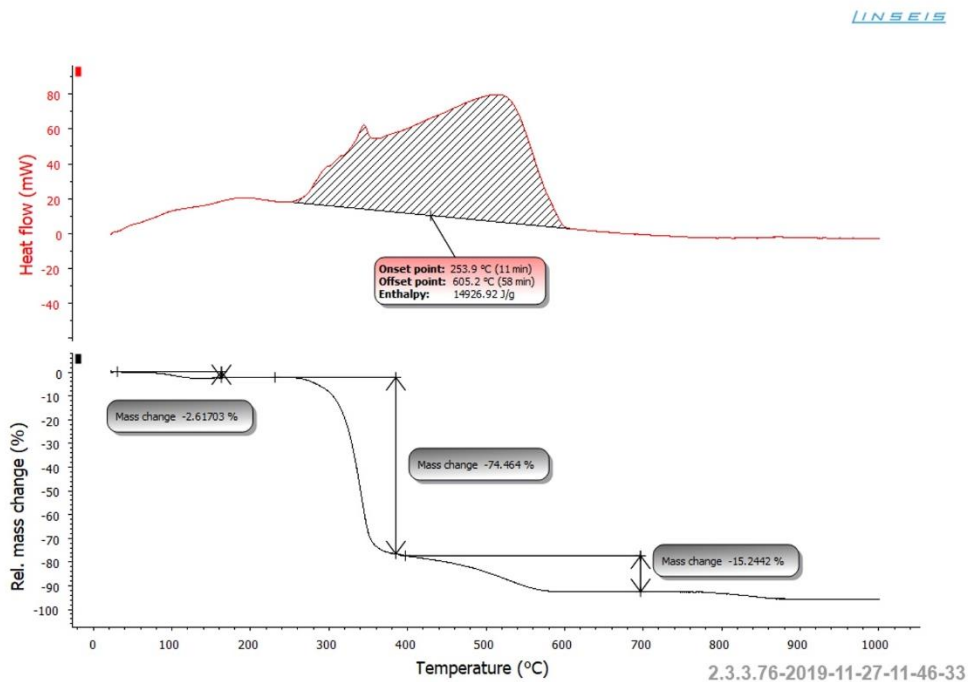
S3

Figure S5. TGA and DSC of CAAS20

Figure S6. TGA and DSC of CAASB3MP

S4
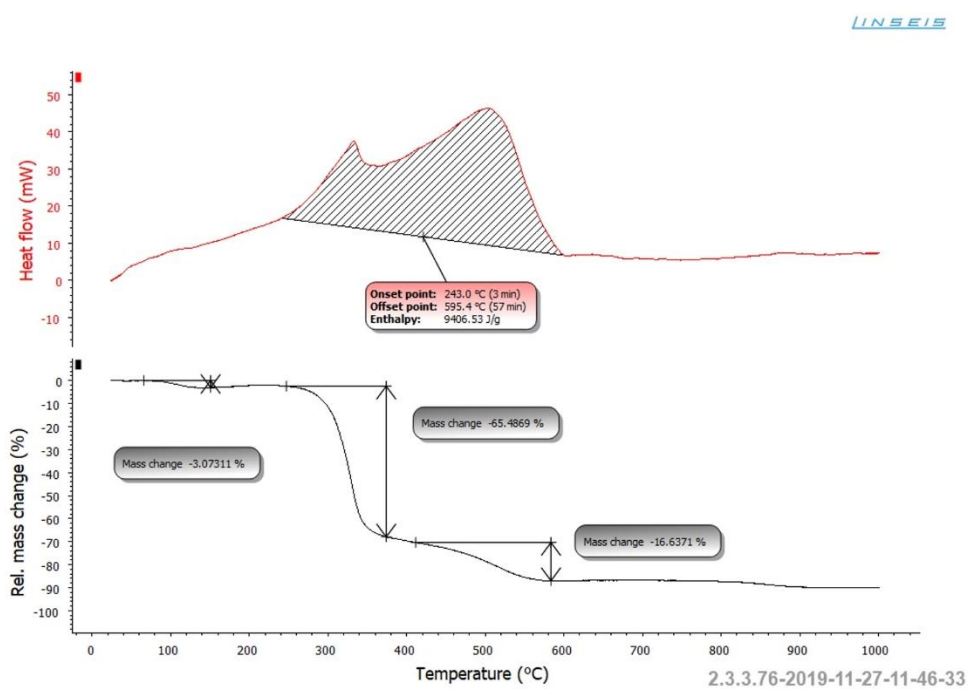
Figure S7. TGA and DSC of CAASFur
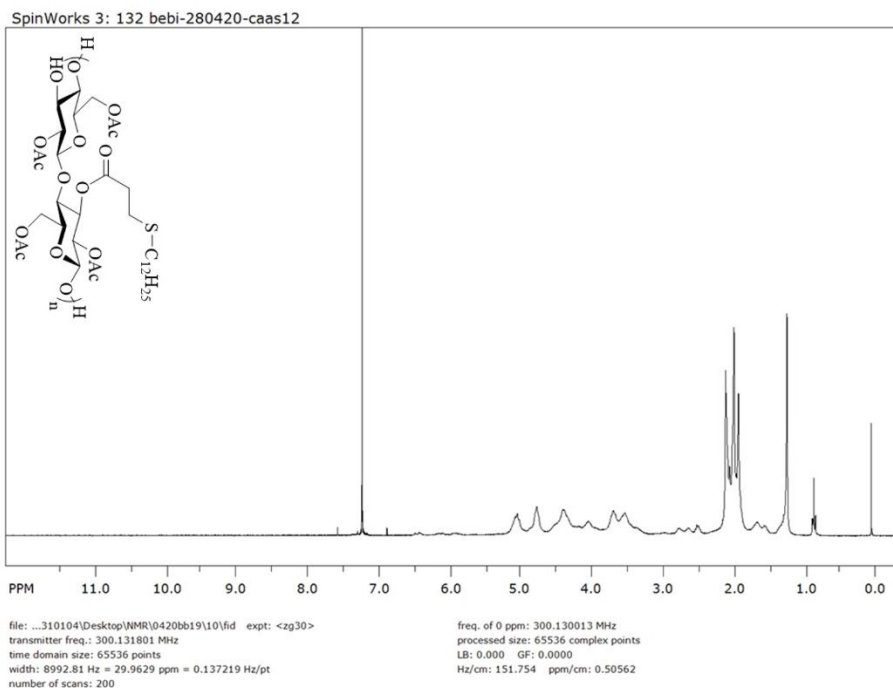
Figure S8. ^{1}H NMR of CAAS12
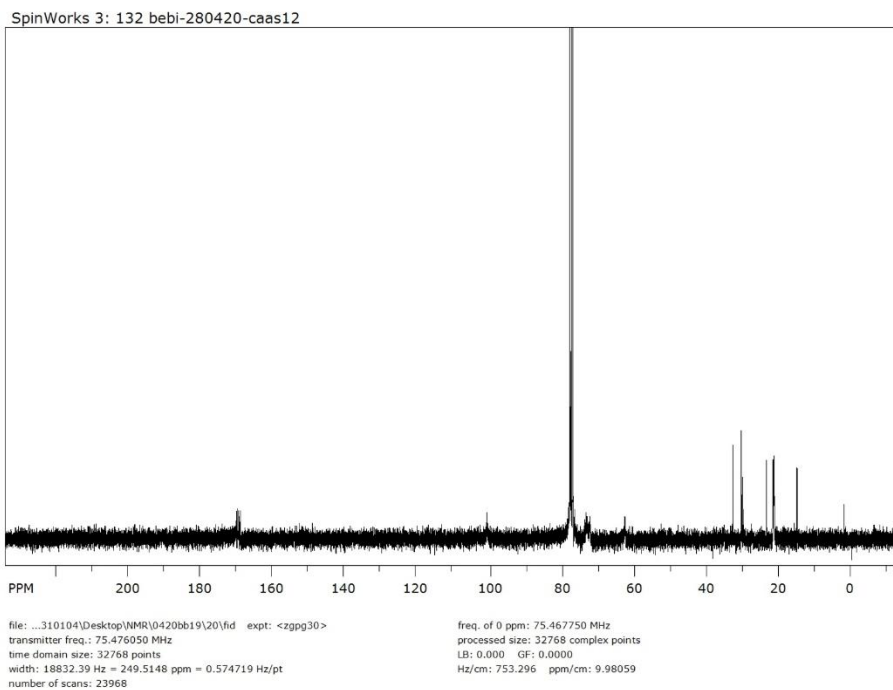
Figure S9. ^{13}C NMR of CAAS12

S6
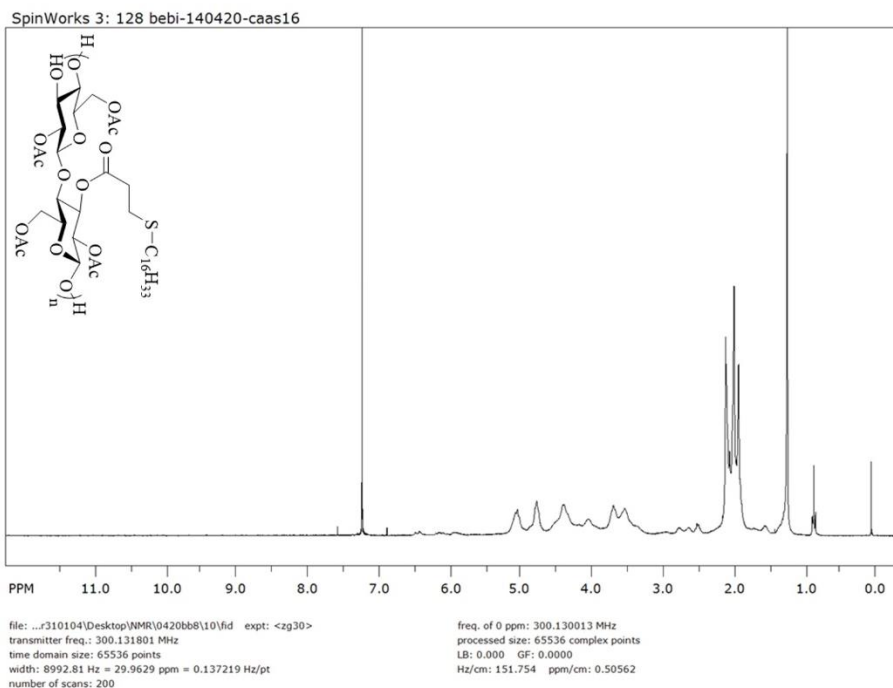
Figure S10. ^{1}H NMR of CAAS16
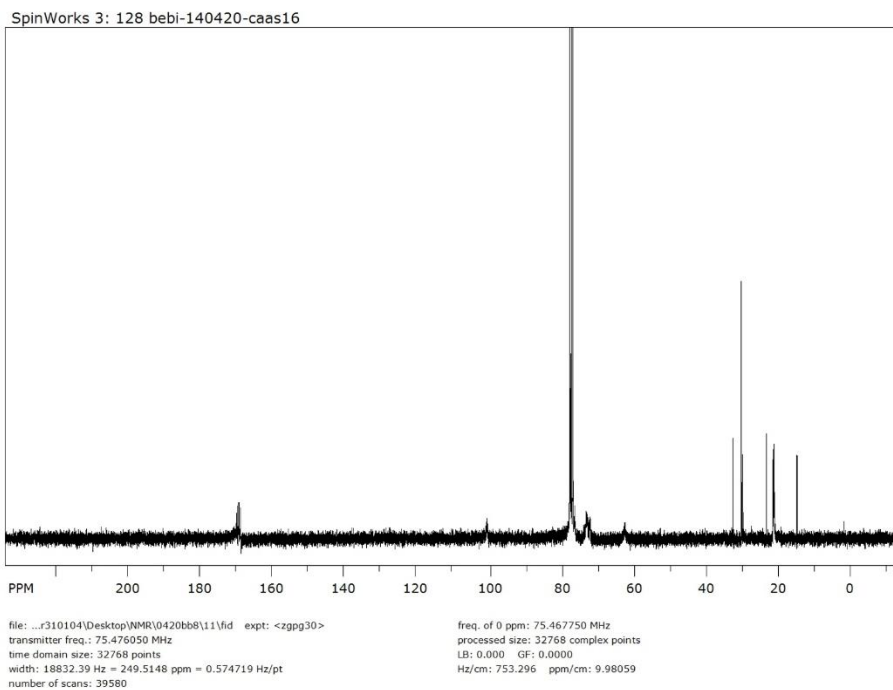
Figure S11. ^{13}C NMR of CAAS16

S7
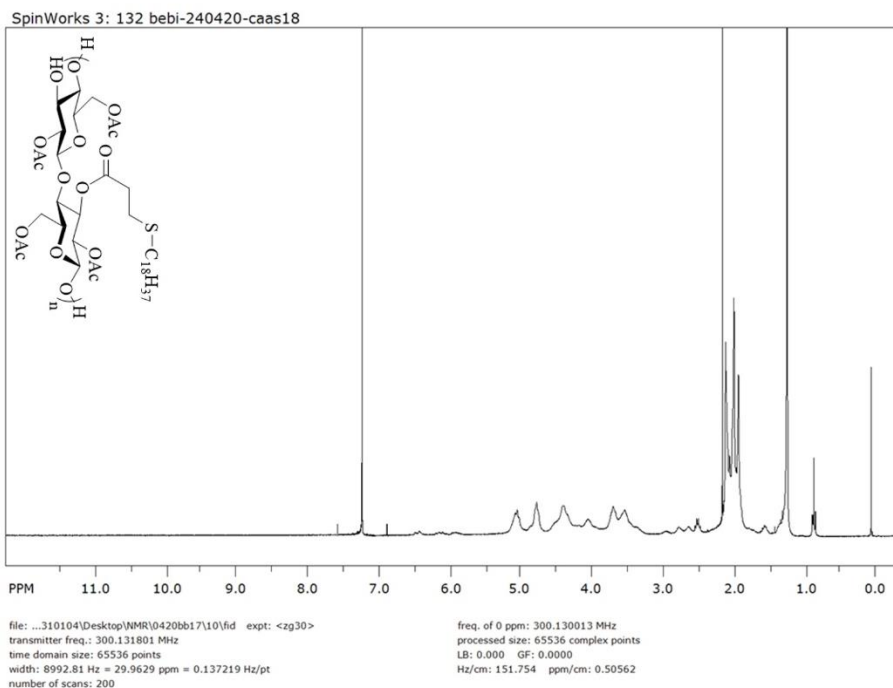
Figure S12. ^{1}H NMR of CAAS18
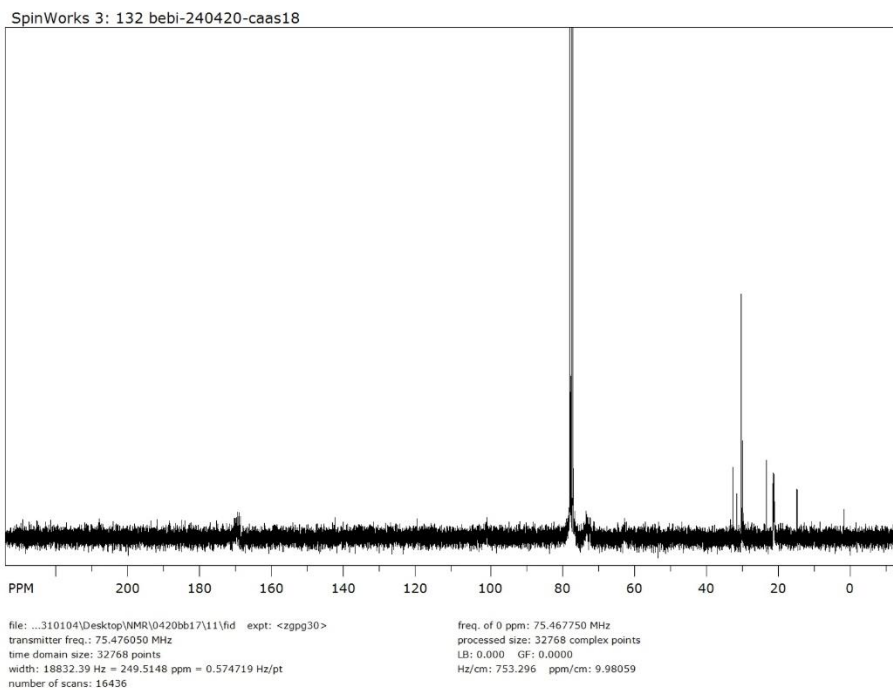
Figure S13. ^{13}C NMR of CAAS18

S8
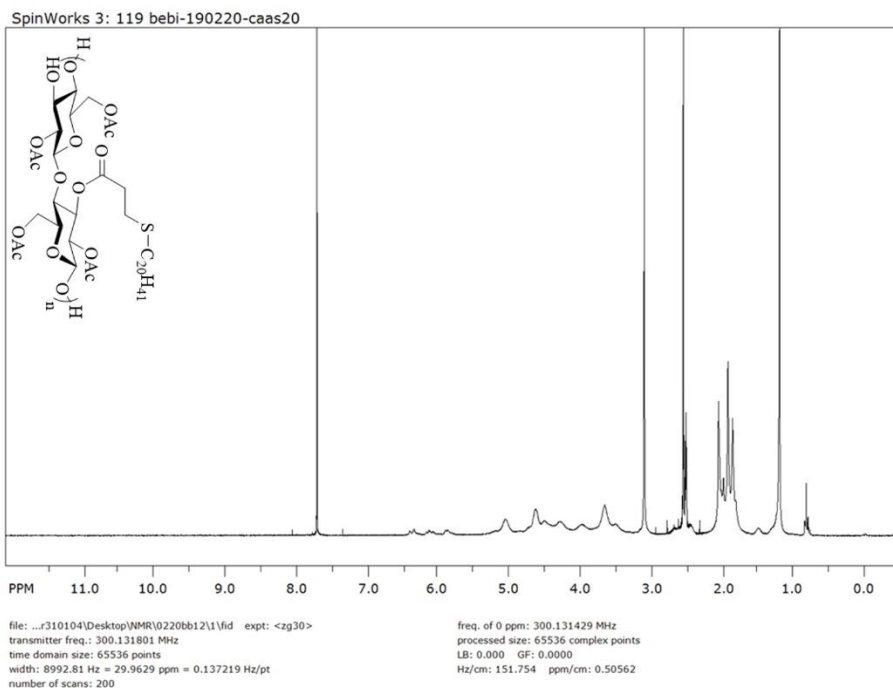
Figure S14. ^{1}H NMR of CAAS20
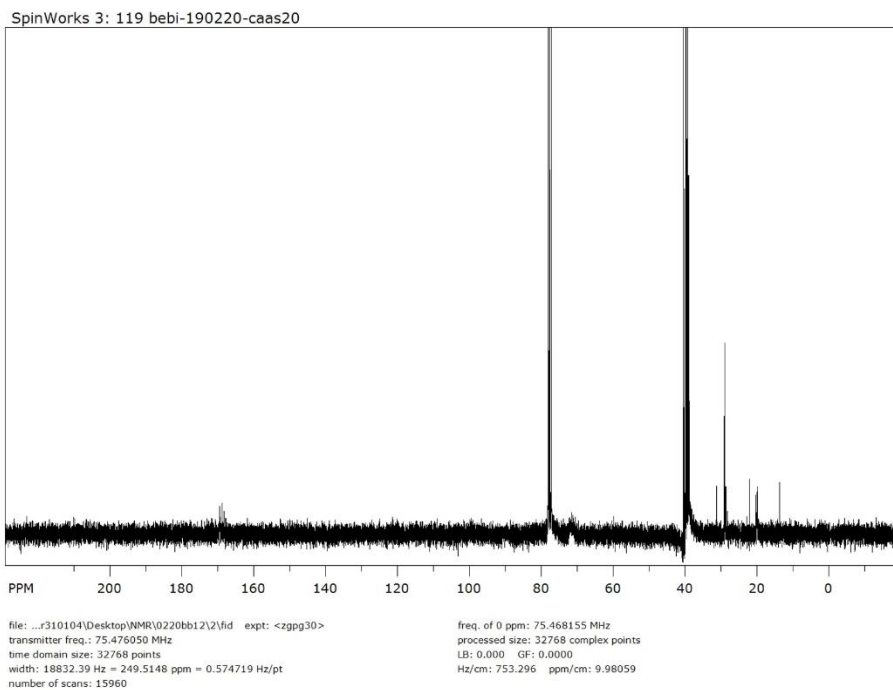
Figure S15. ^{13}C NMR of CAAS20

S9
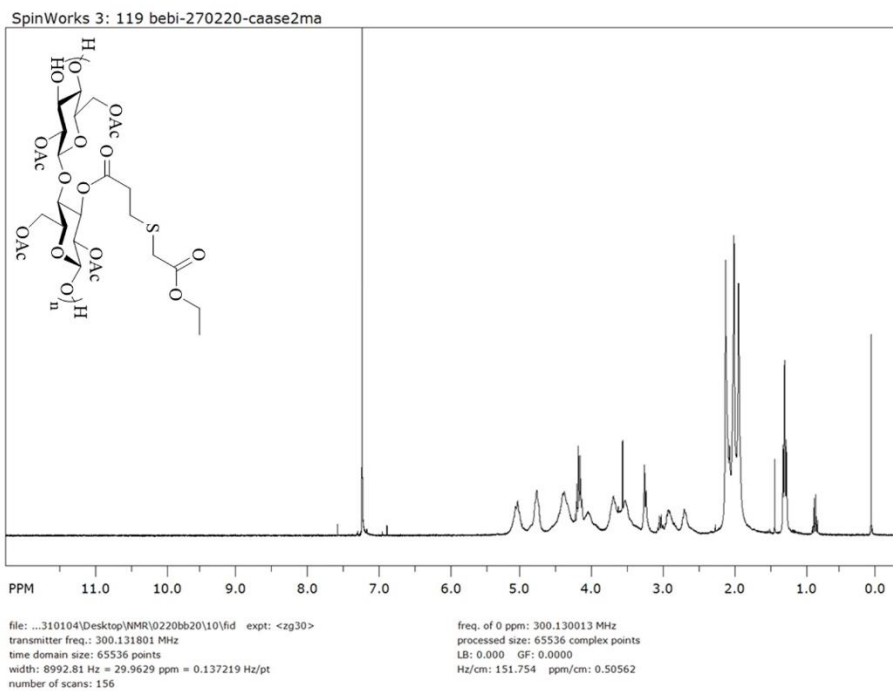
Figure S16. ^{1}H NMR of CAASE2MA
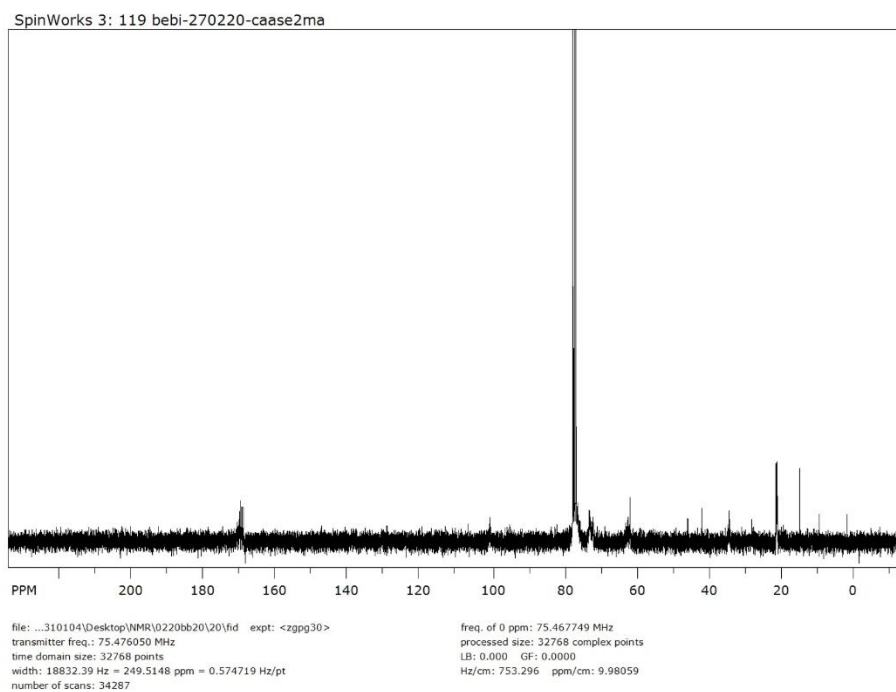
Figure S17. ^{13}C NMR of CAASE2MA

S10

105
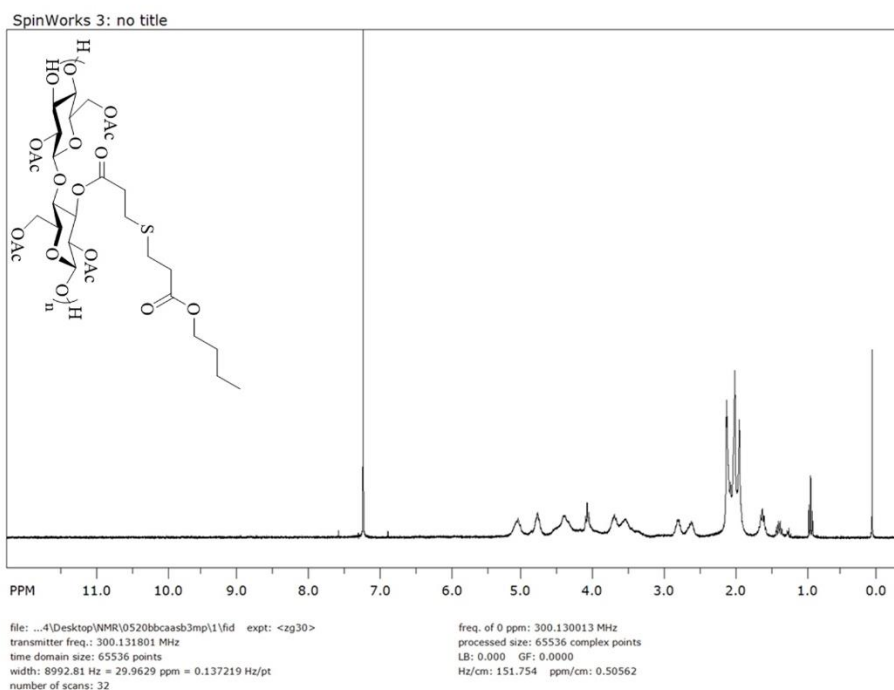
Figure S18. ^{1}H NMR of CAASB3MP
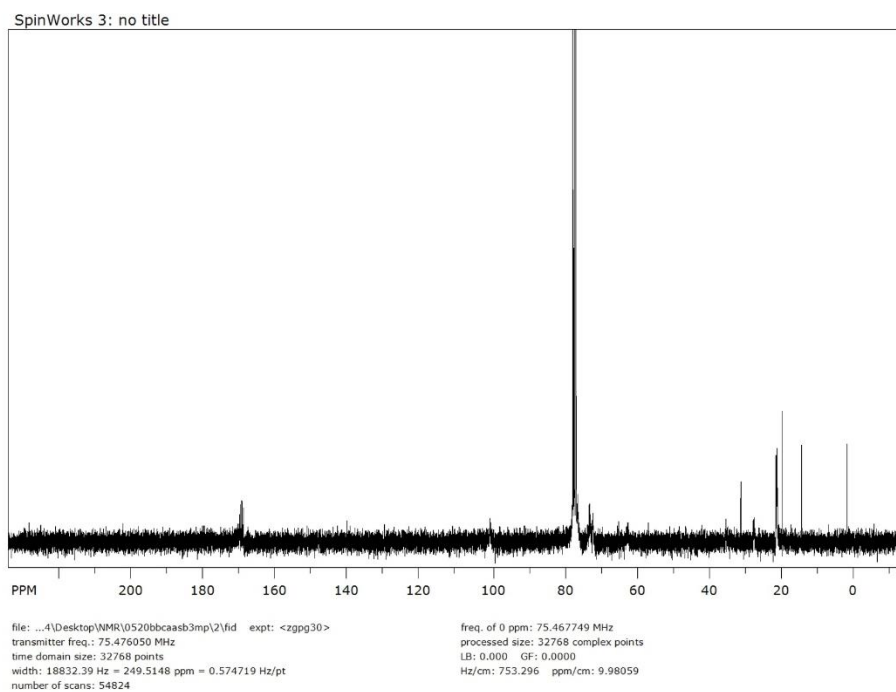
Figure S19. ^{13}C NMR of CAASB3MP

S11

SpinWorks 3: 94 bebi-101019-caasfur

file: ...310104\Desktop\NMR\1019bb18\10\fid   expt: <zg30>
transmitter freq.: 300.131801 MHz
time domain size: 65536 points
width: 8992.81 Hz = 29.9629 ppm = 0.137219 Hz/pt
number of scans: 200

freq. of 0 ppm: 300.130013 MHz
processed size: 65536 complex points
LB: 0.000   GF: 0.0000
Hz/cm: 151.754   ppm/cm: 0.50562
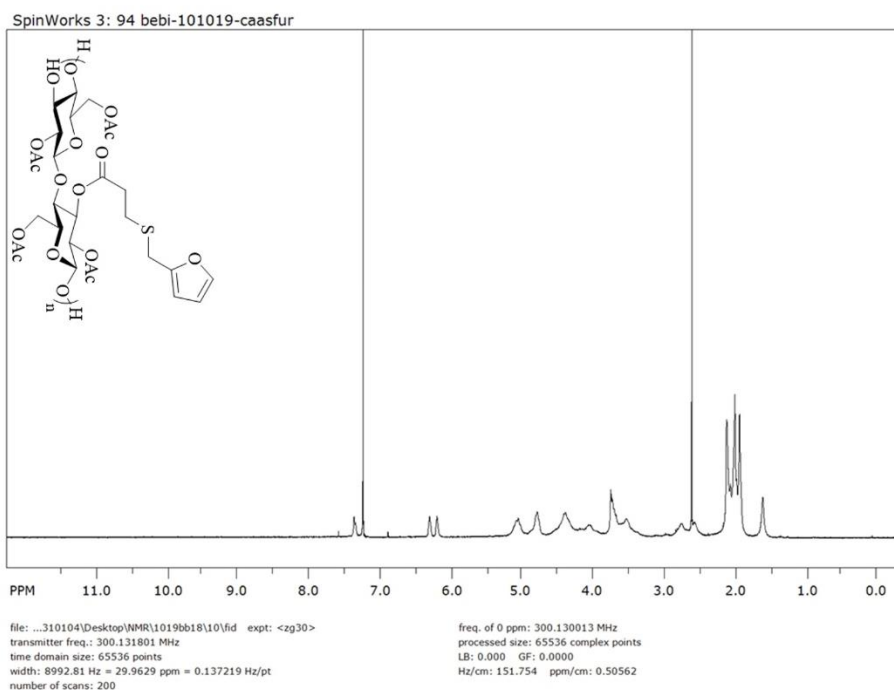
Figure S20. ^{1}H NMR of CAASFur

SpinWorks 3: 94 bebi-101019-caasfur

file: ...310104\Desktop\NMR\1019bb18\20\fid   expt: <zgpg30>
transmitter freq.: 75.476050 MHz
time domain size: 32768 points
width: 18832.39 Hz = 249.5148 ppm = 0.574719 Hz/pt
number of scans: 34600

freq. of 0 ppm: 75.467750 MHz
processed size: 32768 complex points
LB: 0.000   GF: 0.0000
Hz/cm: 753.296   ppm/cm: 9.98059
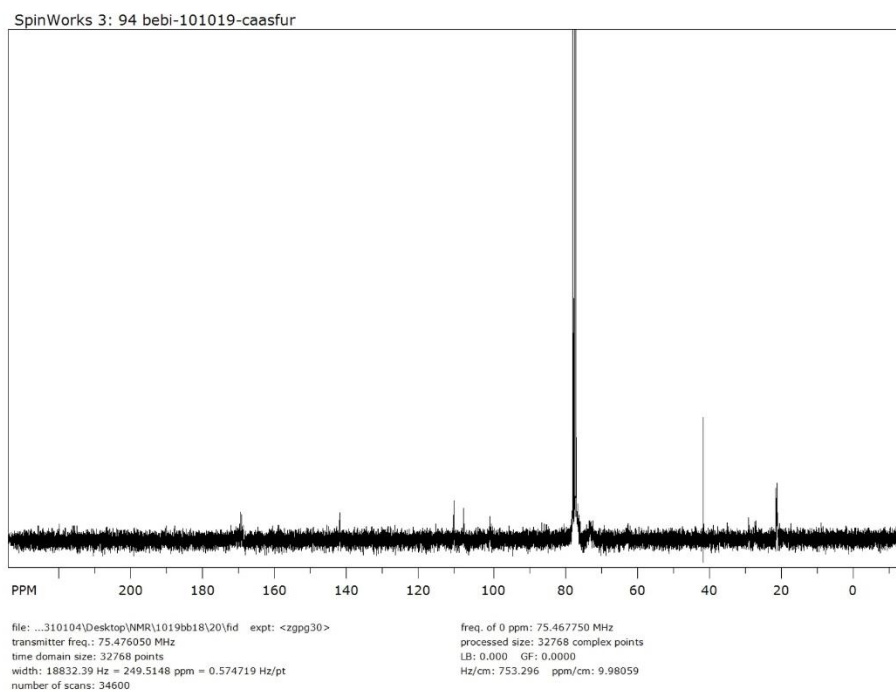
Figure S21. ^{13}C NMR of CAASFur

S12

6.4 Stretchable clay nanocomposite barrier film for flexible packaging

Authors: Maximilian Röhrl, Renee L. Timmins, Sabine Rosenfeldt, Dominik D. Schuchardt, Felix Uhlig, Simon Nürmberger, and Josef Breu

Stretchable Clay Nanocomposite Barrier Film for Flexible Packaging

Maximilian Röhrl, Renee L. Timmins, Sabine Rosenfeldt, Dominik D. Schuchardt, Felix Uhlig, Simon Nürmberger, and Josef Breu*

Cite This: *ACS Appl. Mater. Interfaces* 2023, 15, 22524−22531

Read Online

ACCESS | Metrics & More | Article Recommendations | Supporting Information

ABSTRACT: The goal of reconciling all packaging requirements, e.g., mechanical resistance, transparency, flexibility, and gas barrier properties, is immensely challenging for packaging materials. Particularly, the combination of flexibility and good gas barrier properties poses a serious problem, especially when barrier requirements can only be met by lamination with a metal foil, metalization, or vapor-deposited ceramic layers, as all of these tend to be nonstretchable. In this work, we produced a stretchable nanocomposite barrier composed of one-dimensional (1D) crystalline (Bragg stack) barrier films composed of alternating layers of poly(ethylene glycol) (PEG) and synthetic sodium fluorohectorite (Hec) nanosheets. By sandwiching the Bragg stack type film between two plasticized poly(vinyl alcohol) (PVOH) layers, a waterborne laminate was obtained that outperforms commercial polymer materials in terms of water vapor permeability (WVP = 2.8 g mm m^{-2} day^{-1} bar^{-1} at 23 °C and 85% relative humidity), which is remarkable for an entirely water-soluble film. Moreover, no deterioration of barrier performance up to 10% elongation was observed, rendering the transparent self-standing laminate promising for thermoformed blister packaging, shrink wrap, or vacuum packaging. Besides the low WVP, the scalable and green processing method makes this technology auspicious for real-world applications.

KEYWORDS: *nanocomposite barrier, vacuum-sealed packaging, hydrogen tank, flexible barrier, stretchability*

■ INTRODUCTION

In 2020, the turnover of the European plastic industry was close to 330 billion €, and the converters′ plastics demand was about 49.1 million tons, with the packaging segment alone accountin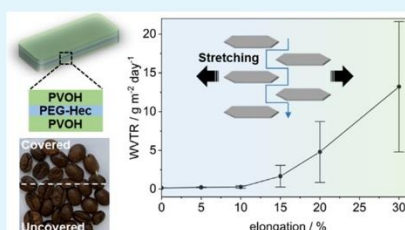g for 40.5% of the total.[1] Depending on the application area, the requirements for packaging plastics are substantially different, but in general, they are desired to be cheap, sustainable, mechanically resistant, transparent, flexible, and protective against gas permeation.[2,3] High-end barrier often requires lamination with thin inorganic layers, like aluminum foils or vapor-deposited aluminum coatings. If transparency is an issue,[2] vapor-deposited Al_2O_3 or glass-like SiO_x coatings in the nanometer range are applied to enhance the barrier properties of plastic wrap.[4,5] Such thin vapor-deposited barriers are, however, nonstretchable and thus sensitive to mechanical stress.[6] Stretching inevitably will cause defects in the inorganic barrier component, and these pinholes will be detrimental to the barrier.[6] For instance, the barrier performance of a vapor-deposited SiO_x coating on a poly(ethylene terephthalate) foil tolerates deformations up to only 4%.[2] This drawback of vapor-deposited barrier coatings has been mitigated to some extent by covering or (nano)-laminating the SiO_x/Al_2O_3-coated substrate. The laminate buffers mechanical stress and counteracts embrittlement of the complete barrier system by the inorganic coating.[2,6,7]

Blister packaging as applied for pharmaceuticals,[8] shrink wraps for vegetables,[9] or vacuum packaging for instant coffee powder as one example, all require thermoformable polymers.

During the thermoforming process, the polymer film gets heated and subsequently either stretched within the forming mold or shrunk around the packaged item, imparting substantial dimensional changes to the polymer foil.[10−13] Stretching and shrinking are, of course, incompatible with inorganic and brittle barrier films, since a wide range of applications require stretching up to 10% or more.[14] In regulated fields, such as pharmaceutical or food packaging, high oxygen and water vapor barrier requirements consequently can only be met by thicker neat polymer films.[15−18] Usually, this is accomplished by using petro-based poly(vinyl chloride) (PVC), polystyrene (PS), polypropylene (PP), ethylene vinyl alcohol (EVOH), or laminates of those as thermoformable polymer films.[16,19]

A promising approach to reconciling the good barrier of inorganic layers with dimensional flexibility of thermoformable polymers applies large aspect ratio inorganic nanosheets arranged into self-standing films of coplanar,[20−22] largely overlapping nanosheets that are mechanically decoupled by a layer of intercalated soft polymers. If the nanosheets overlap by
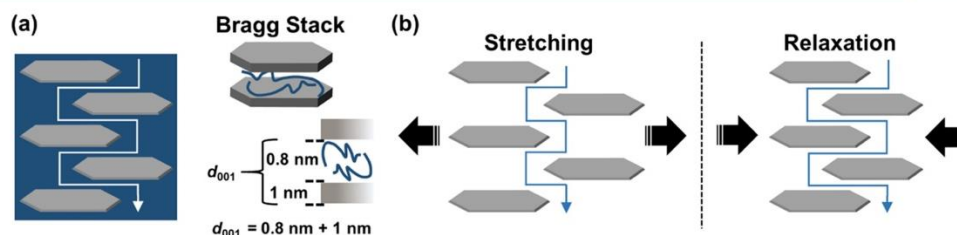
**Figure 1.** Introduction. (a) Sketch of the tortuous path (white) of a gas permeate dodging impermeable clay nanosheets incorporated into a polymer matrix (blue) and a Bragg stack of alternating polymer chains (blue) and clay nanosheets. As the aspect ratio is huge, the filler shape is not shown in scale. Moreover, as the polymer layer is thinner than the filler platelets, the nanocomposite is also not shown in scale to allow depicting the tortuous path. The relative thickness is given, however, depicted in scale for the individual stack. (b) Tortuous path of a clay nanocomposite barrier film upon uniaxial stretching and relaxation.
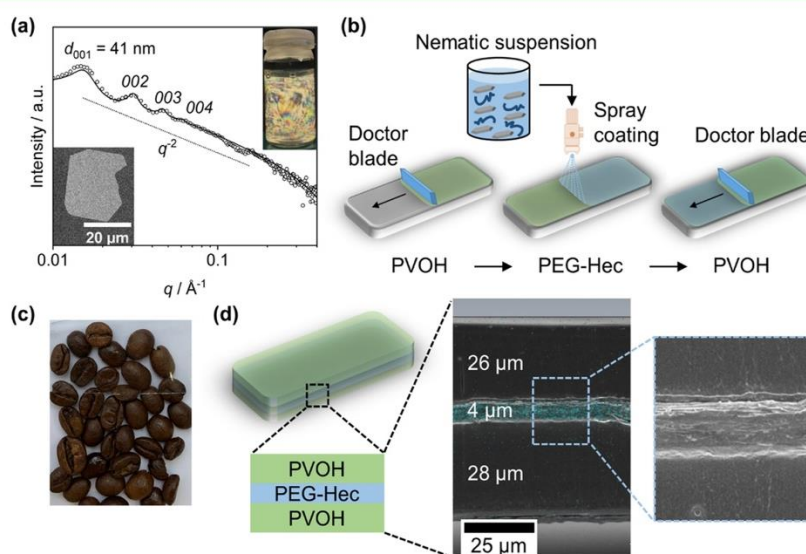
Figure 2. Fabrication of the self-standing barrier laminate. (a) 1D SAXS pattern of a concentrated (4 wt % = 1.5 vol %) nematic aqueous suspension of sodium fluorohectorite (Hec) and poly(ethylene glycol) (PEG) with individual Hec nanosheets being separated to a distance of 41 nm ($\bigcirc$ measured, — fit). The lower left inset displays an SEM image of an individual Hec nanosheet with a diameter >20 μm. The upper right inset shows birefringence between crossed-polarizers due to the nematic nature of a suspension (1 wt %) applied for spray coating of the Bragg stack. (b) Sketch of the sequential coating process to produce the self-standing barrier laminate. (c) Final self-standing laminate may easily be peeled off the substrate. It is highly transparent when covering coffee beans in the upper half of the photograph. (d) Schematic structure and SEM micrographs of a cross section of the self-standing barrier laminate with a total thickness of approx. 58 μm. Element mapping of Si (cyan) via energy-dispersive X-ray (EDX) spectroscopy indicates no interdiffusion of Hec nanosheets into the PVOH layers. The zoom-in displays the sandwiched PEG-Hec Bragg stack barrier.

some 90% of their area, monodomain hybrid films with one-dimensional (1D) crystallinity (Bragg stacks) may be obtained via self-organization of wet coats applied to a substrate foil (Figure 1a).[23−25] It has long been established that the permeability P of such hybrid films is several orders of magnitude reduced compared to the neat polymer films used as a decoupling matrix.[26−32] Based on Cussler's equation (eq 1), incorporating impermeable clay nanosheets increases the diffusion pathway of a gas permeate via the tortuous path theory (Figure 1a).[33] Thus, the relative permeability P_{rel} depends nonlinearly on the aspect ratio α (ratio of filler diameter to filler height) and filler content φ

$$P_{rel} = \frac{P}{P_0} = \left(1 + \mu\left(\frac{\alpha^2\varphi^2}{1-\varphi}\right)\right)^{-1} \tag{1}$$

where P is the permeability of the nanocomposite, P_0 is the permeability of the neat polymer, and μ is a geometrical factor depending on the geometry of the filler.[34]

Decoupling of adjacent nanosheets in the Bragg stacks should allow sliding when stretched. Sliding will reduce the overlap area and is thus expected to hamper the barrier to some degree. However, the tortuous path, and hence the barrier, should stay intact while changing the dimensions of the hybrid film within some limit (Figure 1b). Research on the influence of stretching on clay polymer nanocomposites has been conducted, studying the clay sheets' orientation,[35] mechanical properties,[36,37] and barrier properties.[36,37] However, the results on the barrier properties are contradictory. We hypothesize that this might be related to several issues. The filler may not have been utterly delaminated or may have reaggregated during compounding, and thus adjacent nano-
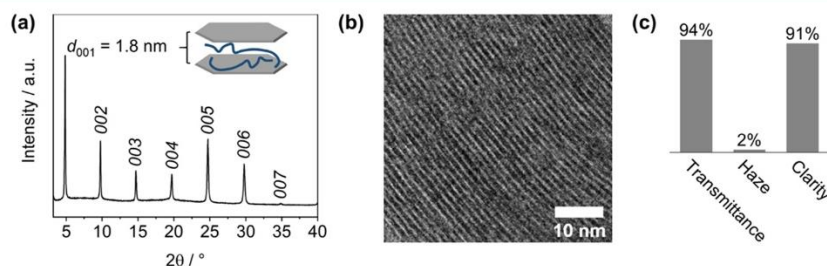
Figure 3. Insight into the structure of the PEG-Hec barrier sandwiched within the self-standing laminate. (a) XRD pattern of the barrier film. The inset sketches the basal spacing of 1.8 nm corresponding to a volume content of 55% for Hec, which is in good agreement with the applied PEG-Hec ratio (Sections S1 and S2). (b) TEM micrographs of a cross section focusing on the PEG-Hec Bragg stack barrier film with Hec nanosheets (dark) decoupled by PEG (bright). (c) Optical properties of the self-standing laminate.

sheets would not have been completely mechanically decoupled. If natural clays like montmorillonite were used, the diameter of the nanosheets would be comparatively small (<200 nm), and thus the overlap area might not be sufficient. Finally, with smaller aspect ratios, it becomes increasingly challenging to ensure a coplanar arrangement of adjacent nanosheets and the nanosheets to the planar substrate.

In this paper, we fabricated a barrier laminate composed of a monodomain Bragg stack comprising alternating layers of poly(ethylene glycol) (PEG) and a large aspect ratio synthetic clay, sodium fluorohectorite (Hec, $[Na_{0.5}]^{inter}[Mg_{2.5}Li_{0.5}]^{oct}[Si_4]^{tet}O_{10}F_2$). By sandwiching this PEG-Hec Bragg stack barrier film between two water-soluble poly(vinyl alcohol) (PVOH) layers, a self-standing laminate was obtained. Substantial uniaxial stretching (<15%) had little effect on the water vapor transmission rate (WVTR) of the PEG-Hec Bragg stack barrier film.

■ RESULTS AND DISCUSSION

The synthetic clay Hec spontaneously delaminates without using mechanical force upon immersion into deionized water via 1D dissolution.[38] Even at low concentrations, individual Hec nanosheets with a thickness of 1 nm and a median diameter of 20 μm are held in a coplanar arrangement at a distance fixed by the concentration while electrostatically repelling each other.[39] The large aspect ratio of ~20,000 (Figure 2a, bottom inset) hinders rotation, and a nematic liquid crystalline phase is obtained that shows birefringence (Figure 2a, top inset).[40] When mixing this nematic Hec suspension with PEG, the nematic character of the suspension is preserved, as evidenced by small-angle X-ray scattering (SAXS). Hec nanosheets are separated to large distances, allowing PEG to diffuse between adjacent Hec nanosheets that are cofacially aligned (Figure 2a). Visible basal reflections up to the fourth order emphasize the highly ordered nematic crystalline nature of the ternary suspension. Moreover, the SAXS curve shows a q^{-2} dependence that is characteristic of platelet-like two-dimensional (2D) colloids.[41] This is additionally corroborated by applying a theoretical model of disks with a diameter of 20,000 nm and a thickness of 1 nm that are separated to 40.5 ± 4.5 nm based on a Gaussian distribution (Figure S1).

The barrier laminate was fabricated by subsequent coatings of a PVOH sublayer, the PEG-Hec barrier film, and a PVOH top layer on a poly(ethylene terephthalate) substrate (Figure 2b). The sub and top layers were produced by doctor blading an aqueous formulation (total solid content of 30 wt %)

consisting of PVOH, sorbitol, and glycerol. Sorbitol and glycerol were added as plasticizing agents, allowing high elongations of the sub and top layers for the stretchability experiments. First, the sublayer was coated on the substrate. Subsequently, a nematic suspension (total solid content of 1 wt %, Figure 2a, top inset) composed of Hec and PEG in a weight ratio of 72:28 was spray-coated on top of the dry PVOH sublayer and dried. The applied weight ratio was cross-checked via thermogravimetric analysis (TGA) (Figure S2). In the last step, a sealing layer of PVOH was coated on top of the PEG-Hec nanocomposite barrier film, resulting in a transparent self-standing laminate (Figure 2c). As each spraying cycle only adds a small amount of aqueous suspension on the dry PVOH surface, interdiffusion of Hec into the PVOH coats could be mitigated. Sharp interfaces were observed between the 4 μm thick PEG-Hec barrier film and the sandwiching PVOH layers in scanning electron microscopy (SEM) coupled with energy-dispersive X-ray (EDX) element mapping (Figure 2d).

As previously reported for the applied PEG/Hec ratio,[24] 1D crystalline, monodomain hybrid Bragg stacks are formed via self-assembly during drying of the spray-coated wet coats. The X-ray diffraction (XRD) confirms a 1D periodicity with a basal spacing of d_{001} = 1.8 nm (Figure 3a). PEG layers of 0.8 nm thickness are intercalated between overlapping, adjacent 1 nm thick Hec nanosheets (Figure 3a inset), and a low coefficient of variation of 0.7% indicates a very good crystallinity.[42] Transmission electron microscopy (TEM) images of the Bragg stack barrier film cross sections confirm the superior periodicity and monodomain character (Figure 3b).

Since transparent packaging materials are desired for visual inspection of packaged goods, the optical properties of the self-standing laminate were investigated. The perfect orientation of Hec nanosheets in the direction of the Bragg stack is corroborated by the high transmittance, clarity, and low haze (Figure 3c). Defects in the 1D periodicity caused by the inclusion of folded Hec nanosheets, larger cavities, or general misalignment would lead to scattering. We want to emphasize this as one significant advantage of the barrier laminate presented here compared to metalized and, thus, non-transparent polymer films.

To achieve a 4 μm thick PEG-Hec Bragg stack barrier film, 100 spraying and drying cycles are necessary, which might appear cumbersome. However, we sided with this coating method for three reasons. First, nematic phases of fully delaminated layered silicates of this high-aspect ratio are already honey-viscous at 3 vol %. Although the suspensions show shear thinning,[43] this represents an upper limit for the

111

www.acsami.org
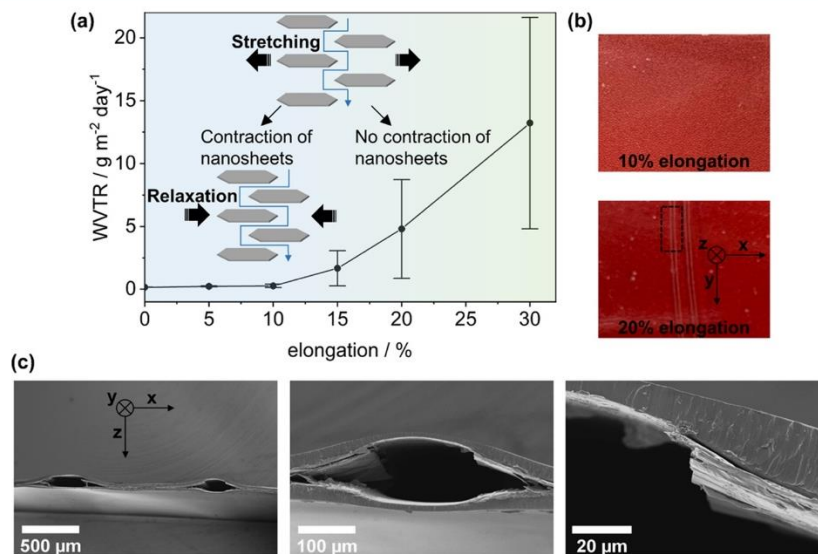
Figure 4. Stretching experiments. (a) WVTR measured at 40 °C and 50% RH as a function of elongation for the self-standing barrier laminate. The inset sketches the Hec nanosheet arrangement within the PEG-Hec Bragg stack barrier layer upon stretching and subsequent relaxation. Below 10% elongation (blueish background), the tortuosity is restored after relaxation, while above 10% elongation, no rearrangement of the tortuous path is observed (greenish background). (b) Photograph with top view (z-direction) of stretched and relaxed self-standing laminate, where x is the direction of stretching. The film elongated by 10% exhibits no defects, while an elongation of 20% causes a fatal rupture. Nanosheets can no longer bridge the macroscopic gap, which acts as pinholes for gas diffusion (dashed rectangle). (c) SEM cross sections (y-direction) of the self-standing laminate elongated by 20%. The sample was prepared from the area marked with a dashed rectangle in (4b). The SEM images display the fatal rupture of the hybrid Bragg stack barrier film in different scales.

concentration regardless of the coating technique, and in any case, >90% water has to be removed. Second, with the low amount of nematic aqueous suspension added for each spraying cycle, drying times are short, which kinetically hinders phase separation within the dry nanocomposite barrier film upon water removal, as recently reported for PVOH and Hec nanocomposite barrier films.[27] Third, spray coating, moreover, prevents the partial dissolution of the water-soluble PVOH sublayer as only a small amount of aqueous suspension is added in each cycle, followed by quick drying. Contrary to this, slot die coating requires much longer drying that triggers an interdiffusion of PVOH sublayer by partial dissolution. As these factors, the degree of order of the nanocomposite and gradient structures at the substrate−nanocomposite interphase developing, will also influence the barrier to some extent, we chose spray coating as the processing method for this study as it facilitates the interpretation of the data. This allows us to study the influence of the perfect hybrid Bragg stack structure of the nanocomposite barrier film as we believe that the alternating layers of PEG and Hec nanosheets that mechanically decouple adjacent silicate nanosheets are crucial to the stretchability, as discussed in detail later. However, barrier films made of nematic Hec suspension fabricated via slot die coating, and industrially benign processing that can easily be transformed to large scale, have already been proven to exhibit extraordinary barrier properties comparable to nanocomposites obtained by spray coating.[27,31,43]

To test for the robustness of the barrier upon dimensional changes of the self-standing laminate, WVTRs were determined at 40 °C and 50% relative humidity (RH) as a function of uniaxial stretching and subsequent relaxation (Table S1). For this, a stretching device built in-house was

used (Figure S3), which allows for mimicking real-world thermoforming involving stretching and shrinking processes. Usually, during thermoforming, the polymer films get heated to a softened state above T_g and then deformed before it is rapidly cooled down to retain the new shape or to allow for relaxation to shrink-wrap around the final item, respectively.[13,15] Hence, the self-standing laminate was clamped in the stretching device and transferred to a heated climate chamber to soften the laminate, followed by the application of a uniaxial elongation. After cooling down, the self-standing laminate was removed from the device, allowing for relaxation and shrinking. We chose plasticized PVOH as the thermoplastic material sandwiching the central barrier film because the laminate can already be softened at relatively low temperatures of 70 °C compared to PP, for example, which requires forming temperatures as high as ∼170 °C.[15] Moreover, the applied climate chamber allows further plasticizing of the hydrophilic barrier laminate with water vapor, which is not feasible with hydrophobic petro-based thermoplastics. In this environment, the neat plasticized PVOH layers can easily be stretched well above 200% elongation. The contribution of the PVOH layers to the total barrier is insignificant. A 20 μm sublayer of plasticized PVOH has a WVTR of 25.4 g m^{-2} day^{-1}, which corresponds to a water vapor permeability (WVP) of 13.7 g mm m^{-2} day^{-1} bar^{-1} by accounting for the sample thickness. By incorporating the PEG-Hec Bragg stack barrier layer, the self-standing laminate with a total thickness of 58 μm attains a WVTR as low as 0.17 g m^{-2} day^{-1}, corresponding to a WVP of 0.3 g mm m^{-2} day^{-1} bar^{-1}. The barrier performance of the laminate is thus assured solely by the central PEG-Hec barrier film.

As already mentioned, the pristine and unstretched (= 0% elongation) self-standing barrier laminate has a WVTR of 0.17 g m^{-2} day^{-1} and is remarkably insensitive to strain (Figure 4a). Up to 15% elongation, the WVTR increases only moderately. For instance, at 10% elongation, the water vapor barrier is still excellent with a WVTR of 0.28 g m^{-2} day^{-1}. This is somewhat surprising since the PEG-Hec barrier film is reported to be brittle and fractures already at approx. 8% of elongation.[24] Apparently, the plasticized PVOH mitigates the catastrophic failure of barrier performance within certain limits (Figure 4b). Even if microcracks should be formed in the brittle Bragg stack film during stretching, the edges are held opposite of each other, and we suppose that upon shrinkage of the PVOH layers upon strain release, they are pressed together, and the tortuosity is restored. This speculation is corroborated by SEM images (Figure S4) of films relaxed after stretching, with no visible defects in the PEG-Hec nanocomposite barrier. Consequently, the good barrier performance is preserved (Figure 4a).

Moreover, the two sandwiching PVOH layers represent a kind of "buffering layers" that alternatively or additionally might explain the tolerance of the barrier system to stretching. Such buffering layers have been shown to improve the flexibility of otherwise nonstretchable thin films or brittle inorganic coatings.[44−46] For instance, it was found for nanometer-thick vapor-deposited SiO$_x$ coatings that an organic silicon sublayer minimized internal stress and improved the barrier properties.[7] Furthermore, the water vapor barrier properties could be maintained upon 10% elongation for a HfO$_2$ thin film made by atomic layer deposition with the support of a polyamide buffering layer providing high tolerance against mechanical stretching.[47] Another approach that can be compared to the "buffer layer" effect is the layer-by-layer assembly of alternating layers of a cationic polymer and negatively charged clay nanosheets that have also been shown to provide stretchability and maintain gas barrier properties upon stretching.[48,49]

Nonetheless, above 15% elongation, the WVTR collapses and increases to 4.80 g m^{-2} day^{-1} at 20% elongation, which is almost 30 times higher than the initial WVTR value. After 20% elongation, fatal macroscopic ruptures perpendicular (= y-direction) to the uniaxial stretching direction (= x-direction) became visible, which no longer "heal" upon shrinkage (Figure 4b). This hypothesis is supported by SEM images of cross sections (z-direction) of one of the fatal ruptures (dashed rectangle) from the 20% elongation sample (Figure 4c). The PEG-Hec barrier film integrity is entirely destroyed, resulting in extended pinholes, which is catastrophic for the barrier performance reflected in the immense surge in the WVTRs and the increasing error at high WVTRs.

In a nutshell, it is assumed that upon stretching the hybrid Bragg stack film, adjacent individual Hec nanosheets slide along the PEG layers, leading to a decrease in the tortuosity. Upon relaxation and below 10% elongation, Hec nanosheets rearrange and rebuild the tortuous path reflected by the constant WVTR values. However, when elongating the hybrid Bragg stack film above 10%, the sliding of adjacent Hec nanosheets becomes irreversible, as indicated by the then substantially increased WVTR values.

A more standardized measurement protocol that reflects real-world conditions is WVTR values obtained at 23 °C and 85% RH after, e.g., DIN EN ISO 15106-3 and ASTM F1249. Hereby, the self-standing laminate with a total thickness of 58

μm exhibits a WVTR of 1.17 g m^{-2} day^{-1}, corresponding to a WVP of 2.8 g mm m^{-2} day^{-1} bar^{-1} that can now be used for comparison with other thermoformable polymer films measured at the same harsh conditions of 85% RH (Table 1). It outperforms commercial petro-based packaging polymers

Table 1. Water Vapor Permeability (WVP) of the Self-Standing Barrier Laminate Compared with Common Polymers Used for Packaging^a

films/polymers	WVP at 23 °C and 85% RH [g mm m^{-2} day^{-1} bar^{-1}]
self-standing barrier laminate (this work)	2.8
poly(vinyl alcohol) (PVOH)[2]	1260
poly(ethylene terephthalate) (PET)[2]	21−84
polypropylene (PP)[2]	8−17
polyethylene (PE)[2]	21−84
poly(vinyl chloride) (PVC)[2]	42−84
poly(lactic acid) (PLA)[6]	158−855

^{a}Values are partially converted from their originally reported units allowing a consistent comparison. Although questioned in literature,[50,51] a linear dependence of WVTR on thickness was assumed.

in terms of WVP like PVC (42−84 g mm m^{-2} day^{-1} bar^{-1}) or PP (8−17 g mm m^{-2} day^{-1} bar^{-1}),[2] which is remarkable considering it is a totally water-soluble laminate obtained from green and aqueous processing. This becomes even more evident by comparison with neat water-soluble PVOH, which exhibits orders of magnitude higher WVP than the self-standing barrier laminate.

■ CONCLUSIONS

Hybrid Bragg stacks composed of transparent ceramic high-aspect ratio nanosheets separated and mechanically decoupled by a soft polymer matrix combine the best of two worlds: superior gas barrier assured by impermeable inorganic nanosheets and stretchability of the mechanically decoupling polymer. As high filler contents as needed for superb barrier performance tend to yield brittle nanocomposite barriers, catastrophic failure at low elongation at break has to be mitigated by laminating the PEG-Hec barrier film between plasticized soft PVOH polymer layers. Besides being auspicious as a flexible packaging material for blister packages in pharmaceuticals or vacuum sealing for food storage, the hybrid Bragg stacks have high potential as flexible barrier liners in ultra-lightweight hydrogen tanks as needed in the automotive industry. Hydrogen-powered vehicles require tanks with liners being impermeable to hydrogen and flexible to minimize external shocks by withstanding structural force exerted on the tank. Lightweight liners made of Hec composites have already demonstrated extraordinary hydrogen barriers,[52] and the additional barrier stretchability presented in this study, making liners of Hec Bragg stacks promising alternatives in tanks such as Type IV composite tanks made of carbon fiber and a thermoplastic polymer liner, which are already being used in vehicles.

■ EXPERIMENTAL SECTION

Materials and Sample Preparation. *Materials.* Sodium fluorohectorite (Hec, [Na$_{0.5}$]^{inter}[Mg$_{2.5}$Li$_{0.5}$]^{oct}[Si$_4$]^{tet}O$_{10}$F$_2$) was synthesized according to a published literature procedure summarized in the supporting information (Section S3).[40,53] Details on the characterization of the synthetic Hec can be found in the supporting

information (Section S4 and Figure S5). Poly(ethylene glycol) (PEG, BioUltra, 10,000 g mol^{-1}, Sigma-Aldrich, Merck KGaA, Germany), poly(vinyl alcohol) (PVOH, Selvol 205, ex Sekisui Chemicals Co., Japan), glycerol (CremerGLYC 3109921, ex Cremer Ole, Germany), and sorbitol (Neosorb P 100 T, Roquette, France) were used without further purification. Poly(ethylene terephthalate) (PET, optimont 501, 36 μm, Bleher Folientechnik GmbH, Germany) foils were used as substrates without further surface treatment.

Sample Preparation. Pristine Hec powder was added to double-distilled water to obtain a 1 wt % suspension and was subsequently placed in an overhead shaker for 5 days to achieve complete delamination into single Hec nanosheets. PEG was dissolved in double-distilled water to obtain a 1 wt % solution. The ternary nematic suspension was produced by immersing the PEG solution into the Hec suspension at the desired weight ratio (72:28 Hec/PEG), yielding a total solid content of 1 wt %.

The PVOH suspension for coating the sub and top layers was produced by adding 24 g PVOH, 3 g glycerol, and 3 g sorbitol to 70 g double-distilled water, yielding a total solid content of 30 wt % and a PVOH/glycerol/sorbitol weight ratio of 80:10:10. The solution was kept at 85 °C under reflux for 2 h while stirring at 200 rpm using a magnetic stirring bar to dissolve all components. Prior to coating, the PVOH solution was homogenized and defoamed under vacuum (50 mbar) for 10 min and up to 2500 rpm using a SpeedMixer DAC 400.2 VAC-P (Hauschild, Germany).

The sub and top layers of PVOH were produced from the 30 wt % PVOH suspension by applying automated doctor blading (ZAA 2300, Zehntner GmbH Testing Instruments, Switzerland). The speed of the blade was set to 15 mm s^{-1}, and the blade height was 250 μm (10 mil). The layers were dried for 30 min at a table temperature of 60 °C. The sublayer was coated onto the PET substrate in the first step.

The central PEG-Hec nanocomposite barrier film was prepared by spray coating. A fully automatic spray coating system that employs a SATA 4000 LAB HVLP 1.0 mm spray gun (SATA GmbH & Co. KG, Germany) was used. The distance between the spray gun and the PVOH sublayer was set to 17 cm. Subsequently, the 1 wt % nematic PEG-Hec suspension was sprayed on the PVOH sublayer where the spraying and nozzle pressure were adjusted to a constant 4 bar. To dry the wet PEG-Hec layer after each cycle, the sample gets moved under infrared lamps having a temperature of 50 °C for 30 min until the evaporation of water is completed. The round-per-flat fan generated ambient air circulation for mild drying conditions. 100 spraying and drying cycles were conducted, and the final PEG-Hec barrier thickness was approx. 4 μm.

In the final step, the top layer of PVOH was coated onto the PEG-Hec nanocomposite barrier film, and a self-supporting laminate was obtained after carefully peeling it off the PET substrate.

Characterization Methods. *Small-Angle X-ray Scattering (SAXS).* SAXS measurements of the nematic suspension were conducted in 1 mm glass capillaries (Hilgenberg, Germany) at room temperature using the system Ganesha Air (SAXSLAB, Xenocs). The system is equipped with a rotating anode copper X-ray source MicroMax 007HF (Rigaku Corp., Japan) and a position-sensitive detector PILATUS 300K (Dectris, Switzerland). The sample-to-detector positions are adjustable, covering a wide range of scattering vectors q. The resulting 1D data ($I(q)$ vs q, with Intensity $I(q)$) are background-corrected. In addition, the birefringence of the suspension was checked with a self-made crossed-polarizer.

Scanning Electron Microscopy (SEM). SEM images of a single Hec nanosheet were recorded with the microscope ZEISS LEO 1530 (Carl Zeiss AG, Germany) operating at 3 kV and equipped with an In-Lens secondary electron detector. The 1 wt % Hec suspension was diluted to 0.001 wt % and drop-cast on a plasma-treated silicon wafer. Subsequently, the sample was sputtered with 1.2 nm of platinum.

SEM images of the self-standing laminate cross sections were recorded with the microscope ZEISS Ultra plus (Carl Zeiss AG, Germany) operating at 5 kV and equipped with an In-Lens and secondary electron detector. The cross sections were obtained by cutting the PET-supported laminate with a scalpel toward the PET side to protect the laminate. Subsequently, the self-standing laminate

was carefully peeled off from PET and sputtered with 1.2 nm of platinum. In addition, the cross sections of the laminate were analyzed via electron dispersive X-ray spectroscopy (EDX) using an UltraDry-EDX detector (Thermo Fisher Scientific).

Thermogravimetric Analysis (TGA). TGA was performed on a Linseis STA PT 1600 (Linseis Messgeräte GmbH, Germany). The samples were dried under vacuum (10^{-3} bar) at 70 °C for 7 days. The dry samples were heated up from room temperature to 1000 °C under an argon atmosphere with a heating rate of 10 °C min^{-1}. For comparison, individual layers and pristine Hec were additionally measured.

X-ray Diffraction (XRD). Diffraction patterns were attained on a Bragg-Brentano-type instrument (Empyrean Malvern Panalytical BV, The Netherlands) applying Cu Kα radiation (λ = 1.54187 Å). The diffractometer is equipped with a PIXcel-1D detector, and the patterns were analyzed using Malvern Panalytical's Highscore Plus software.

Transmission Electron Microscopy (TEM). TEM images of the self-standing laminate cross sections were recorded with the microscope JEOL-JEM-2200FS (JEOL GmbH, Germany). Cross sections were prepared from the peeled-off laminates by applying a JEOL EM-09100IS Cryo Ion Slicer (JEOL GmbH, Germany).

Optical Properties. Optical properties were measured on a BYK-Gardner Haze-Gard Plus (BYK-Gardner GmbH, Germany). An average of five measurements of the self-standing laminate was taken as the reported result for transmittance, haze, and clarity values.

Water Vapor Transmission Rate (WVTR). WVTR values of the self-standing laminate were determined on the system PERMATRAN-W 3/33 (Mocon) at 40 °C and 50% RH or 23 °C and 85% RH, respectively. All samples were sufficiently equilibrated to guarantee moisture conditioning. The permeation area of the film sample was 5 cm^{-2}, and the carrier gas flow (Nitrogen) was set to approx. 10 cm^3 min^{-1}. The barometer works in the mode 'Passed In,' automatically adjusting the pressure on both film sides to 760 mmHg. The principle of the measurement is explained in the Supporting Information (Figure S6 and Section S5).

The stretching experiments were performed on an in-house stretching device, and the self-standing laminate was uniaxially elongated in the x-direction to 5, 10, 15, 20, and 30% (Figure S3). Each elongation point is repeated three times with a new laminate sample, and the statistical average was given as a result (Table S1). Prior to the elongation, the laminate was clamped and equilibrated in a humidity chamber type Memmert HCP105 (Memmert GmbH + Co. KG, Germany) at a temperature of 70 °C and 35% RH for 30 min to soften the outer PVOH layers. For further details, please refer to Figure S3.

Film Thickness. The film thickness obtained from SEM micrographs was cross-checked by employing a high-accuracy digimatic micrometer (Mitutoyo, Japan) with a measuring range of 0−25 mm and a resolution of 0.1 μm.

■ ASSOCIATED CONTENT

🄢 Supporting Information

The Supporting Information is available free of charge at https://pubs.acs.org/doi/10.1021/acsami.3c02504.

> Sketch of the model applied for the SAXS pattern; TGA of the used films and laminates; calculations of expected volume contents and details on the stretching experiments, including WVTR values and SEM images of the stretched laminates; summary of the synthesis of sodium fluorohectorite and details on the characterization of the filler; and measurement principle of a water barrier measurement (PDF)

■ AUTHOR INFORMATION

Corresponding Author

Josef Breu − *Bavarian Polymer Institute and Department of Chemistry, University of Bayreuth, Bayreuth 95447, Germany;* ● orcid.org/0000-0002-2547-3950; Email: josef.breu@uni-bayreuth.de

Authors

Maximilian Röhrl − *Bavarian Polymer Institute and Department of Chemistry, University of Bayreuth, Bayreuth 95447, Germany*

Renee L. Timmins − *Bavarian Polymer Institute and Department of Chemistry, University of Bayreuth, Bayreuth 95447, Germany*

Sabine Rosenfeldt − *Bavarian Polymer Institute and Department of Chemistry, University of Bayreuth, Bayreuth 95447, Germany*

Dominik D. Schuchardt − *Bavarian Polymer Institute and Department of Chemistry, University of Bayreuth, Bayreuth 95447, Germany*

Felix Uhlig − *Bavarian Polymer Institute and Department of Chemistry, University of Bayreuth, Bayreuth 95447, Germany*

Simon Nürmberger − *Bavarian Polymer Institute and Department of Chemistry, University of Bayreuth, Bayreuth 95447, Germany*

Complete contact information is available at:
https://pubs.acs.org/10.1021/acsami.3c02504

Author Contributions

The manuscript was written through contributions of all authors. All authors have given approval to the final version of the manuscript.

Notes

The authors declare no competing financial interest.

■ REFERENCES

(1) *Plastics - the Facts 2021: An Analysis of European Latest Plastics Production, Demand and Waste Data* PlasticsEurope: Brussels, Belgium; 2021.

(2) Lange, J.; Wyser, Y. Recent Innovations in Barrier Technologies for Plastic Packaging-a Review. *Packag. Technol. Sci.* 2003, 16, 149−158.

(3) Khajavi, M. Z.; Ebrahimi, A.; Yousefi, M.; Ahmadi, S.; Farhoodi, M.; Alizadeh, A. M.; Taslikh, M. Strategies for Producing Improved Oxygen Barrier Materials Appropriate for the Food Packaging Sector. *Food Eng. Rev.* 2020, 12, 346−363.

(4) Hirvikorpi, T.; Vähä-Nissi, M.; Harlin, A.; Karppinen, M. Comparison of Some Coating Techniques to Fabricate Barrier Layers on Packaging Materials. *Thin Solid Films* 2010, 518, 5463−5466.

(5) Dukalska, L.; Ungure, E.; Augspole, I.; Muizniece-Brasava, S.; Levkane, V.; Tatjana, R.; Krasnova, I. Evaluation of the Influence of Various Biodegradable Packaging Materials on the Quality and Shelf Life of Different Food Products. *Proc. Latvia Univ. Agric.* 2014, 30, 20−34.

(6) Wu, F.; Misra, M.; Mohanty, A. K. Challenges and New Opportunities on Barrier Performance of Biodegradable Polymers for Sustainable Packaging. *Prog. Polym. Sci.* 2021, 117, No. 101395.

(7) Vassallo, E.; Pedroni, M.; Aloisio, M.; Chen, H.; Firpo, G.; Pietralunga, S. M.; Ripamonti, D. Plasma Deposition to Improve Barrier Performance of Biodegradable and Recyclable Substrates Intended for Food Packaging. *Plasma* 2022, 5, 451−461.

(8) Pilchik, R. Pharmaceutical Blister Packaging. *Pharm. Technol.* 2000, 56−78.

(9) Dhall, R. K.; Sharma, S. R.; Mahajan, B. V. C. Effect of Shrink Wrap Packaging for Maintaining Quality of Cucumber During Storage. *J. Food Sci. Technol.* 2012, 49, 495−499.

(10) Müller, D.; Bonten, C. In *Investigation on the Processability of Sheets for Thermoforming*, Fracture and Damage Mechanics: Theory, Simulation and Experiment; AIP Publishing, 2020; p 020040.

(11) Wittmann, L.-M.; Kurth, K.; Drummer, D. Elongation Behaviour of Filled Semi-Crystalline Polymers in Thermoforming. *Adv. Mater. Process. Technol.* 2020, 6, 647−660.

(12) Münstedt, H.; Kurzbeck, S.; Stange, J. Importance of Elongational Properties of Polymer Melts for Film Blowing and Thermoforming. *Polym. Eng. Sci.* 2006, 46, 1190−1195.

(13) Kellerman, L. S. Moving Fragile Materials. *Collect. Manage.* 1994, 18, 117−128.

(14) White, M. S.; Kaltenbrunner, M.; Głowacki, E. D.; Gutnichenko, K.; Kettlgruber, G.; Graz, I.; Aazou, S.; Ulbricht, C.; Egbe, D. A. M.; Miron, M. C.; Major, Z.; Scharber, M. C.; Sekitani, T.; Someya, T.; Bauer, S.; Sariciftci, N. S. Ultrathin, Highly Flexible and Stretchable Pleds. *Nat. Photonics* 2013, 7, 811−816.

(15) Martin, P. J. 12 - Thermoforming of Polymers. In *Advances in Polymer Processing*; Thomas, S.; Weimin, Y., Eds.; Woodhead Publishing, 2009; pp 352−383.

(16) Giménez, E.; Lagarón, J. M.; Maspoch, M. L.; Cabedo, L.; Saura, J. J. Uniaxial Tensile Behavior and Thermoforming Characteristics of High Barrier Evoh-Based Blends of Interest in Food Packaging. *Polym. Eng. Sci.* 2004, 44, 598−608.

(17) Zadbuke, N.; Shahi, S.; Gulecha, B.; Padalkar, A.; Thube, M. Recent Trends and Future of Pharmaceutical Packaging Technology. *J. Pharm. BioAllied Sci.* 2013, 5, 98−110.

(18) Lacroix, M. Mechanical and Permeability Properties of Edible Films and Coatings for Food and Pharmaceutical Applications. In *Edible Films and Coatings for Food Applications*; Huber, K. C.; Embuscado, M. E., Eds.; Springer New York: New York, NY, 2009; pp 347−366.

(19) Throne, J. 19 - Thermoforming. In *Applied Plastics Engineering Handbook*; Kutz, M., Ed.; William Andrew Publishing: Oxford, 2011; pp 333−358.

(20) Ebina, T. Development of Clay-Based Films. *The Chemical Record* 2018, 18, 1020−1032.

(21) Umemura, Y. 12 - Preparation and Application of Clay Mineral Films. In *Developments in Clay Science*; Schoonheydt, R.; Johnston, C. T.; Bergaya, F., Eds.; Elsevier, 2018; Vol. 9, pp 377−396.

(22) Teepakakorn, A.; Ogawa, M. Interactions of Layered Clay Minerals with Water-Soluble Polymers; Structural Design and Functions. *Appl. Clay Sci.* 2022, 222, No. 106487.

(23) Rolle, K.; Schilling, T.; Westermeier, F.; Das, S.; Breu, J.; Fytas, G. Large Tg Shift in Hybrid Bragg Stacks through Interfacial Slowdown. *Macromolecules* 2021, 54, 2551−2560.

(24) Dörres, T.; Bartkiewicz, M.; Herrmann, K.; Schöttle, M.; Wagner, D.; Wang, Z.; Ikkala, O.; Retsch, M.; Fytas, G.; Breu, J. Nanoscale-Structured Hybrid Bragg Stacks with Orientation- and Composition-Dependent Mechanical and Thermal Transport Properties: Implications for Nacre Mimetics and Heat Management Applications. *ACS Appl. Nano Mater.* 2022, 5, 4119−4129.

115

(25) Wang, Z.; Rolle, K.; Schilling, T.; Hummel, P.; Philipp, A.; Kopera, B. A. F.; Lechner, A. M.; Retsch, M.; Breu, J.; Fytas, G. Tunable Thermoelastic Anisotropy in Hybrid Bragg Stacks with Extreme Polymer Confinement. *Angew. Chem., Int. Ed.* **2020**, *59*, 1286−1294.

(26) Ding, F.; Liu, J.; Zeng, S.; Xia, Y.; Wells, K. M.; Nieh, M.-P.; Sun, L. Biomimetic Nanocoatings with Exceptional Mechanical, Barrier, and Flame-Retardant Properties from Large-Scale One-Step Coassembly. *Sci. Adv.* **2017**, *3*, No. e1701212.

(27) Röhrl, M.; Federer, L. K. S.; Timmins, R. L.; Rosenfeldt, S.; Dörres, T.; Habel, C.; Breu, J. Disorder−Order Transition-Improving the Moisture Sensitivity of Waterborne Nanocomposite Barriers. *ACS Appl. Mater. Interfaces* **2021**, *13*, 48101−48109.

(28) Schiessl, S.; Kucukpinar, E.; Cros, S.; Miesbauer, O.; Langowski, H.-C.; Eisner, P. Nanocomposite Coatings Based on Polyvinyl Alcohol and Montmorillonite for High-Barrier Food Packaging. *Front. Nutr.* **2022**, *9*, No. 790157.

(29) Schilling, T.; Habel, C.; Rosenfeldt, S.; Röhrl, M.; Breu, J. Impact of Ultraconfinement on Composite Barriers. *ACS Appl. Polym. Mater.* **2020**, *2*, 3010−3015.

(30) Eckert, A.; Rudolph, T.; Guo, J.; Mang, T.; Walther, A. Exceptionally Ductile and Tough Biomimetic Artificial Nacre with Gas Barrier Function. *Adv. Mater.* **2018**, *30*, No. 1802477.

(31) Timmins, R. L.; Kumar, A.; Röhrl, M.; Havlíček, K.; Agarwal, S.; Breu, J. High Barrier Nanocomposite Film with Accelerated Biodegradation by Clay Swelling Induced Fragmentation. *Macromol. Mater. Eng.* **2021**, *307*, No. 2100727.

(32) Song, Y.; Gerringer, J.; Qin, S.; Grunlan, J. C. High Oxygen Barrier Thin Film from Aqueous Polymer/Clay Slurry. *Ind. Eng. Chem. Res.* **2018**, *57*, 6904−6909.

(33) Cussler, E. L.; Hughes, S. E.; Ward, W. J.; Aris, R. Barrier Membranes. *J. Membr. Sci.* **1988**, *38*, 161−174.

(34) DeRocher, J. P.; Gettelfinger, B. T.; Wang, J.; Nuxoll, E. E.; Cussler, E. L. Barrier Membranes with Different Sizes of Aligned Flakes. *J. Membr. Sci.* **2005**, *254*, 21−30.

(35) Rajeev, R. S.; Harkin-Jones, E.; Soon, K.; McNally, T.; Menary, G.; Armstrong, C. G.; Martin, P. J. A Method to Study the Dispersion and Orientation of Nanoclay Tactoids in Pet Matrix-Focused Ion Beam Milling Combined with Electron Microscopy. *Mater. Lett.* **2008**, *62*, 4118−4120.

(36) Shen, Y.; Harkin-Jones, E.; Hornsby, P.; McNally, T.; Abu-Zurayk, R. The Effect of Temperature and Strain Rate on the Deformation Behaviour, Structure Development and Properties of Biaxially Stretched Pet−Clay Nanocomposites. *Compos. Sci. Technol.* **2011**, *71*, 758−764.

(37) Harkin-Jones, E.; Figiel, L.; Spencer, P.; Abu-Zurayk, R.; Al-Shabib, W.; Chan, V.; Rajeev, R.; Soon, K.; Buckley, P.; Sweeney, J.; Menary, G.; Armstrong, C.; Assender, H.; Coates, P.; Dunne, F.; McNally, T.; Martin, P. Performance Enhancement of Polymer Nanocomposites Via Multiscale Modelling of Processing and Properties. *Plast., Rubber Compos.* **2008**, *37*, 113−123.

(38) Dudko, V.; Khoruzhenko, O.; Weiß, S.; Daab, M.; Loch, P.; Schwieger, W.; Breu, J. Repulsive Osmotic Delamination: 1d Dissolution of 2d Materials. *Adv. Mater. Technol.* **2023**, *8*, No. 2200553.

(39) Rosenfeldt, S.; Stöter, M.; Schlenk, M.; Martin, T.; Albuquerque, R. Q.; Förster, S.; Breu, J. In-Depth Insights into the Key Steps of Delamination of Charged 2d Nanomaterials. *Langmuir* **2016**, *32*, 10582−10588.

(40) Stöter, M.; Kunz, D. A.; Schmidt, M.; Hirsemann, D.; Kalo, H.; Putz, B.; Senker, J.; Breu, J. Nanoplatelets of Sodium Hectorite Showing Aspect Ratios of ≈20 000 and Superior Purity. *Langmuir* **2013**, *29*, 1280−1285.

(41) Boldon, L.; Laliberte, F.; Liu, L. Review of the Fundamental Theories Behind Small Angle X-Ray Scattering, Molecular Dynamics Simulations, and Relevant Integrated Application. *Nano Rev* **2015**, *6*, No. 25661.

(42) Moore, D. M.; Reynolds, R. C. *X-ray Diffraction and the Identification and Analysis of Clay Minerals*; Oxford university press: Oxford, 1989; Vol. 322.

(43) Röhrl, M.; Mettke, J. H.; Rosenfeldt, S.; Schmalz, H.; Mansfeld, U.; Timmins, R. L.; Habel, C.; Breu, J.; Durst, F. Shear Orientation of Nematic Phases of Clay Nanosheets: Processing of Barrier Coatings. *J. Coat. Technol. Res.* **2021**, *19*, 487−495.

(44) Abadias, G.; Chason, E.; Keckes, J.; Sebastiani, M.; Thompson, G. B.; Barthel, E.; Doll, G. L.; Murray, C. E.; Stoessel, C. H.; Martinu, L. Review Article: Stress in Thin Films and Coatings: Current Status, Challenges, and Prospects. *J. Vac. Sci. Technol., A* **2018**, *36*, No. 020801.

(45) Yu, Z.-n.; Zhao, J.-j.; Xia, F.; Lin, Z.-j.; Zhang, D.-p.; Leng, J.; Xue, W. Enhanced Electrical Stability of Flexible Indium Tin Oxide Films Prepared on Stripe Sio2 Buffer Layer-Coated Polymer Substrates by Magnetron Sputtering. *Appl. Surf. Sci.* **2011**, *257*, 4807−4810.

(46) Liu, D.-S.; Wu, C.-Y. Adhesion Enhancement of Hard Coatings Deposited on Flexible Plastic Substrates Using an Interfacial Buffer Layer. *J. Phys. D: Appl. Phys.* **2010**, *43*, No. 175301.

(47) Tseng, M.-H.; Su, D.-Y.; Chen, G.-L.; Tsai, F.-Y. Nano-Laminated Metal Oxides/Polyamide Stretchable Moisture- and Gas-Barrier Films by Integrated Atomic/Molecular Layer Deposition. *ACS Appl. Mater. Interfaces* **2021**, *13*, 27392−27399.

(48) Holder, K. M.; Spears, B. R.; Huff, M. E.; Priolo, M. A.; Harth, E.; Grunlan, J. C. Stretchable Gas Barrier Achieved with Partially Hydrogen-Bonded Multilayer Nanocoating. *Macromol. Rapid Commun.* **2014**, *35*, 960−964.

(49) Qin, S.; Song, Y.; Floto, M. E.; Grunlan, J. C. Combined High Stretchability and Gas Barrier in Hydrogen-Bonded Multilayer Nanobrick Wall Thin Films. *ACS Appl. Mater. Interfaces* **2017**, *9*, 7903−7907.

(50) Tsurko, E. S.; Feicht, P.; Habel, C.; Schilling, T.; Daab, M.; Rosenfeldt, S.; Breu, J. Can High Oxygen and Water Vapor Barrier Nanocomposite Coatings Be Obtained with a Waterborne Formulation? *J. Membr. Sci.* **2017**, *540*, 212−218.

(51) Xianda, Y.; Anlai, W.; Suqin, C. Water-Vapor Permeability of Polyvinyl Alcohol Films. *Desalination* **1987**, *62*, 293−297.

(52) Habel, C.; Tsurko, E. S.; Timmins, R. L.; Hutschreuther, J.; Kunz, R.; Schuchardt, D. D.; Rosenfeldt, S.; Altstädt, V.; Breu, J. Lightweight Ultra-High-Barrier Liners for Helium and Hydrogen. *ACS Nano* **2020**, *14*, 7018−7024.

(53) Kalo, H.; Möller, M. W.; Ziadeh, M.; Dolejš, D.; Breu, J. Large Scale Melt Synthesis in an Open Crucible of Na-Fluorohectorite with Superb Charge Homogeneity and Particle Size. *Appl. Clay Sci.* **2010**, *48*, 39−45.

Supporting information

Stretchable clay nanocomposite barrier film for flexible packaging

Maximilian Röhrl, Renee L. Timmins, Sabine Rosenfeldt, Dominik D. Schuchardt, Felix Uhlig, Simon Nürmberger, and Josef Breu*

*Corresponding author (Josef.Breu@uni-bayreuth.de)

Bavarian Polymer Institute and Department of Chemistry, University of Bayreuth, Bayreuth 95447, Germany

Keywords: nanocomposite barrier, vacuum-sealed packaging, hydrogen tank, flexible barrier, stretchability
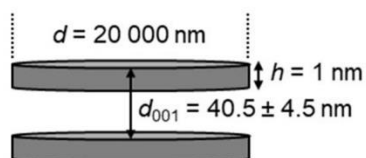
Figure S1. Applied model for the theoritical calculcation of the SAXS curve. In this assumption, the disks have a diameter d of 20 000 nm ($\pm$ 15%) and a thickness h of 1 nm ($\pm$3 %) and are separated to 40.5 $\pm$ 4.5 nm using a Gauss distribution.

1
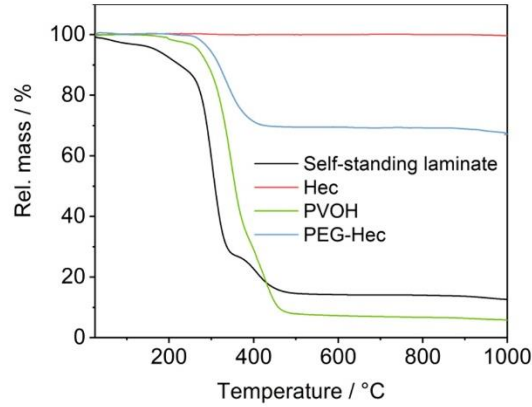
Figure S2. Thermogravimetric Analysis (TGA). TGA curve of the self-standing laminate (black). For comparison neat sodium fluorohectorite (Hec) (red), the neat polyethylene glycol (PEG)-Hec nanocomposite barrier film (blue), and the neat plasticized polyvinyl alcohol (PVOH) sub/top layer (green) are additionally depicted. Mass loss below 100 °C can be attributed to residual water in the films. Around 200 °C, the sub/top layer of PVOH starts to thermally degrade (green). In addition, the intercalated PEG in the Bragg Stacks begins to thermally degrade at 350 °C (blue). The synthetic clay Hec shows no thermal degradation (red).

Section S1. Calculation of the volume content of 1 nm thick Hec nanosheets $\varphi(Hec)$ and volume content of PEG $\varphi(PEG)$ in the dry hybrid Bragg stack barrier based on the basal spacing d_{001}

$$\varphi(Hec) \approx \frac{1\ nm}{d_{001}} \approx \frac{1\ nm}{1.8\ nm} \approx 0.55 \qquad \text{(E S1)}$$

$$\varphi(PEG) \approx 1 - 0.55 \approx 0.45 \qquad \text{(E S2)}$$

Section S2. Conversion of weight content to volume content of Hec in PEG-Hec films with $\rho(PEG) = 1.2\ g/cm^3$, $\rho(Hec) = 2.7\ g/cm^3$ as the respective densities and the weight content of 72 wt% Hec in the dry hybrid Bragg stack barrier film;

$$\varphi(Hec) = \frac{wt\%\ (Hec) \cdot \rho(PEG)}{wt\%\ (Hec) \cdot \rho(PEG) + \cdot \left(100\ wt\% - wt\%\ (Hec)\right) \cdot \rho(PEG)} = 0.53 \qquad \text{(E S3)}$$

2

Table S1. Water vapor transmission rates (WVTR) at 40 °C and 50% RH for the self-standing barrier laminate obtained after the respective elongation experiment. Each elongation experiment is repeated three times and subsequently the WVTRs are measured and individual values averaged.

Elongation / %	WVTR / g m^{-2} day^{-1}	Error / g m^{-2} day^{-1}
0	0.17	0.00
5	0.23	0.04
10	0.28	0.14
15	1.67	1.40
20	4.80	3.93
30	13.22	8.41
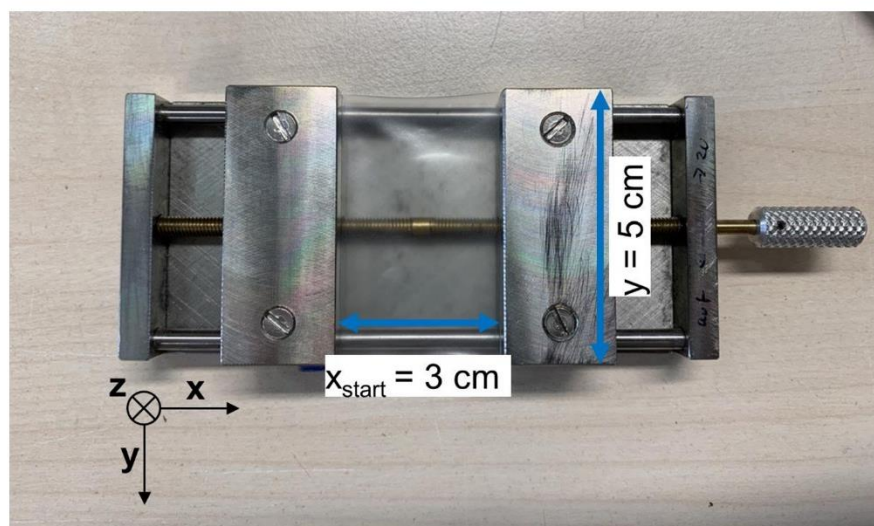
Figure S3. Principle of stretching experiments with an in-house made stretching device. In a first step, each sample is cut with a template (x = 4.5 cm, y = 5 cm) and clamped within the roughened brackets (each side by 0.75 cm in x-direction). The starting area is 3 cm in x-direction and 5 cm in y-direction. After equilibration, the sample is stretched in x-direction to the respective elongation point. Afterwards, the sample is carefully removed and allowed for relaxation in x-direction. The stretchable sub and top polyvinyl alcohol layer contracts to a certain extent. For the next measuring point, a new sample is prepared and the procedure is repeated.

3
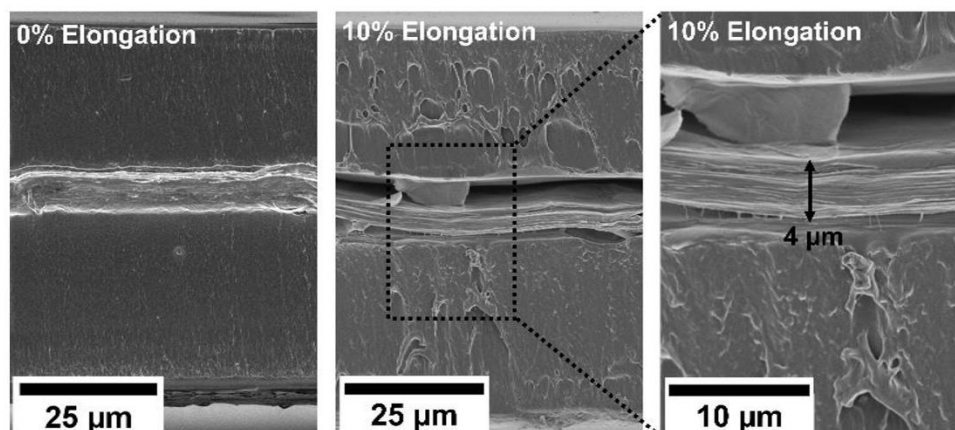
Figure S4. Scanning electron microscope images of cross-sections of the self-standing barrier laminates upon stretching and shrinkage. Upon 10% elongation and shrinkage, the 4 μm PEG-Hec barrier film exhibits no fractures or changes in dimensions, and consequently, the tortuosity is restored after shrinkage. Solely, the top layer of PVOH slightly detaches from the PEG-Hec barrier film.

Section S3. Summary of synthesis of the synthetic filler sodium fluorohectorite (Hec).

The high-purity reagents of SiO_2 (Merck, fine granular, washed and calcined quartz pa), LiF (ChemPur, 99.9%, powder), MgF_2 (ChemPur, 99.9%, 3-6 mm pieces), MgO (Alfa Aesar, 99.95%, 1-3 mm fused lumps) and NaF (Alfa Aesar, 99.995%, powder) were carefully weighed out in line with the composition corresponding to the formula ($[Na_{0.5}]^{inter}[Mg_{2.5}Li_{0.5}]^{oct}[Si_4]^{tet}O_{10}F_2$).

For cleaning purposes, a molybdenum crucible is heated to 1600°C inside a quartz tube under vacuum using a copper high-frequency induction coil. Once cleaned, the crucible is filled with reagents within an argon glovebox, and residual water is removed by heating the crucible to 1200°C in the quartz tube under vacuum. The crucible is then sealed with a molybdenum lid by heating it to the melting point of molybdenum within the copper induction coil. To synthesize Hec, the crucible is placed horizontally in a graphite furnace and rotated at 1750°C for 80 minutes under an argon atmosphere. After cooling and quenching, the synthesized Hec is ground using a planetary ball mill and dried under vacuum at 250°C for 14 hours. The dried Hec is then filled into a cleaned molybdenum crucible within an argon glovebox and sealed again within the copper induction coil. Finally, to increase the homogeneity of Hec, the crucible is placed inside an evacuated quartz ampule and annealed in a chamber furnace for 6 weeks at 1045°C.

4

Section S4. Characterization of the synthetic filler sodium fluorohectorite (Hec).

Section S4.1 Experimental

Cation exchange capacity (CEC). The CEC of Hec was determined with the $[Cu(trien)]^{2+}$ method.[1] After the exchange procedure, the supernatant was analyzed by UV/Vis spectroscopy using a Varian Cary 300 Scan spectrophotometer.

Layer charge determination.

The layer charge of Hec was determined according to Lagaly.[2] Alkylammonium chloride ($C_nH_{2n+1}NH_3^+Cl^-$) solutions, with alkyl chain lengths ranging from C_4-C_8, were adjusted to a pH of 8 and blended with Hec. The Hec was exchanged 3 times with 3 mL of respective amine solutions. After the quantitative exchange, the Hec was separated by centrifugation and washed 6 times with ethanol-water mixture (1:1) and 4 times with pure ethanol. After drying, the basal spacing of a complete series of alkylammonium derivatives was monitored by X-Ray diffraction.

Fourier-transform infrared spectroscopy (FTIR).

An FTIR spectrum of Hec was recorded by employing a Jasco FTIR 6100 spectrometer. The spectrum was recorded for the region 4000-400 cm^{-1} with a resolution of 4 cm^{-1}. The observed vibration bands are in-line with previously published FTIR spectra of Hec.[3]
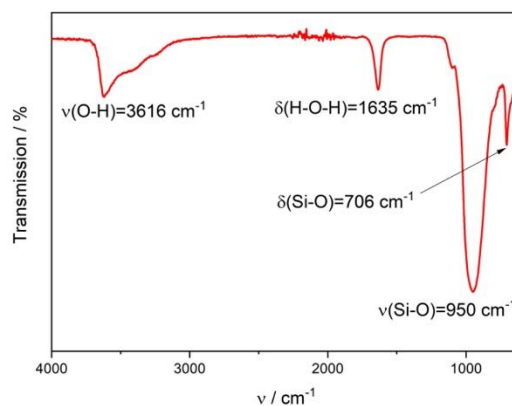
Figure S5. FTIR spectrum of the neat sodium fluorohectorite.

Section S4.2 Results and Discussion

The synthetic Hec features a cation exchange capacity of 1.27 mmol g^{-1}, and the layer charge x can be narrowed down to ~0.5 < x < 0.54, which is in excellent agreement with previously published values.[4,5] FTIR spectroscopy revealed vibration bands assigned to Hec that align with previously investigated FTIR spectra of Hec.[3] The particular synthesis route followed by long-term annealing yields a cation composition of $[Na_{0.48}]^{inter}[Mg_{2.57}Li_{0.47}]^{oct}[Si_4]^{tet}$ that is close to the target composition.[4] Adsorption isotherms of Hec with Ar revealed a non-porous structure with a BET surface as low as 4 m^2 g^{-1}, i.e., Ar or N_2 with a similar kinetic diameter has no access to the interlayer surfaces in the collapsed state.[6] However, in the delaminated state, as

5

121

applied in this work, by neglecting the edges of high-aspect-ratio Hec nanosheets, a surface of ~744 m^2 g^{-1} is available, which can be approximated from crystallographic data.[4]
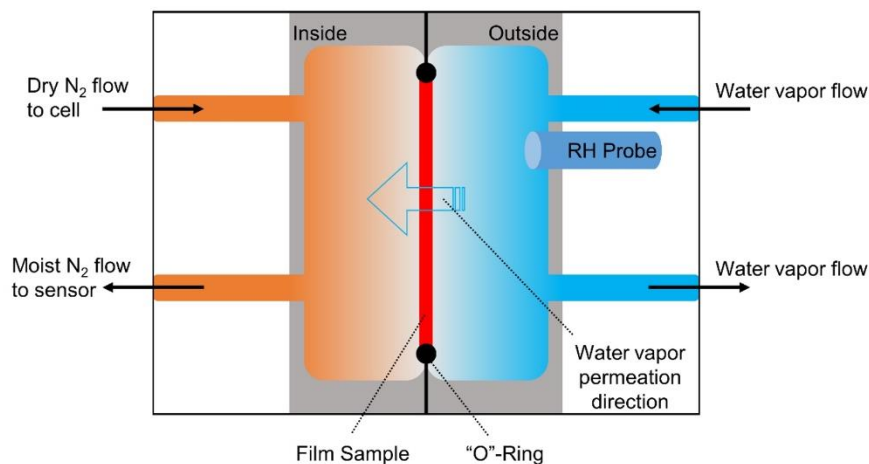
Figure S6. Principle of a water vapor barrier measurement using the system PERMATRAN-W 3/33 (Mocon, US). The system employs a patented modulated infrared sensor to detect water vapor transmission in both flat materials and packages with exceptional sensitivity in parts per million. During testing, the flat film sample is placed in a test cell divided into two chambers separated by the sample material. The outer chamber is filled with water vapor (test gas), while the inner chamber is filled with nitrogen (carrier gas). A relative humidity (RH) probe controls the RH in the outer chamber. The O-Ring seals the film sample with the chambers. The water molecules, delivered to the outer chamber by the test gas, permeate through the film to the inner chamber and are conveyed to the sensor by the carrier gas. The computer monitors the increase in water vapor concentration in the carrier gas and reports the value on the screen as the water vapor transmission rate (WVTR).

Section S5. Conversion of WVTR to water vapor permeability (WVP) with d_{film} as the thickness of the film and Δp as the partial pressure difference of water vapor between the outer and inner chamber. The WVP calculation is shown for the measurement at 23 °C and 85 %RH with a vapor pressure of water of $p(H_2O) = 0.0281$ bar at 23 °C.

$$WVP = \frac{WVTR \cdot d_{film}}{\Delta p} = \frac{1.17 \, \mathrm{g \, m^{-2} day^{-1}} \cdot 0.058 \, \mathrm{mm}}{0.024 \, \mathrm{bar}} = 2.8 \, \mathrm{g \, mm \, m^{-2} day^{-1} bar^{-1}} \quad \text{(E S4)}$$

$$\Delta p = [p_{Outside}(H_2O) - p_{Inside}(H_2O)] \quad \text{(E S5)}$$

$$p_{Outside}(H_2O) = RH \cdot p(H_2O) = 0.85 \cdot 0.0281 \, \mathrm{bar} \quad \text{(E S6)}$$

$$p_{Inside}(H_2O) = RH \cdot p(H_2O) = 0 \cdot 0.0281 \, \mathrm{bar} \quad \text{(E S7)}$$

6

Literature

1.   Ammann, L.; Bergaya, F.; Lagaly, G., Determination of the cation exchange capacity of clays with copper complexes revisited. *Clay Minerals* **2005,** *40* (4), 441-453.
2.   Mermut, A. R.; Lagaly, G., Baseline studies of the clay minerals society source clays: Layer-charge determination and characteristics of those minerals containing 2:1 layers. *Clays and Clay Minerals* **2001,** *49* (5), 393-397.
3.   Schuchardt, D.; Röhrl, M.; Rosenfeldt, S.; Breu, J., Gas Barriers from In Situ Polymerized Poly(ethylene glycol) Diacrylate Clay Nanocomposites for Food Packaging. *ACS Applied Polymer Materials* **2023,** *5* (1), 576-582.
4.   Stöter, M.; Kunz, D. A.; Schmidt, M.; Hirsemann, D.; Kalo, H.; Putz, B.; Senker, J.; Breu, J., Nanoplatelets of Sodium Hectorite Showing Aspect Ratios of ≈20 000 and Superior Purity. *Langmuir* **2013,** *29* (4), 1280-1285.
5.   Dörres, T.; Bartkiewicz, M.; Herrmann, K.; Schöttle, M.; Wagner, D.; Wang, Z.; Ikkala, O.; Retsch, M.; Fytas, G.; Breu, J., Nanoscale-Structured Hybrid Bragg Stacks with Orientation- and Composition-Dependent Mechanical and Thermal Transport Properties: Implications for Nacre Mimetics and Heat Management Applications. *ACS Applied Nano Materials* **2022,** *5* (3), 4119-4129.
6.   Ament, K.; Köwitsch, N.; Hou, D.; Götsch, T.; Kröhnert, J.; Heard, C. J.; Trunschke, A.; Lunkenbein, T.; Armbrüster, M.; Breu, J., Nanoparticles Supported on Sub-Nanometer Oxide Films: Scaling Model Systems to Bulk Materials. *Angewandte Chemie International Edition* **2021,** *60* (11), 5890-5897.
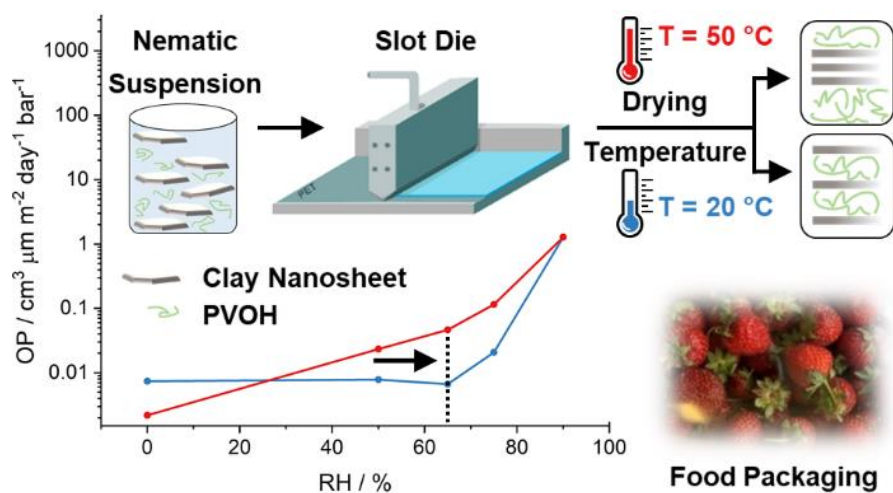
6.5 Disorder-order transition – Improving the moisture sensitivity of waterborne nanocomposite barriers

Authors: Maximilian Röhrl, Lukas K. S. Federer, Renee L. Timmins, Sabine Rosenfeldt, Theresa Dörres, Christoph Habel, and Josef Breu

Research Article

Disorder−Order Transition—Improving the Moisture Sensitivity of Waterborne Nanocomposite Barriers

Maximilian Röhrl, Lukas K. S. Federer, Renee L. Timmins, Sabine Rosenfeldt, Theresa Dörres, Christoph Habel, and Josef Breu*

Read Online

ACCESS | 📊 Metrics & More | 📖 Article Recommendations | 🆂�ᵢ Supporting Information

ABSTRACT: Systematic studies on the influence of crystalline vs disordered nanocomposite structures on barrier properties and water vapor sensitivity are scarce as it is difficult to switch between the two morphologies without changing other critical parameters. By combining water-soluble poly(vinyl alcohol) (PVOH) and ultrahigh aspect ratio synthetic sodium fluorohectorite (Hec) as filler, we were able to fabricate nanocomposites from a single nematic aqueous suspension by slot die coating that, depending on the drying temperature, forms different desired morphologies. Increasing the drying temperature from 20 to 50 °C for the same formulation triggers phase segregation and disordered nanocomposites are obtained, while at room temperature, one-dimensional (1D) crystalline, intercalated hybrid Bragg Stacks form. The onset of swelling of the crystalline morphology is pushed to significantly higher relative humidity (RH). This disorder−order transition renders PVOH/Hec a promising barrier material at RH of up to 65%, which is relevant for food packaging. The oxygen permeability (OP) of the 1D crystalline PVOH/Hec is an order of magnitude lower compared to the OP of the disordered nanocomposite at this elevated RH (OP = 0.007 cm^3 μm m^{-2} day^{-1} bar^{-1} cf. OP = 0.047 cm^3 μm m^{-2} day^{-1} bar^{-1} at 23 °C and 65% RH).

KEYWORDS: *Cussler, clay, slot die coating, water vapor and oxygen permeability, food packaging*
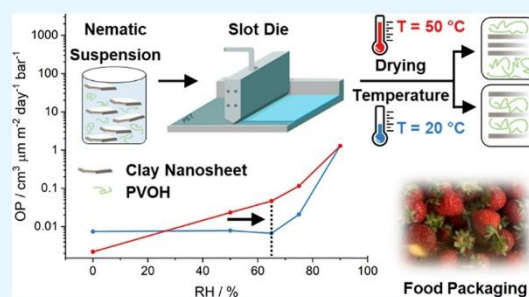
INTRODUCTION

In 2019, the total European plastic converters' demand was 50.7 million tons of plastics, with packaging and electronics sectors sharing almost 50% of the end-use market.[1] Particularly for food packaging, materials are desired to be metal-free, transparent, flexible, and protective against gas permeation.[2,3] The shelf life of packaged groceries is limited by the permeability of the packaging as, for instance, oxygen fosters microbiological spoilage,[4] while water vapor renders crisp products stale.

Poly(vinyl alcohol) (PVOH) is a commercial, affordable, water-soluble, and biodegradable polymer that moreover is approved for food contact by the Food and Drug Administration.[5,6] Its high water solubility furthermore allows for eco-friendly waterborne processing by solution casting.[7] Moreover, at low relative humidity (RH), PVOH possesses good barrier properties with oxygen permeabilities (OP) as low as 0.09 cm^3 μm m^{-2} day^{-1} bar^{-1} in the dry state (Table S3). This excellent performance can be attributed to strong inter- and intramolecular hydrogen bonds between the highly polar hydroxyl (OH) groups.[8] At a threshold humidity around 55%, however, swelling sets in, and the incorporated water molecules break the inter- and intramolecular hydrogen

bonds,[9,10] which increases segment mobility to a great extent.[11] Thus, the OP of a PVOH film increases by 600% when increasing the RH from 0 to 80%,[12] and PVOH becomes a poor barrier at high RH. Additionally, the swelling increases the solubility of water molecules. As the permeability (P) of a barrier film can be expressed by $P = S \times D$, where S is the solubility and D is the diffusivity parameter of the permeate,[13] the increase of H_2O concentration in the PVOH film not only increases OP but also concomitantly the water vapor permeability. Thus, as barrier properties deteriorate with increasing RH, the barrier at 65% RH is more relevant for food packaging. Consequently, barriers measured at ≤50% RH, which is below the threshold of PVOH swelling, are misleading and irrelevant. In the same line, pushing the swelling threshold to higher RH values is highly desired, as this will enable wider usage of PVOH.

48101
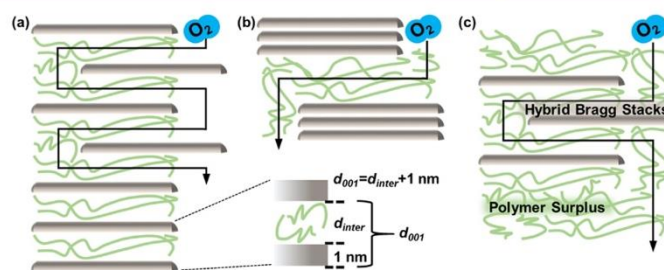
Figure 1. Different types of polymer-clay nanocomposites. (a) Ideal hybrid Bragg stacks of periodically alternating clay nanosheets and polymer layers. The d_{001} is given by the sum of 1 nm thick nanosheets and d_{inter} the interlayer space filled by the polymer severely confined between the clay nanosheets as shown in the inset. (b) Complete phase segregation producing separated clay-only and polymer domains. (c) Composite of segregated intercalated, 1D crystalline Bragg stacks in surplus of the polymer matrix. In addition, a sketch of the tortuous path for an oxygen molecule is explicitly shown displaying the difference in the diffusion pathway depending on the type of nanocomposite structure.

To counteract the moisture sensitivity of commercial PVOH packages in terms of barrier performance, they are either laminated, e.g., with polyethylene, or copolymerized with more hydrophobic monomers, such as ethylene vinyl alcohol (EVOH).[14,15] Especially for EVOH, the hydrophobicity, and hence the onset of swelling, can easily be fine-tuned by adjusting the ethylene content.[10,16]

It has long been established that by compounding of impermeable silicate layers (clay) into a polymer P can be decreased by several orders of magnitude via elongating the diffusion pathway (Figure 1).[17−22] P depends nonlinearly on the aspect ratio α and filler content φ of the platelet-like filler

$$P_{rel} = \frac{P}{P_0} = \left(1 + \mu\left(\frac{\alpha^2\varphi^2}{1-\varphi}\right)\right)^{-1} \quad (1)$$

with P being the permeability of the filled polymer matrix, P_0 the permeability of the neat polymer matrix, and μ being a geometrical factor depending on the shape of the filler.[23] However, we more recently found that in addition to reducing permeability, the threshold humidity for the onset of swelling can be increased by arranging the filler periodically into one-dimensional (1D) crystalline films.[24] Alternatively, it was found for a poly(vinylpyrrolidone) (PVP) nanocomposite that by increasing the filler content, P can be reduced beyond what is expected from Cussler's tortuous path theory (eq 1),[25] suggesting that increasing confinement of the polymer also hampers swelling and renders the nanocomposite more hydrophobic.[26]

Clay and PVOH-based nanocomposites show exceptional mechanical,[27−29] flame-retardant,[30,31] and barrier properties.[32−34] However, the literature regarding the issue of segregated vs the 1D crystalline, intercalated nature (Figure 1) of clay/PVOH nanocomposites is contradictory. While both hydrophilic clays and PVOH are dispersible/soluble and hence perfectly miscible in water, some reports found complete phase segregation being triggered upon drying.[33,35] The segregation produces restacked clay-only aggregates (Figure 1b) as indicated by interlayer distances corresponding to the pristine clay filler. Although this phase segregation is apparently driven by thermodynamics, the kinetics limit it to small length scales as the diffusion of PVOH becomes increasingly more difficult with the tortuous path building up upon solvent removal. In any case, the restacking reduces the effective aspect ratio, which according to Cussler, will hamper the barrier potential of the filler. The majority of reports, however, observed

intercalated nanocomposite structures where PVOH is incorporated between the clay nanosheets producing basal spacings clearly exceeding the pristine clay spacing. The intercalated morphology was observed for clay/PVOH nanocomposites fabricated by various solvent casting methods such as dip coating,[31,36] doctor blading,[27] or film casting.[28,37,38] It should be mentioned that, nevertheless, most reported intercalated clay/PVOH nanocomposites are biphasic. As the ideal intercalated phase requires a well-defined volume ratio of clay to PVOH, this ratio needs to be iteratively identified to obtain a single-phase intercalated material. The composite with the correct volume ratio of clay to PVOH represents hybrid Bragg Stacks (Figure 1a).[39−41] Whenever this ratio is not optimized, nanocomposites are obtained, where the intercalated hybrid phase is actually embedded into the surplus of the polymer matrix (Figure 1c).

In this paper, we report the fabrication of both morphologies (Figure 1a,b) composed of PVOH as the polymer matrix and synthetic sodium fluorohectorite (Hec) nanosheets as fillers from a single nematic aqueous suspension using a highly scalable slot die coating process. Furthermore, we show that the type of nanocomposite can simply be switched from intercalated to completely phase segregated by increasing the drying temperature. This allows us for the first time to evaluate the impact of 1D crystallinity on oxygen and water vapor permeability, while keeping the nature of the filler, aspect ratio (α), filler content (φ), and processing constant. Crystallinity was found to clearly push the onset of swelling by water vapor to higher RH.

■ RESULTS AND DISCUSSION

The synthetic clay sodium fluorohectorite (Hec) shows the phenomenon of repulsive osmotic swelling.[42] By immersing Hec in deionized water, delamination is thermodynamically driven by simple hydration of the interlayer sodium cation. Generally, overcoming the attractive layer interactions requires the separation of adjacent Hec layers by hydration to a certain distance (Gouy−Chapman length).[43] At this point, the layer interactions become repulsive, allowing to gently delaminate the material into single Hec nanosheets of 1 nm thickness.[43] This soft top-down procedure provides nanosheets with a lateral diameter of 20 μm yielding an ultrahigh aspect ratio of ~20 000 (Figure 2a inset).[44] Even at low concentrations (<1 vol %) of aqueous Hec suspensions, this extraordinary aspect ratio hinders rotation of adjacent negatively charged Hec nanosheets and forces them to adopt a cofacial arrangement
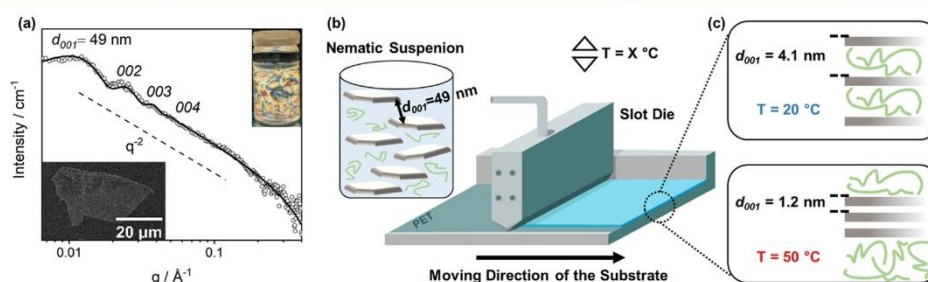
Figure 2. Sketch of the processing method. (a) 1D SAXS pattern indicates a homogeneous aqueous suspension composed of PVOH and single Hec nanosheets that are uniformly separated by 49 nm (O, measured; -, calculated). To increase the signal-to-noise ratio of the SAXS pattern, the suspension (5 wt % total solid content) was centrifuged to obtain a concentrated gel (∼8 wt % corresponding to ∼5 vol % total solid content). The insets show birefringence of the diluted nematic ternary suspension between crossed polarizers and a scanning electron micrograph (SEM) of an individual Hec nanosheet with a diameter of >20 μm. (b) The nematic suspension was slot die coated on a corona-treated poly(ethylene terephthalate) (PET) foil. (c) Depending on the drying temperature $T = X$ °C of the wet coating, upon solvent removal, the constituents either self-assemble into single domain hybrid Bragg stacks or completely phase-segregated composites. At $T = 20$ °C, 1D ordered single domain films of Bragg stacks are obtained with a periodicity of 4.1 nm comprised of a 3.1 nm thick PVOH layer being confined between 1 nm thick clay nanosheets. Raising the drying temperature to 50 °C leads completely to phase-segregated nanocomposites comprised of clay-only domains with a periodicity of 1.2 nm.

due to the strong electrostatic repulsion. Consequently, nematic liquid crystalline phases are obtained.[43] Mixing an aqueous solution of PVOH and delaminated Hec nanosheets results in a translationally homogeneous phase with individual Hec nanosheets separated to long distances (e.g., 49 nm at 8 wt %), as evidenced in small-angle X-ray scattering (SAXS) (Figure 2a). This allows dissolved PVOH to diffuse between adjacent nanosheets that are confined in the cofacial geometry. A series of basal reflections are visible up to the fourth order, emphasizing the highly crystalline nature of the lamellar lyotropic suspension. Moreover, the SAXS curve exhibits a q^{-2} dependence at low- and intermediate q ranges that is characteristic for platy two-dimensional (2D) colloids.[45] This is highlighted by applying a calculated model of disks with a diameter of 20 μm and thickness of 1 nm separated to a d_{001} of 49 ± 5.5 nm using a Gauss distribution (Figure 2a).

A ternary aqueous suspension comprised of Hec nanosheets and PVOH in a wt % ratio of Hec/PVOH 40:60 totaling to a solid content of 5 wt % was used to fabricate nanocomposite liners via slot die coating on a corona-treated poly(ethylene terephthalate) (PET) foil (Figure 2b). Slot die coating is a universally applicable coating tool that can be easily adapted to an industrial scale with high throughput. Recently, we showed that it is ideally suitable for processing nematic phases consisting of high aspect ratio nanosheets.[46] It gives access to perfectly textured 1D "single domain crystalline" wet films, where the nanosheets are aligned in parallel with the PET substrate due to the high shear fields beneath the lips of a slot die. The shear-oriented nanosheets have sufficient inertness to maintain their orientation upon solvent removal and drying, yielding outstanding barrier coatings with clay nanosheets oriented parallel to the flat substrate.

It is known that processing influences the nanocomposite morphology[47] and consequently affects barrier properties.[24,48−52] Although starting from a single nematic suspension, tuning the drying temperature interestingly leads to different self-assembled nanocomposite morphologies (Figure 2c). At high filler contents, a polymer experiences severe confinement and is estimated to be exposed to high pressure[53] because the interlayer height between nanosheets is in the same range as the diameter of polymer chains. Here, we

worked with 40 wt % Hec corresponding to 23 vol % in the dried nanocomposite film as cross-checked by thermogravimetric analysis (Figure S1). Assuming an equidistant 1D crystalline ordering of 1 nm thick Hec nanosheets, this provides an interlayer space of only 3.3 nm for the polymer (Section S1), which is certainly far below the radius of gyration. Therefore, a polymer is forced to rearrange into a densely packed structure within the confined space of clay nanosheets, which involves a drastic depletion of conformational freedom for the polymer chain segments.[54−56] It is known that conformational entropy plays a significant role in interfacial self-assembly, especially for long-chain molecules such as polymers,[57] and thus confinement can dictate the structural formation direction.[58,59] As intercalated clay/PVOH nanocomposite structures could be obtained,[27,28,31,36−38] apparently, this entropic loss may be compensated with an enthalpic contribution, i.e., attractive complexation interactions with interlayer cations and potentially hydrogen bonding to the clay surface.[48] Most studies focus on modifying clay nanosheets by ion exchange to enhance the attractive interactions with polymers, but less attention has been paid to entropic effects. For a more detailed discussion of entropic effects in the polymer nanocomposite self-assembly, we refer to a recently published review from Yan et al.[60]

Surprisingly, we found that for PVOH/Hec nanocomposites, the balance of entropy and enthalpy happens to be subtle enough to be pushed in favor of one or the other simply by changing the temperature of the wet coating drying by some 30 °C. Four samples were prepared (Figure 3a) and denoted as PVOH/Hec X °C, where X is the respective drying temperature of the wet coatings. The X-ray diffraction (XRD) pattern of PVOH/Hec 20 °C displays a rational series of basal reflections with a d-spacing of 4.1 nm, corresponding to an interlayer height of 3.1 nm, which is in good agreement with expectations for the given filler content of 23 vol %. As indicated by a rational $00l$ series up to the third order, the 1D crystallinity of the intercalated single domain film is good. This is corroborated by transmission electron microscopic (TEM) cross-sectional images (Figure 3b) showing an equidistant spacing of Hec nanosheets.
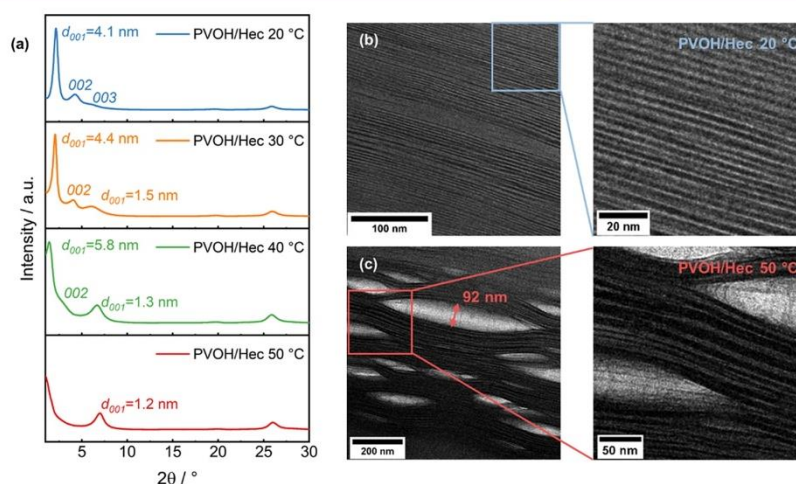
Figure 3. Structural investigation of nanocomposites. (a) XRD patterns of PVOH/Hec films on PET dried at different temperatures. The broad reflexes at $2\theta \approx 26$ °C arise from the PET foil (Figure S2). Cross-sectional TEM images of (b) PVOH/Hec 20 °C (blue) and (c) PVOH/Hec 50 °C (red). The red arrow shows bright segregated lenses of neat PVOH up to 92 nm thickness. The right TEM images display zoomed-in regions (dark: Hec nanosheets, bright: PVOH).

Upon raising the drying temperature from 20 to 30 °C, a second basal spacing becomes apparent at $d_{001} = 1.5$ nm, while the basal spacing of the intercalated domain shifts slightly to 4.4 nm. Such shifts are due to effects of the so-called random interstratification.[61] If different domain sizes are stacked, the X-ray beam produces an apparent weighted average within the coherence length of the X-ray beam (460 nm for in-house X-ray tubes). In this line and according to Meuring's rules,[61] domains producing an apparent d-spacing of 1.5 nm are comprised of a random stack of clay-only ($d_{001} = 0.96$ nm) and intercalated ($d_{001} = 4.1$ nm) stacks. The domains producing an apparent d-spacing of 4.4 nm, in turn, are comprised of intercalated stacks and phase-segregated, but thin, PVOH lenses (Figure S3). The tendency to phase-segregate becomes gradually more pronounced at a drying temperature of 40 °C. The nanocomposite films obtained at this temperature continue to be biphasic, while the weight fraction of clay-only domains in the first and segregated PVOH lenses in the second increases shifting the apparent d-spacings to 1.3 and 5.8 nm, respectively. Finally, at the maximum drying temperature of 50 °C allowed by the slot die table, phase segregation is almost complete. The apparent basal spacing of the random interstratification of intercalated and phase-segregated PVOH lenses is out of the measuring range of the applied diffractometer. The presence of some intercalated domains was, however, confirmed by TEM micrographs (Figure 3c). The apparent basal spacing of randomly interstratified domains of clay-only and intercalated stacks approached the basal spacing of Hec ($d_{001} = 0.96$ nm), which exhibits a distinct d_{001} reflection of 1.2 nm in the diffractogram of PVOH/Hec 50 °C. Aside from this phase, bright slabs of segregated neat PVOH lenses are also a prominent feature in the TEM micrographs (Figure 3c). We assume that further increasing the drying temperature of the wet coating would increase the phase separation to a higher extent approaching the basal spacing of neat Hec ($d_{001} = 0.96$ nm) and finally realizing total phase separation with apparent Hec- and PVOH-only domains as indicated in Figure 1b.

Upon solvent removal, a thermodynamically driven partial phase segregation occurs when increasing the drying temperature of the wet film. The entropic cost of confining PVOH in the interlayer gap of 3.1 nm becomes increasingly higher at elevated temperatures until finally preferring segregation. However, segregation is kinetically slowed down due to the large 20 μm diameter of the Hec nanosheets creating a tortuous path that gradually becomes more tortuous as the solvent is removed and restricts mass transport.[62]

As the application of PVOH as a barrier material is critically limited by the onset of swelling at a low RH of 55%, the influence of crystallinity on this swelling onset and barrier properties was investigated. Measuring water vapor transmission rates (WVTR) at 23 °C as a function of RH is the most sensitive probe for the moisture sensitivity of the four differently dried samples (Figure 4a). Indeed, a clear trend is discernible in the entire range of 0−90% RH. The WVTR values decrease at any given RH with decreasing drying temperature (Table S1). For PVOH/Hec 20 °C and PVOH/Hec 50 °C, water vapor uptake was determined gravimetrically (Figure 4b). For the crystalline sample PVOH/Hec 20 °C, no mass gain was observed up to 50% RH though above this threshold, swelling quickly sets in. On the contrary, the PVOH/Hec 50 °C sample adsorbs water vapor even below 50% RH, and the mass increases continuously throughout the complete humidity range. Interestingly, at 95% RH, the two samples showed a similar mass gain. Adsorbed water molecules in a 1D hybrid structure could either fill voids in the intercalated polymer matrix, or swelling might be accompanied by increasing the interlayer height. The latter is the case for PVOH/Hec 20 °C at 65% RH, where the d-spacing starts to increase (Figure S4), which is in line with the gravimetric results. However, swelling is limited to an increase of basal spacing of only 17% even at a high RH of 90% (Figure 4c). Unfortunately, as discussed above, apparent basal spacings of PVOH/Hec 50 °C are influenced by interstratification and, therefore, may not be interpreted to reflect the swelling of intercalated domains. In summary, as compared to the
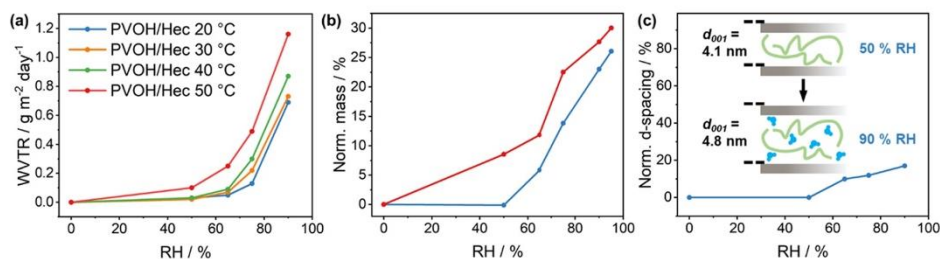
Figure 4. Swelling and its impact on permeability. (a) WVTR at 23 °C of the PVOH/Hec nanocomposite coatings on PET dried at different temperatures as a function of RH. (b) Normalized gravimetric water uptake as a function of RH for PVOH/Hec 20 °C (blue) and PVOH/Hec 50 °C (red). (c) Normalized d-spacing as a function of RH for PVOH/Hec 20 °C. The inset sketches the increase of the d-spacing above 50% RH for PVOH/Hec 20 °C upon water intercalation into the interlayer space.

disordered, segregated films, the 1D crystalline, intercalated PVOH films show less moisture sensitivity at elevated RH. The more hydrophobic character might render them appropriate for the oxygen barrier at relevant RH of 65% as per ISO 21309-2:2019 standard.

As the oxygen transmission rates (OTR) are dependent on the thickness of the barrier liner and the substrate permeability, Roberts et al. suggested removing the substrate influence by employing a series expansion to obtain the OTR of the neat coating.[63] Moreover, OTR was converted into OP by normalizing to 1 μm to facilitate comparability.

For both PVOH/Hec 20 °C and PVOH/Hec 50 °C, the incorporation of Hec nanosheets into PVOH shows an improvement of the OP by several orders of magnitude (Section S2, Tables S2, S3, and S4). While the OP values of PVOH/Hec 50 °C at any given RH are much lower than those of neat PVOH, the variation with RH is similar (Figure 5).
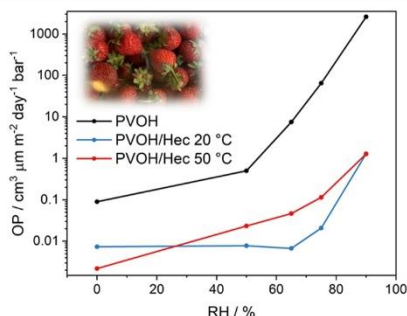
Figure 5. Oxygen barrier properties. Oxygen permeability at 23 °C of neat PVOH, PVOH/Hec 20 °C, and PVOH/Hec 50 °C coatings as a function of RH. The coating thickness is measured to be 3.7 μm for the nanocomposites and 4.6 μm for the neat PVOH film. The inset shows the high transparency of a PVOH/Hec 20 °C coating on PET of a strawberry packaging.

Interestingly, at an industrially less relevant RH of 0%, the OP for PVOH/Hec 50 °C is lower than the OP of the 1D crystalline Bragg Stack film of PVOH/Hec 20 °C. Strong inter- and intramolecular H bonding yields very good oxygen barrier performance for bulk PVOH in a dry state as present in the segregated lenses of PVOH/Hec 50 °C.[8,9] These cohesive forces might get disrupted due to the confinement present in the intercalated state of PVOH/Hec 20 °C.

As suggested by Grunlan et al.,[64] most OH groups of PVOH in the intercalated state are involved in H bonding with the clay basal surface and potentially in the complexation of the interlayer cations, which are less prone to hydrolysis and hence swelling. This hinders the adsorption of water molecules and consequently the plasticization of PVOH. This, in turn, pushes the onset of swelling to higher RH, and the OP of PVOH/Hec 20 °C was found to be hardly affected up to a RH of 65%. As previously observed for PVP/Hec hybrid Bragg stacks,[26] OP even slightly decreases up to 65% RH. This is somewhat counterintuitive since above 50% RH, water uptake sets in (Figure 4b,c). This observation has been attributed to water molecules initially filling free volume.[65,66] While the OP at 65% RH (which is relevant for food packaging) for neat PVOH is inferior and for PVOH/Hec 50 °C is roughly in line with a standard material like EVOH, realizing the 1D crystalline Bragg stack structure makes the same nanocomposite formulation by far superior to EVOH.[67] The PVOH/Hec 20 °C coating is, moreover, completely transparent due to the perfect textured orientation of the barrier pigment (Figure 5 inset). Optical properties of food packaging are of economic importance as customers prefer to check groceries visually. The total transmittance of the PVOH/Hec 20 °C coated PET substrate is almost not affected compared to the neat PET foil (Figure S5). Only haze and clarity of the PVOH/Hec 20 °C coated PET are slightly increased and decreased, respectively. In conclusion, the optical properties and the solid barrier performance at 65% RH render this biodegradable material highly appropriate for food packaging.

■ CONCLUSIONS

PVOH/Hec represents a special nanocomposite system where the balance of cohesive enthalpic interactions of the polymer and filler and entropic effects due to confinement are balanced subtle enough to allow for controlling the morphology by the temperature of drying of wet coatings. This, for the first time, allows studying the impact of crystallinity vs disordered morphology on the gas permeabilities and moisture sensitivity, while the composition, type of filler, and processing are kept constant. 1D crystalline hybrid Bragg Stacks clearly are less prone to swelling, rendering the crystalline PVOH/Hec system a promising, low-cost, waterborne, and biodegradable barrier material even at an elevated RH of up to 65%.

■ EXPERIMENTAL SECTION

Materials and Fabrication of Nanocomposite Films. The synthetic clay sodium fluorohectorite (Hec,

129

$[Na_{0.5}]^{inter}[Mg_{2.5}Li_{0.5}]^{oct}[Si_4]^{tet}O_{10}F_2)$ was produced according to a published literature procedure and features a cation exchange capacity of 1.27 mmol g^{-1}.[68,69] PVOH Mowiol 20-98 (M_w = 125 000 g mol^{-1}, 98 mol % hydrolyzed) was purchased from Sigma-Aldrich. Corona-treated PET foils (36 μm) were obtained from Bleher Folientechnik GmbH (Germany) and polylactic acid (PLA) foils (25 μm) from Pütz GmbH (Germany).

Pristine Hec powder was equilibrated at 43% RH for 7 days in a desiccator to assure a uniform crystalline swelling state. Subsequently, the powder was added to double-distilled water to obtain a 5 wt % sample. The sample was placed in an overhead shaker for 7 days to produce a nematic suspension with delaminated, single Hec nanosheets via soft osmotic swelling. PVOH (Mowiol 20−98) powder was added to double-distilled water and dissolved under reflux for 2 h at 80 °C to obtain a 5 wt % solution. The Hec sample was added dropwise to the PVOH solution under gentle stirring to realize a ternary suspension with a total solid content of 5 wt % and a wt % ratio of Hec/PVOH of 40:60.

Slot Die Coating. Prior to slot die coating, the ternary suspension was homogenized under vacuum to remove residual air bubbles (5 min, 50 mbar, and up to 2500 rpm) using a SpeedMixer DAC 400.2 VAC-P (Hauschild, Germany). The nanocoatings were fabricated employing a TSE Table Coater with a 1-Layer Slot Die 300 mm, AAA (TSE Troller AG, Switzerland). The coating width was set to 210 mm by applying a 165 μm thick shim as slot height, and the coating gap was adjusted to 186 μm (150 μm coating height + 36 μm PET). Accordingly, the pump flow rate (3.8 mL min^{-1}) and the table speed (0.2 m min^{-1}) were set. The table temperature referred to as the drying temperature in this study was adjusted to the desired experiment (20, 30, 40, and 50 °C).

For comparison, an aqueous solution comprised of 5 wt % PVOH (Mowiol 20-98) was doctor bladed on a PLA foil yielding a dry coating thickness of 4.6 μm.

Characterization Methods. *Small-Angle X-ray Scattering (SAXS).* SAXS investigations were conducted using the system "Ganesha Air" (SAXSLAB, Denmark), equipped with a rotating anode X-ray source (copper, MicoMax 007HF, Rigaku Corporation, Japan). Different sample-to-detector positions were adopted to cover a wide range of scattering vectors. A position-sensitive detector (PILATUS 300K, Dectris, Switzerland) was used. Measurements of the suspension were performed in 1 mm glass capillaries (Hilgenberg, Germany) at room temperature. The 1D data ($I(q)$ vs q with intensity $I(q)$ and scattering vector q) are in absolute scale and are background corrected. In addition, by employing a self-made crossed polarizer, the birefringence of the suspension was checked.

Scanning Electron Microscopy (SEM). SEM pictures were recorded using the system ZEISS LEO 1530 (Carl Zeiss AG, Germany) operating at 3 kV, equipped with an in-lens secondary electron detector. Samples were prepared by drop casting a 0.0001 wt % Hec suspension on a plasma-treated silicon wafer and subsequently sputtered with 1.2 nm platinum.

Transmission Electron Microscopy (TEM). TEM images of the cross sections were recorded employing a JEOL-JEM-2200FS (JEOL GmbH, Germany) microscope. Cross sections were prepared from the nanocomposite films using a JEOL EM-09100IS Cryo Ion Slicer (JEOL GmbH, Germany).

X-ray Diffraction (XRD). XRD patterns were obtained on a Bragg−Brentano-type diffractometer (Empyrean, Malvern Panalytical BV, The Netherlands) equipped with a PIXcel-1D detector using Cu Kα radiation (λ = 1.54187 Å). All patterns were analyzed using Malvern Panalyticals's HighScore Plus software.

Moisture Sensitivity Investigations. Prior to measurements, the nanocomposite films were dried under vacuum (10^{-3} mbar) at 70 °C for 7 days. The gravimetric water adsorption was analyzed by an increase in the weight of a specific film area. The weight was measured on a Mettler Toledo Microbalance Type WXT s3DU (Mettler-Toledo GmbH, Germany) with a lower repeatability range of 0.008 mg. The specific film area was obtained using a punching tool. XRD and weight measurements were first performed on the dry samples allowing normalization to the starting values. Subsequently, the

nanocomposite films were equilibrated for 7 days at every respective RH in a humidity chamber type Memmert HCP105 (Memmert GmbH + Co. KG, Germany) and were later weighed or analyzed via XRD. For each respective RH, the average mass of three PET-only samples was subtracted to yield access to the neat mass of the nanocomposite coatings.

Water Vapor Transmission Rate (WVTR). WVTR figures were obtained employing a Mocon PERMATRAN-W Model 3/33 (Mocon Inc.). The measurements were performed at 23 °C and sufficient time for moisture conditioning was guaranteed. WVTR values were determined at 50, 65, 75, and 90% RH. The WVTR was assumed to be 0 g m^{-2} day^{-1} at 0% RH and certainly not measured.

Oxygen Transmission Rate (OTR). OTR figures were determined using a Mocon OX-TRAN 2/21 M10× (Mocon Inc.) for the nanocomposite coatings and a Mocon OX-TRAN 2/21 (Mocon Inc.) for the neat PVOH film. The measurements were conducted at 23 °C and RH of 0, 50, 65, 75, and 90%. All samples were carefully equilibrated at the relevant RH. A mixture of 98 vol % nitrogen and 2 vol % hydrogen was used as the carrier gas and pure oxygen as permeant (>99.95%, Linde Sauerstoff 3.5).

Optical Properties. Transmittance, haze, and clarity were measured on a BYK-Gardner Haze-Gard Plus (BYK-Gardner GmbH, Germany). An average of five measurements per film sample were taken.

Coating Thickness. The coating thickness was determined by employing a High-Accuracy Digimatic Micrometer (Mitutoyo, Japan) with a measuring range of 0−25 mm and a resolution of 0.1 μm. A mean value was obtained from 10 measurement points in the permeability area of the film. The thickness of the substrate was subsequently subtracted.

■ ASSOCIATED CONTENT

ⓈI Supporting Information

The Supporting Information is available free of charge at https://pubs.acs.org/doi/10.1021/acsami.1c14246.

Thermogravimetric analysis and WVTR/OTR/OP values of nanocomposite films; XRD pattern of the neat PET foil and XRD patterns of PVOH/Hec 20 °C as a function of RH; TEM image of PVOH/Hec 30 °C; evaluation of the optical properties of the films; calculation of the expected *d*-spacings of nanocomposites (PDF)

■ AUTHOR INFORMATION

Corresponding Author

Josef Breu − *Bavarian Polymer Institute and Department of Chemistry, University of Bayreuth, Bayreuth 95447, Germany;* ⊙ orcid.org/0000-0002-2547-3950; Email: josef.breu@uni-bayreuth.de

Authors

Maximilian Röhrl − *Bavarian Polymer Institute and Department of Chemistry, University of Bayreuth, Bayreuth 95447, Germany*
Lukas K. S. Federer − *Bavarian Polymer Institute and Department of Chemistry, University of Bayreuth, Bayreuth 95447, Germany*
Renee L. Timmins − *Bavarian Polymer Institute and Department of Chemistry, University of Bayreuth, Bayreuth 95447, Germany*
Sabine Rosenfeldt − *Bavarian Polymer Institute and Department of Chemistry, University of Bayreuth, Bayreuth 95447, Germany*

Theresa Dörres − *Bavarian Polymer Institute and Department of Chemistry, University of Bayreuth, Bayreuth 95447, Germany*

Christoph Habel − *Bavarian Polymer Institute and Department of Chemistry, University of Bayreuth, Bayreuth 95447, Germany*

Complete contact information is available at:
https://pubs.acs.org/10.1021/acsami.1c14246

Author Contributions

The manuscript was written through the contributions of all authors. All authors have given approval to the final version of the manuscript.

Notes

The authors declare no competing financial interest.

■ **REFERENCES**

(1) Plastics - the Facts 2020. *An Analysis of European Latest Plastics Production, Demand and Waste Data*; PlasticsEurope, Brussels, 2020.

(2) Zabihzadeh Khajavi, M.; Ebrahimi, A.; Yousefi, M.; Ahmadi, S.; Farhoodi, M.; Mirza Alizadeh, A.; Taslikh, M. Strategies for Producing Improved Oxygen Barrier Materials Appropriate for the Food Packaging Sector. *Food Eng. Rev.* **2020**, *12*, 346−363.

(3) Lange, J.; Wyser, Y. Recent innovations in barrier technologies for plastic packaging—a review. *Packag. Technol. Sci.* **2003**, *16*, 149−158.

(4) Akelah, A. Polymers in Food Packaging and Protection. In *Functionalized Polymeric Materials in Agriculture and the Food Industry*, Springer US: Boston, 2013, pp 293−347.

(5) Baker, M. I.; Walsh, S. P.; Schwartz, Z.; Boyan, B. D. A review of polyvinyl alcohol and its uses in cartilage and orthopedic applications. *J. Biomed. Mater. Res., Part B* **2012**, *100B*, 1451−1457.

(6) Goodship, V.; Jacobs, D. Polyvinyl Alcohol: Materials, Processing and Applications. *Rapra Rev. Rep.* **2009**, *16*, No. 130.

(7) Aslam, M.; Kalyar, M. A.; Raza, Z. A. Polyvinyl alcohol: A review of research status and use of polyvinyl alcohol based nanocomposites. *Polym. Eng. Sci.* **2018**, *58*, 2119−2132.

(8) Iwanami, T.; Hirai, Y. Ethylene vinyl alcohol resins for gas-barrier material. *Tappi J.* **1983**, *66*, 85−90.

(9) Kollen, W.; Gray, D. Controlled Humidity for Oxygen Barrier Determinations. *J. Plast. Film Sheeting* **1991**, *7*, 103−117.

(10) Zhang, Z.; Britt, I. J.; Tung, M. A. Permeation of oxygen and water vapor through EVOH films as influenced by relative humidity. *J. Appl. Polym. Sci.* **2001**, *82*, 1866−1872.

(11) Cooksey, K. Food Packaging, Principles and Practices. In *Packaging Technology and Science*; Robertson, G., Ed.; CRC, Taylor and Francis, Boca Raton, FL, 2008; Vol. 21, pp 57−59.

(12) Nyflött, Å.; Meriçer, Ç.; Minelli, M.; Moons, E.; Järnström, L.; Lestelius, M.; Baschetti, M. G. The influence of moisture content on the polymer structure of polyvinyl alcohol in dispersion barrier coatings and its effect on the mass transport of oxygen. *J. Coat. Technol. Res.* **2017**, *14*, 1345−1355.

(13) Thomas, S.; Joseph, K.; Malhotra, S. K.; Goda, K.; Sreekala, M. S. *Polymer Composites, Macro- and Microcomposites*. Wiley, 2012.

(14) Kim, J. M.; Lee, M. H.; Ko, J. A.; Kang, D. H.; Bae, H.; Park, H. J. Influence of Food with High Moisture Content on Oxygen Barrier Property of Polyvinyl Alcohol (PVA)/Vermiculite Nanocomposite Coated Multilayer Packaging Film. *J. Food Sci.* **2018**, *83*, 349−357.

(15) GmbH, K. E. EVALTM Properties. http://www.evalevoh.com/en/eval-properties/barrier-to-oxygen/relative-humidity.aspx (accessed June 29, 2021).

(16) López-Rubio, A.; Hernández-Muñoz, P.; Gimenez, E.; Yamamoto, T.; Gavara, R.; Lagarón, J. M. Gas barrier changes and morphological alterations induced by retorting in ethylene vinyl alcohol−based food packaging structures. *J. Appl. Polym. Sci.* **2005**, *96*, 2192−2202.

(17) Habel, C.; Schöttle, M.; Daab, M.; Eichstaedt, N. J.; Wagner, D.; Bakhshi, H.; Agarwal, S.; Horn, M. A.; Breu, J. High-Barrier, Biodegradable Food Packaging. *Macromol. Mater. Eng.* **2018**, *303*, No. 1800333.

(18) Ebina, T. Development of Clay-Based Films. *Chem. Rec.* **2018**, *18*, 1020−1032.

(19) Kunz, D. A.; Schmid, J.; Feicht, P.; Erath, J.; Fery, A.; Breu, J. Clay-Based Nanocomposite Coating for Flexible Optoelectronics Applying Commercial Polymers. *ACS Nano* **2013**, *7*, 4275−4280.

(20) Sarfraz, J.; Gulin-Sarfraz, T.; Nilsen-Nygaard, J.; Pettersen, M. K. Nanocomposites for Food Packaging Applications: An Overview. *Nanomaterials* **2021**, *11*, 10.

(21) Zhu, J.; Kumar, A.; Hu, P.; Habel, C.; Breu, J.; Agarwal, S. Layering-Triggered Delayering with Exfoliated High-Aspect Ratio Layered Silicate for Enhanced Gas Barrier, Mechanical Properties, and Degradability of Biodegradable Polymers. *Global Challenges* **2020**, *4*, No. 2000030.

(22) Doblhofer, E.; Schmid, J.; Rieß, M.; Daab, M.; Suntinger, M.; Habel, C.; Bargel, H.; Hugenschmidt, C.; Rosenfeldt, S.; Breu, J.; Scheibel, T. Structural Insights into Water-Based Spider Silk Protein−Nanoclay Composites with Excellent Gas and Water Vapor Barrier Properties. *ACS Appl. Mater. Interfaces* **2016**, *8*, 25535−25543.

(23) DeRocher, J. P.; Gettelfinger, B. T.; Wang, J.; Nuxoll, E. E.; Cussler, E. L. Barrier membranes with different sizes of aligned flakes. *J. Membr. Sci.* **2005**, *254*, 21−30.

(24) Tsurko, E. S.; Feicht, P.; Nehm, F.; Ament, K.; Rosenfeldt, S.; Pietsch, I.; Roschmann, K.; Kalo, H.; Breu, J. Large Scale Self-Assembly of Smectic Nanocomposite Films by Doctor Blading versus Spray Coating: Impact of Crystal Quality on Barrier Properties. *Macromolecules* **2017**, *50*, 4344−4350.

(25) Cussler, E. L.; Hughes, S. E.; Ward, W. J.; Aris, R. Barrier membranes. *J. Membr. Sci.* **1988**, *38*, 161−174.

(26) Schilling, T.; Habel, C.; Rosenfeldt, S.; Röhrl, M.; Breu, J. Impact of Ultraconfinement on Composite Barriers. *ACS Appl. Polym. Mater.* **2020**, *2*, 3010−3015.

(27) Walther, A.; Bjurhager, I.; Malho, J.-M.; Pere, J.; Ruokolainen, J.; Berglund, L. A.; Ikkala, O. Large-Area, Lightweight and Thick Biomimetic Composites with Superior Material Properties via Fast, Economic, and Green Pathways. *Nano Lett.* **2010**, *10*, 2742−2748.

(28) Morits, M.; Verho, T.; Sorvari, J.; Liljeström, V.; Kostiainen, M. A.; Gröschel, A. H.; Ikkala, O. Toughness and Fracture Properties in Nacre-Mimetic Clay/Polymer Nanocomposites. *Adv. Funct. Mater.* **2017**, *27*, No. 1605378.

(29) Eckert, A.; Rudolph, T.; Guo, J.; Mang, T.; Walther, A. Exceptionally Ductile and Tough Biomimetic Artificial Nacre with Gas Barrier Function. *Adv. Mater.* **2018**, *30*, No. 1802477.

(30) Chen, H.-B.; Schiraldi, D. A. Flammability of Polymer/Clay Aerogel Composites: An Overview. *Polym. Rev.* **2019**, *59*, 1−24.

(31) Ding, F.; Liu, J.; Zeng, S.; Xia, Y.; Wells, K. M.; Nieh, M.-P.; Sun, L. Biomimetic nanocoatings with exceptional mechanical, barrier, and flame-retardant properties from large-scale one-step coassembly. *Sci. Adv.* **2017**, *3*, No. e1701212.

(32) Song, Y.; Gerringer, J.; Qin, S.; Grunlan, J. C. High Oxygen Barrier Thin Film from Aqueous Polymer/Clay Slurry. *Ind. Eng. Chem. Res.* **2018**, *57*, 6904−6909.

(33) Habel, C.; Tsurko, E. S.; Timmins, R. L.; Hutschreuther, J.; Kunz, R.; Schuchardt, D. D.; Rosenfeldt, S.; Altstädt, V.; Breu, J. Lightweight Ultra-High-Barrier Liners for Helium and Hydrogen. *ACS Nano* **2020**, *14*, 7018−7024.

(34) Gaume, J.; Taviot-Gueho, C.; Cros, S.; Rivaton, A.; Thérias, S.; Gardette, J.-L. Optimization of PVA clay nanocomposite for ultra-barrier multilayer encapsulation of organic solar cells. *Sol. Energy Mater. Sol. Cells* **2012**, *99*, 240−249.

(35) Tsurko, E. S.; Feicht, P.; Habel, C.; Schilling, T.; Daab, M.; Rosenfeldt, S.; Breu, J. Can high oxygen and water vapor barrier nanocomposite coatings be obtained with a waterborne formulation? *J. Membr. Sci.* **2017**, *540*, 212−218.

(36) Zhang, B.; Wang, Q.; Zhang, Y.; Gao, W.; Hou, Y.; Zhang, G. A self-assembled, nacre-mimetic, nano-laminar structure as a superior charge dissipation coating on insulators for HVDC gas-insulated systems. *Nanoscale* **2019**, *11*, 18046−18051.

(37) Strawhecker, K. E.; Manias, E. Structure and Properties of Poly(vinyl alcohol)/Na+ Montmorillonite Nanocomposites. *Chem. Mater.* **2000**, *12*, 2943−2949.

(38) Sapalidis, A. A.; Katsaros, F. K.; Steriotis, T. A.; Kanellopoulos, N. K. Properties of poly(vinyl alcohol)—Bentonite clay nano-composite films in relation to polymer−clay interactions. *J. Appl. Polym. Sci.* **2012**, *123*, 1812−1821.

(39) Philipp, A.; Hummel, P.; Schilling, T.; Feicht, P.; Rosenfeldt, S.; Ertl, M.; Schöttle, M.; Lechner, A. M.; Xu, Z.; Gao, C.; Breu, J.; Retsch, M. Anisotropic Thermal Transport in Spray-Coated Single-Phase Two-Dimensional Materials: Synthetic Clay Versus Graphene Oxide. *ACS Appl. Mater. Interfaces* **2020**, *12*, 18785−18791.

(40) Wang, Z.; Rolle, K.; Schilling, T.; Hummel, P.; Philipp, A.; Kopera, B. A. F.; Lechner, A. M.; Retsch, M.; Breu, J.; Fytas, G. Tunable Thermoelastic Anisotropy in Hybrid Bragg Stacks with Extreme Polymer Confinement. *Angew. Chem., Int. Ed.* **2020**, *59*, 1286−1294.

(41) Rolle, K.; Schilling, T.; Westermeier, F.; Das, S.; Breu, J.; Fytas, G. Large Tg Shift in Hybrid Bragg Stacks through Interfacial Slowdown. *Macromolecules* **2021**, *54*, 2551−2560.

(42) Lerf, A. Storylines in intercalation chemistry. *Dalton Trans.* **2014**, *43*, 10276−10291.

(43) Rosenfeldt, S.; Stöter, M.; Schlenk, M.; Martin, T.; Albuquerque, R. Q.; Förster, S.; Breu, J. In-Depth Insights into the Key Steps of Delamination of Charged 2D Nanomaterials. *Langmuir* **2016**, *32*, 10582−10588.

(44) Stöter, M.; Kunz, D. A.; Schmidt, M.; Hirsemann, D.; Kalo, H.; Putz, B.; Senker, J.; Breu, J. Nanoplatelets of Sodium Hectorite Showing Aspect Ratios of ≈20 000 and Superior Purity. *Langmuir* **2013**, *29*, 1280−1285.

(45) Boldon, L.; Laliberte, F.; Liu, L. Review of the fundamental theories behind small angle X-ray scattering, molecular dynamics simulations, and relevant integrated application. *Nano Rev.* **2015**, *6*, No. 25661.

(46) Röhrl, M.; Mettke, J. H.; Rosenfeldt, S.; Schmalz, H.; Mansfeld, U.; Timmins, R. L.; Habel, C.; Breu, J.; Durst, F. Shear orientation of nematic phases of clay nanosheets: processing of barrier coatings. *J. Coat. Technol. Res.* **2021**, accepted; DOI: 10.1007/s11998-021-00535-4.

(47) Jordan, J.; Jacob, K. I.; Tannenbaum, R.; Sharaf, M. A.; Jasiuk, I. Experimental trends in polymer nanocomposites—a review. *Mater. Sci. Eng.: A* **2005**, *393*, 1−11.

(48) Duncan, T. V. Applications of nanotechnology in food packaging and food safety: Barrier materials, antimicrobials and sensors. *J. Colloid Interface Sci.* **2011**, *363*, 1−24.

(49) Yeh, J.-M.; Liou, S.-J.; Lai, M.-C.; Chang, Y.-W.; Huang, C.-Y.; Chen, C.-P.; Jaw, J.-H.; Tsai, T.-Y.; Yu, Y.-H. Comparative studies of the properties of poly(methyl methacrylate)−clay nanocomposite materials prepared by in situ emulsion polymerization and solution dispersion. *J. Appl. Polym. Sci.* **2004**, *94*, 1936−1946.

(50) Pereira, D.; Losada, P. P.; Angulo, I.; Greaves, W.; Cruz, J. M. Development of a polyamide nanocomposite for food industry:

(51) Gorrasi, G.; Tortora, M.; Vittoria, V.; Pollet, E.; Lepoittevin, B.; Alexandre, M.; Dubois, P. Vapor barrier properties of polycapro-lactone montmorillonite nanocomposites: effect of clay dispersion. *Polymer* **2003**, *44*, 2271−2279.

(52) Zhu, J.; Habel, C.; Schilling, T.; Greiner, A.; Breu, J.; Agarwal, S. Filter-Through Method of Making Highly Efficient Polymer-Clay Nanocomposite Membranes. *Macromol. Mater. Eng.* **2019**, *304*, No. 1800779.

(53) Saito, T.; Okamoto, M.; Hiroi, R.; Yamamoto, M.; Shiroi, T. Poly(p-phenylenesulfide)-based nano-composite formation: Delami-nation of organically modified layered filler via solid-state processing. *Polymer* **2007**, *48*, 4143−4151.

(54) Chrissopoulou, K.; Andrikopoulos, K. S.; Fotiadou, S.; Bollas, S.; Karageorgaki, C.; Christofilos, D.; Voyiatzis, G. A.; Anastasiadis, S. H. Crystallinity and Chain Conformation in PEO/Layered Silicate Nanocomposites. *Macromolecules* **2011**, *44*, 9710−9722.

(55) Khan, P.; Goel, G. Martini Coarse-Grained Model for Clay−Polymer Nanocomposites. *J. Phys. Chem. B* **2019**, *123*, 9011−9023.

(56) Bollas, S.; Chrissopoulou, K.; Andrikopoulos, K. S.; Voyiatzis, G. A.; Anastasiadis, S. H. Polymer Conformation under Confinement. *Polymers* **2017**, *9*, No. 73.

(57) Zhu, G.; Huang, Z.; Xu, Z.; Yan, L.-T. Tailoring Interfacial Nanoparticle Organization through Entropy. *Acc. Chem. Res.* **2018**, *51*, 900−909.

(58) Zhang, R.; Lee, B.; Stafford, C. M.; Douglas, J. F.; Dobrynin, A. V.; Bockstaller, M. R.; Karim, A. Entropy-driven segregation of polymer-grafted nanoparticles under confinement. *Proc. Natl. Acad. Sci. U.S.A.* **2017**, *114*, 2462−2467.

(59) Liu, Z.; Guo, R.; Xu, G.; Huang, Z.; Yan, L.-T. Entropy-Mediated Mechanical Response of the Interfacial Nanoparticle Patterning. *Nano Lett.* **2014**, *14*, 6910−6916.

(60) Dai, X.; Hou, C.; Xu, Z.; Yang, Y.; Zhu, G.; Chen, P.; Huang, Z.; Yan, L.-T. Entropic Effects in Polymer Nanocomposites. *Entropy* **2019**, *21*, No. 186.

(61) Moore, D. M.; Reynolds, R. C. *X-ray Diffraction and the Identification and Analysis of Clay Minerals*, Oxford University Press, Oxford, 1989; Vol. 322.

(62) Habel, C.; Maiz, J.; Olmedo-Martínez, J. L.; López, J. V.; Breu, J.; Müller, A. J. Competition between nucleation and confinement in the crystallization of poly(ethylene glycol)/large aspect ratio hectorite nanocomposites. *Polymer* **2020**, *202*, No. 122734.

(63) Roberts, A. P.; Henry, B. M.; Sutton, A. P.; Grovenor, C. R. M.; Briggs, G. A. D.; Miyamoto, T.; Kano, M.; Tsukahara, Y.; Yanaka, M. Gas permeation in silicon-oxide/polymer (SiOx/PET) barrier films: role of the oxide lattice, nano-defects and macro-defects. *J. Membr. Sci.* **2002**, *208*, 75−88.

(64) Grunlan, J. C.; Grigorian, A.; Hamilton, C. B.; Mehrabi, A. R. Effect of clay concentration on the oxygen permeability and optical properties of a modified poly(vinyl alcohol). *J. Appl. Polym. Sci.* **2004**, *93*, 1102−1109.

(65) Muramatsu, M.; Okura, M.; Kuboyama, K.; Ougizawa, T.; Yamamoto, T.; Nishihara, Y.; Saito, Y.; Ito, K.; Hirata, K.; Kobayashi, Y. Oxygen permeability and free volume hole size in ethylene−vinyl alcohol copolymer film: temperature and humidity dependence. *Radiat. Phys. Chem.* **2003**, *68*, 561−564.

(66) Wang, J.; Gardner, D. J.; Stark, N. M.; Bousfield, D. W.; Tajvidi, M.; Cai, Z. Moisture and Oxygen Barrier Properties of Cellulose Nanomaterial-Based Films. *ACS Sustainable Chem. Eng.* **2018**, *6*, 49−70.

(67) Attractive protection for your food - Chlorine-free water-borne barriers https://www.kuraray-poval.com/fileadmin/technical_information/brochures/poval/Kuraray_Exceval_attractive_protection_for_your_food_engl.pdf (accessed June 22, 2021).

(68) Breu, J.; Seidl, W.; Stoll, A. J.; Lange, K. G.; Probst, T. U. Charge Homogeneity in Synthetic Fluorohectorite. *Chem. Mater.* **2001**, *13*, 4213−4220.

(69) Kalo, H.; Möller, M. W.; Ziadeh, M.; Dolejš, D.; Breu, J. Large scale melt synthesis in an open crucible of Na-fluorohectorite with superb charge homogeneity and particle size. *Appl. Clay Sci.* **2010**, *48*, 39−45.

Supporting Information

Disorder-Order Transition - Improving the Moisture Sensitivity of Waterborne Nanocomposite Barriers

Maximilian Röhrl, Lukas K. S. Federer, Renee L. Timmins, Sabine Rosenfeldt, Theresa Dörres,

Christoph Habel, and Josef Breu*

Bavarian Polymer Institute and Department of Chemistry, University of Bayreuth, Bayreuth

95447, Germany

*Email: josef.breu@uni-bayreuth.de

1

METHODS

Thermogravimetric Analysis (TGA). TGA measurements were performed employing a Linseis STA PT 1600 (Linseis Messgeräte GmbH, Germany). Prior to the analysis, the films were scratched off the PET substrate using a scalpel. Afterward, the samples were dried under vacuum (10^{-3} mbar) at 70 °C for 7 days. The dry samples were heated up under nitrogen atmosphere with a heating rate of 10 °C min^{-1} from room temperature to 1000°C.
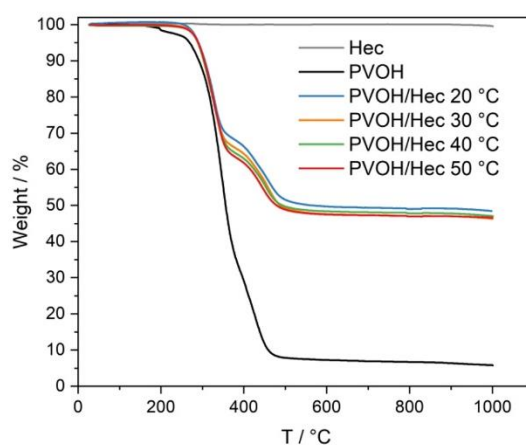
Figure S1. TGA curves of the nanocomposite films. For comparison, neat Hec and PVOH (Mowiol 20-98) are probed. The mass loss beginning from 300 °C are attributed to the thermal degradation of PVOH. Hec shows no decomposition up to 1000 °C. No decisive difference is observed in the thermal degradation of intercalated or bulk PVOH.

2

Section S1. Calculation of the expected d-spacing (d_{001}) in the dry nanocomposite film.
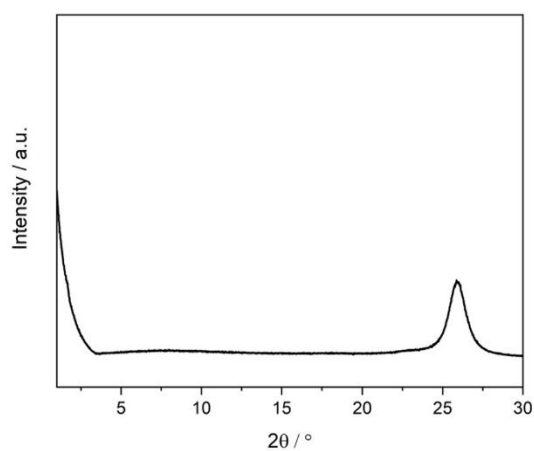
$$\varphi = \frac{wt\% \, (Hec) \cdot \rho(PVOH)}{wt\% \, (Hec) \cdot \rho(PVOH) + \cdot \left(100 \, wt\% - wt\% \, (Hec)\right) \cdot \rho(Hec)} \qquad \text{(E S1)}$$

With $\rho(PVOH) = 1.2 \, g/cm^3$, $\rho(Hec) = 2.7 \, g/cm^3$ as the respective densities, and 40 wt% (*Hec*) in the dry nanocomposite film; the volume content $\varphi(Hec) = 0.23$.

$$d_{001} = \frac{1 \, nm}{\varphi} \approx 4.3 \, nm \qquad \text{(E S2)}$$

The gallery height is given by the difference of d_{001} and the thickness of a Hec nanosheet of 1 nm. For 40 wt% Hec in the dry film, this yields a gallery height of ~3.3 nm for PVOH.

Figure S2. XRD pattern of the corona treated neat PET foil.

3
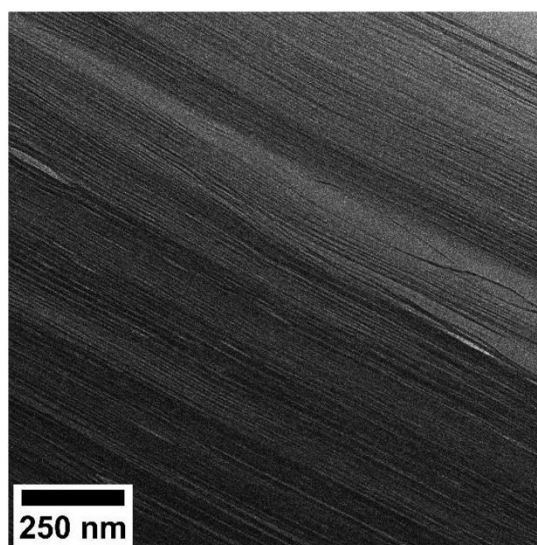
Figure S3. Cross-sectional TEM image of PVOH/Hec 30 °C showing intercalated stacks and thin phase segregated neat PVOH lenses.

4
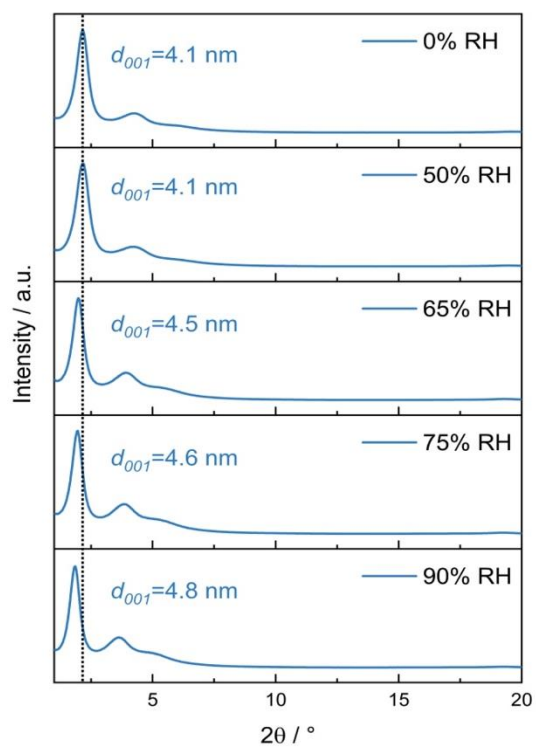
Figure S4. XRD patterns of PVOH/Hec 20 °C as a function of the relative humidity (RH). The dotted line refers to the basal spacing of d_{001}=4.1 nm of the dry nanocomposite.

5
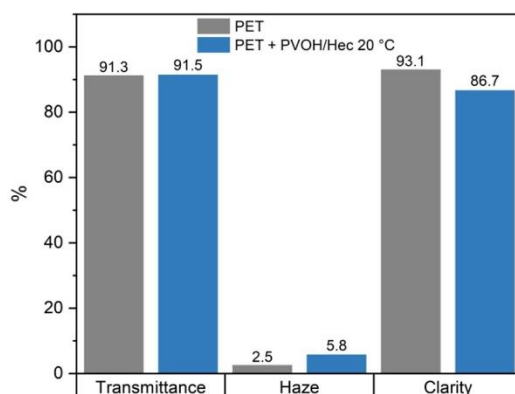
Figure S5. Optical properties (transmittance, haze, clarity) of the neat PET substrate and PET with slot die coated PVOH/Hec 20 °C.

6

Table S1: Water vapor transmission rates (WVTR) of PVOH/Hec nanocomposites dried at different temperatures, measured at 23 °C, and various relative humidities (RH) on PET.

Sample	WVTR / g m^{-2} day^{-1}				
	0 % RH	50 % RH	65 % RH	75 % RH	90 % RH
PVOH/Hec 20 °C	0	0.03	0.05	0.13	0.69
PVOH/Hec 30 °C	0	0.02	0.07	0.22	0.73
PVOH/Hec 40 °C	0	0.03	0.09	0.30	0.87
PVOH/Hec 50 °C	0	0.10	0.25	0.49	1.16

Table S2: Oxygen transmission rates (OTR) of PVOH (Mowiol 20-98), PVOH/Hec 20 °C, and PVOH/Hec 50 °C measured at 23 °C and various relative humidities (RH) on PET.

Sample	OTR / cm^3 m^{-2} day^{-1} bar^{-1}				
	0 % RH	50 % RH	65 % RH	75 % RH	90 % RH
PVOH (Mowiol 20-98)	0.02	0.11	1.62	13.91	302.47
PVOH/Hec 20 °C	0.0020	0.0021	0.0018	0.0056	0.3434
PVOH/Hec 50 °C	0.0006	0.0063	0.0126	0.0309	0.3415

Table S3: Oxygen permeability (OP) of neat PVOH (Mowiol 20-98), PVOH/Hec 20 °C, and PVOH/Hec 50 °C coatings at 23 °C and various relative humidities (RH).

Sample	OP/ cm^3 μm m^{-2} day^{-1} bar^{-1}				
	0 % RH	50 % RH	65 % RH	75 % RH	90 % RH
PVOH (Mowiol 20-98)	0.09	0.50	7.45	64.89	2596.67
PVOH/Hec 20 °C	0.0074	0.0078	0.0067	0.0207	1.2864
PVOH/Hec 50 °C	0.0022	0.0233	0.0466	0.1145	1.2792

7

Section S2. Calculation of the barrier improvement factor (BIF) upon the incorporation of impermeable Hec nanosheets into PVOH.

$$BIF = (P_{rel})^{-1} = \left(\frac{P}{P_0}\right)^{-1}$$

With P as permeability of nanocomposite film and P_0 as permeability of neat PVOH (Mowiol 20-98).

Table S4: BIF of PVOH/Hec 20 °C and PVOH/Hec 50 °C coatings at 23 °C and various relative humidities (RH) according to Section S2.

Sample	BIF				
	0 % RH	50 % RH	65 % RH	75 % RH	90 % RH
PVOH/Hec 20 °C	12	65	1119	3131	2019
PVOH/Hec 50 °C	41	22	160	567	2030

8

List of publications and patents

Publications and manuscripts:

(1) Schilling, T.; Habel, C.; Rosenfeldt, S.; Röhrl, M.; Breu, J., Impact of Ultraconfinement on Composite Barriers. *ACS Applied Polymer Materials* **2020**, *2* (7), 3010-3015.

(2) Venkateshaiah, A.; Havlíček, K.; Timmins, R. L.; Röhrl, M.; Wacławek, S.; Nguyen, N. H. A.; Černík, M.; Padil, V. V. T.; Agarwal, S., Alkenyl succinic anhydride modified tree-gum kondagogu: A bio-based material with potential for food packaging. *Carbohydrate Polymers* **2021**, *266*, 118126.

(3) Röhrl, M.; Federer, L. K. S.; Timmins, R. L.; Rosenfeldt, S.; Dörres, T.; Habel, C.; Breu, J., Disorder–Order Transition—Improving the Moisture Sensitivity of Waterborne Nanocomposite Barriers. *ACS Applied Materials & Interfaces* **2021**, *13* (40), 48101-48109.

(4) Timmins, R. L.; Kumar, A.; Röhrl, M.; Havlíček, K.; Agarwal, S.; Breu, J., High Barrier Nanocomposite Film with Accelerated Biodegradation by Clay Swelling Induced Fragmentation. *Macromolecular Materials and Engineering* **2021**, *307* (6), 2100727.

(5) Röhrl, M.; Mettke, J. H.; Rosenfeldt, S.; Schmalz, H.; Mansfeld, U.; Timmins, R. L.; Habel, C.; Breu, J.; Durst, F., Shear orientation of nematic phases of clay nanosheets: processing of barrier coatings. *Journal of Coatings Technology and Research* **2021**, *19* (2), 487-495.

(6) Dudko, V.; Timmins, R. L.; Khoruzhenko, O.; Röhrl, M.; Greve, C.; Rosenfeldt, S.; Tammelin, T.; Agarwal, S.; Herzig, E. M.; Breu, J., Spontaneous delamination of affordable natural vermiculite as a high barrier filler for biodegradable food packaging. *Materials Advances* **2022**, *3* (24), 9052-9062.

(7) Röhrl, M.; Timmins, R. L.; Rosenfeldt, S.; Schuchardt, D. D.; Uhlig, F.; Nürmberger, S.; Breu, J., Stretchable Clay Nanocomposite Barrier Film for Flexible Packaging. *ACS Applied Materials & Interfaces* **2023**, *15* (18), 22524-22531.

(8) Röhrl, M.; Ködel, J. F.; Timmins, R. L.; Callsen, C.; Aksit, M.; Fink, M. F.; Seibt, S.; Weidinger, A.; Battagliarin, G.; Ruckdäschel, H.; Schobert, R.; Breu,

J.; Biersack, B., New Functional Polymer Materials via Click Chemistry-Based Modification of Cellulose Acetate. *ACS Omega* **2023**, *8* (11), 9889-9895.

(9)   Schuchardt, D. D.; <u>Röhrl, M.</u>; Rosenfeldt, S.; Breu, J., Gas Barriers from In Situ Polymerized Poly(ethylene glycol) Diacrylate Clay Nanocomposites for Food Packaging. *ACS Applied Polymer Materials* **2023**, *5* (1), 576-582.

(10)   <u>Röhrl, M.</u>; Timmins, R. L.; Ghosh, D.; Schuchardt, D. D.; Rosenfeldt, S.; Nürmberger, S.; Bölz, U.; Agarwal, S.; Breu, J., Green and scalable processing of water-soluble, biodegradable polymer/clay barrier films. *Journal of Applied Polymer Science* **2023**, *140* (37), e54418.

(11)   Schuchardt, D.; <u>Röhrl, M.</u>; Federer, L.; Rosenfeldt, S.; Kalo, H.; Breu, J., Spraying Transparent Nanoglass Coatings for Food Packaging. *ACS Applied Nano Materials* **2023**, *6* (18), 17000-17008.

Patents:

(1) Caruso PL., Boswell E., Breu J., <u>Röhrl, M.</u>: Water-soluble nanocomposite barrier film. US20230234096A1 (Pub. Date: **2023-07-27**).

(2) Caruso PL., Boswell E., Breu J., <u>Röhrl, M.</u>: Nanocomposite barrier paper laminate. US20230235510A1 (Pub. Date: **2023-07-27**).

Eidesstattliche Versicherungen und Erklärungen

(§ 9 Satz 2 Nr. 3 PromO BayNAT)

Hiermit versichere ich eidesstattlich, dass ich die Arbeit selbstständig verfasst und keine anderen als die von mir angegebenen Quellen und Hilfsmittel benutzt habe (vgl. Art. 64 Abs. 1 Satz 6 BayHSchG).

(§ 9 Satz 2 Nr. 3 PromO BayNAT)

Hiermit erkläre ich, dass ich die Dissertation nicht bereits zur Erlangung eines akademischen Grades eingereicht habe und dass ich nicht bereits diese oder eine gleichartige Doktorprüfung endgültig nicht bestanden habe.

(§ 9 Satz 2 Nr. 4 PromO BayNAT)

Hiermit erkläre ich, dass ich Hilfe von gewerblichen Promotionsberatern bzw. -vermittlern oder ähnlichen Dienstleistern weder bisher in Anspruch genommen habe noch künftig in Anspruch nehmen werde.

(§ 9 Satz 2 Nr. 7 PromO BayNAT)

Hiermit erkläre ich mein Einverständnis, dass die elektronische Fassung meiner Dissertation unter Wahrung meiner Urheberrechte und des Datenschutzes einer gesonderten Überprüfung unterzogen werden kann.

(§ 9 Satz 2 Nr. 8 PromO BayNAT)

Hiermit erkläre ich mein Einverständnis, dass bei Verdacht wissenschaftlichen Fehlverhaltens Ermittlungen durch universitätsinterne Organe der wissenschaftlichen Selbstkontrolle stattfinden können.

…………………………………………………………………………………………

Ort, Datum, Unterschrift